This is to certify that the

dissertation entitled

INTERACTION OF ELF—LF ELECTROMAGNETIC FIELDS WITH

BIOLOGICAL SYSTEMS AND CONDUCTING OBJECTS

presented by

Huey-Ru Chuang

has been accepted towards fulfillment
of the requirements for

_Ph.D._ degree in _Electrical_ Engr.

_____
Major professor

Date ___10/14/87___

0-12771

06/29/92 153

INTERACTION OF ELF-LF ELECTROMAGNETIC FIELDS WITH BIOLOGICAL SYSTEMS AND CONDUCTING OBJECTS

By

Huey-Ru Chuang

To my beloved parents, brothers, and my future wife

e

p

ir
C
m

En
wit
hel

thei
pani
Ph.D

ACKNOWLEDGEMENTS

The longer in the journey of a man's life, the more he realizes how much of his achievements have come from the help of his family, friends, and fellow travelers.

I owe a great intellectual debt to my academic advisor, Dr. Kun-Mu Chen, for his enthusiastic guidance and advice, without which this research could not have been accomplished.

I am deeply grateful to Dr. Dennis P. Nyquist for the valuable assistance he gave me in the course of this research. Grateful thanks extend to committee members, Dr. Byron C. Drachman, Professor of the Department of Mathematics, and Dr. Edward Rothwell for many helpful comments and criticisms to this dissertation.

A special thank is due to Dr. Chun-Ju Lin, Professor of the Department of Electrical Engineering at the University of Detroit. Most part of this research was in joint effort with him. This dissertation was word-processed by PC-WRITE. Mr. Steven S. Leung's help in generating mathematical formulas and Greek symbols is highly appreciated.

Finally, I wish to express the most sincere gratitude to my parents and brothers for their love and encouragement. Their spoken and unspoken words of caring have accompanied me from the very beginning of my education to the final accomplishment of this Ph.D. degree.

IN

bod

elec

ante

indu

and

situa

syste

(surf

surfa

indu

indu

cha:

solu

meth

has

with

ABSTRACT

INTERACTION OF ELF-LF ELECTROMAGNETIC FIELDS WITH BIOLOGICAL SYSTEMS AND CONDUCTING OBJECTS

By

Huey-Ru Chuang

The knowledge of the induced electric field and current in a biological body is very important for investigating the potential health hazard due to the electromagnetic field of an extremely high voltage (EHV) power line and ELF antenna systems. This thesis presents a new numerical technique for quantifying the induced electric field at the body surface and inside the body as well as the steady and the transient current induced in a biological body that has a realistic shape and situated in a realistic environment, when exposed to ELF-LF electromagnetic fields.

As an introduction, the interaction of an ELF-LF electric field with a biological system is considered. An integral equation for the induced surface charge density (*surface charge integral equation*) is developed. By using the *Moment Method*, the body surface is partitioned into a number of patches for numerical calculation. After the induced surface charge density is determined, the electric field and the current density induced inside the body can be computed on the basis of the conservation of electric charge, Ohm's law, and Maxwell's equations.

Various numerical results have been generated to compare with closed form solutions and existing experimental results for establishing the accuracy of the present method. The agreement is excellent. The *surface charge integral equation* (SCIE) method has also been applied to realistic models of the human body standing on the ground with various grounding impedances at various frequencies of the incident electric

t

t

b

in

th

N

fl

pro

ind

cre

volt

met

as a

equi

on t

den

sph

can

fie

field. Various sizes and postures of the human body are considered. The induced surface charge, the short-circuit current, and the induced electric field as well as the induced current density inside the body are quantified. The frequency range limitation of the SCIE method is also investigated and is found to be valid up to the HF range.

In order to compare the *surface charge integral equation* method with other theoretical methods, a tensor *electric field integral equation* (EFIE) has been applied to calculate the induced electric field inside the biological body. By subdividing the body into many small cubical cells, the method of moments is used to transform the integral equation to a large matrix equation. The *Conjugate Gradient Method* (CGM) and the *Guass-Seidel Method* (GSM) are employed to solve the matrix equation iteratively. Numerical results and convergence rates of both methods are compared and discussed.

The *coupled surface charge integral equations* have also been applied to determine floating potentials and short-circuit currents of human body and metallic object at proximity immersed in a 60-Hz electric field. Equivalent circuits for computing induced currents of a human body and a vehicle are constructed. The shock current created between the vehicle and the nearby human body under the exposure of a high voltage 60-Hz electric field is analyzed by utilizing the equivalent circuit model.

To treat heterogeneous-body problem, the *surface charge integral equation* (SCIE) method is combined with an *impedance network method* by which the body is modeled as an equivalent impedance network and the induced surface charge is viewed as an equivalent current source. The current flowing at any impedance can be determined on the basis of the Kirchhoff's current law and from which the induced current density and electric field inside the body can be mapped. A conducting concentric-sphere is chosen to test the validity and accuracy of the present method. The method can be applied to any heterogeneous biological body when exposed to ELF-LF electric field.

TABLE OF CONTENTS

LIST OF FIGURES

LIST OF TABLES

The int

electromagne

important su

fields of an

systems beco

Resear

and health c

several repo

yard workers

Since then,

fields with

investigated

all the expe

and it is ne

information

reliable the

fields with

subject have

invariably u

Spiegle [11]

spheroidal m

CHAPTER 1

INTRODUCTION

The interaction of extremely low frequency (ELF; 0-100 Hz) electromagnetic fields with human body has become an increasingly important subject, since a potential health hazard due to the EM fields of an extremely high voltage (EHV) power line and ELF antenna systems become a public concern [1-4].

Research in the area of the relation between ELF electricity and health can be traced to 1960s. Researchers in U.S.S.R. published several reports of nonspecific physiological complaints among switch-yard workers when line voltages were raised to levels of 400-500 kV [4]. Since then, the biological effects and the interaction of ELF electric fields with human body have been studied extensively. Many workers have investigated this subject experimentally or empirically [5-10]. However, all the experiments were conducted on animals or scale model of man, and it is necessary to extrapolate these experimental data to provide information for human risk analysis. This is not an easy task if a reliable theoretical method for predicting the interaction of ELF EM fields with human body is not available. Theoretical studies on this subject have been conducted by a number of researchers, but they invariably used over simplified body geometries or inaccurate methods. Spiegle [11] used spheres as human models and Shiau et al. [12] used spheroidal models of man, and their results from these idealized models

may have littl

accurate block

method, but hi

insufficient p

Chiba et al. [

revolution geo

human body. K

a cylindrical

practical valu

This thes

surface charge

realistic mode

realistic envi

impedances betw

is developed on

surface charge

charge. This

induced electr

induced body cu

an incident EL

possible to pre

ncy with LF-HI

of the surface

arge. It is a

is numerically

In chapte

induced surface

may have little practical values. Spiegle [13-14] has also used a more accurate block model and an *electric field integral equation* (EFIE) method, but his results disagree with experimental results mainly due to insufficient partition of the body model in the numerical calculation. Chiba et al. [15] used a *finite-element method* (FEM) and a body model of revolution geometry. Their results are still not accurate for a realistic human body. Kaune and McCreary [16] developed a numerical method on a cylindrical model of man. Since this model is over simplified, the practical values of their results are questionable.

This thesis presents a recently developed numerical technique, *surface charge integral equation* (SCIE) method, which is based on a realistic model of man with arbitrary shape and posture, and under a realistic environmental condition such as assuming arbitrary grounding impedances between some parts of the body and the ground. The method is developed on the basis of an integral equation for the induced surface charge density, the Ohm's law, and the conservation of electric charge. This integral equation method can be used to quantify the induced electric field at the body surface and inside the body, the induced body current, as well as effects of the grounding impedance by an incident ELF electric field. And it is found that this method is possible to predict experimental results on the interaction of human body with LF-HF electromagnetic fields. This seems to extend the validity of the surface charge integral equation method to LF or even up to HF range. It is also noted that this surface charge integral equation method is numerically quite efficient.

In **chapter 2**, the theoretical development for calculating the induced surface charge and the induced body current of an arbitrarily

shaped biolo

A scalar inte

The method o

a matrix equa

Chapte

surface char

objects when

are compared

the integral

and analytica

of a grounded

calculated to

agreement is

In chap

quantify the

bodies. The

body, the inc

are quantifie

excellent ag

grounding imp

impedance has

130 cm. For

body causing

to compute th

induced by el

~ 50 MHz) and

shaped biological body, when exposed to an ELF electric fields, is given. A scalar integral equation for the induced surface charge is derived. The method of moments is used to transform the integral equation into a matrix equation for numerical solution.

Chapter 3 contains calculated numerical results of the induced surface charge density of spherical and spheroidal models of biological objects when exposed to ELF electric fields. These numerical results are compared with existing analytical solutions to check the validity of the integral equation method. An excellent agreement between numerical and analytical solutions is obtained. Also the short-circuit currents of a grounded biological sphere and a grounded biological spheroid are calculated to compare with the existing empirical formulas. A very good agreement is observed.

In **chapter 4** the surface charge integral equation is applied to quantify the interaction of 60-Hz electric fields with animal and human bodies. The induced electric fields at the body's surface and inside the body, the induced body current, and effects of the grounding impedances are quantified and compared with existing experimental results. An excellent agreement is obtained. Also it is found that, for an inductive grounding impedance, there is a possible resonance phenomenon when the impedance has a value in the order of 100 MΩ for a man with a height of 180 cm. For this case, there may be a very large current induced in the body causing possible health hazard. The **SCIE** method is also employed to compute the short-circuit currents of the human body (1.8 m in height) induced by electric fields at frequencies over the ELF and HF range (60 Hz ~ 50 MHz) and they are compared with experimental results measured by

various worke

which is the

the frequency

is up to the f

Chapter

field and curr

electric field

EM fields. Ir

SCIE method,

free space dya

large. The pu

method for the

of moments, ir

the body needs

create the pro

this problem,

and the Guass.

iteratively.

discussed.

Chapter

between a biol

exposure of the

coupled surface

floating potent

vehicle at prox

based on these

vehicle are con

various workers. A satisfactory agreement is obtained up to about 40 MHz which is the resonant frequency for the human body. This indicates that the frequency range applicability of the **SCIE** method for the human body is up to the first resonant frequency in the HF range.

Chapter 5 is devoted to the calculation of the induced electric field and current in a model of man as used in chapter 4 by the tensor *electric field integral equation* (**EFIE**) method, when exposed to ELF EM fields. Instead of using the low-frequency approximations as the **SCIE** method, this tensor integral equation method is derived by using the free space dyadic Green's function, and is valid for the whole frequency range. The purpose of using this method is to compare with the **SCIE** method for the numerical accuracy and efficiency. By using the method of moments, in order to yield accurate numerical results from **EFIE** method, the body needs to be partitioned into many small cubical cells. This will create the problem of solving a very large matrix equation. To overcome this problem, two iterative methods - the *Conjugate Gradient Method* (**CGM**) and the *Guass-Seidel Method* (**GSM**) are employed to solve the matrix equation iteratively. The convergence rate of the **CGM** and **GSM** are compared and discussed.

Chapter 6 covers the study of transient response of the interaction between a biological body and a nearby metallic object both under the exposure of the ELF electric field of a high-voltage power line. The *coupled surface charge integral equation* method is applied to determine floating potentials and short-circuit currents of a human body and a vehicle at proximity both immersed in a 60-Hz high-voltage electric field. Based on these data, the equivalent circuits for a human body and a nearby vehicle are constructed. The shock current flowing between a human body

and a vehicle

equivalent-cir

experimental r

    In chap

EF-LF electri

(SCIE) method

heterogeneous

induced body-s

currents flowi

current law an

can be mapped.

check the vali

that concentric

fields are con

    Chapter

and a vehicle through direct or spark contact is then analyzed using the equivalent-circuit model. Numerical results of the present method and experimental results by Reilly [32] are compared and discussed.

In **chapter 7**, the problem of heterogeneous bodies exposed to ELF-LF electric fields is treated. The *surface charge integral equation* **(SCIE)** method is combined with an *impedance network method* by which a heterogeneous body is modeled as an equivalent impedance network and the induced body-surface charge is viewed as an equivalent current source. The currents flowing in the network can be determined based on the Kirchhoff's current law and from which the induced current densities inside the body can be mapped. A conducting concentric-sphere is chosen as a test case to check the validity of the present method. Induced currents inside muscle-fat concentric-spheres with various thickness immersed in 60-Hz electric fields are computed and compared with analytical solutions.

Chapter 8 is the conclusion.

1.1 Introduc

In this

EF electric

pantities of

(a) The indu

factor o

ground,

(b) The shor

through

electric

(c) The indu

(d) the elec

electric

The validity

it to idealiz

form solution

by comparing

a phantom mod

CHAPTER 2

INTERACTION OF ELF ELECTRIC FIELDS WITH

BIOLOGICAL BODIES

2.1 Introduction

In this chapter, the theoretical study on the interaction of
ELF electric fields with biological bodies will be presented. The
quantities of interest to be discussed are :

(a) The induced surface charge and the electric field enhancement
     factor on an arbitrarily shaped biological body standing on the
     ground, when exposed to an ELF electric field.

(b) The short-circuit current from the biological body to the ground
     through grounding impedances Z_L's under the exposure of an ELF
     electric field.

(c) The induced body currents and current densities as well as

(d) the electric field inside the biological body due to the ELF
     electric field.

The validity of this theoretical method will be verified by applying
it to idealized geometries of a sphere and a spheroid for which closed
form solutions exist. The accuracy of the method will also be checked
by comparing with existing experimental results for a guinea pig and
a phantom model of man.

2.2 Theory

When a bi...

ground and bei...

circuit curren...

Also an electri...

in the body sur...

the ground bei...

contact impedar...

by Z_i ($i = 1 -$...

of the body is...

angular frequer...

In order t...

have been prove...

(1) The quasi-...

dimension...

ELF electr...

(2) The body w...

potential...

(3) The ground...

image.

(4) The induce...

small comp...

Since unde...

2.2 Theory

When a biological system, such as a human body standing on the ground and being exposed to an ELF electric field (Fig. 2.1), a short-circuit current will be maintained between the human body and the ground. Also an electric current is induced inside the body and surface charge on the body surface. Consider a geometry of a human body standing on the ground being exposed to an ELF electric field, as shown in Fig. 2.2. Contact impedances between the ground and the human body are represented by Z_{Li} (i = 1 ~ k). The impressed ELF electric field at the location of the body is assumed to be spatially uniform and oscillates with an angular frequency of ω.

In order to simplify the problem, following approximations which have been proved valid [5] will be used:

(1) The quasi-static approximation will be used, since the body dimension is small compared with the wavelength of the impressed ELF electric field.

(2) The body will be assumed to be equipotential with an unknown potential ϕ_b.

(3) The ground effect will be taken into account by the method of image.

(4) The induced electric charge inside the body is assumed to be small compared with the induced charge on the body surface. Since under the quasistatic approximation, the induced surface

charge a

$\eta = \epsilon_2 (\partial$

and ϵ th

surface

in one r

the medi

higher t

ϵ are gr

of diffe

assumpti

(5) Inside t

greater

on the fa

The effect due

not be conside

compared with

2.2.1 Surface

The fir

charge induced

The induced su

can be express

follows.

charge at the interface between media 1 and 2 is given by, $\eta = \epsilon_2(\hat{\sigma}_1/\hat{\sigma}_2 - \epsilon_1/\epsilon_2)(\hat{n}\cdot\vec{E}_1)$, where $\hat{\sigma}$ is the complex conductivity and ϵ the permittivity (shown in the Fig. 2.3). Thus, the induced surface charge is proportional to the normal component of E field in one region and also depends on the discontinuity of $\hat{\sigma}$ and ϵ of the media. $(\hat{n}\cdot\vec{E}_1)$ at the body's surface is many orders of magnitude higher than that inside the body, and the discontinuity of $\hat{\sigma}$ and ϵ are greater at the body-air interface than at the interface of different body tissues (as shown in Fig. 2.4). Thus, this assumption is valid.

(5) Inside the body, the conducting current is assumed to be much greater than the capacitive current. This assumption is based on the fact that $\sigma \gg \omega\epsilon$ inside the body in the ELF range.

The effect due to the magnetic field of ELF electromagnetic fields will not be considered here, since this effect is believed to be insignificant compared with that due to the electric field.

2.2.1 Surface Charge Integral Equation

The first step in this approach is to determine the electric charge induced on the body surface by the impressed electric field. The induced surface charge density $\eta(\vec{r})$ and the body potential ϕ_b can be expressed as unknowns in a pair of integral equations as follows.
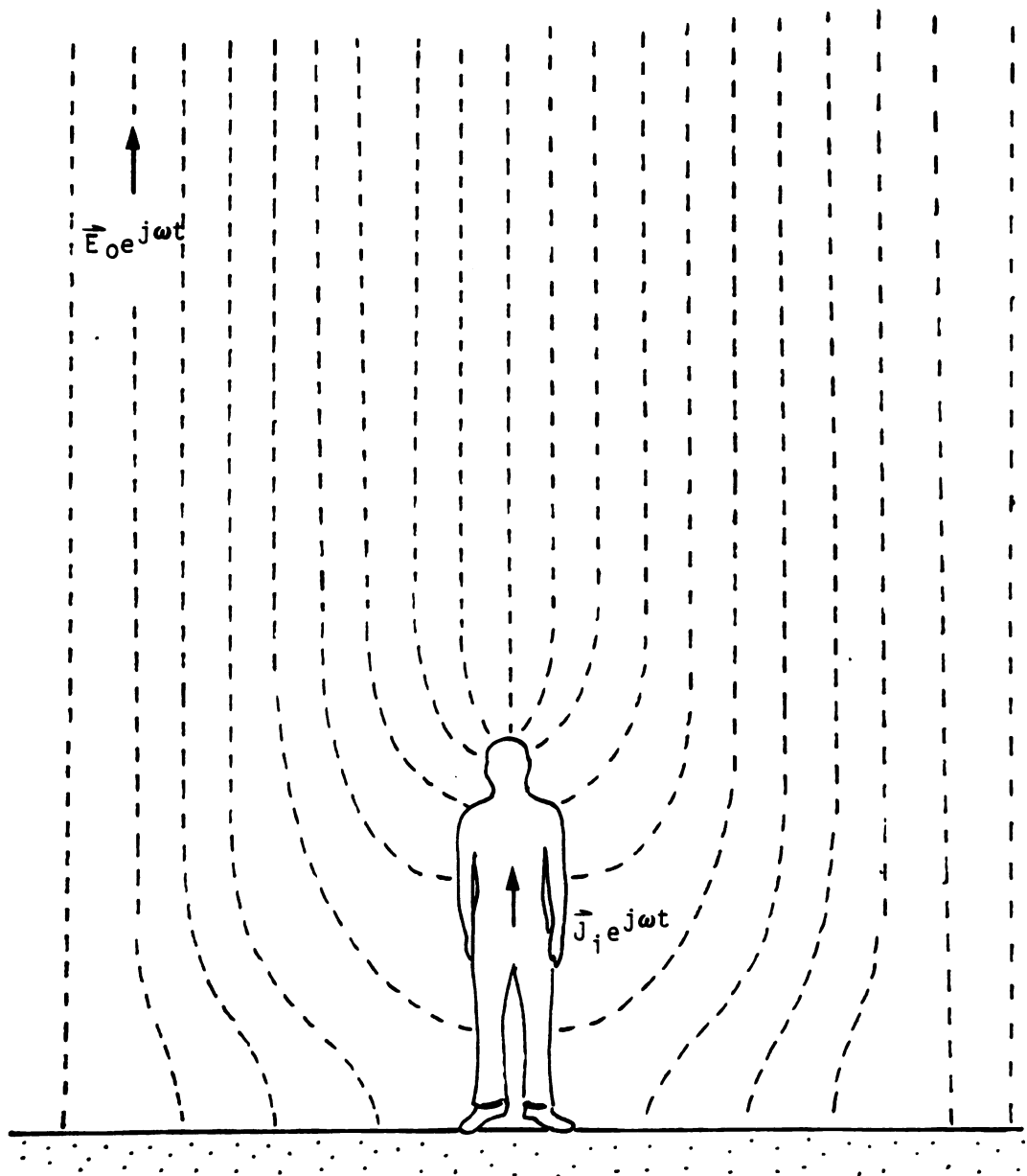
EHV POWER LINE

Fig. 2.1. A human standing on the ground is exposed to an ELF electric
field $E_0 \exp(j\omega t)$ maintained by an EHV power line. Induced
current inside the human body is $J_i \exp(j\omega t)$.
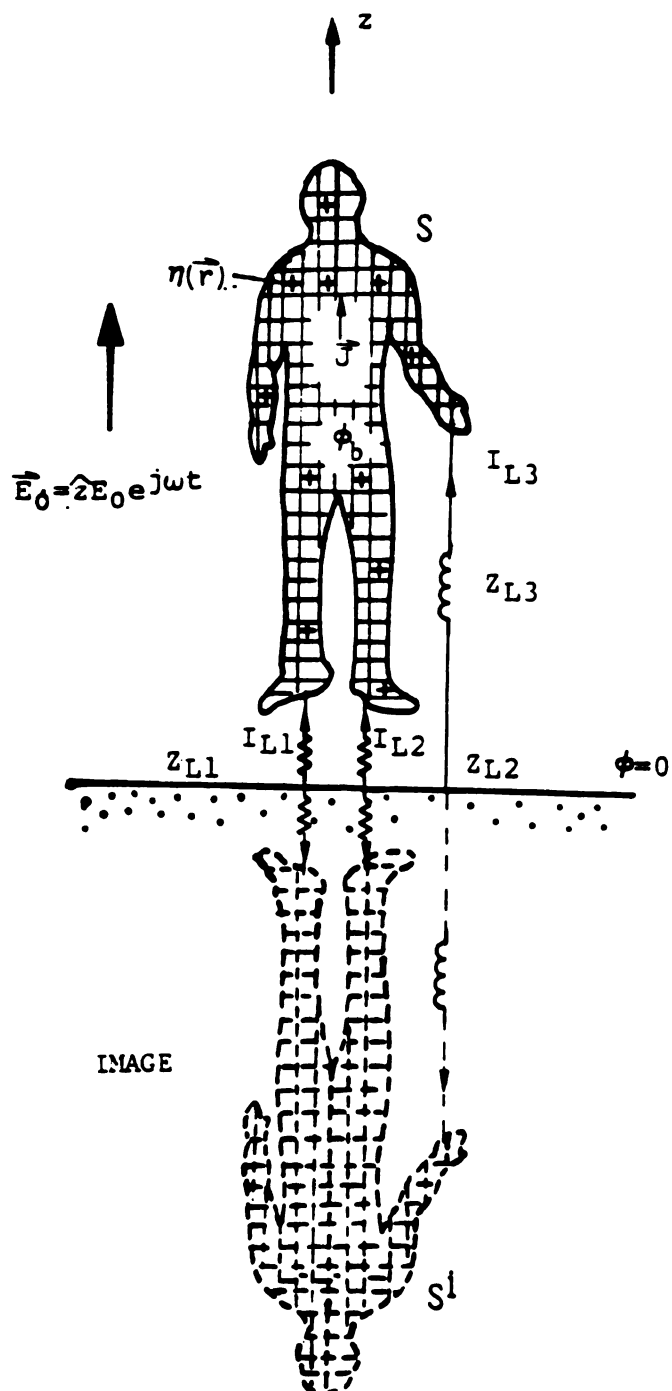
Fig. 2.2.

Fig. 2.2. A man standing on the ground is exposed to an electric field of ELF range. The contacts between the feet as well as the left hand and the ground are represented by Z_{Li} (i = 1 ~ 3).

MUS

FAT

comp

conc

disp

at

sig

fre

pol

Fig. 2.3.
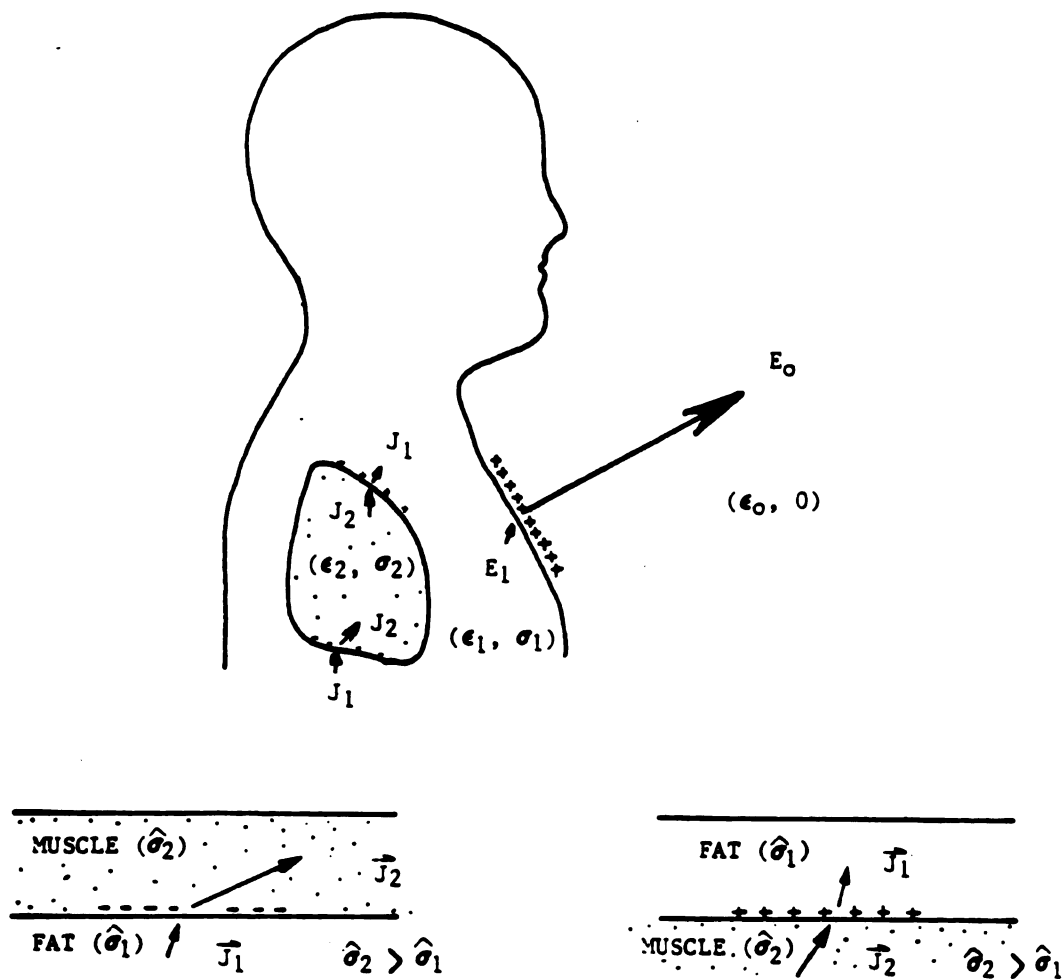
complex conductivity: $\hat{\sigma} = \sigma + j\omega\epsilon$

conducting current density : $\vec{J}_c = \sigma\vec{E}$

displacement current density: $\vec{J}_d = j\omega\vec{E}$

$\left.\right\}$ $\vec{J} = \hat{\sigma}\vec{E} = (\sigma + j\omega\epsilon)\vec{E}$

· **at interface**

$$J_{1n} = J_{2n} \Rightarrow \hat{\sigma}_1 E_{1n} = \hat{\sigma}_2 E_{2n}$$

$$E_{1t} = E_{2t}$$

· **electrical charge density at interface**

free charge density : $\eta_f = \epsilon_2 E_{2n} - \epsilon_1 E_{1n} = \epsilon_2(\hat{\sigma}_1/\hat{\sigma}_2 - \epsilon_1/\epsilon_2)E_{1n}$

polarization charge density: $\eta_p = (\epsilon_2 - \epsilon_1)E_{2n}$

· total charge density: $\eta_t = \eta_f + \eta_p$

Fig. 2.3. Induced surface charges at the interface of different media.

DIELECTRIC CONSTANT ϵ_r
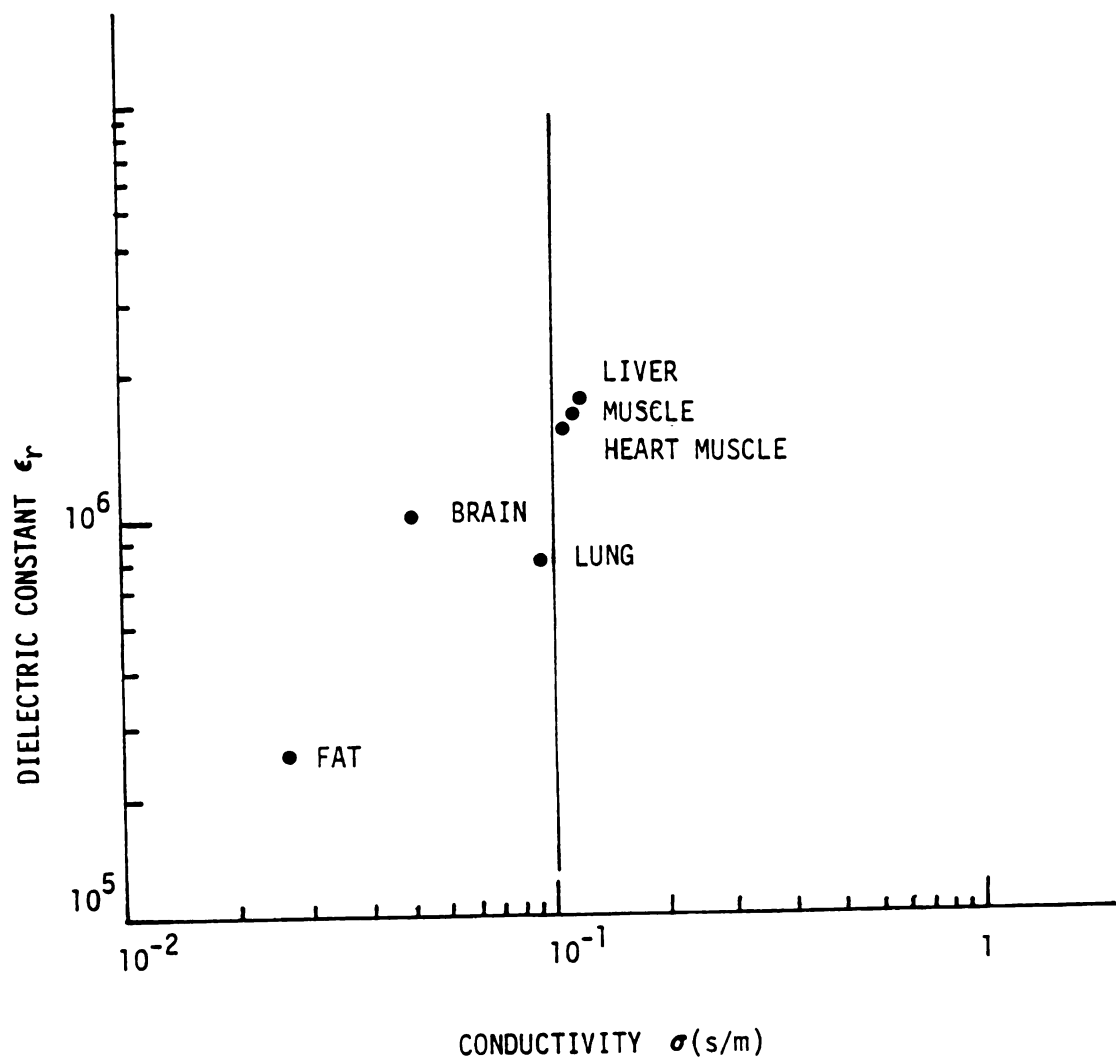
Fig. 2.

Fig. 2.4. Conductivity and dielectric constant of various tissues
in the ELF range [15].

Physic

over the body

is maintained

$\phi_o(\vec{r})$ which i

$$\phi_s(\vec{r})$$

By using the c

image effect,

$$\phi_s(\vec{r})$$

here S is the

$\vec{r}$ is a field

on the body s

be expressed

for the geome

quantity and

electric fiel

Equati

$$\frac{1}{4\pi\epsilon_o}$$

Physically, the body potential ϕ_b, which is spatially constant over the body, can be considered as sum of the potential $\phi_s(\vec{r})$ which is maintained by the induced surface charge $\eta(\vec{r})$, and the potential $\phi_o(\vec{r})$ which is maintained by the impressed electric field,

$$\phi_s(\vec{r}) + \phi_o(\vec{r}) = \phi_b \tag{2.1}$$

By using the quasistatic approximation and considering the ground image effect, $\phi_s(\vec{r})$ can be expressed as

$$\phi_s(\vec{r}) = \frac{1}{4\pi\epsilon_o} \int_{S+S^i} \eta(\vec{r}') \frac{1}{|\vec{r} - \vec{r}'|} ds' \tag{2.2}$$

where S is the body surface and S^i is the surface of the body image, $\vec{r}$ is a field point on the body surface and $\vec{r}'$ represents a source point on the body surface and the image surface. The potential $\phi_o(\vec{r})$ can be expressed in terms of the impressed electric field, $\phi_o(\vec{r}) = -E_o z$, for the geometry of Fig. 2.2. The body potential ϕ_b is an unknown quantity and its value depends on the body geometry, the impressed electric field and the grounding impedances Z_{Li}.

Equation (2.1) can now be rewritten as

$$\frac{1}{4\pi\epsilon_o} \int_{S+S^i} \eta(\vec{r}') \frac{1}{|\vec{r} - \vec{r}'|} ds' + \phi_o(\vec{r}) = \phi_b \tag{2.3}$$

Eq. (2.3) i

density $\eta(\vec{r}$

To de

second equa

conservatio

flowing bet

currents fl

$$I_L -$$

$$-$$

n other ha

charge Q, b

$$I_L -$$

Combining E

$$\phi_b -$$

Eqs. (2.6) i

the unknowns

Eq. (2.3) is a scalar integral equation for the induced charge density $\eta(\vec{r})$ and the unknown body potential ϕ_b.

To determine $\eta(\vec{r})$ and ϕ_b, another equation is needed. This second equation is obtained on the basis of Ohm's law and the conservation of electric charge. Let I_L be the total current flowing between the body and the ground. It is the sum of the currents flowing through the grounding impedances Z_{Li}:

$$I_L = \phi_b \cdot [(1/Z_{L1}) + (1/Z_{L2}) + \ldots + (1/Z_{Lk})]$$
$$= \phi_b \cdot \left[\sum_{i=1}^{k} (1/Z_{Li}) \right] \tag{2.4}$$

On other hand, I_L can be expressed in terms of the total surface charge Q, based on the conservation of electric charge, as

$$I_L = j\omega Q = j\omega \int_S \eta(\vec{r}') \, ds' \tag{2.5}$$

Combining Eqs. (2.4) and (2.5), ϕ_b can be written as

$$\phi_b = \frac{j\omega}{\sum_{i=1}^{k} (1/Z_{Li})} \int_S \eta(\vec{r}') \, ds' \tag{2.6}$$

Eqs. (2.6) is the desired second equation which has $\eta(\vec{r})$ and ϕ_b as the unknowns.

The Mo

at certain d

Method, the

ΔS_n (n = 1 -

that $\eta(\vec{r})$ ar

point $\vec{r}_m$ on

expressed as

$$\sum_{n=1}^{N} \frac{1}{4\pi\epsilon_o} \Bigg\{$$

where

$$\eta_n =$$

$$\int_{\Delta S}$$

$$\int_{\Delta}$$

and $\vec{r}_m$ i

patch.

above i

2.2.2 Transformation of Integral Equation - Moment Method

The Moment Method is applied to solve the integral equation at certain discrete points in the region of interest. In the Moment Method, the total surface of the body is partitioned into N patches ΔS_n (n = 1 ~ N). These patches are assumed to be electrically small so that $\eta(\vec{r})$ are assumed to be constant. Mathematically, at a observation point $\vec{r}_m$ on the body surface, the integral equation (2.3) can be expressed as

$$\sum_{n=1}^{N} \frac{1}{4\pi\epsilon_0} \left\{ \int_{\Delta S_n} \frac{\eta_n}{|\vec{r}_m - \vec{r}'|} \, ds' - \int_{\Delta S_n^i} \frac{\eta_n}{|\vec{r}_m - \vec{r}'_i|} \, ds'_i \right\} + \phi_0(\vec{r}_m) = \phi_b$$

$$(2.7)$$

where

$$\eta_n = \eta(\vec{r}_n)$$

$$\int_{\Delta S_n} \frac{\eta_n}{|\vec{r}_m - \vec{r}'|} \, ds' = \text{potential at } \vec{r}_m \text{ maintained}$$
$$\text{by the charge of } \Delta S_n \text{ patch}$$

$$\int_{\Delta S_n^i} \frac{(-\eta_n)}{|\vec{r}_m - \vec{r}'_i|} \, ds'_i = \text{potential at } \vec{r}_m \text{ maintained}$$
$$\text{by the charge of } \Delta S_n^i \text{ patch}$$

and $\vec{r}_m$ is the central point of the ΔS_m patch and $\vec{r}_n$ is that of ΔS_n patch. Since the patches are assumed to be small, for m ≠ n, the above integrals can be approximated as,

$$\int_{\Delta S}$$

$$\int_{\Delta S}$$

when $m = n$,

thus, $|\vec{r}_m - $

However, this

Eq. (2.8).

circular dis;

gives the fol

$$a_m =$$

where ΔS_m is

radius of the

Now, fo

written as

$$\int_{D_m}$$

$$\int_{\Delta S_n} \frac{\eta_n}{|\vec{r}_m - \vec{r}'|} \, ds' \doteq \frac{\eta_n \Delta S_n}{|\vec{r}_m - \vec{r}_n|}$$

(2.8)

$$\int_{\Delta S_n^i} \frac{\eta_n}{|\vec{r}_m - \vec{r}'_i|} \, ds' \doteq \frac{\eta_n \Delta S_n}{|\vec{r}_m - \vec{r}_n^i|}$$

When $m = n$, $\vec{r}_m$ is at the center of ΔS_n patch and $\vec{r}'$ is within ΔS_n, thus, $|\vec{r}_m - \vec{r}'|$ will vanish in the first integral of Eq. (2.8). However, this singularity is removable through the integral of Eq. (2.8). First the ΔS_m patch is approximated by a equivalent circular disk D_m with the same area, as shown in Fig. 2.5. This gives the following relationship:

$$a_m = \frac{(\Delta S_m)^{1/2}}{\sqrt{\pi}}$$

(2.9)

where ΔS_m is the surface area of the mth patch and a_m is the radius of the disk D_m.

Now, for $m = n$, the first integral in the Eq. (2.8) can be written as

$$\int_{D_m} \frac{ds}{R} = \int_0^{2\pi} \int_0^{a_m} \frac{R dR d\theta}{R}$$

$$= 2\pi a_m = 2\sqrt{\pi} \, \Delta S_m$$

(2.10)

x

Fig. 2.5.

$$\Delta S_m = \pi a_m^2$$

D_m : equivalent disk of the patch ΔS_m
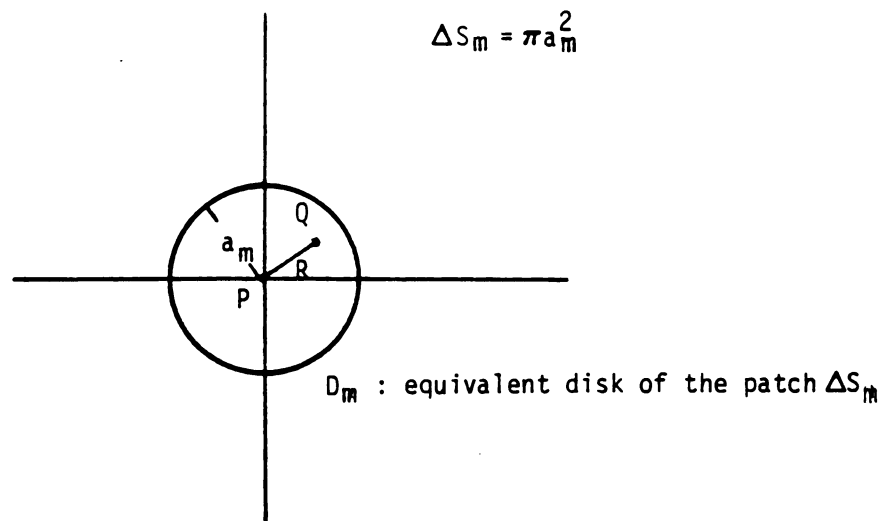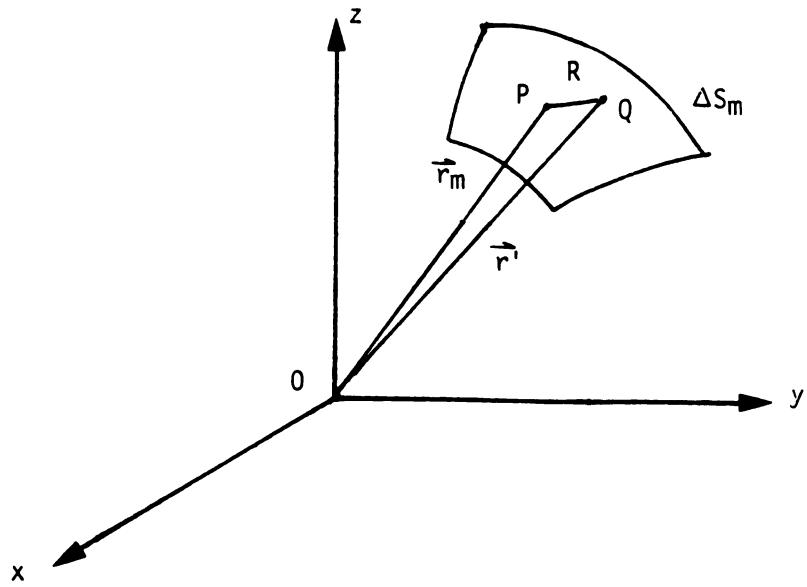
Fig. 2.5. Geometries for integration of Eq. (2.8) when m = n.

Also Eq. (2

ϕ_b

Eq. (2.7) a

$$\begin{bmatrix} M_{11} & M_{12} \\ M_{21} & M_{22} \\ \cdot & \cdot \\ \cdot & \cdot \\ \cdot & \cdot \\ M_{N1} & M_{N2} \\ \Delta S_1 & \Delta S_2 \end{bmatrix}$$

where

M_{mn}

M_{mn}

ϕ_{on}

Also Eq. (2.6) can be approximated as

$$\phi_b = \frac{j\omega}{[\sum\limits_{i=1}^{k} (1/Z_{Li})]} \sum\limits_{n=1}^{N} (\eta_n \Delta S_n) \qquad (2.11)$$

Eq. (2.7) and (2.11) are then transformed into a matrix equation as

$$\begin{bmatrix} M_{11} & M_{12} & \cdots\cdots & M_{1N} & -1 \\ M_{21} & M_{22} & \cdots\cdots & M_{2N} & -1 \\ \cdot & \cdot & & \cdot & \cdot \\ \cdot & \cdot & & \cdot & \cdot \\ \cdot & \cdot & & \cdot & \cdot \\ M_{N1} & M_{N2} & \cdots\cdots & M_{NN} & -1 \\ \Delta S_1 & \Delta S_2 & \cdots\cdots & \Delta S_N & -[\sum\limits_{i=1}^{k} (1/Z_{Li})]/j\omega \end{bmatrix} \begin{bmatrix} \eta_1 \\ \eta_2 \\ \cdot \\ \cdot \\ \cdot \\ \eta_N \\ \phi_b \end{bmatrix} = \begin{bmatrix} \phi_{o1} \\ \phi_{o2} \\ \cdot \\ \cdot \\ \cdot \\ \phi_{oN} \\ 0 \end{bmatrix}$$

where   (2.12)

$$M_{mn} = \frac{1}{4\pi\epsilon_o} \Delta S_n \left\{ \frac{1}{|\vec{r}_m - \vec{r}_n|} - \frac{1}{|\vec{r}_m - \vec{r}_n^i|} \right\} \qquad m \neq n$$

$$M_{mm} = \frac{1}{4\pi\epsilon_o} \Delta S_m \left\{ \frac{2\sqrt{\pi}}{(\Delta S_m)^{1/2}} - \frac{1}{|\vec{r}_m - \vec{r}_m^i|} \right\} \qquad m = n$$

$$\phi_{on} = \phi_o(\vec{r}_n) = - E_o z$$

In this matri

$(N + 1) \times (N$

matrices. $[\eta$

potential at

equipotential

the matrix as

$$[\eta] =$$

The conventio

the matrix eq

Gauss-Seidel

if the matrix

    There

(1) The case

  i. The

  reduced

  the last

$$\begin{bmatrix} M_{11} & M \\ M_{21} & M \\ \cdot & \\ \cdot & \\ \cdot & \\ M_{N1} & M \end{bmatrix}$$

The unkn

In this matrix equation, $[M][\eta]=[\phi]$, the matrix $[M]$ represents a $(N + 1) \times (N + 1)$ matrix and $[\eta]$ as well as $[\phi]$ are $(N + 1)$ column matrices. $[\eta_n]$ and $[\phi_{on}]$ are charge density and impressed field potential at the central point of the nth patch. ϕ_b is the unknown equipotential of the body. $[\eta_n]$ and ϕ_b can be determined by inverting the matrix as follows :

$$[\eta] = [M]^{-1}[\phi] \qquad (2.13)$$

The conventional Guass Elimination Method (GEM) can be used to solve the matrix equation, and the Conjugate Gradient Method (CGM) or the Guass-Seidel Method (GSM) can also be applied to solve it iteratively if the matrix size becomes excessively large.

There are two special cases of interest:

(1) The case when the body is shorted to the ground, $Z_{Li} = 0$ for any i. The body potential ϕ_b will be zero, therefore, Eq. (2.12) is reduced to a $(N \times N)$ matrix equation, with the last column and the last row of the matrix in Eq. (2.12) removed, as

$$
\begin{bmatrix}
M_{11} & M_{12} & \cdots\cdots & M_{1N} & -1 \\
M_{21} & M_{22} & \cdots\cdots & M_{2N} & -1 \\
\cdot & \cdot & & \cdot & \cdot \\
\cdot & \cdot & & \cdot & \cdot \\
\cdot & \cdot & & \cdot & \cdot \\
M_{N1} & M_{N2} & \cdots\cdots & M_{NN} & -1
\end{bmatrix}
\begin{bmatrix}
\eta_1 \\
\eta_2 \\
\cdot \\
\cdot \\
\cdot \\
\eta_N
\end{bmatrix}
= -
\begin{bmatrix}
\phi_{o1} \\
\phi_{o2} \\
\cdot \\
\cdot \\
\cdot \\
\phi_{oN}
\end{bmatrix}
\qquad (2.14)
$$

The unknown surface charge density $[\eta_n]$ can then be determined

accordi

(2) The cas

all i.

zero, t

$$
\begin{bmatrix}
M_{11} \\
M_{21} \\
\cdot \\
\cdot \\
\cdot \\
M_{N1} \\
\Delta S_1
\end{bmatrix}
$$

This in

$$
\sum_{n=1}^{N} \eta_n
$$

that is

$[\eta_n]$ an

After the in

electric fie

$$
E_s -
$$

according.

(2) The case when the body is isolated from the ground, $Z_{Li} = \infty$ for

all i. Hence the last element of the matrix of Eq. (2.12) becomes

zero, the matrix equation is

$$
\begin{bmatrix}
M_{11} & M_{12} & \cdots\cdots & M_{1N} & -1 \\
M_{21} & M_{22} & \cdots\cdots & M_{2N} & -1 \\
\cdot & \cdot & & \cdot & \cdot \\
\cdot & \cdot & & \cdot & \cdot \\
\cdot & \cdot & & \cdot & \cdot \\
M_{N1} & M_{N2} & \cdots\cdots & M_{NN} & -1 \\
\Delta S_1 & \Delta S_2 & \cdots\cdots & \Delta S_N & 0
\end{bmatrix}
\begin{bmatrix}
\eta_1 \\
\eta_2 \\
\cdot \\
\cdot \\
\cdot \\
\eta_N \\
\phi_b
\end{bmatrix}
= -
\begin{bmatrix}
\phi_{o1} \\
\phi_{o2} \\
\cdot \\
\cdot \\
\cdot \\
\phi_{oN} \\
0
\end{bmatrix}
\qquad (2.15)
$$

This implies that

$$
\sum_{n=1}^{N} \eta_n \, \Delta S_n = 0 \qquad (2.16)
$$

that is, the total net charge on the body is zero. For this case

$[\eta_n]$ and ϕ_b are determined from Eq. (2.15).

After the induced surface charge density is determined, the induced

electric field at the body surface is simply obtained from

$$
E_s = \eta/\epsilon_o \qquad (2.17)
$$

assuming th

the body su

The

of the indu

field, E_s/E

stretched a

exposed to

field at so

already a ve

2.2.3 Ind

Afte

the body su

the body car

electric cha

The

current at a

is assumed t

the body is

currents wi

sectional cu

at the right

If

$^7 J + j \omega \rho =$

assuming that the induced electric field is totally perpendicular to the body surface.

The electric field enhancement factor is defined as the ratio of the induced electric field at the surface to the impressed electric field, E_s/E_o. This value can exceed 10 at the head or the tip of a stretched arm and hand as calculated in *chapter 4*. Thus, when a man is exposed to the electric field of an EHV power line, the induced electric field at some points of the body can be extremely high since E_o is already a very high value in this case.

2.2.3 Induced Current Inside the Body

After the induced surface charge density η_n at any point on the body surface is determined, the induced current density inside the body can be determined on the basis of the conservation of the electric charge and employing Maxwell's equations.

The first quantity to be determined is the total sectional current at any cross section of the body. Referring to Fig. 2.6, it is assumed that the positive sectional current at any cross section of the body is directed toward the head. As for example, three sectional currents will be considered: the sectional current at the chest I_1, the sectional current at the lower abdomen I_2, and the sectional current at the right arm I_3.

If the equation of the conservation of electric charge, $\nabla \cdot J + j\omega\rho = 0$, is integrated over the volume V_1 which encloses the

S
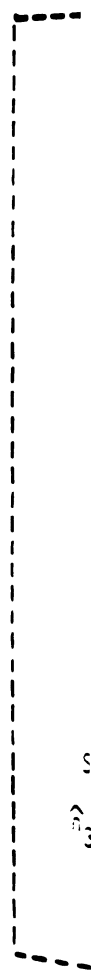
$\hat{n}_3$
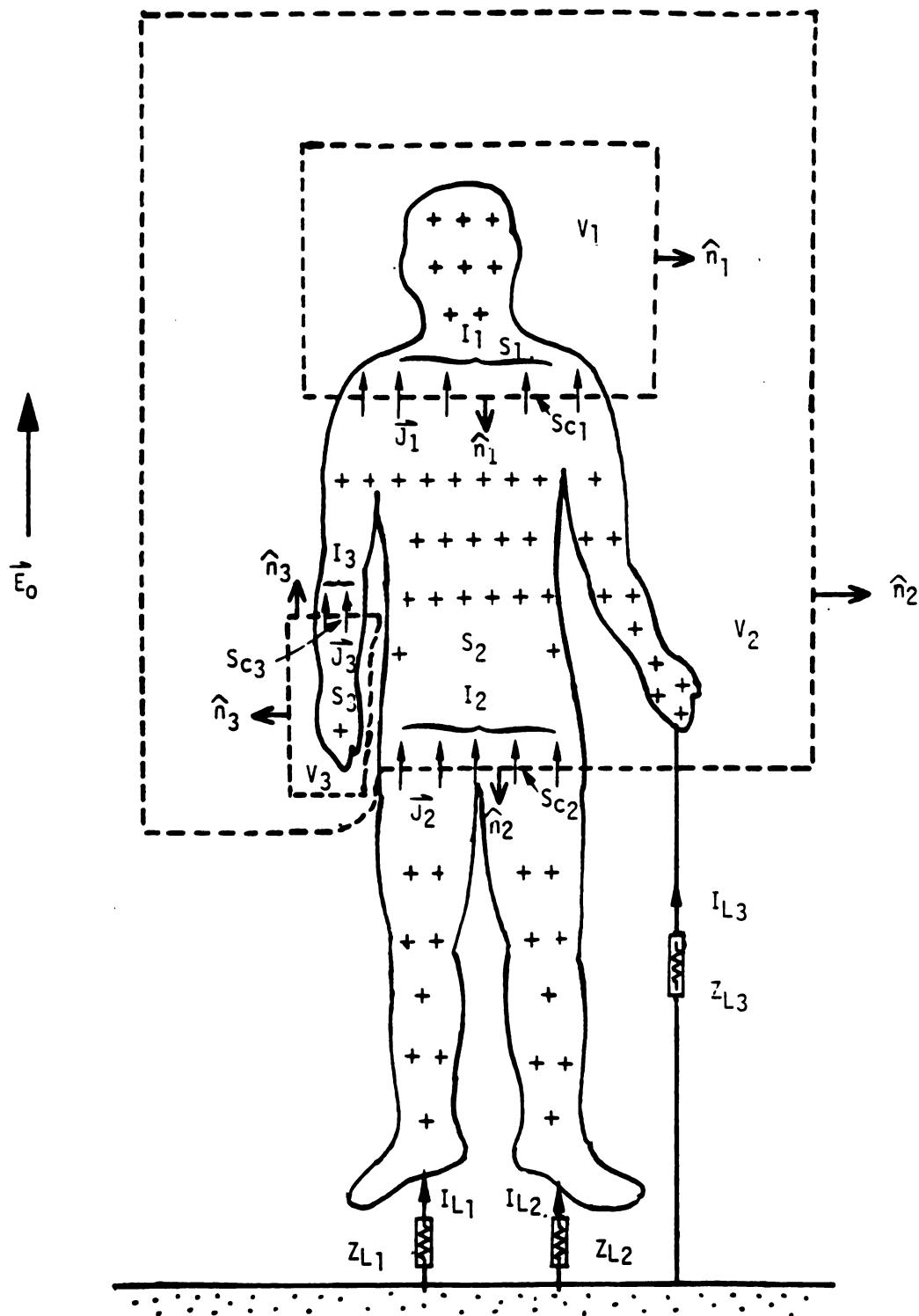
Fig. 2.6.

Fig. 2.6. Geometry for calculating the induced current in the body.

upper body

obtained,

$$I_1$$

where $\hat{n}_1$ i

sectional

cross sect

A

portion of

cutting th

Z_3 connec

$$\int_S$$

or

$$I_2$$

where $\hat{n}_2$ i

density at

current fl

impedance

upper body above the chest cross section (see Fig. 2.6), it can be obtained,

$$I_1 = - \int_{S_{c1}} (\hat{n}_1 \cdot \vec{J}_1) ds' - j\omega \int_{S_1} \eta \, ds' \qquad (2.18)$$

where $\hat{n}_1$ is the unit vector pointing outward from V_1, S_{c1} is the cross sectional area at the chest, S_1 is the body surface above the chest cross section of S_{c1}, and $\vec{J}_1$ is the current density at S_{c1}.

A similar integral over the volume V_2, which includes the portion of the body above the lower abdomen and has a boundary surface cutting through the lower abdomen section S_{c2} and a grounding impedance Z_{L3} connecting the left hand to the ground, will lead to

$$\int_{S_{c2}} (\hat{n}_2 \cdot \vec{J}_2) ds' - I_{L3} = -j\omega \int_{S_2} \eta \, ds'$$

or   (2.19)

$$I_2 + I_{L3} = j\omega \int_{S_2} \eta \, ds'$$

where $\hat{n}_2$ is the unit vector pointing outward from V_2, J_2 is the current density at S_{c2}, S_2 is the body surface enclosed by V_2, and I_{L3} is the current flowing from the ground to the left hand through the grounding impedance Z_{L3}. I_{L3} can be easily determined from ϕ_b/Z_{L3} .

Ano

the right a

I_3

where n_3 is

sectional a

S_3 is the s

that $\hat{n}_3$ and

$\vec{i}_3$ has a ne

the phenome

to that flo

One

is the shor

between the

the feet an

impedances

are infinit

approach as

I_{sc}

Another similar integral over the volume V_3 which contains the right arm and hand leads to

$$I_3 = \int_{S_{c3}} (\hat{n}_3 \cdot \vec{J}_3)ds' = -j\omega \int_{S_3} \eta \ ds' \qquad (2.20)$$

where n_3 is the unit vector pointed outward from V_3, S_{c3} is the cross sectional area at the right arm, $\vec{J}_3$ is the current density at S_{c3} and S_3 is the surface of the right arm and hand enclosed in V_3. It is noted that $\hat{n}_3$ and $\vec{J}_3$ are in the same direction. Therefore, the expression of I_3 has a negative sign in Eq. (2.20). This negative sign will lead to the phenomenon that the current in the arm flows in the opposite direction to that flowing in the other parts of the body.

One of the most important quantities concerning the body current is the short-circuit current I_{sc}. I_{sc} is defined as the current flowing between the feet and the ground when the grounding impedances between the feet and the ground, Z_{L1} and Z_{L2}, are zero and other grounding impedances between other parts of the body and the ground, such as Z_{L3}, are infinity (open circuit). I_{sc} can be easily obtained by the same approach as above and is given by

$$I_{sc} = j\omega \int_S \eta \ ds' \qquad (2.21)$$

where

charge

poten

densi

from

or

For th

Eq. (2

body w

sectio

compone

This ap

sectio

compone

where S includes the total body surface, and η is the induced surface

charge density at the body surface under the condition that the body

potential ϕ_b is zero.

After the determination of the sectional current, the volume

density of the induced current inside the body $\vec{J}$ can be determined

from the Maxwell's equation,

$$\nabla \times \vec{H} = (\sigma + j\omega\epsilon)\vec{E}$$

or   (2.22)

$$\nabla \cdot [(\sigma + j\omega\epsilon)\vec{E}] = 0$$

For the ELF-LF range, $\sigma \gg \omega\epsilon$ inside the human body, therefore

$$\nabla \cdot (\sigma\vec{E}) = \nabla \cdot \vec{J} = 0 \tag{2.23}$$

Eq. (2.23) can be used to predict the distribution of $\vec{J}$ inside the

body with the prior knowledge of the sectional current I at any cross

section of the body.

Assume that $\vec{J}$ at any cross section of the body has only two

components: the longitudinal component J_ℓ and the radial component J_r.

This approximation assumes a cylindrical geometry for the body cross

section as shown in Fig. 2.7, and also ignores the circumferential

component J_φ.
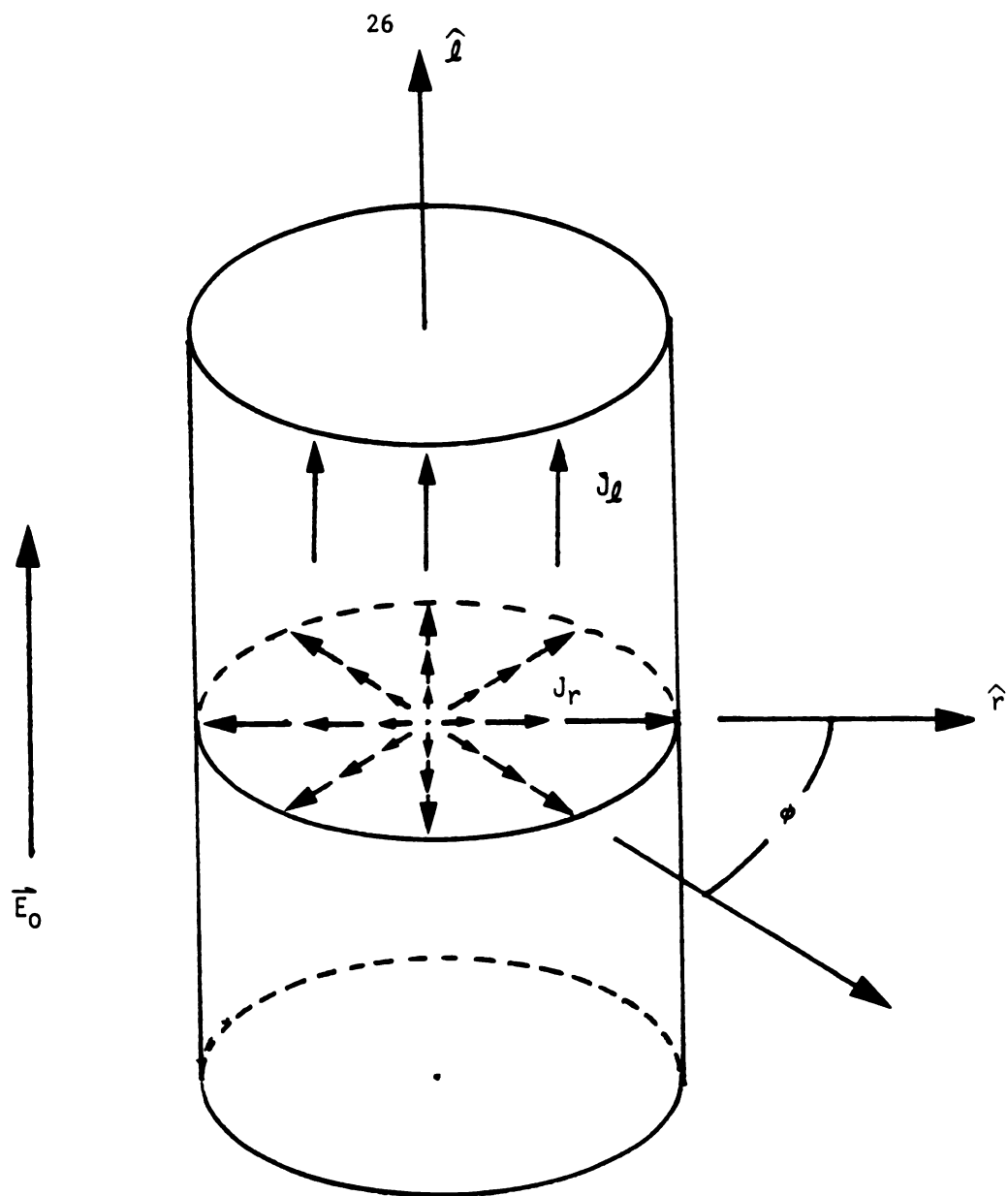
Fig. 2

$$\nabla \cdot \vec{J} = \frac{1}{r}\frac{\partial}{\partial r}(rJ_r) + \frac{1}{r}\left(\frac{\partial J_\varphi}{\partial \varphi}\right) + \frac{\partial J_\ell}{\partial \ell}$$

Fig. 2.7. Cylindrical geometry for calculating the induced current density inside the body.

The

as

$$J_{1}$$

where I is

the cross s

is applied.

but it may

based on th

equation (E

independent

Now

the radial

cylindrical

From (assum

$$\nabla \cdot J$$

it leads to

$$\frac{\partial}{\partial}$$

The longitudinal component J_ℓ can be approximately obtained as

$$J_\ell = I/S_c \tag{2.24}$$

where I is the already determined total sectional current and S_c is the cross sectional area of the body at the position where Eq. (2.24) is applied. The calculation of J_ℓ is valid for a homogeneous body, but it may also be a fair approximation for a heterogeneous body, based on the finding by Spiegel [14] using the *electric field integral equation* (EFIE) method that the induced current density $\vec{J}$ is rather independent of the electric parameters of the body at the ELF range.

Now that J_ℓ is determined at any cross section of the body, the radial component J_φ can be derived from Eq. (2.23), using a cylindrical geometry (shown in Fig. 2.7), as follows:
From (assuming J_φ component is zero)

$$\nabla \cdot \vec{J} = \frac{1}{r} \frac{\partial}{\partial r} (rJ_r) + \frac{\partial}{\partial \ell} J_\ell = 0 \tag{2.25}$$

it leads to

$$\frac{\partial}{\partial r} (rJ_r) = -r \left(\frac{\partial J_\ell}{\partial \ell} \right) \tag{2.26}$$

After

where

and (

Since

estim

of the

direc

the bo

an

where

After integrating both sides, it gives

$$J_r = - \frac{r}{2} \left(\frac{\partial J_\ell}{\partial \ell} \right) \qquad (2.27)$$

where r is the radial distance from the center of the cross section, and $(\partial J_\ell/\partial \ell)$ is the rate of change of J_ℓ in the longitudinal direction. Since J_ℓ is known at any cross section, the value of $(\partial J_\ell/\partial \ell)$ can be estimated easily. Eq. (2.27) indicates that J_r is zero at the center of the body and linearly increases toward the body surface. The direction of J_r is dictated by the sign of $(\partial J_\ell/\partial \ell)$.

After J is dertermined, the electric field induced inside the body is determined from

$$\vec{E} = \vec{J}/\sigma \qquad (2.28)$$

and the SAR (*specific absorption rate*) value is calculated from

$$SAR \ (W/Kg) = \frac{1}{2\sigma} |J|^2/\rho \qquad (2.29)$$

where ρ is the volume density of mass in Kg/m^3.

APPLIC

3.1 I

In

equatio

the SC

isolate

Also th

to ELF

same co

standin

3.2 C

P

Co

immerse

solution

charge

CHAPTER 3

APPLICATIONS OF SURFACE CHARGE INTEGRAL EQUATION METHOD

TO SPHERICAL AND SPHEROIDAL MODELS OF

BIOLOGICAL BODIES

3.1 Introduction

In order to compare the numerical solutions of the integral equation developed in chapter 2 with existing analytical solutions, the *SCIE* method is applied to an isolated conducting sphere and an isolated conducting spheroid under the exposure of ELF electric fields. Also the case of a sphere locating above the ground plane and exposed to ELF electric fields as well as the case of a spheroid under the same condition are studied, for simulating a human or an animal body standing on the ground.

3.2 Closed Form Solution for a Sphere and Comparision with Present Numerical Results

Consider a perfectly conducting sphere with radius a which is immersed in an uniform electric field as shown in Fig. 3.1. Analytical solutions of the induced surface electric field $\vec{E}(a,\theta)$ and the surface charge density $\eta(a,\theta)$ can be written as [17]
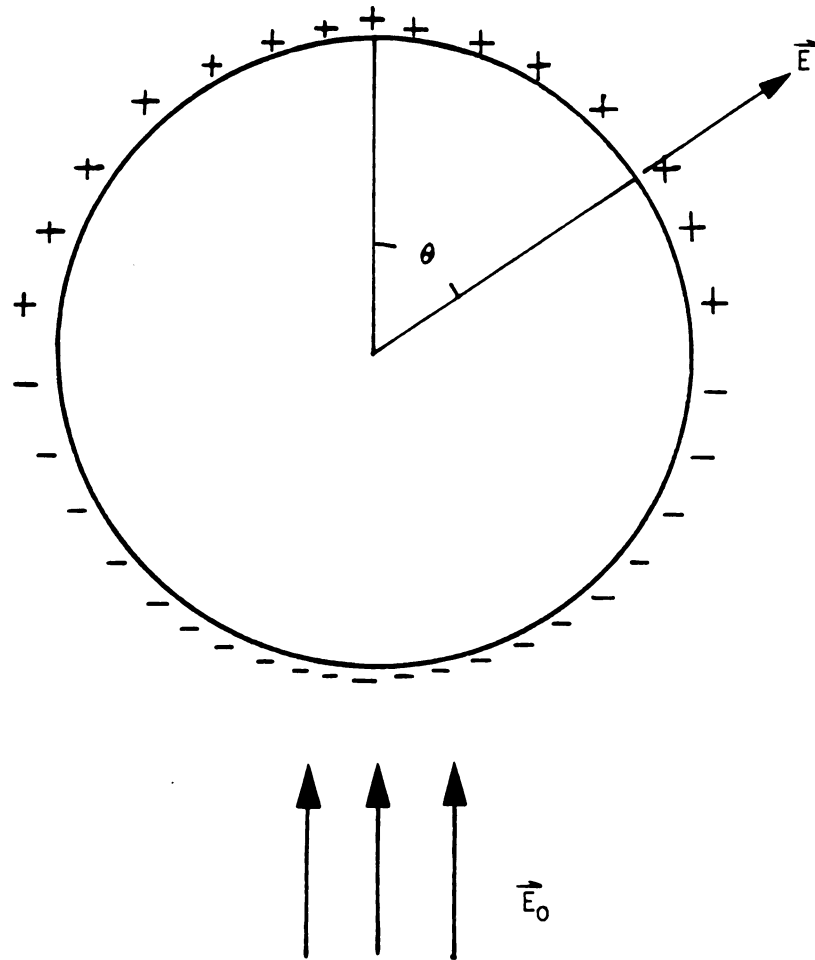
Fig. 3

surface electric field $\vec{E}(\theta) = \hat{r} 3E_0 \cos(\theta)$

surface charge density $\eta(\theta) = \epsilon_0 E(\theta)$

$$= 3\epsilon_0 E_0 \cos(\theta)$$

Fig. 3.1. The induced surface electric field and the induced surface charge density on a perfectly conducting sphere immersed in an uniform electric field.

N ri

shown

surfac

two sa

and a

the m

$\dot{r}_n$,

point

of the

R

where

$$\vec{E}(a,\theta) - 3E_o\cos\theta\hat{r} \qquad (3.1)$$

$$\eta(a,\theta) - \epsilon_o E_r(a,\theta)$$

$$- 3\epsilon_o E_o\cos\theta \qquad (3.2)$$

For numerical calculation, the sphere surface is divided into 2N rings and each ring occupies a radian angle of $\Delta\theta$ ($- \pi/2N$), as shown in Fig. 3.2(a). Due to the rotational symmetry, the induced surface charge is assumed to be uniform within each ring. Consider two sample rings as shown in Fig. 3.2(b): the nth ring with radius ρ_n and a reference source point $Q(\vec{r}_n)$, $\vec{r}_n - (r_n, \theta_n, \psi_n)$, as well as the mth ring with radius ρ_m and a reference field point $P(\vec{r}_m)$, $\vec{r}_m - (r_m, \theta_m, \psi_m)$. The distance between the field point P and the source point Q is R_{mn}. In order to calculate R_{mn}, a more detailed geometries of these two rings are depicted in Fig. 3.3. It can be found that

$$R_{mn} - |\vec{r}_m - \vec{r}_n|$$

$$- [z_{mn}^2 + d_{mn}^2]^{1/2} \qquad (3.3)$$

where

$$z_{mn}^2 - (Z_m - Z_n)^2 - (a\cos\theta_m - a\cos\theta_n)^2$$

$$d_{mn}^2 - (a\sin\theta_m)^2 + (a\sin\theta_n)^2 - 2(a\sin\theta_m)(a\sin\theta_n)\cos(\psi_m - \psi_n)$$
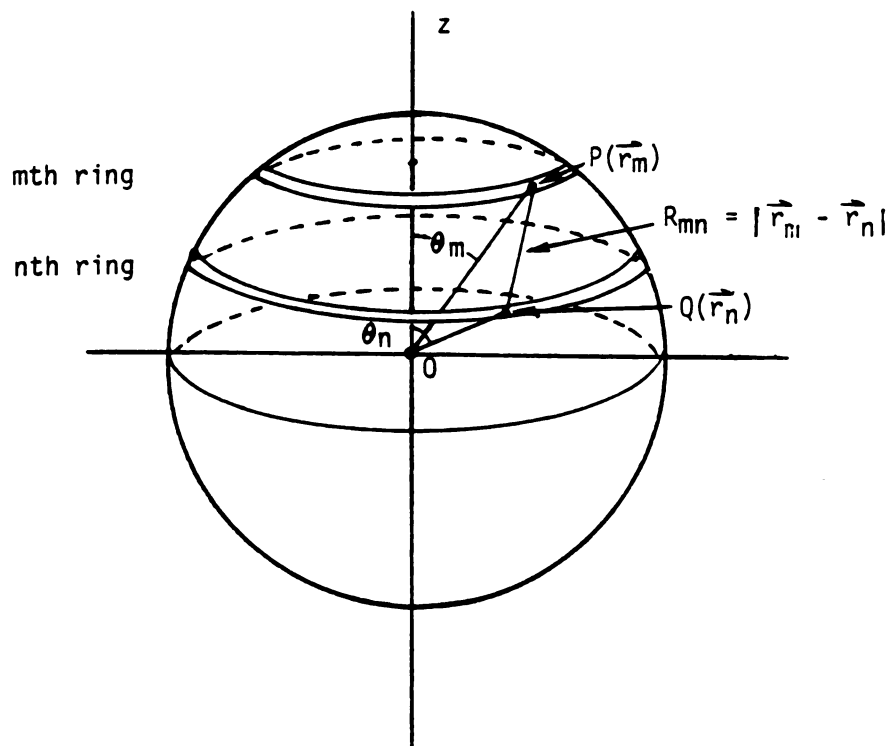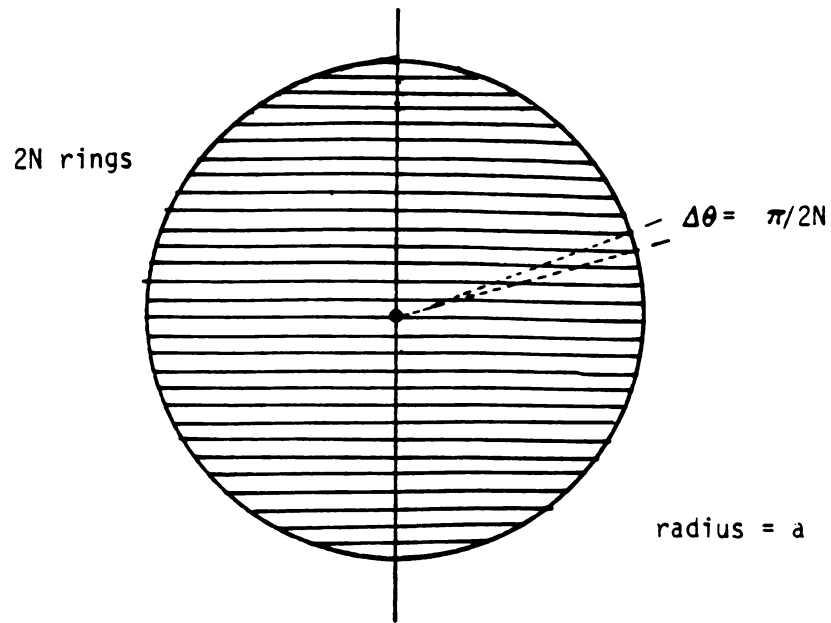
Fig. 3.2. The surface of a perfectly conducting sphere is divided into 2N rings and each ring occupies a radian angle of $\Delta\theta$ ($= \pi/2N$).
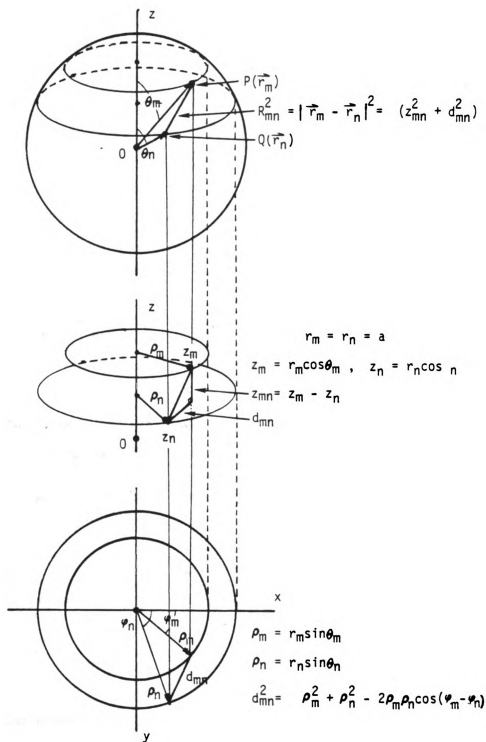
Fig. 3.3. Geometries of two sample rings on the spherical surface.

and hex

R

I

the sca

charge

ϕ

where

S$_n$

η_n

The rot

$\phi_{mn} = -$

$= H$

The tota

charge c

and hence

$$R_{mn} = [2a^2(1 - \cos\theta_m \cos\theta_n - \sin\theta_m \sin\theta_n \cos(\psi_m - \psi_n)]^{1/2} \qquad (3.4)$$

If the surface charge density at the nth ring is denoted as η_n, the scalar potential at the field point P of mth ring due to the surface charge at the nth ring can be expressed as

$$\phi_{mn} = \frac{\eta_n}{4\pi\epsilon_o} \int_{S_n} \frac{1}{R_{mn}} ds' \qquad (3.5)$$

where

S_n = surface area of the nth ring

η_n = surface charge density of the nth ring

The rotational symmetry gives (for simplicity, let $\psi_m = 0$)

$$\phi_{mn} = \frac{\eta_n}{2\pi\epsilon_o} \int_0^\pi \int_{\theta_n - \Delta\theta/2}^{\theta_n + \Delta\theta/2} \frac{a^2 \sin\theta' d\theta' d\psi'}{[2a^2(1 - \cos\theta_m \cos\theta' - \sin\theta_m \sin\theta' \cos\psi')]^{1/2}}$$

$$= M_{mn}\eta_n \qquad (3.6)$$

The total scalar potential at the field P maintained by the surface charge on the entire sphere surface is then obtained as

From

at tw

same

where

can be

where

$$\phi_m = \sum_{n=1}^{2 \times N} (M_{mn} \eta_n) \qquad (3.7)$$

From the symmetry of the sphere, it can be seen that surface charges at two symmetrical rings on the upper and lower hemispheres have the same magnitude but different polarity. ϕ_m can then be written

$$\phi_m = \sum_{n=1}^{N} (M_{mn}^{o} \eta_n - M_{mn}^{s} \eta_n) \qquad (3.8)$$

where o indicates the upper hemisphere and s the lower hemisphere.

By applying Eq. (3.8) to the equation (2.14), a matrix equation can be derived

$$\begin{bmatrix} M_{11} & M_{12} & \cdots\cdots & M_{1N} & -1 \\ M_{21} & M_{22} & \cdots\cdots & M_{2N} & -1 \\ \cdot & \cdot & & \cdot & \cdot \\ \cdot & \cdot & & \cdot & \cdot \\ \cdot & \cdot & & \cdot & \cdot \\ M_{N1} & M_{N2} & \cdots\cdots & M_{NN} & -1 \end{bmatrix} \begin{bmatrix} \eta_1 \\ \eta_2 \\ \cdot \\ \cdot \\ \cdot \\ \eta_N \end{bmatrix} = - \begin{bmatrix} \phi_{o1} \\ \phi_{o2} \\ \cdot \\ \cdot \\ \cdot \\ \phi_{oN} \end{bmatrix} \qquad (3.9)$$

where

$$M_{mn} = M_{mn}^{o} - M_{mn}^{s}$$

$$\phi_{on} = -E_o z_n$$

and

$$M_{mn}^{o} = \frac{1}{2\pi\epsilon_0} \int_0^{\pi} \int_{\theta_n - \Delta\theta/2}^{\theta_n + \Delta\theta/2} \frac{a\sin\theta' d\theta' d\psi'}{[2(1 - \cos\theta_m\cos\theta' - \sin\theta_m\sin\theta'\cos\psi')]^{1/2}}$$

$$M_{mn}^{s} = \frac{1}{2\pi\epsilon_0} \int_0^{\pi} \int_{\theta_{n'} - \Delta\theta/2}^{\theta_{n'} + \Delta\theta/2} \frac{a\sin\theta' d\theta' d\psi'}{[2(1 - \cos\theta_m\cos\theta' - \sin\theta_m\sin\theta'\cos\psi')]^{1/2}}$$

$$0 \leq \theta_n \leq \pi/2, \qquad \theta_{n'} = \pi - \theta_n$$

The numerical results for the case which the sphere is divided into 20 rings are shown in Fig. 3.4. Numerical results of the closed form solution are also listed in the figure for comparison. It is apparent that the agreement between the numerical solution and the closed form solution is excellent. The validity of the surface charge integral equation method is confirmed.

3.3   Sphere above the Ground Plane

To simulate a human or an animal body standing on the ground, a biological sphere located above the ground plane with a grounding impedance Z_L and exposed to an ELF electric field is studied in this section. Consider a biological sphere with radius a located at distance d from the ground plane and immersed in an uniform ELF

$$\vec{E}(\theta) = \hat{r} E(\theta)$$
$$= \hat{r} 3\vec{E}_0 \cos(\theta)$$
$$\eta(\theta) = \epsilon_0 E(\theta)$$

EXACT SOLUTION

$\theta°$	$\eta(\theta)$ $(\times 10^{-10})$	
	exact sol.	numerical sol.
4.5	0.2644	0.2578
13.5	0.2579	0.2561
22.5	0.2450	0.2452
31.5	0.2262	0.2267
40.5	0.2017	0.2021
49.5	0.1723	0.1724
58.5	0.1386	0.1385
67.5	0.1015	0.1014
76.5	0.0620	0.0618
85.5	0.0221	0.0211
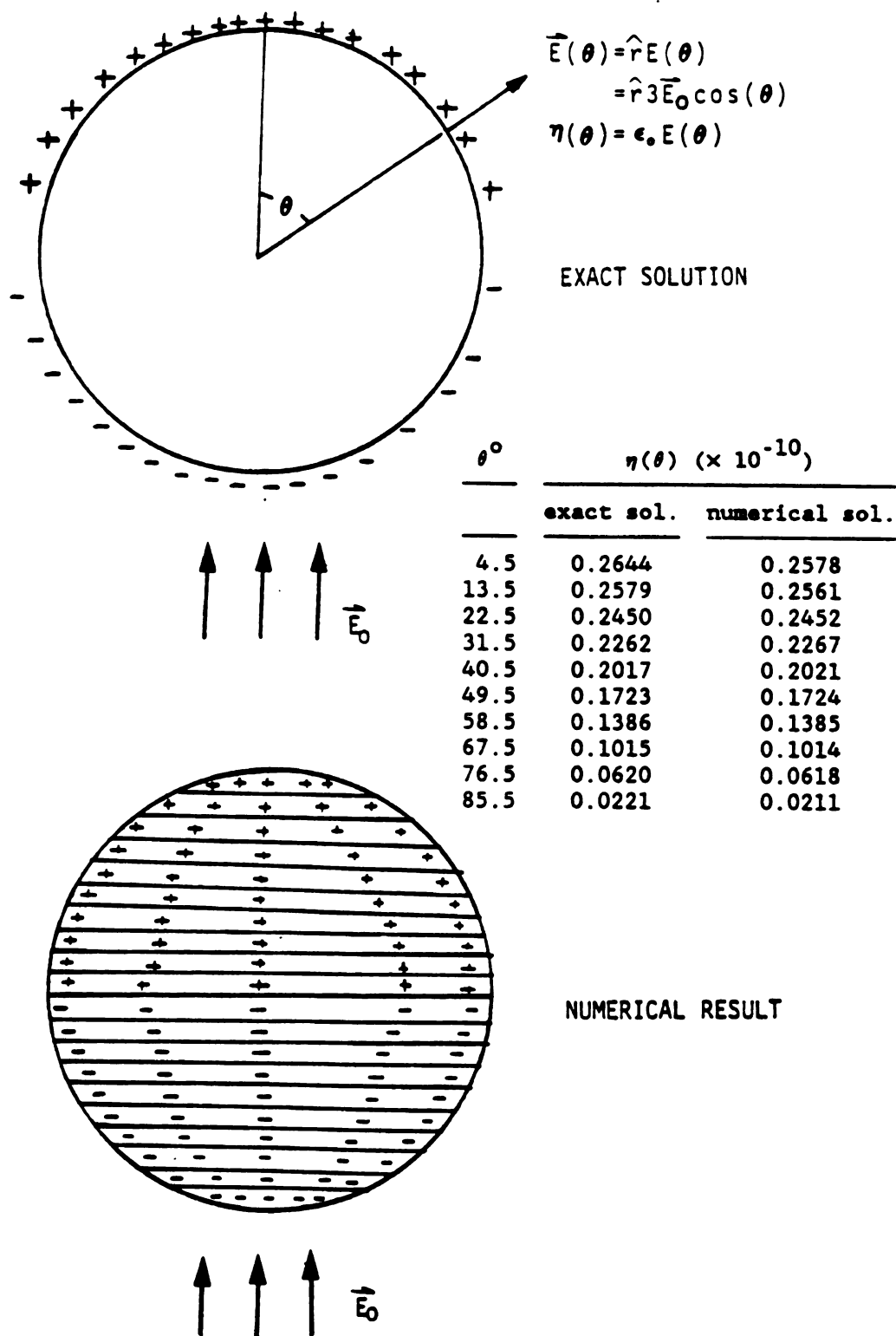
NUMERICAL RESULT

Fig. 3.4. Comparison of numerical results by the present method
with the exact solution on the surface charge density
of a perfectly conducting sphere induced by an uniform
electric field.

ele

gro

the

elec

surf

surf

rota

that

Now

$p \vec{r}$

poin

radi

in F

To ca

and

where

and he

electric field as shown in Fig. 3.5. To take into account of the ground effect, an image sphere is considered. The problem becomes the case of two spheres with a seperation of 2d immersed in an uniform electric field . Again, for numerical calculation each spherical surface is divided into N rings, as shown in Fig. 3.6. The induced surface charge is assumed to be uniform within each ring, due to the rotational symmetry. Also induced surface charges on each ring and that on its image ring have the same magnitude but opposite polarity. Now consider the mth ring with radius ρ_m and a reference field point $P(\vec{r}_m)$, $\vec{r}_m = (r_m, \theta_m, \psi_m)$, the nth ring with radius ρ_n and a source point $Q(\vec{r}_n)$, $\vec{r}_n = (r_n, \theta_n, \psi_n)$ as well as the image n'th ring with radius $\rho_{n'}$ and a source point $Q^i(\vec{r}_{n'})$, $\vec{r}_{n'} = (r_{n'}, \theta_{n'}, \psi_{n'})$, as shown in Fig. 3.6. The distance R_{mn} $(=|\vec{r}_m - \vec{r}_n|)$ is the same as Eqs. (3.4). To calculate the distance $R_{mn'}$ $(=|\vec{r}_m - \vec{r}_{n'}|)$ between the field point P and the image source point Q^i, it can be found that

$$R_{mn'} = |\vec{r}_m - \vec{r}_{n'}| = [z^2_{mn'} + d^2_{mn'}]^{1/2} \tag{3.11}$$

where

$$z^2_{mn'} = (Z_m - Z_{n'})^2 = (2D + a\cos\theta_m + a\cos\theta_{n'})^2$$

$$d^2_{mn'} = (a\sin\theta_m)^2 + (a\sin\theta_{n'})^2 - 2(a\sin\theta_m)(a\sin\theta_{n'})\cos(\psi_m - \psi_{n'})$$

and hence

OBJECT SPHERE

$\vec{E}_0$

radius = a

GROUND

d

Z_L

IMAGE SPHERE

Fig. 3.5. A perfectly conducting sphere located above the ground
with a grounding impedance Z_L is illuminated by an uniform
electric field.
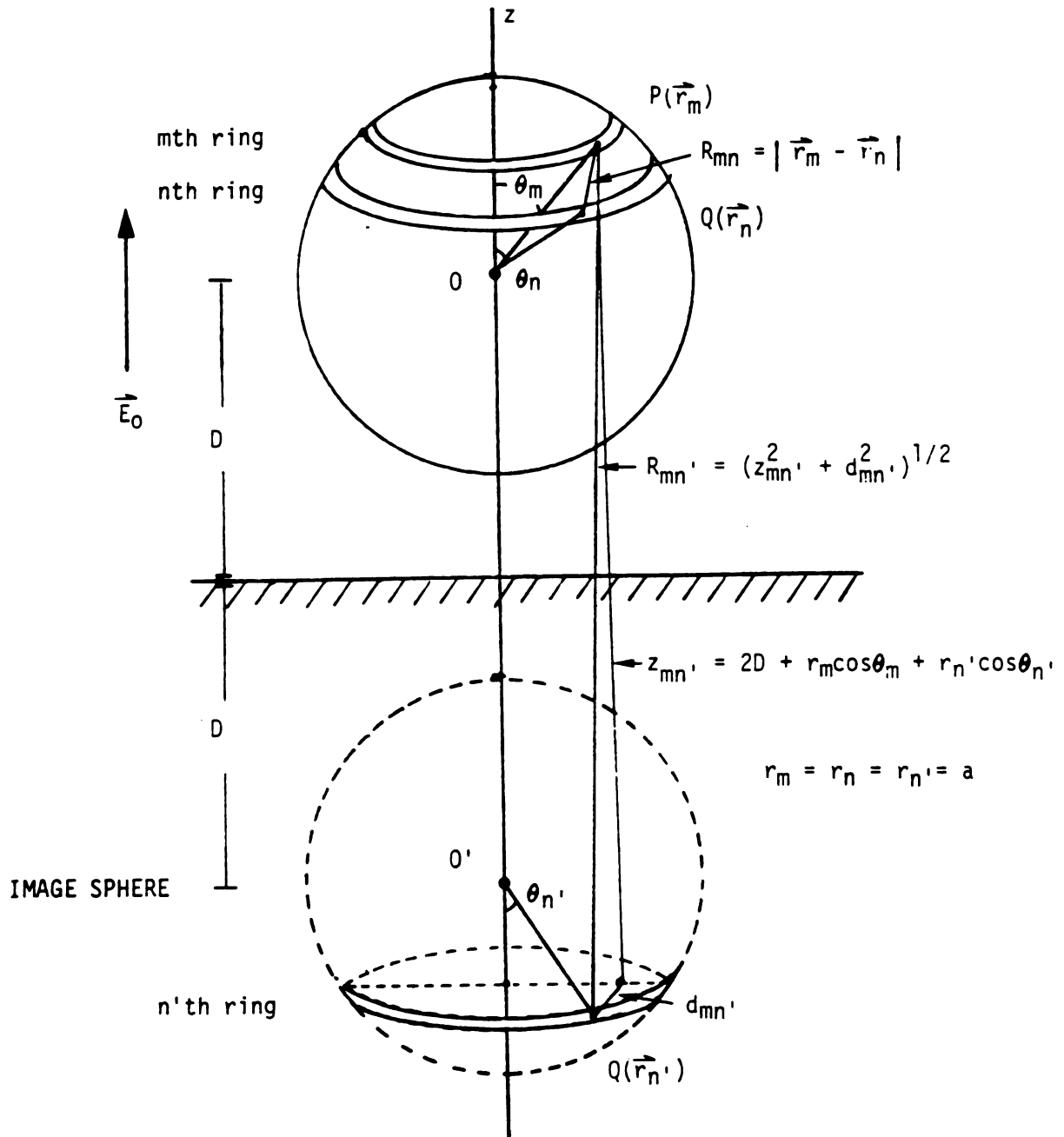
Fig. 3.6. Geometries of three sample rings on the surfaces of a sphere and its image sphere.

the

po

rir

th

ar

The

$$R_{mn'} = [2a^2(1 + \cos\theta_m\cos\theta_{n'} - \sin\theta_m\sin\theta_{n'}\cos(\psi_m - \psi_{n'}) +$$

$$4aD(\cos\theta_m + \cos\theta_{n'})]^{1/2} \qquad (3.12)$$

If the surface charge density at the nth ring is denoted as η_n, then it is $(-\eta_n)$ at the n'th ring. The scalar potential at the field point P of mth ring due to the surface charges at the nth and the n'th ring can be expressed as

$$\phi_{mn} = \phi_{mn}^o + \phi_{mn}^i \qquad (3.13)$$

where

$$\phi_{mn}^o = \frac{\eta_n}{4\pi\epsilon_o} \int_{S_n} \frac{1}{R_{mn}} \, ds'$$

$$\phi_{mn}^i = \frac{-\eta_n}{4\pi\epsilon_o} \int_{S_{n'}} \frac{1}{R_{mn'}} \, ds'$$

and

S_n = surface area of the nth ring

$S_{n'}$ = surface area of the n'th ring

The rotational symmetry gives (for simplicity, let $\psi_m = 0$)

$$\phi^o_{mn} = \frac{\eta_n}{4\pi\epsilon_o} \int_0^\pi \int_{\theta_n-\Delta\theta/2}^{\theta_n+\Delta\theta/2} \frac{a^2\sin\theta' d\theta' d\psi'}{[2a^2(1 - \cos\theta_m\cos\theta' - \sin\theta_m\sin\theta'\cos\psi')]^{1/2}}$$

$$= M^o_{mn}\eta_n$$

$$\phi^i_{mn} = \frac{-\eta_n}{4\pi\epsilon_o} \int_0^\pi \int_{\theta_{n'}-\Delta\theta/2}^{\theta_{n'}+\Delta\theta/2} \frac{a^2\sin\theta' d\theta' d\psi'}{[2a^2(1 + \cos\theta_m\cos\theta' - \sin\theta_m\sin\theta'\cos\psi') +}$$

$$\frac{}{4aD(\cos\theta_m + \cos\theta')]^{1/2}}$$

$$= M^i_{mn}(-\eta_n) \tag{3.14}$$

The total scalar potential at the field point P maintained by the total surface charge of the sphere and the image sphere is then obtained as

$$\phi_m = \sum_{n=1}^{N} (M^o_{mn} - M^i_{mn})\eta_n \tag{3.15}$$

By applying Eq. (3.15) to the equation (2.12), a matrix equation is obtained

$$
\begin{bmatrix}
M_{11} & M_{12} & \cdots\cdots\cdots & M_{1N} & -1 \\
M_{21} & M_{22} & \cdots\cdots\cdots & M_{2N} & -1 \\
\cdot & \cdot & & \cdot & \cdot \\
\cdot & \cdot & & \cdot & \cdot \\
\cdot & \cdot & & \cdot & \cdot \\
M_{N1} & M_{N2} & \cdots\cdots\cdots & M_{NN} & -1 \\
S_1 & S_2 & \cdots\cdots\cdots & S_N & -1/(j\omega Z_L)
\end{bmatrix}
\begin{bmatrix}
\eta_1 \\
\eta_2 \\
\cdot \\
\cdot \\
\cdot \\
\eta_N \\
\phi_b
\end{bmatrix}
= -
\begin{bmatrix}
\phi_{o1} \\
\phi_{o2} \\
\cdot \\
\cdot \\
\cdot \\
\phi_{oN} \\
0
\end{bmatrix}
\tag{3.16}
$$

where

$$M_{mn} = M^o_{mn} - M^i_{mn}$$

$$\phi_{on} = -E_o z_n$$

and

$$M^o_{mn} = \frac{1}{4\pi\epsilon_o} \int_0^\pi \int_{\theta_n - \Delta\theta/2}^{\theta_n + \Delta\theta/2} \frac{a\sin\theta' d\theta' d\psi'}{[2(1 - \cos\theta_m\cos\theta' - \sin\theta_m\sin\theta'\cos\psi')]^{1/2}}$$

$$M^i_{mn} = \frac{1}{4\pi\epsilon_o} \int_0^\pi \int_{\theta_{n'} - \Delta\theta/2}^{\theta_{n'} + \Delta\theta/2} \frac{a\sin\theta' d\theta' d\psi'}{[2(1 + \cos\theta_m\cos\theta' - \sin\theta_m\sin\theta'\cos\psi') +}$$

$$\overline{4aD(\cos\theta_m + \cos\theta')]^{1/2}}$$

Since there is no closed form solution for the problem of two spheres, the way to check the validity of the numerical solution is to let the seperation between the two spheres approaching infinity and then compute the induced surface charge. Numerical results of this case should be the same as that of an isolated sphere. Fig. 3.7 shows results on induced surface charges of both cases. A good agreement is obtained. The validity of this integral equation method for a conducting object above the ground is then confirmed. Also surface charge distributions on a sphere located at various distances from the ground plane are shown in Fig. 3.8. It can be seen that the

θ

$\vec{E}_0$

$\eta(\theta)$: induced surface charge density

$d \longrightarrow \infty$

GROUND
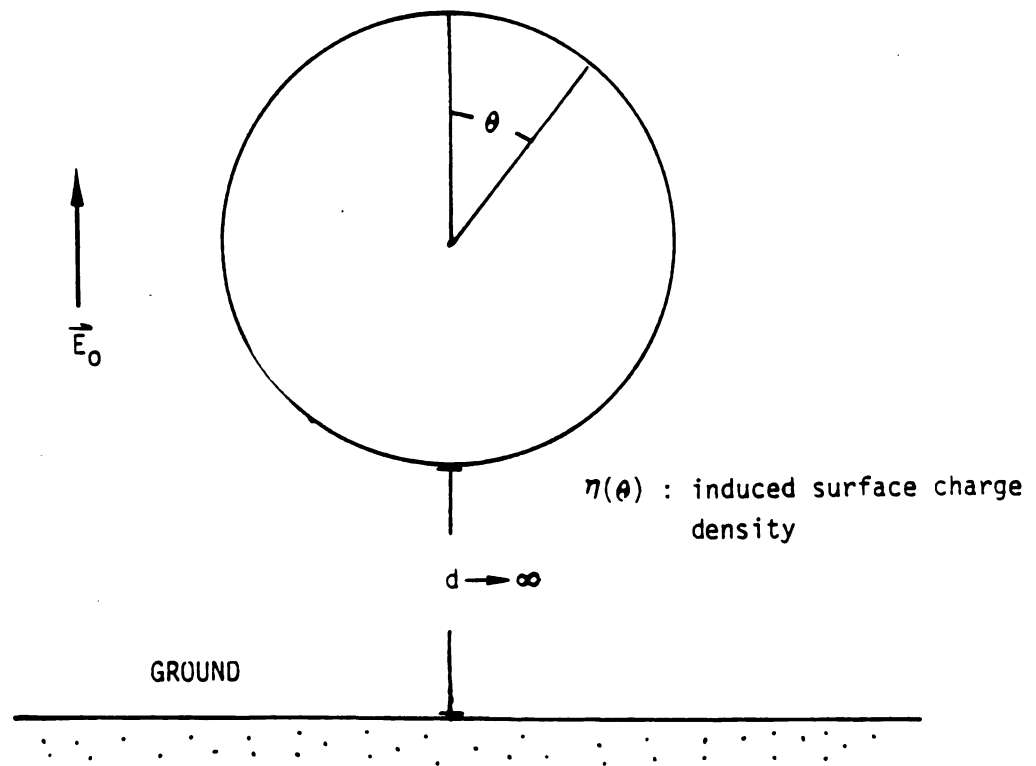
θ°	$\eta(\theta)$ $(\times 10^{-10})$	
	present case	isolated sphere
4.5	0.2578	0.2578
13.5	0.2560	0.2561
22.5	0.2451	0.2452
31.5	0.2265	0.2267
40.5	0.2021	0.2021
49.5	0.1724	0.1724
58.5	0.1386	0.1385
67.5	0.1012	0.1014
76.5	0.0620	0.0618
85.5	0.0211	0.0211

$* \; \eta(180^\circ - \theta) = -\eta(\theta) \quad 0^\circ \leq \theta \leq 90^\circ$

Fig. 3.7. The distribution of surface charge density on a floating perfectly conducting sphere located at an infinite distance from the ground induced by an uniform electric field.
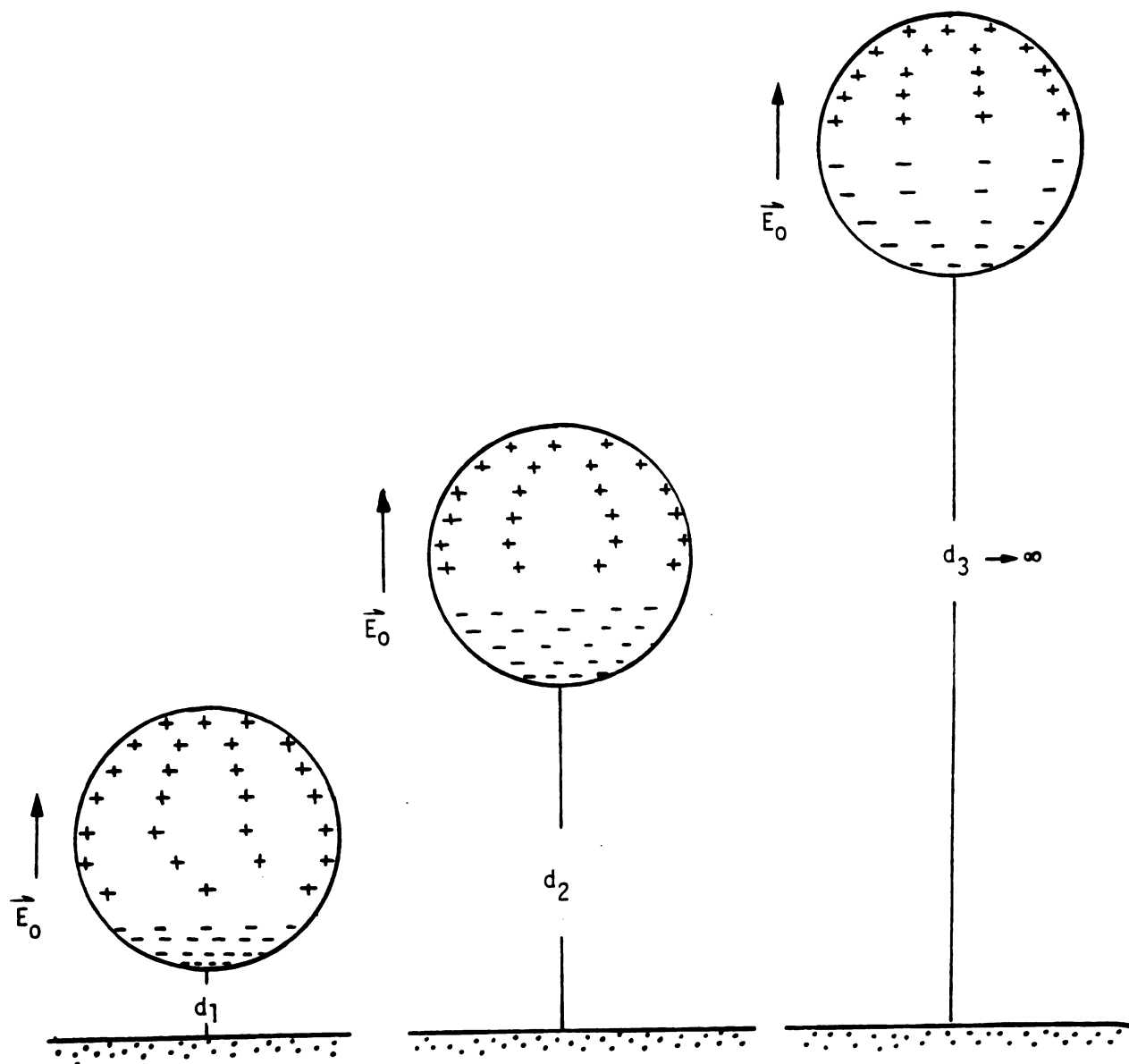
Fig. 3.8. Surface charge distributions on perfectly conducting spheres located at various distances from the ground and exposed to an uniform electric field.

closer the sphere to the ground, the surface charge distribution will be more asymmetric along the vertical direction due to a stronger coupling effect.

The short-circuit current I_{sc} of a grounded sphere ($Z_L = 0$) can be expressed as (from Eq. (2.5))

$$I_{sc} = j\omega \sum_{n=1}^{N} (\eta_n S_n) \tag{3.17}$$

The empirical formula of the short-circuit current of a grounded biological body can be written as [8][9]

$$I_{sc} = 4.2 \times 10^{-5} \times f E_o w^{2/3} \tag{3.18}$$

where I_{sc} is in $\mu A/(kV/m)$, f in Hz, E_o in kV/m, and w(weight) in g. To compare empirical results with numerically evaluated results, short-circuit currents of various size (weight) spheres are calculated and shown in Fig. 3.9. It is observed that the agreement between numerical solutions and existing empirical results is very good. It is of interest to find the effect of grounding impedances on the short-circuit current of a biological body exposed to a 60 Hz electric field. The grounding impedance is assumed to be resistive, capacitive or inductive. The short-circuit current as the function of grounding impedance is shown in Fig. 3.10 ~ 3.12. For a sphere with a radius of 0.25m (volume = 6.5×10^3 cm^3, corresponding to a 65 Kg sphere),

$$W(\text{WEIGHT})=(4/3)\pi a^3$$

PRESENT THEORY

EMPIRICAL FORMULA

$$I_{sc}=4.5\times10^{-5}\times fE_0W^{2/3}$$

$\begin{cases} I_{sc}(\mu A) \\ f \quad (H_z) \\ E_0 \quad (kV/m) \\ W \quad (g) \end{cases}$
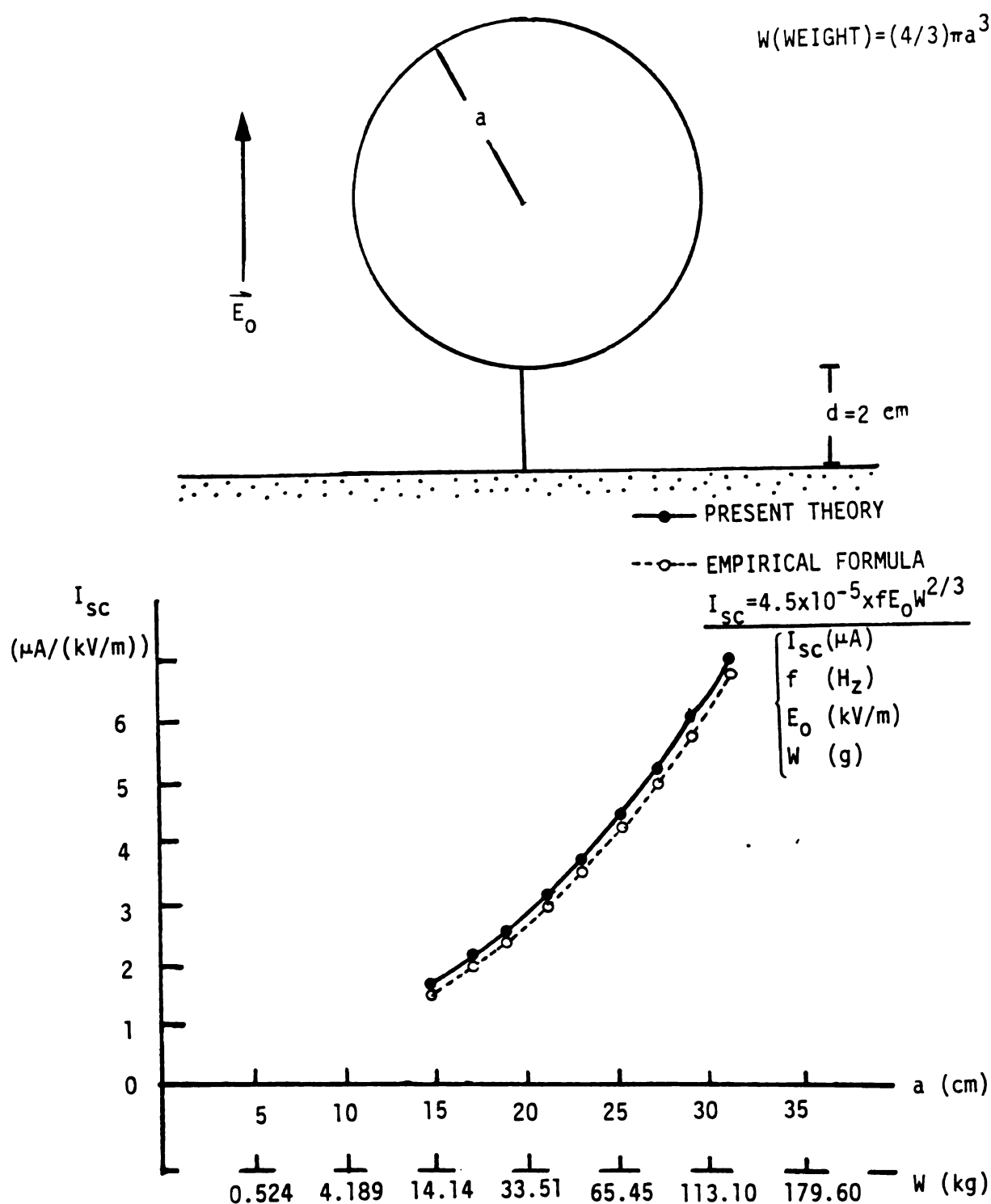
Fig. 3.9. Comparison of theoretical results by the present method with empirical results on the short-circuit current for a biological sphere as a function of the radius when exposed to a 1 kV/m, 60-Hz electric field.
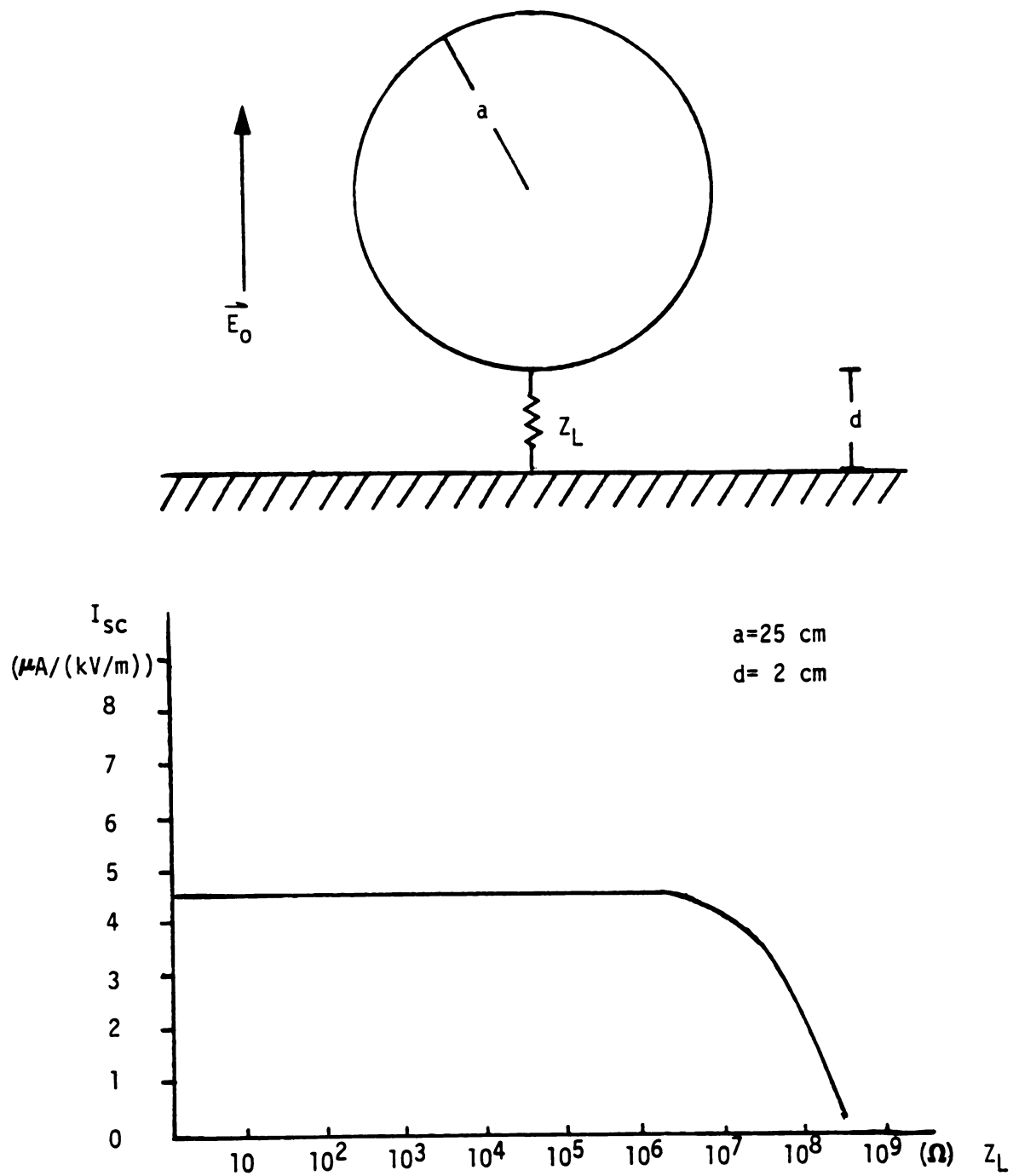
Fig. 3.10. Theoretical results on the short-circuit current for a biological sphere as a function of the grounding resistance when exposed to a 1 kV/m, 60-Hz electric field.

$\vec{E}_0$

a

C

d

$Z_L = \left| 1/j\omega c \right|$

I_{sc}

$(\mu A/(kV/m))$

a=25 cm

d= 2 cm

7

6

5

4

3

2

1

0

| 10 | 10^2 | 10^3 | 10^4 | 10^5 | 10^6 | 10^7 | 10^8 | 10^9 | (Ω) | Z_L |

10^{-3} 10^{-4} 10^{-5} 10^{-6} 10^{-7} 10^{-8} 10^{-9} 10^{-10} (F)   C

(x 0.265)
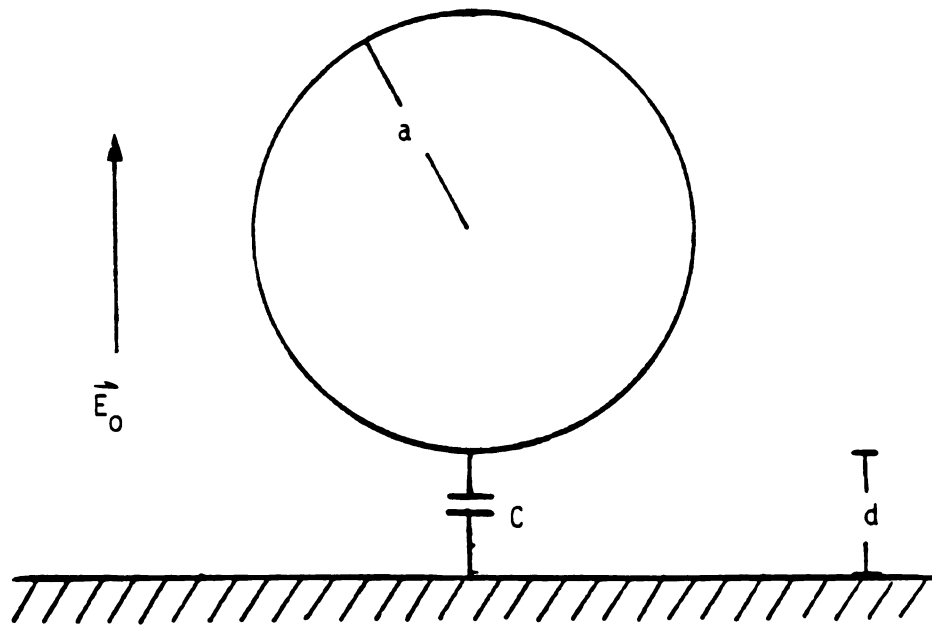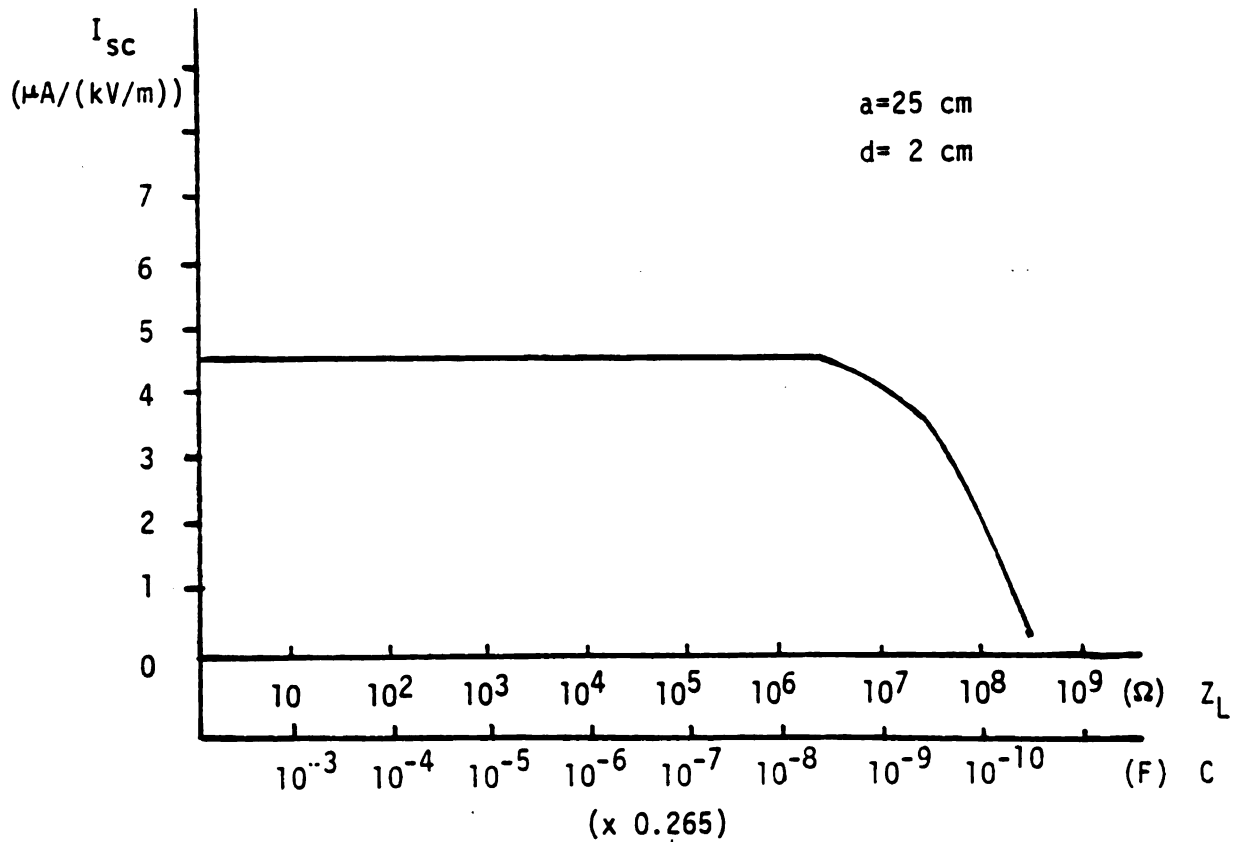
Fig. 3.11. Theoretical results on the short-circuit current for a biological sphere as a function of the grounding capacitance when exposed to a 1 kV/m, 60-Hz electric field.
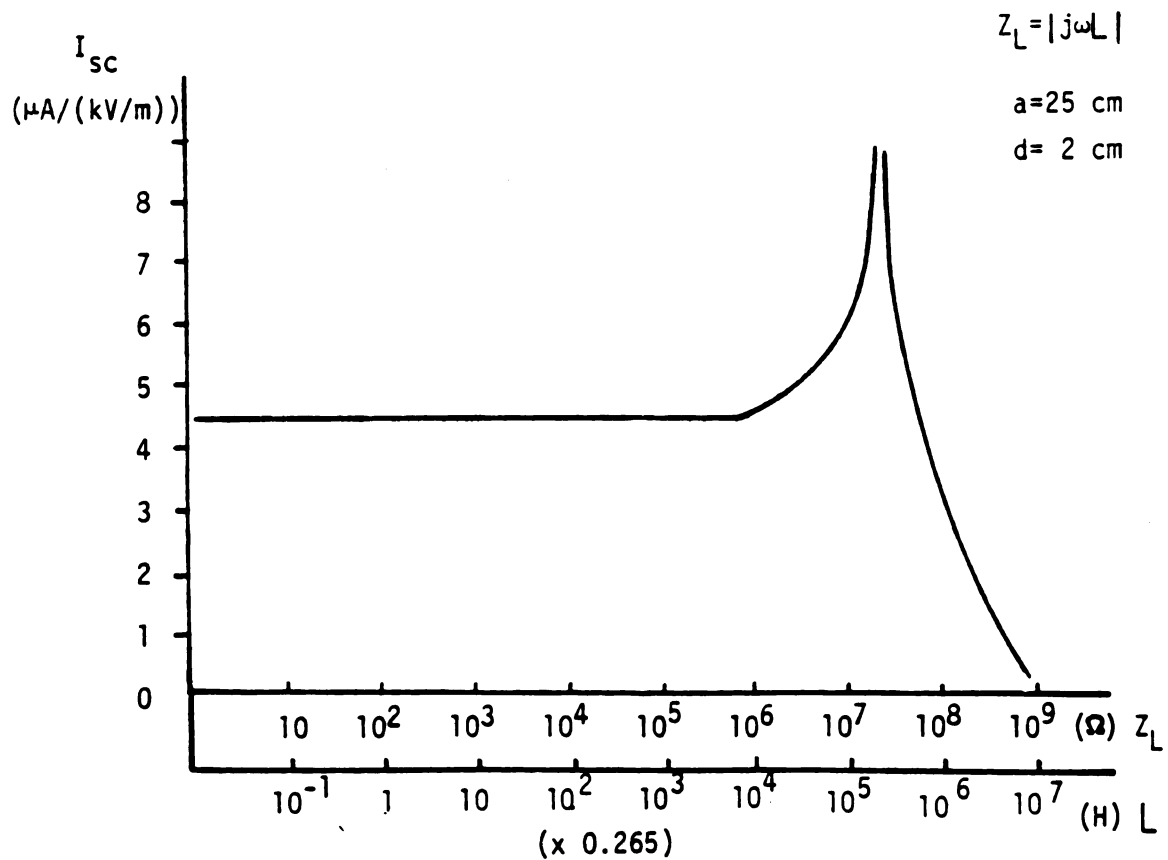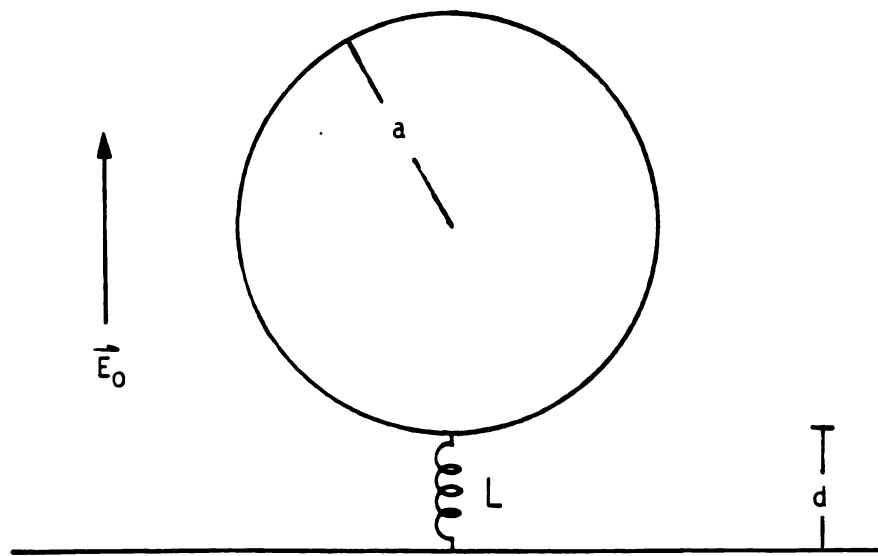
Fig. 3.12. Theoretical results on the short-circuit current for a biological sphere as a function of the grounding inductance when exposed to a 1 kV/m, 60-Hz electric field.

the short-circuit current is found to remain practically unchanged,
maintaining a value of about 4.5 μA/(kV/m), when the grounding
impedance is varied from zero to 5.0 MΩ. Only after the grounding
impedance exceeds the value of 5.0 MΩ, the short-circuit current
starts to fall for a resistive or capacitive grounding impedance.
For an inductive grounding impedance, there is a possible resonance
phenomenon when the impedance has a value in the order of 20 MΩ,
corresponding to an inductance of 0.53 $\times$ 10^5 henries. This implies
that in a very unlikely case when the grounding impedance is an
extremely large inductance of about 53000 henries, there may be a
very large current induced in the body. The physical explanation of
this phenomenon can be discussed from a circuit point of view. Let
C denoted as the capacitance between a small area element A on the
sphere surface and the energized electrode (such as the power line),
as shown in Fig. 3.13, a displacement current, I, will pass from the
overhead electrode through C, then through A, and to the ground
through the grounding impedance Z_L. Since the sphere is assumed as
perfectly conducting, the current I will not flow through inside of
the sphere. The total capacitance C_t between the electrode and the
whole sphere surface can be derived by the equivalent circuit method
(*Chapter 7*). The impedance of this capacitance C_t is found to be very
large. Hence for a resistive or capacitive grounding impedance, the
current I starts to fall only after the grounding impedance becomes
as large as the impedance of C_t. While for an inductive grounding
impedance, the resonance phenomenon is observed, when the inductance

HIGH VOLTAGE ELECTRODE

I

C

surface area element A

BODY

Z_L

GROUND
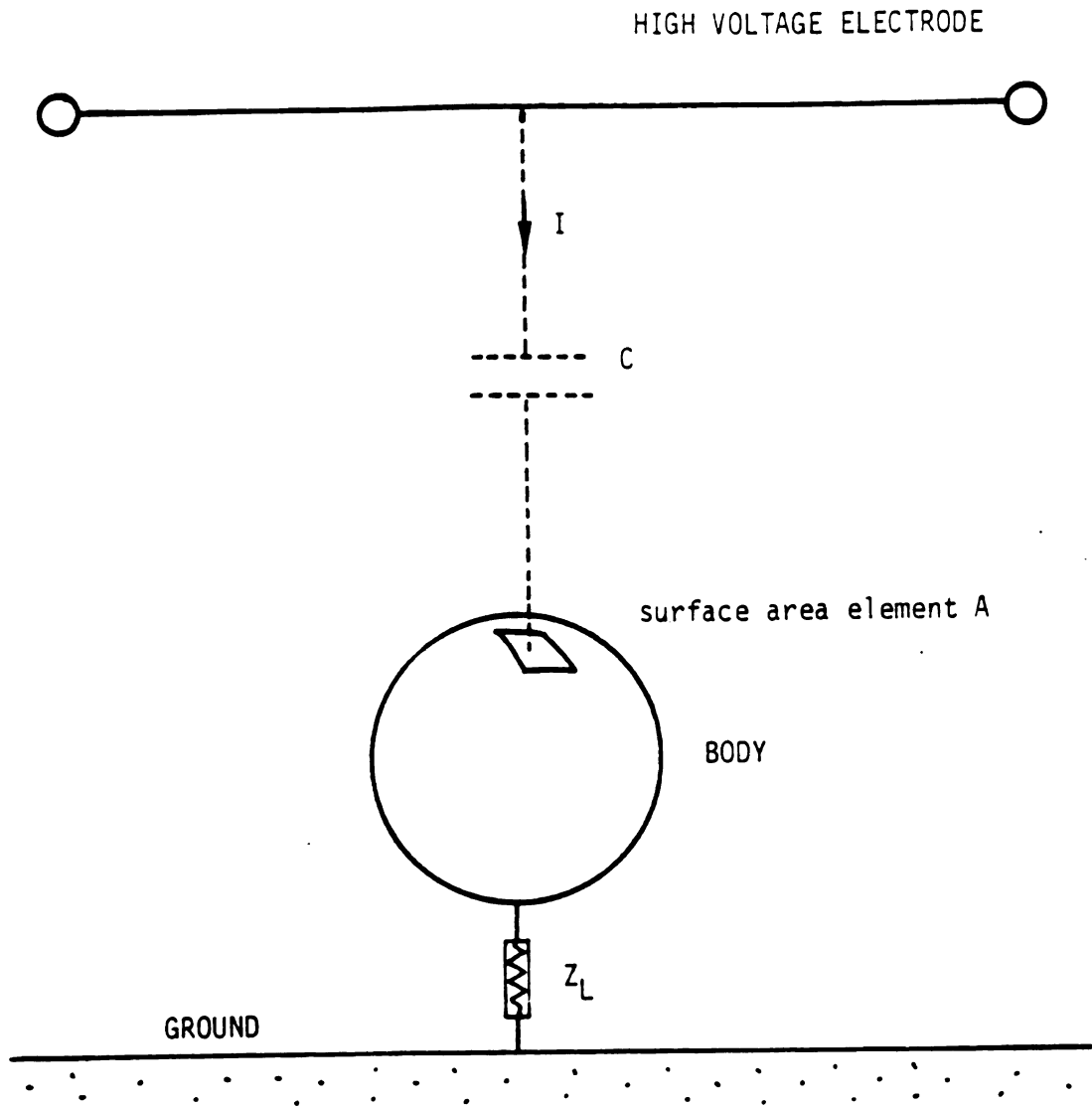
Fig. 3.13. A displacement current, I, is coupled from the overhead electrode through a capacitance C to a surface area element A of the subject body.

has a certain value L in series with the capacitance C_t for which

$(j\omega L + 1/j\omega C_t) = 0$.

3.4 Applications to Spheroidal Models of Biological Bodies

Since geometric shapes of many living objects such as human or animal bodies are far from spherical, a spheroid is considered to be a more realistic model for a biological object than a sphere. Consider a perfectly conducting prolate spheroid with major axis a and minor axis b immersed in an uniform electric field, as shown in Fig. 3.14. For numerical calaulation, the spheroidal surface is divided into N rings, as shown in Fig. 3.14. The induced surface charge is assumed to be uniform within each ring due to the rotational symmetry. Consider two sample rings as shown in Fig. 3.15; the nth ring with radius ρ_n and a reference source point $Q(\vec{r}_n)$, $\vec{r}_n = (r_n, R_n, \psi_n)$, and the mth ring with radius ρ_m and a reference field point $P(\vec{r}_m)$, $\vec{r}_m = (r_m, \theta_m, \psi_m)$. R_{mn} is the distance between the field point P and the source point Q. It can be found that (Fig. 3.15) [18]

$$R_{mn} = [z_{mn}^2 + d_{mn}^2]^{1/2} \qquad (3.19)$$

where

$$z_{mn}^2 = (Z_m - Z_n)^2 = (r_m \cos\theta_m - r_n \cos\theta_n)^2$$

$$d_{mn}^2 = (r_m \sin\theta_m)^2 + (r_n \sin\theta_n)^2 - 2(r_m \sin\theta_m)(r_n \sin\theta_n)\cos(\psi_m - \psi_n)$$
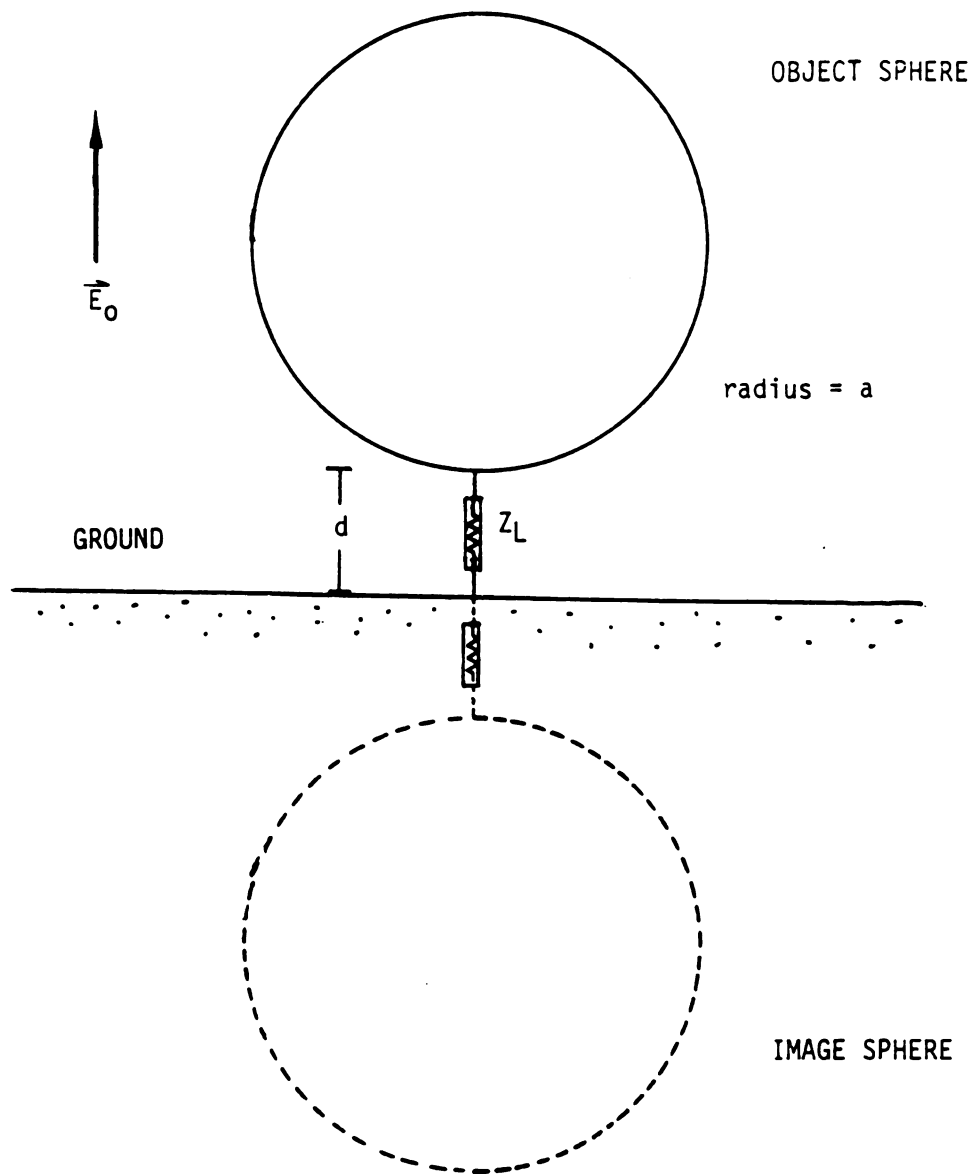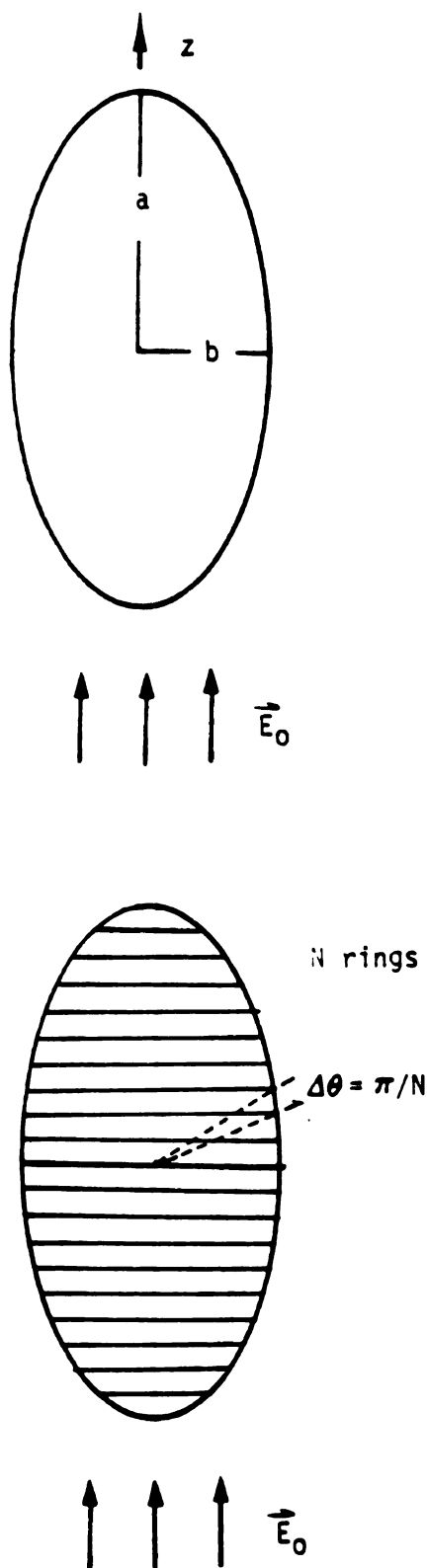
Fig. 3.14. A perfectly conducting prolate spheroid with major axis a and minor axis b immersed in an uniform electric field. The surface of the spheroid is divided into N rings for numerical calculation.
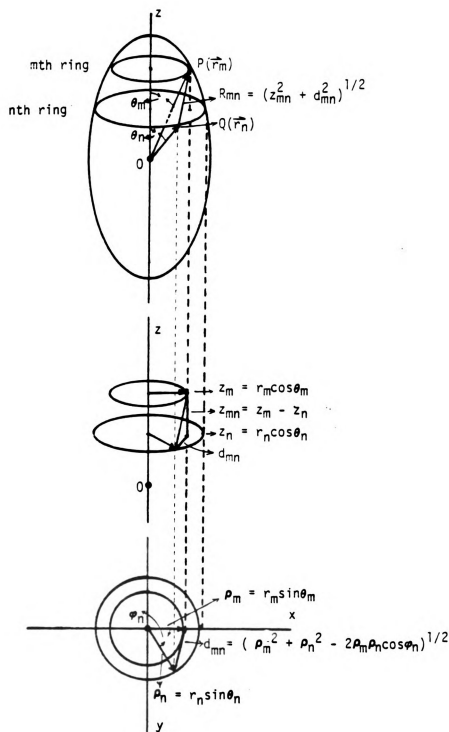
Fig. 3.15. Geometries of two sample rings on the surface of a spheroid.

and

$$r_m = \frac{ab}{[(a\sin\theta_m)^2 + (b\cos\theta_m)^2]^{1/2}} \quad , \quad r_n = \frac{ab}{[(a\sin\theta_n)^2 + (b\cos\theta_n)]^{1/2}}$$

The scalar potential ϕ_{mn} at the field point P due to the surface charge at the nth ring can be expressed as

$$\phi_{mn} = \frac{1}{4\pi\epsilon_o} \int_{S_n} \frac{\eta_n}{R_{mn}} \, ds' \qquad (3.20)$$

where

S_n = surface area of the nth ring

η_n = surface charge density of the nth ring

It can be found that (*Appendix 1*)

$$dS_n = r_n \sin\theta_n d\psi_n d\lambda_n \qquad (3.21)$$

where

$$d\lambda_n = \frac{ab}{[(a\sin\theta_n)^2 + (b\cos\theta_n)^2]^{1/2}} \left\{ 1 + \frac{[(a^2 - b^2)\sin\theta_n\cos\theta_n]^2}{[(a\sin\theta_n)^2 + (b\cos\theta_n)^2]^2} \right\}^{1/2} d\theta_n$$

By Using Eq. (3.20) - (3.21) and rotational symmetry we have (let $\psi_m = 0$)

$$\phi_{mn} = M_{mn}\eta_n \qquad\qquad (3.22)$$

where

$$M_{mn} = \frac{1}{2\pi\epsilon_o} \int_0^\pi \int_{\theta_n - \Delta\theta/2}^{\theta_n + \Delta\theta/2} \frac{abr_n \sin\theta'}{R_{mn}[(a\sin\theta')^2 + (b\cos\theta')^2]^{1/2}} \times$$

$$\left\{ 1 + \frac{[(a^2 - b^2)\sin\theta'\cos\theta']^2}{[(a\sin\theta')^2 + (b\cos\theta')^2]^2} \right\}^{1/2} d\theta' d\psi'$$

The total scalar potential at the field point P maintained by the total surface charge on the entire spheroid is

$$\phi_m = \sum_{n=1}^N (M_{mn}\eta_n). \qquad\qquad (3.23)$$

By applying Eq. (3.23) to the equation (2.14), a matrix equation is given

$$\begin{bmatrix} M_{11} & M_{12} & \cdots\cdots\cdots & M_{1N} & -1 \\ M_{21} & M_{22} & \cdots\cdots\cdots & M_{2N} & -1 \\ \cdot & \cdot & & \cdot & \cdot \\ \cdot & \cdot & & \cdot & \cdot \\ \cdot & \cdot & & \cdot & \cdot \\ M_{N1} & M_{N2} & \cdots\cdots\cdots & M_{NN} & -1 \end{bmatrix} \begin{bmatrix} \eta_1 \\ \eta_2 \\ \cdot \\ \cdot \\ \cdot \\ \eta_N \end{bmatrix} = - \begin{bmatrix} \phi_{o1} \\ \phi_{o2} \\ \cdot \\ \cdot \\ \cdot \\ \phi_{oN} \end{bmatrix} \qquad (3.24)$$

where

$$\phi_{on} = -E_o z_n$$

$$\eta_n = \text{surface charge density of the nth ring}$$

$$\phi_b = \text{equipotential of the spheroid}$$

Fig. 3.16 depicts two numerical examples of spheroids with the same volume but different axis ratio. The surface of each spheroid is divided into 20 rings. Numerical results of the induced surface charge for the spheroid with axis ratio equal to 1 should be the same as that of a sphere given in Fig. 3.4. It can be seen that the agreement is excellent. Also it is observed that the electric field enhancement factor at the top of the spheroid increases as the axis ratio increases, since the spheroid becomes thinner and sharper.

3.5   Spheroid above the Ground Plane

To simulate an animal or human body standing on the ground, a biological prolate spheroid located above the ground plane with a grounding impedance Z_L and exposed to an ELF electric field, as shown in Fig. 3.17, is studied in this section. Again, an image spheroid is considered for the ground effect. Each spheroidal surface is divided into N rings. The induced surface charge within each ring is assumed to be uniform due to the rotational symmetry. Consider

a : major axis
b : minor axis

a/b = 1 (sphere)
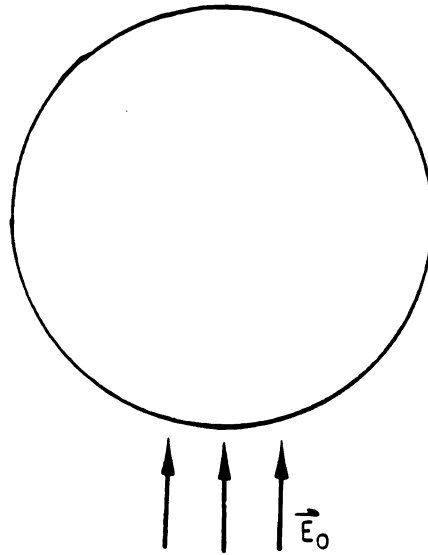
θ°	$\eta(\theta)$ $(\times 10^{-10})$
4.5	0.2577
13.5	0.2562
22.5	0.2450
31.5	0.2267
40.5	0.2020
49.5	0.1726
58.5	0.1388
67.5	0.1014
76.5	0.0620
85.5	0.0223

$\vec{E}_0$

a/b = 2
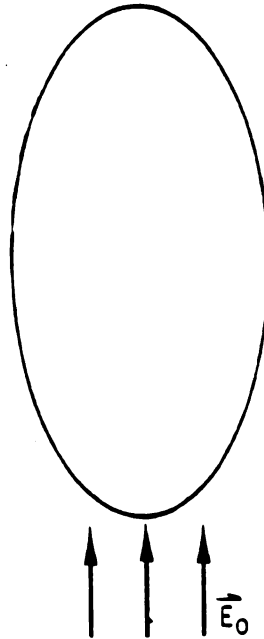
θ°	$\eta(\theta)$ $(\times 10^{-10})$
4.5	0.4750
13.5	0.3754
22.5	0.2667
31.5	0.2023
40.5	0.1475
49.5	0.1022
58.5	0.0753
67.5	0.0521
76.5	0.0316
85.5	0.0085

$\vec{E}_0$

Fig. 3.16. Distributions of surface charge density on spheroids
with two different axis-ratios (a/b = 1 & a/b = 2) induced
by an uniform electric field.
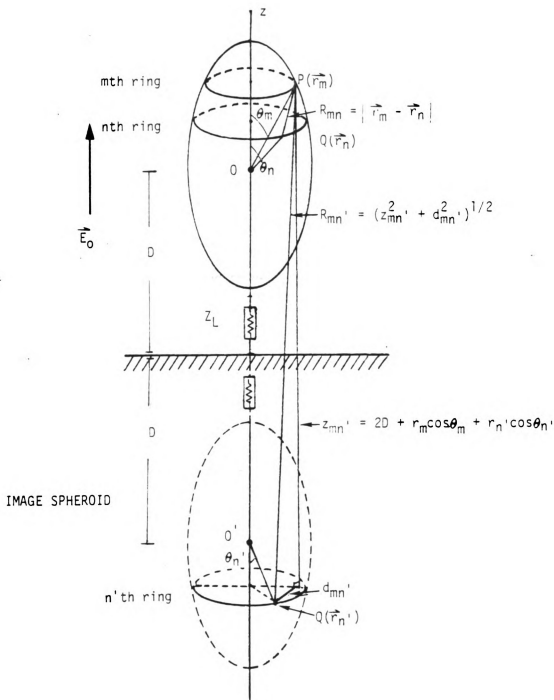
Fig. 3.17. A spheroid located above the ground with a grounding impedance Z_L exposed to an uniform electric field. Geometries of three sample rings on the surfaces of the spheroid and the image spheroid are also shown in the figure.

mth ring : radius ρ_m & a reference field point $P(\vec{r}_m)$, $\vec{r}_m = (r_m, \theta_m, \psi_m)$

nth ring : radius ρ_n & a reference source point $Q(\vec{r}_n)$, $\vec{r}_n = (r_n, \theta_n, \psi_n)$

n'th ring : radius $\rho_{n'}$ & a reference source point $Q^i(\vec{r}_{n'})$,

$\qquad \vec{r}_{n'} = (r_{n'}, \theta_{n'}, \psi_{n'})$, (n'th ring = image ring of nth ring)

as shown in Fig. 3.17. The distances between the field point P and source points Q & Q' are found to be

$$R_{mn} = [z^2_{mn} + d^2_{mn}]^{1/2}$$

$$(3.25)$$

$$R_{mn'} = [z^2_{mn'} + d^2_{mn'}]^{1/2}$$

where R_{mn}, Z_{mn} and d_{mn} are in Eq. (3.19) and $Z_{mn'}$ & $d_{mn'}$ are

$$z^2_{mn'} = (Z_m - Z_{n'})^2 = (2D + r_m\cos\theta_m + r_{n'}\cos\theta_{n'})^2$$

$$d^2_{mn'} = (r_m\sin\theta_m)^2 + (r_{n'}\sin\theta_{n'})^2 - 2(r_m\sin\theta_m)(r_{n'}\sin\theta_{n'})\cos(\psi_m - \psi_{n'})$$

and

$$r_m = \frac{ab}{[(a\sin\theta_m)^2 + (b\cos\theta_m)^2]^{1/2}} \quad , \quad r_{n'} = \frac{ab}{[(a\sin\theta_{n'})^2 + (b\cos\theta_{n'})^2]^{1/2}}$$

Let the surface charge density of the nth ring denoted as η_n and $(-\eta_n)$ is that of the n'th ring. Now the scalar potential at the

field point P due to the surface charge on the nth & n'th ring can be expressed as

$$\phi_{mn} = \phi_{mn}^{o} + \phi_{mn}^{i} \qquad (3.26)$$

where

$$\phi_{mn}^{o} = \frac{\eta_n}{4\pi\epsilon_o} \int_{S_n} \frac{1}{R_{mn}} \, ds'$$

$$\phi_{mn}^{i} = \frac{-\eta_n}{4\pi\epsilon_o} \int_{S_{n'}} \frac{1}{R_{mn'}} \, ds'$$

and

S_n = surface area of the nth ring

$S_{n'}$ = surface area of the n'th ring

Using Eq. (3.25) ~ (3.26) and rotational symmetry, it leads to (let $\psi_m = 0$)

$$\phi_{mn}^{o} = M_{mn}^{o} \eta_n$$

$$\qquad (3.27)$$

$$\phi_{mn}^{i} = M_{mn}^{i} (-\eta_n)$$

where

$$M_{mn}^{o} = \frac{1}{2\pi\epsilon_{o}} \int_{0}^{\pi} \int_{\theta_{n}-\Delta\theta/2}^{\theta_{n}+\Delta\theta/2} \frac{abr_{n}\sin\theta'}{R_{mn}[(a\sin\theta')^{2} + (b\cos\theta')]^{1/2}} \times$$

$$\left\{ 1 + \frac{[(a^{2} - b^{2})\sin\theta'\cos\theta']^{2}}{[(a\sin\theta')^{2} + (b\cos\theta')^{2}]^{2}} \right\}^{1/2} d\theta'd\psi'$$

$$M_{mn}^{i} = \frac{1}{2\pi\epsilon_{o}} \int_{0}^{\pi} \int_{\theta_{n'}-\Delta\theta/2}^{\theta_{n'}+\Delta\theta/2} \frac{abr_{n'}\sin\theta'}{R_{mn'}[(a\sin\theta')^{2} + (b\cos\theta')]^{1/2}} \times$$

$$\left\{ 1 + \frac{[(a^{2} - b^{2})\sin\theta'\cos\theta']^{2}}{[(a\sin\theta')^{2} + (b\cos\theta')^{2}]^{2}} \right\}^{1/2} d\theta'd\psi'$$

The total scalar potential at P maintained by the total surface charge on the object spheroid and the image spheroid is then obtained as

$$\phi_{m} = \sum_{n=1}^{N} (M_{mn}^{o} - M_{mn}^{i})\eta_{n} \qquad (3.28)$$

By applying Eq. (3.28) to the matrix equation (2.15), a matrix equation is obtained as

$$
\begin{bmatrix}
M_{11} & M_{12} & \cdots\cdots\cdots & M_{1N} & -1 \\
M_{21} & M_{22} & \cdots\cdots\cdots & M_{2N} & -1 \\
\cdot & \cdot & & \cdot & \cdot \\
\cdot & \cdot & & \cdot & \cdot \\
\cdot & \cdot & & \cdot & \cdot \\
M_{N1} & M_{N2} & \cdots\cdots\cdots & M_{NN} & -1 \\
S_{1} & S_{2} & \cdots\cdots\cdots & S_{N} & -1/(j\omega Z_{L})
\end{bmatrix}
\begin{bmatrix}
\eta_{1} \\
\eta_{2} \\
\cdot \\
\cdot \\
\cdot \\
\eta_{N} \\
\phi_{b}
\end{bmatrix}
= -
\begin{bmatrix}
\phi_{o1} \\
\phi_{o2} \\
\cdot \\
\cdot \\
\cdot \\
\phi_{oN} \\
0
\end{bmatrix}
\qquad (3.29)
$$

whe

(Z

of

ag:

It

E₄

a

fo₁

Th₃

whe

to

where

$$M_{mn} = M_{mn}^{o} - M_{mn}^{1}$$

$$\phi_{on} = - E_{o} z_{n}$$

To check the validity of the numerical solution, let $(d \rightarrow \infty)$ & $(Z_{L} \rightarrow 0)$ and then compare the numerical result of this case with that of an isolated spheroid in the free space as shown in Fig. 3.18. The agreement is very good.

The short-circuit current of a grounded spheroid $(Z_{L} = 0)$ is

$$I_{sc} = j\omega \sum_{n=1}^{N} (\eta_{n} S_{n}) \tag{3.30}$$

It is known that the empirical formula of the short-circuit current, Eq. (3.18), is good for a biological object with a body shape close to a sphere. Since a human body is far from spherical, the empirical formula for the short-circuit current given by Deno [5] and used by Chiba et al. [15],

$$I_{sc} = 5.4 \times 10^{-9} \times (f/60) E_{o} H^{2} \tag{3.31}$$

where I_{sc} in $\mu A/(kV/m)$, f in Hz, E_{o} in kV/m, H (height) in m, was found to be much better for a human body. It is interesting to find out the

a

$a/b = 2$

θ

b

$\eta(\theta)$: induced surface charge density

$\vec{E}_0$

GROUND

$d \longrightarrow \infty$
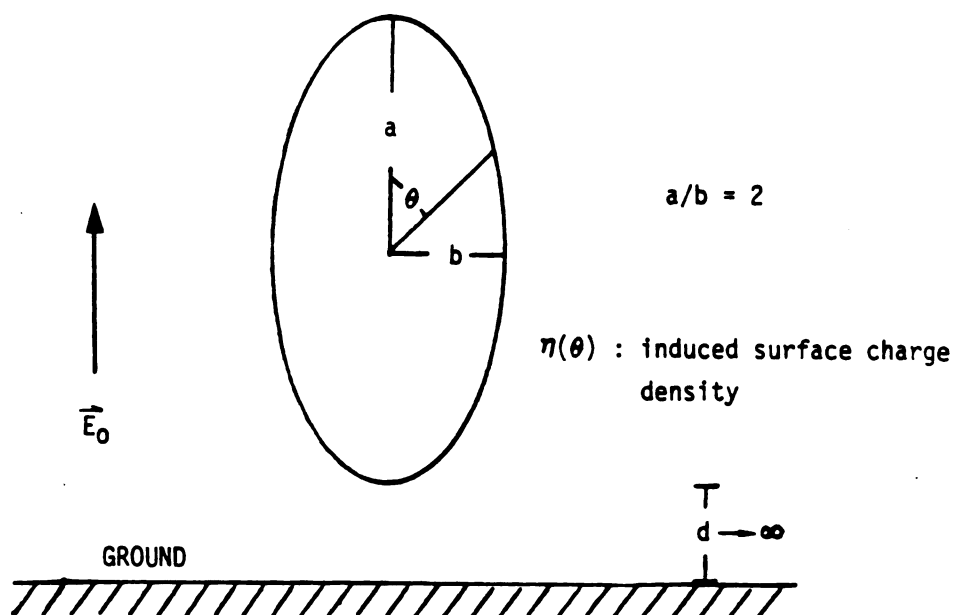
θ°	$\eta(\theta)$ ($\times 10^{-10}$)	
	present case	isolated spheroid
4.5	0.4751	0.4750
13.5	0.3753	0.3754
22.5	0.2667	0.2667
31.5	0.2023	0.2023
40.5	0.1475	0.1475
49.5	0.1032	0.1022
58.5	0.0753	0.0753
67.5	0.0521	0.0521
76.5	0.0316	0.0316
85.5	0.0085	0.0085

* $\eta(180^{\circ} - \theta) = -\eta(\theta)$ $0^{\circ} \le \theta \le 90^{\circ}$

Fig. 3.18. The distribution of surface charge density on a floating perfectly conducting spheroid located at an infinite distance from the ground induced by an uniform electric field.

relation of the short-circuit current and the floating potential of a human body with respect to height and weight, when exposed to ELF electric fields. A spheroid is a good model for a human body for this aspect, since the major axis and the minor axis of the spheroid can be adjusted to simulate the physical shape of human body. First, short-circuit currents of various spheroids with the same volume (weight) but different axis ratio are calculated and shown in Fig. 3.19. It can be observed that the short-circuit current will increase as the spheroid becomes longer and thinner. As shown in Fig. 3.19, it seems that a spheroid with the axis ratio of 2.2 is the closest model for a man to calculate the short-circuit current. Now, floating potentials of various spheroids with the same axis ratio (= 2.2) but different volume (weight) are calculated and shown in Fig. 3.20. It can be seen that the floating potential will increase as the spheroid becomes longer (higher and larger), and the function of the floating potential with respect to the height (H) of the spheroid is approximately linear as

$$\phi_b \approx \alpha E_o H \ , \qquad\qquad \alpha \approx 4.5 \sim 5.0 \qquad\qquad (3.32)$$

where ϕ_b in kV, E_o in kV/m and H in m.
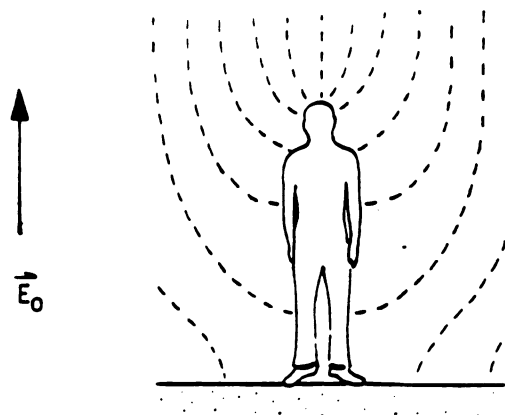
EMPIRICAL FORMULA

$\bullet$ $I_{sc} = 5.4 \cdot 10^{-9} \cdot H^2 \cdot E_0 \cdot f/60$

for $H = 1.70$ m (HEIGHT)

$W = 65$ kg (WEIGHT)

$I_{sc} = 15.6$ $\mu A/kV/m$

(f = 60 Hz)
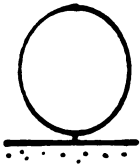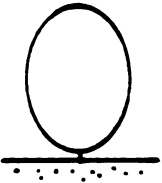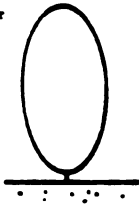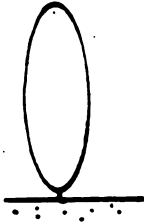
a : major axis b : minor axis			*	
a/b	1.2	1.8	2.2	3
a	28.23 cm	37.0 cm	42.3 cm	52.0 cm
b	23.53 cm	20.6 cm	19.2 cm	17.3 cm
H(=2a)	56.46 cm	74.0 cm	84.6 cm	104.0 cm
W	65.0 kg	65.0 kg	65.0 kg	65.0 kg
I_{sc}	7.5 $\mu A/kV/m$	11 $\mu A/kV/m$	16 $\mu A/kV/m$	25 $\mu A/kV/m$

Fig. 3.19. Comparison of theoretical results by the present method with empirical results on the short-circuit current for spheroidal models of man with various axis ratios when exposed to a 1 kV/m, 60-Hz electric field.

a: major axis
b: minor axis
HEIGHT: H=2a

E_0= 1 kV/m

(a/b=2.2)

ϕ_b = 240 V

ϕ_b = 281 V

ϕ_b = 323 V

$\vec{E}_0$

$\vec{E}_0$

$\vec{E}_0$

H = 50 cm

H = 60 cm

H = 70 cm

ϕ_b = 364 V

ϕ_b = 405 V

ϕ_b = 487 V

$\vec{E}_0$

$\vec{E}_0$

$\vec{E}_0$

H = 80 cm

H = 90 cm

H = 110 cm
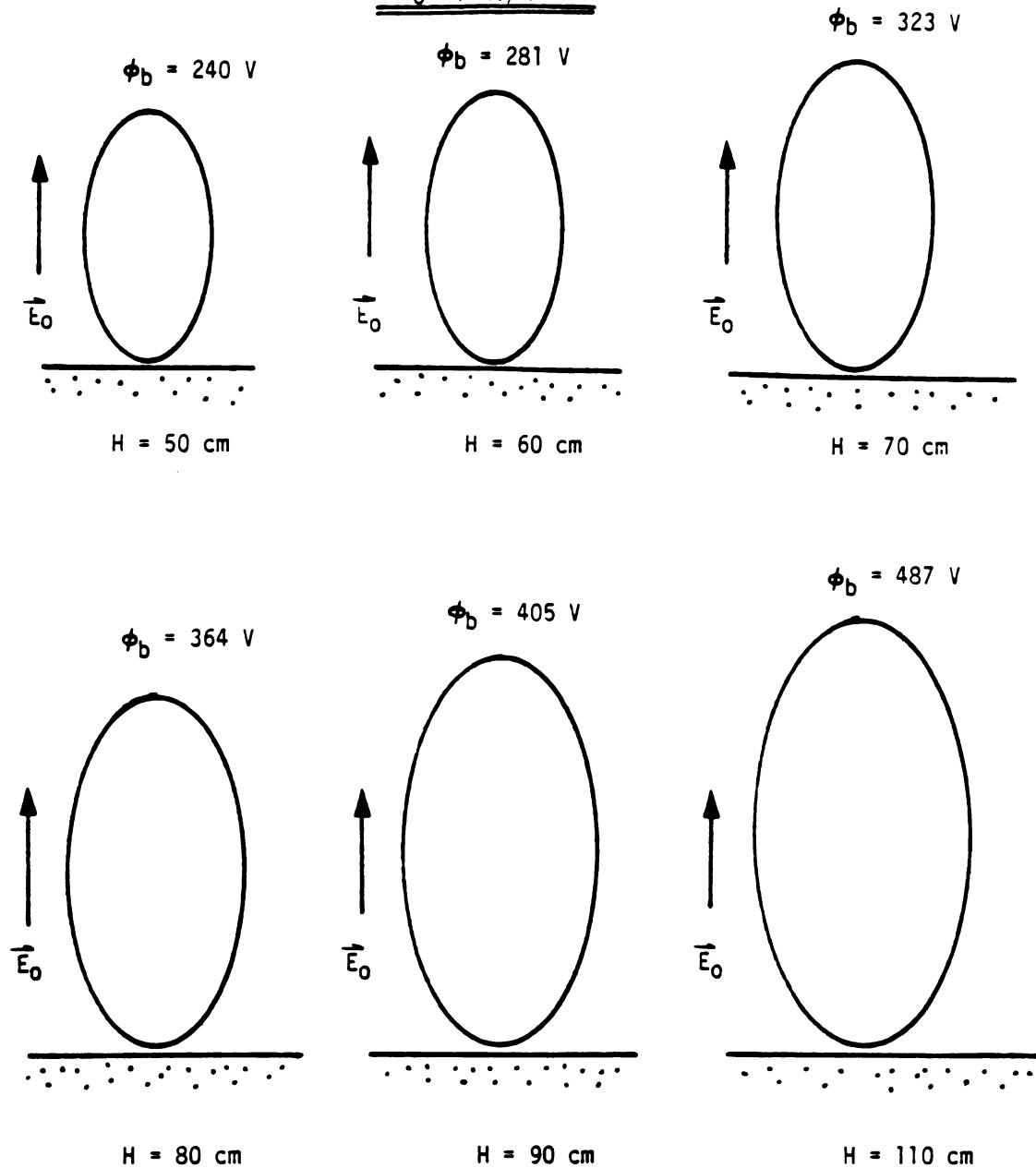
Fig. 3.20. Floating potentials of spheroids with the same axis-ratio
(a/b = 2.2) and various sizes when exposed to a 1 kV/m,
60-Hz electric field.

A

4

no
ol
be
Th
re
in
sh
fi
ar

4.

sh
of
An
in
)

CHAPTER 4

APPLICATIONS OF SURFACE CHARGE INTEGRAL EQUATION METHOD

TO ANIMAL AND HUMAN BODIES

4.1 Introduction

The validity of the *surface charge integral equation* (SCIE)

method developed in chapter 2 was confirmed in chapter 3. In this

chapter, the SCIE method is applied to quantify the interaction

between 60-Hz electric fields and animals as well as human bodies.

Theoretical results will be compared with existing experimental

results to check the accuracy of this method. Also in order to

investigate the frequency range limitation of the *SCIE* method, the

short-circuit current of a human body induced by LF-HF electric

fields is computed by the surface charge integral equation method

and compared with experimental results by other workers.

4.2 Numerical Results for Animal Bodies and Comparison with Existing Experimental Results

In this section, the SCIE method is applied to quantify the

short-circuit current, the induced surface charge and body current

of a grounded guinea pig with a length of 22 cm and a height of 8 cm.

An incident ELF electric field of 60-Hz and 10 kV/m has been considered

in order to compare with the experimental results of Kaune and Miller

[9]. In the experiment by Kaune & Miller, two guinea pigs, weighting

69

794 and 844 g, were adopted. Surface areas of two subjects were measured to be 0.05 m^2 and 0.053 m^2. A simplistic model of a guinea pig which simulates the actual animal used by Kaune & Miller is shown in Fig. 4.1. For the numerical calculation, the body surface of the guinea pig is partitioned into 228 patches. Due to the symmetry of the body along the x-axis, only a half of the body surface (114 patches) will be computed. Let the central point of the mth patch be $P(\vec{r}_m)$, $\vec{r}_m = (x_m, y_m, z_m)$, and that of the nth patch be $Q(\vec{r}_n)$, $\vec{r}_n = (x_n, y_n, z_n)$, then the matrix equation (2.14) of the SCIE method can be written as,

$$
\begin{bmatrix}
M_{11} & M_{12} & \cdots\cdots\cdots & M_{1N} & -1 \\
M_{21} & M_{22} & \cdots\cdots\cdots & M_{2N} & -1 \\
\cdot & \cdot & & \cdot & \cdot \\
\cdot & \cdot & & \cdot & \cdot \\
\cdot & \cdot & & \cdot & \cdot \\
M_{N1} & M_{N2} & \cdots\cdots\cdots & M_{NN} & -1 \\
\Delta S_1 & \Delta S_2 & \cdots\cdots\cdots & \Delta S_N & 0
\end{bmatrix}
\begin{bmatrix}
\eta_1 \\
\eta_2 \\
\cdot \\
\cdot \\
\cdot \\
\eta_N \\
\phi_b
\end{bmatrix}
= -
\begin{bmatrix}
\phi_{o1} \\
\phi_{o2} \\
\cdot \\
\cdot \\
\cdot \\
\phi_{oN} \\
0
\end{bmatrix}
\qquad (4.1)
$$

where

η_n = surface charge density of the nth patch

ΔS_n = surface area of the nth patch

$$
M_{mn} = \frac{\Delta S_n}{4\pi\epsilon_o} \left\{ \frac{1}{|\vec{r}_m - \vec{r}_{1n}|} + \frac{1}{|\vec{r}_m - \vec{r}_{2n}|} - \frac{1}{|\vec{r}_m - \vec{r}_{3n}|} - \frac{1}{|\vec{r}_m - \vec{r}_{4n}|} \right\}
$$

for $m \neq n$
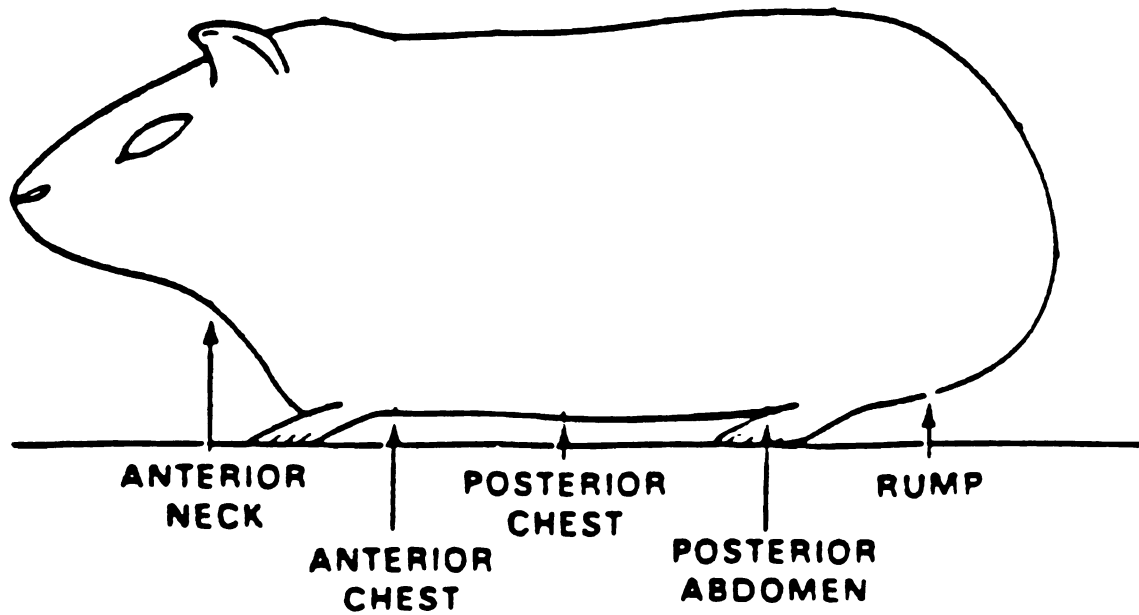
EXPERIMENTAL GUINEA PIG (Kaune & Miller)
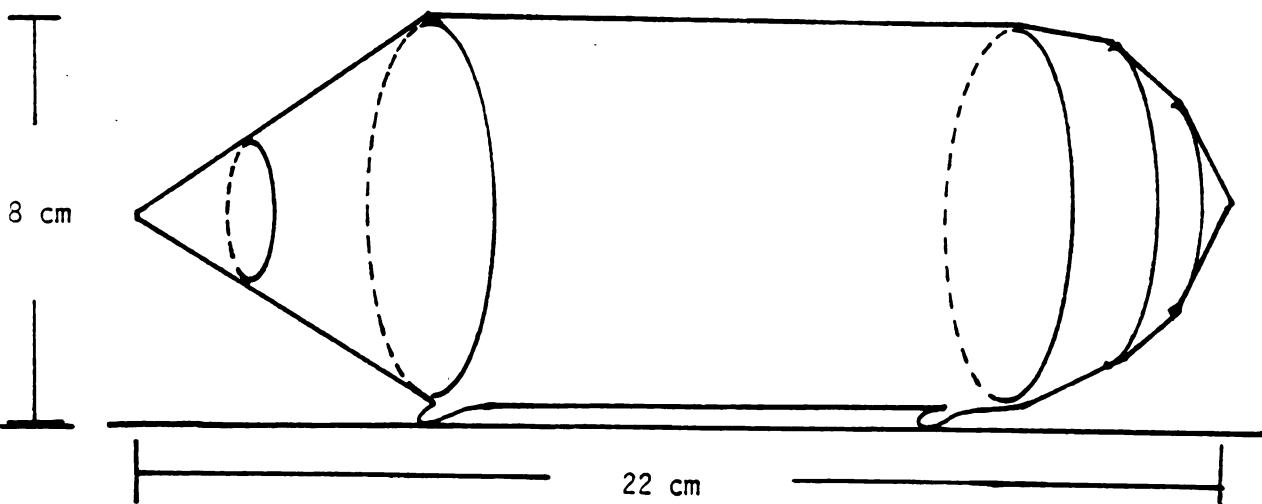
THEORETICAL MODEL FOR GUINEA PIG

Fig. 4.1. Experimental guinea pig and the theoretical model for the SCIE numerical computation.

$$M_{mm} = \frac{\Delta S_n}{4\pi\epsilon_o} \left\{ \frac{2\sqrt{\pi}}{(\Delta S_m)^{1/2}} + \frac{1}{|\vec{r}_m - \vec{r}_{2m}|} - \frac{1}{|\vec{r}_m - \vec{r}_{3m}|} - \frac{1}{|\vec{r}_m - \vec{r}_{4m}|} \right\}$$

$$\text{for } m = n$$

and

$$\vec{r}_{1n} = (x_n, y_n, z_n), \qquad \vec{r}_{2n} = (x_n, -y_n, z_n)$$

$$\vec{r}_{3n} = (x_n, y_n, -z_n), \qquad \vec{r}_{4n} = (x_n, -y_n, -z_n)$$

After surface charge densities are computed, the short-circuit current can be calculated by using Eq. (2.5).

The experimental results of Kaune & Miller and numerically evaluated results on the surface electric field enhancement factor, the short-circuit current and the axial sectional current are shown in Fig. 4.2(a) & (b) for comparison. Fig. 4.2(a) shows the electric field enhancement factors measured at various locations on the surface and the sectional currents at five cross sections of a guinea pig. Fig. 4.2(b) shows the electric field enhancement factors and five sectional currents calculated for the theoretical model of the guinea pig. Good agreement is obvious when the corresponding experimental and numerical values of these quantities shown in these two figures are compared. The tables at the bottom of Fig. 4.2(a) & (b) indicate the comparison of the measured short-circuit currents and the calculated values. The measured short-circuits for two guinea pigs are 0.219 and 0.225 $\mu A/(kV/m)$ and the calculate result is 0.212 $\mu A/(kV/m)$. The results shown in Fig. 4.2 demonstrate the accuracy of the SCIE method.

(ELECTRIC FIELD ENHANCEMENT FACTOR)
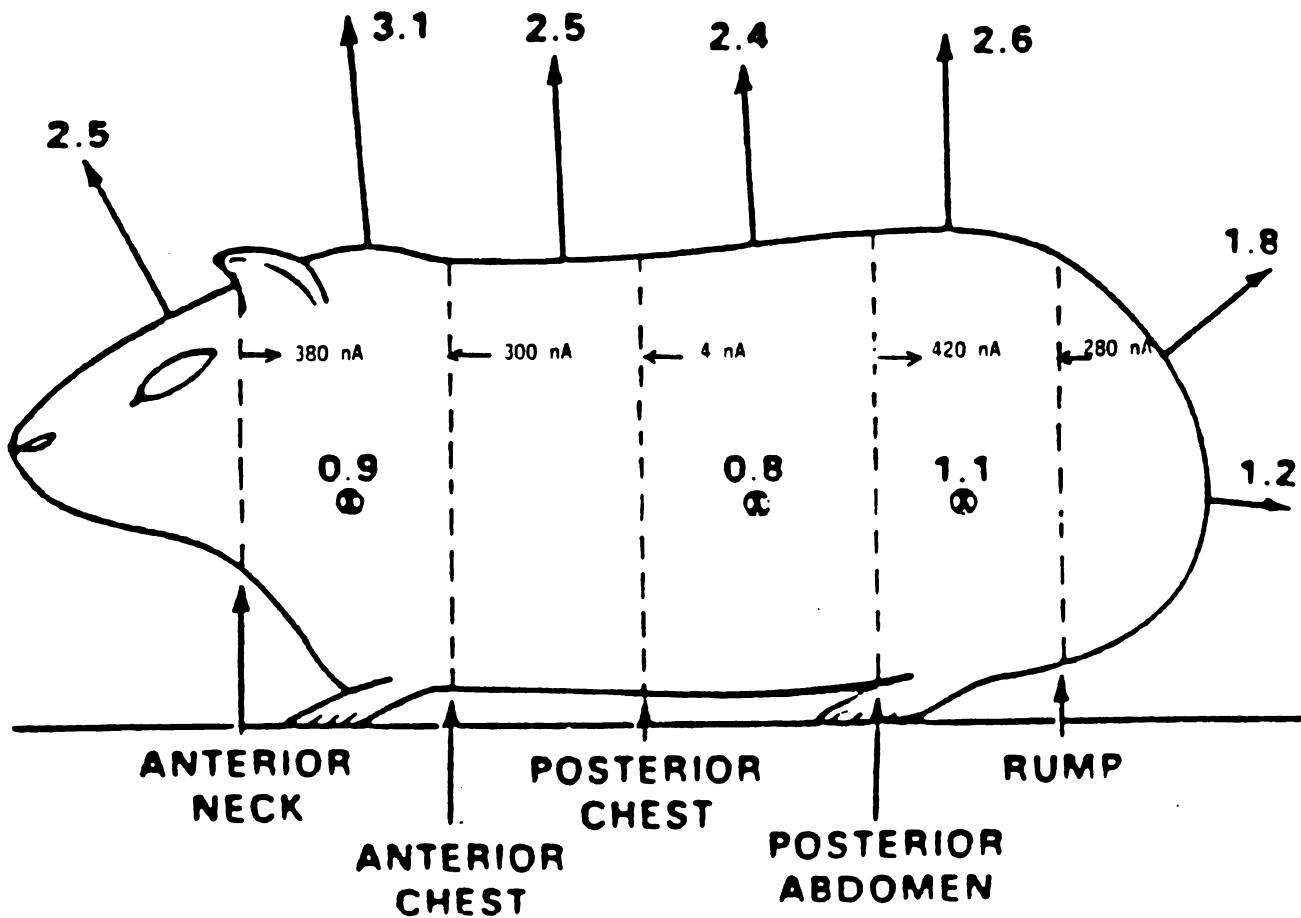

```
*********************************
*   EXPERIMENT (Kaune & Miller)  *
*********************************
```

	Surface Area	Weight	I_{sc} $(\mu A/(kV/m))$
(1)	0.050 m^2	794 g	0.219
(2)	0.053 m^2	844 g	0.225

Fig. 4.2(a).   Experimental results of Kaune and Miller on the electric field enhancement factor, the sectional current and the short-circuit current for a grounded guinea pig exposed to a 60-Hz, 10 kV/m electric field.

74

(ELECTRIC FIELD ENHANCEMENT FACTOR)
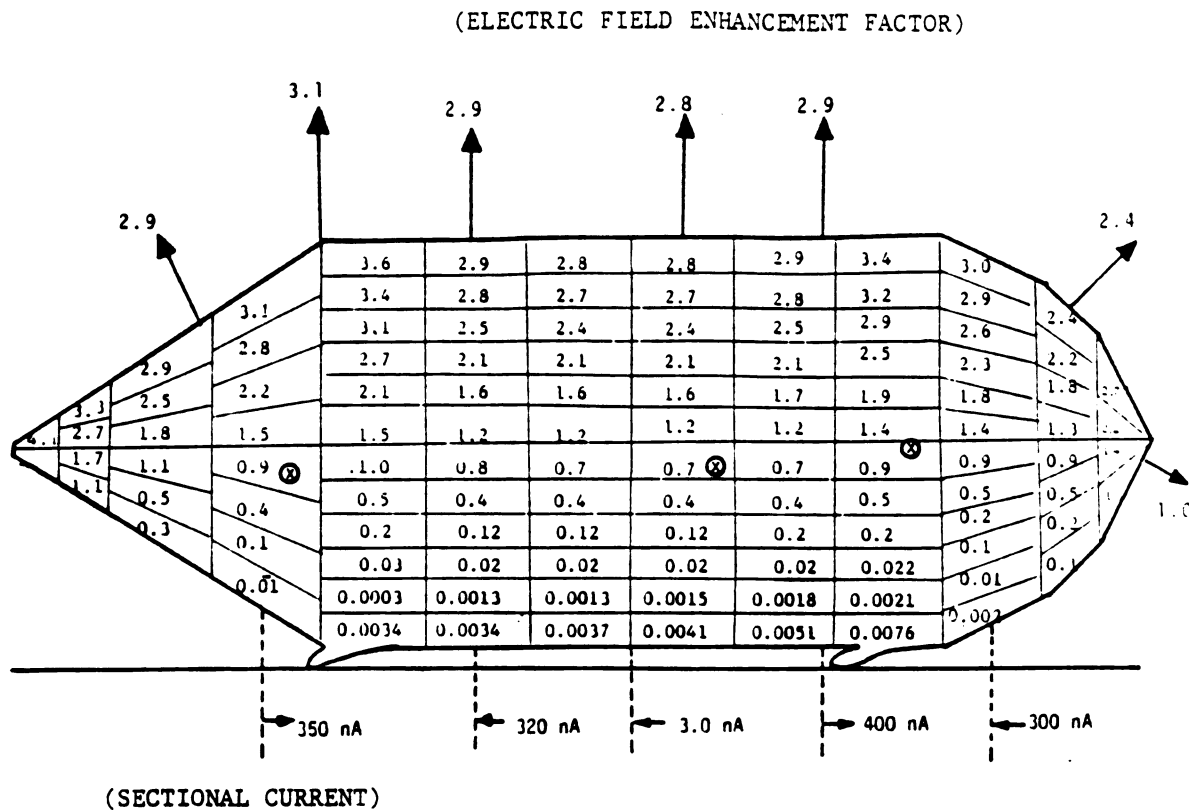
(SECTIONAL CURRENT)

```
*********************
*  PRESENT THEORY  *
*********************
```

Surface Area	weight	I_{sc} (μA/(kV/m))
0.048 m^2	790 g	0.212

Fig. 4.2(b). Theoretical results by the present method on the electric field enhancement factor, the sectional current and the short-circuit current for a grounded guinea pig exposed to a 60-Hz, 10 kV/m electric field.

4.3 Numerical Results for Human Model and Comparison with Existing Experimental and Theoretical Results

In th experiment by Kaune and Forsythe [10], induced current densities were measured in a homogeneous grounded phantom model of man (45 cm in height, as shown in Fig. 4.3) exposed to a vertical, 60-Hz electric field. To compare the present method with their experimental results, the SCIE method is employed to quantify the interaction of a 60-Hz, 10 kV/m electric field with a similar theoretical model of man (Fig. 4.3).

In the numerical calculation, in order to reduce the size of the matrix equation, the theoretical human model is constructed to have 4-quarter symmetries along the x-axis and the y-axis. The body surface is partitioned into 472 patches and that leads to 118 unknowns with a quarter-body symmetry. Let the central point of the mth patch be $P(\vec{r}_m)$, $\vec{r}_m = (x_m, y_m, z_m)$, and that of the nth patch be $Q(\vec{r}_n)$, $\vec{r}_n = (x_n, y_n, z_n)$. The matrix equation of the surface charge integral equation can then be written as

$$
\begin{bmatrix}
M_{11} & M_{12} & \cdots\cdots\cdots & M_{1N} & -1 \\
M_{21} & M_{22} & \cdots\cdots\cdots & M_{2N} & -1 \\
\cdot & \cdot & & \cdot & \cdot \\
\cdot & \cdot & & \cdot & \cdot \\
\cdot & \cdot & & \cdot & \cdot \\
M_{N1} & M_{N2} & \cdots\cdots\cdots & M_{NN} & -1 \\
\Delta S_1 & \Delta S_2 & \cdots\cdots\cdots & \Delta S_N & 0
\end{bmatrix}
\begin{bmatrix}
\eta_1 \\
\eta_2 \\
\cdot \\
\cdot \\
\cdot \\
\eta_N \\
\phi_b
\end{bmatrix}
= -
\begin{bmatrix}
\phi_{o1} \\
\phi_{o2} \\
\cdot \\
\cdot \\
\cdot \\
\phi_{oN} \\
0
\end{bmatrix}
\qquad (4.2)
$$

where

THEORETICAL MODEL OF MAN (Present Method)

EXPERIMENTAL MODEL OF MAN (Kaune & Forsythe)

40 cm

30 cm

20 cm

10 cm

0 cm
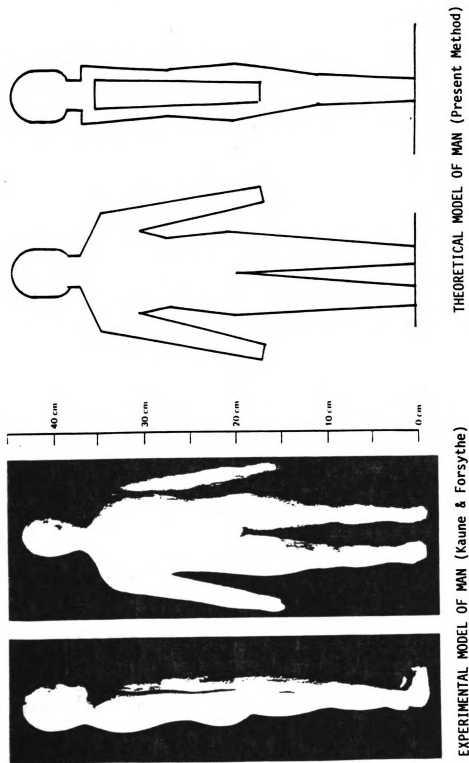
Fig. 4.3. Experimental model of man (height = 45 cm) and its theoretical model for the SCIE numerical computation.

η_n - surface charge density of the nth patch

ΔS_n - surface area of the nth patch

$$M_{mn} = \frac{\Delta S_n}{4\pi\epsilon_o} \left\{ \frac{1}{|\vec{r}_m - \vec{r}_{1n}|} + \frac{1}{|\vec{r}_m - \vec{r}_{2n}|} + \frac{1}{|\vec{r}_m - \vec{r}_{3n}|} + \frac{1}{|\vec{r}_m - \vec{r}_{4n}|} \right.$$

$$\left. - \frac{1}{|\vec{r}_m - \vec{r}_{5n}|} - \frac{1}{|\vec{r}_m - \vec{r}_{6n}|} - \frac{1}{|\vec{r}_m - \vec{r}_{7n}|} - \frac{1}{|\vec{r}_m - \vec{r}_{8n}|} \right\} \quad m \neq n$$

$$M_{mm} = \frac{\Delta S_n}{4\pi\epsilon_o} \left\{ \frac{2\sqrt{\pi}}{(\Delta S_m)^{1/2}} + \frac{1}{|\vec{r}_m - \vec{r}_{2m}|} + \frac{1}{|\vec{r}_m - \vec{r}_{3m}|} + \frac{1}{|\vec{r}_m - \vec{r}_{4m}|} \right.$$

$$\left. - \frac{1}{|\vec{r}_m - \vec{r}_{5m}|} - \frac{1}{|\vec{r}_m - \vec{r}_{6m}|} - \frac{1}{|\vec{r}_m - \vec{r}_{7m}|} - \frac{1}{|\vec{r}_m - \vec{r}_{8m}|} \right\} \quad m = n$$

and

$$\vec{r}_{1n} = (x_n, y_n, z_n), \qquad \vec{r}_{2n} = (-x_n, y_n, z_n)$$

$$\vec{r}_{3n} = (x_n, -y_n, z_n), \qquad \vec{r}_{4n} = (-x_n, -y_n, z_n)$$

$$\vec{r}_{5n} = (x_n, y_n, -z_n), \qquad \vec{r}_{6n} = (-x_n, y_n, -z_n)$$

$$\vec{r}_{7n} = (x_n, -y_n, -z_n), \qquad \vec{r}_{8n} = (-x_n, -y_n, -z_n)$$

After surface charge densities have been computed, the short-circuit current and induced body currents can be calculated accordingly. Fig. 4.4(a) & (b) shows numerical results of the surface electric field enhancement factor and the short-circuit current of the theoretical human model. Fig. 4.5 depicts the comparison of the experimental and numerical results of the induced current density inside the experimental model and the corresponding theoretical model of man. The right figure shows the measured current densities at various points inside the body. The induced current is mainly longitudinal (or vertical) with a small radial (or horizontal) component as shown in the figure. Notice that the direction of the radial component is outward in the chest region but it is inward at the neck and the abdomen region. The most interesting observation is that the induced current in the arm is directed downward, or in the opposite direction to the current flowing in other parts of the body. The numerical results on the induced current density in the theoretical model which approximates the experimental model are shown in the left figure. It can be seen that the computed current densities, in amplitude and direction, at various points inside the body agree very well with the measured values. It is also noted that the present theory correctly predicted the reversed direction of the induced current in the arm, and the directions of the radial components of the currents at different parts of the body. The results of Fig. 4.5 again give a positive verification on the accuracy of the SCIE technique.

79

12

16

13

9 7.5

7.0

3.7

6.7

14

6

7

5

4.6

4

4

1.3

1.3

1.1

0.8

0.5

0.1

$\vec{E}_0$

45 cm

FRONT VIEW
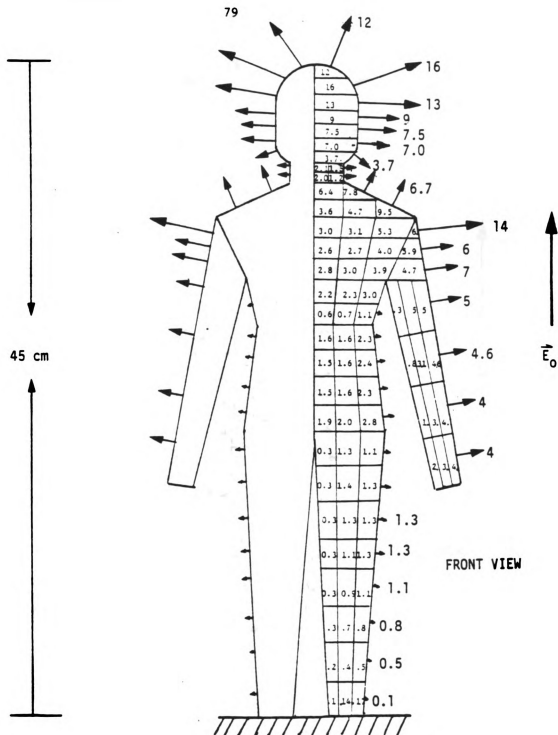
I_{SC} = 12.76 μA (PRESENT THEORY)

I_{SC} = 10.95 μA (BASED ON I_{SC} = 5.4·10⁻⁹·H²·E·f/60

see Chiba et al.)

Fig. 4.4(a). Theoretical results on the electric field enhancement factor
and the short-circuit current for the experimental model of
man (used by Kaune & Forsythe) standing on the ground and
exposed to a 60-Hz, 1kV/m electric field.

Fig. 4.4(b). Theoretical results on the electric field enhancement factor and the short-circuit current for the experimental model of man (used by Kaune & Forsythe) standing on the ground and exposed to a 60-Hz, 1kV/m electric field.

81
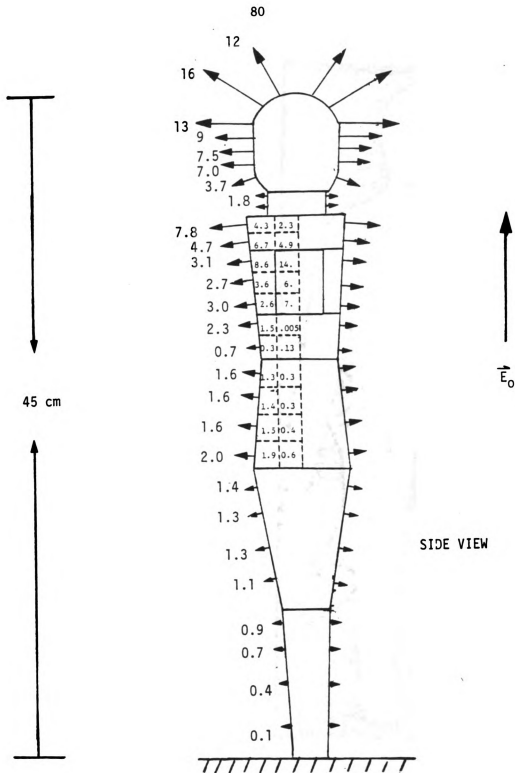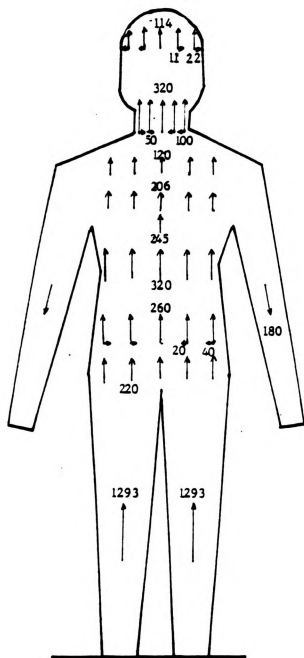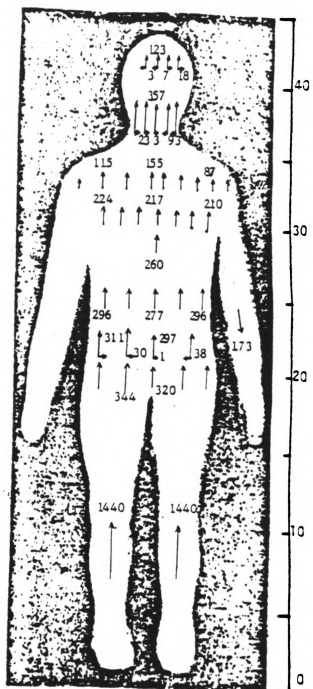
Fig. 4.5. Comparison of theoretical results by the present method with experimental results of Kaune and forsythe on vertical and horizontal current densities for a grounded human model exposed to a 60-Hz, 10 kV/m electric field. Induced current densities are given in units of nA/cm².

4.4 Numerical Results for the Model of Adult Man with Arbitrary Posture

In this section, the surface charge integral equation method is applied to a model of man with a height of 180 cm and a weight of 68.2 kg standing on the ground plane with grounding impedances, and is exposed to a 60-Hz electric field of 1 kV/m. For numerical calculation, the body surface is partitioned into 424 patches leading to 106 unknowns with a quarter body symmetry. Fig. 4.6 shows the calculated electric field enhancement factors on the body surface and the short-circuit current of a man standing upright and in direct contact (short-circuit case) with the ground. The enhancement factor on the head is about 18 which is almost the same as the measurement reported by Deno [5]. The calculated short-circuit current is 18.0 $\mu A/(kV/m)$. This value is very close to 17.5 $\mu A/(kV/m)$ which is calculated with the empirical formula of

$$I_{sc} = 5.4 \times 10^{-9} \times (f/60)E_oH^2 \tag{4.3}$$

used by Deno [5] and Chiba et al. [15].

Fig. 4.7 depicts the electric field enhancement factors and the short-circuit current in the same man with stretched arms indeced by the same electric field as the case of Fig. 4.6. It is observed that the surface electric field can be very high at the tip of the hand due to its sharp geometry. Also it is noted that when the arms are stretched, the short-circuit current is increased 23.3 μA. This value is quite different from the value of 17.5 μA

83
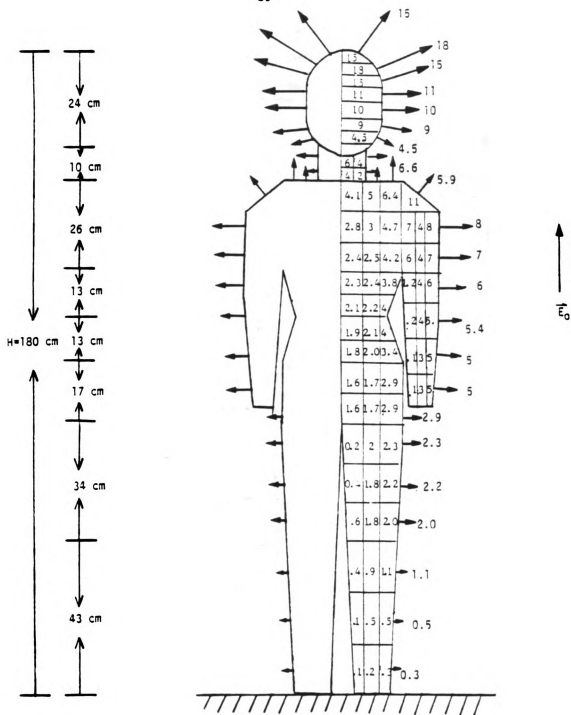
$I_{SC} = 18.0 \ \mu A$ (Present Theory)

$I_{SC} = 17.5 \ \mu A$ (Based on $I_{SC} = 5.4 \cdot 10^{-9} \cdot H^2 \cdot E \cdot f/60$
see Chiba et al.)

Fig. 4.6. Theoretical results on the electric field enhancement factor
and the short-circuit current for a realistic model of man
standing on the ground and exposed to a 60-Hz, 1 kV/m electric
field.

$I_{sc} = 23.3 \ \mu A$ (PRESENT THEORY)
$I_{sc} = 17.5 \ \mu A$ (BASED ON $I_{sc} = 5.4 \cdot 10^{-9} \cdot H^2 \cdot E \cdot f/60$)
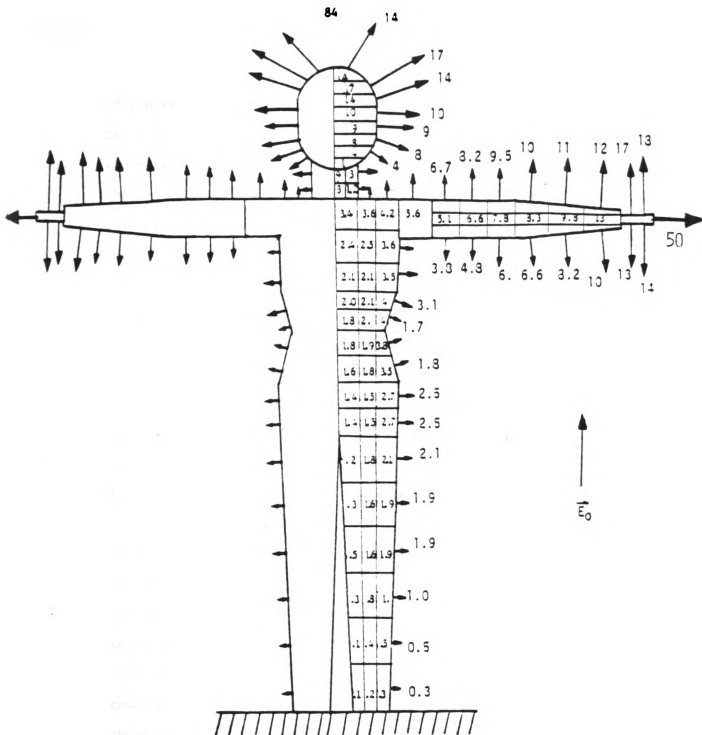
Fig. 4.7. Theoretical results on the electric field enhancement factor
and the short-circuit current for a realistic model of man
with hands stretching horizontally standing on the ground
being exposed to a 60-Hz, 1 kV/m electric field.

if the same formula used by Deno [5] and Chiba et al. [15] is used.
It is because stretching arms will increase more induced surface
charge and hence short-circuit current. In general, we found that
the induced electric field at the body's surface, the short-circuit
current, and consequently the induced current inside the body, are
strongly dependent on the body geometry and posture. Even though
the phenomenon involed is rather complicated, the present method
is capable of predicting them.

The effect of grounding impedances on the short-circuit current
of a man exposed to a 60-Hz electric field of 1 kV/m is given in
Fig. 4.8 to 4.10. Grounding impedances are assumed to be resistive,
capacitive or inductive. As the same phenomena observed in Sec. 3.3,
for the resistive or capacitive impedance, the short-circuit current
is found to remain practically unchanged, maintaining a value of about
18 μA/(kV/m) when the grounding impedance is varied from zero to about
10 MΩ. Only after the grounding impedance exceeds the value of 10 MΩ,
the short-circuit current starts to fall down. For an inductive grounding
impedance, there is a possible resonance phenomenon when the impedance
has a value of 100 MΩ, corresponding to an inductance of 3×10^5 H
(henries). This implies that in a in a very unlikely case when the
grounding impedance is an extremely large inductance of about 3×10^5 H,
there may be a very large current induced in the body causing health
hazard.

Chiba et al. [15] applied the Finite Element Method (FEM) to analyze
induced current densities inside an axially symmetrical human model of
revolutional geometry, when exposed to a 60-Hz electric field as shown
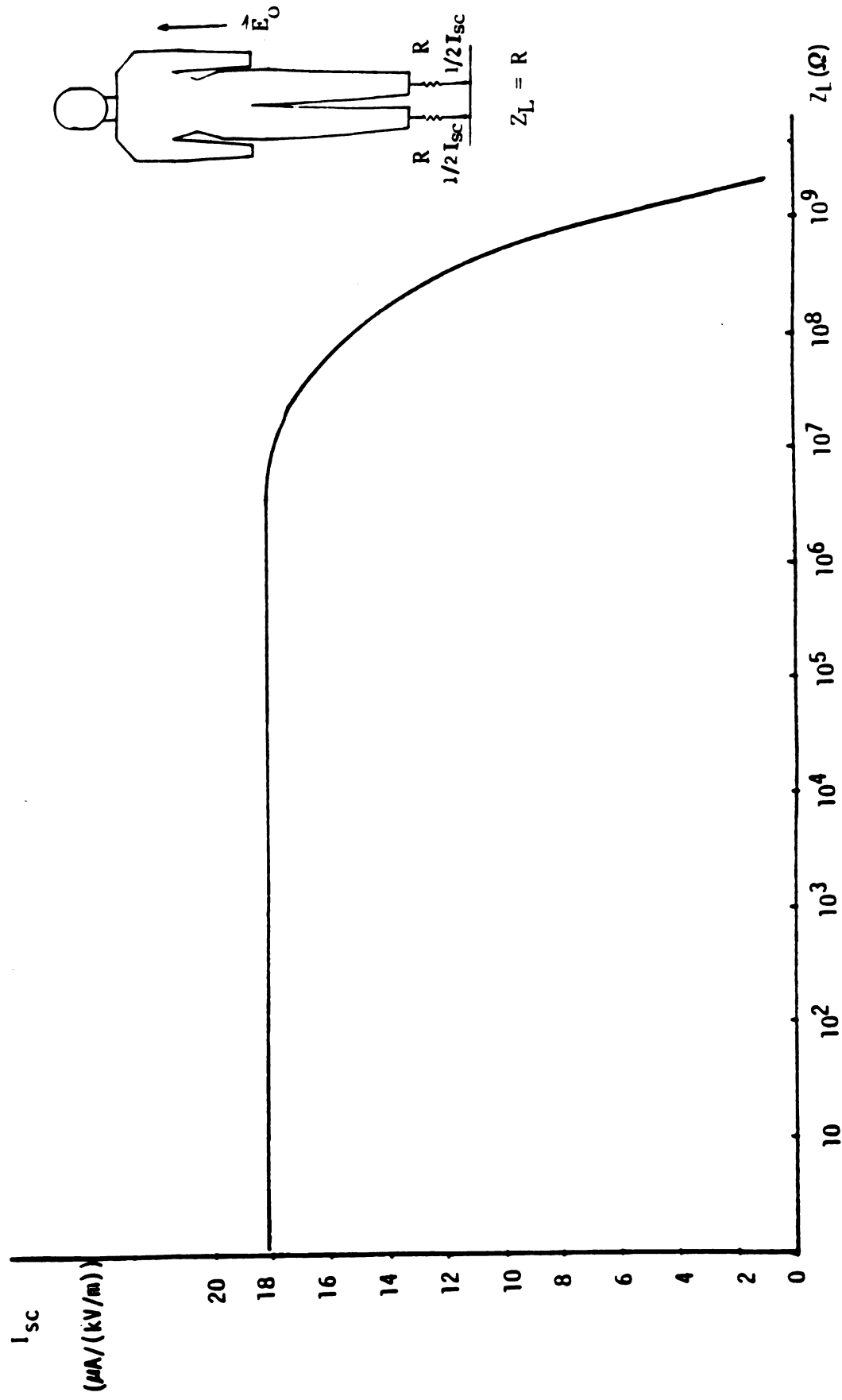
Fig. 4.8. Short-circuit current as a function of grounding resistance.
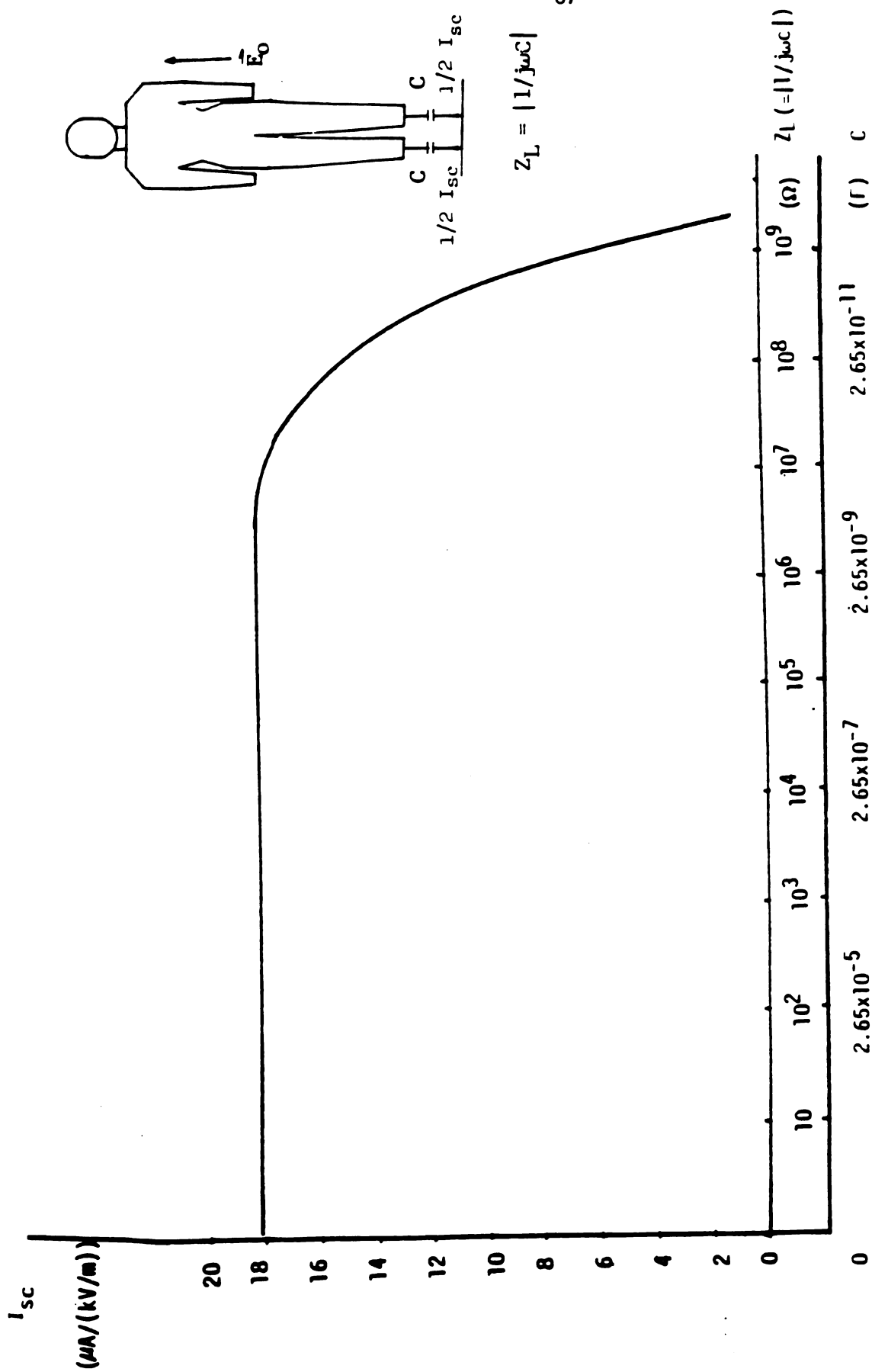
Fig. 4.9. Short-circuit current as a function of grounding capacitance
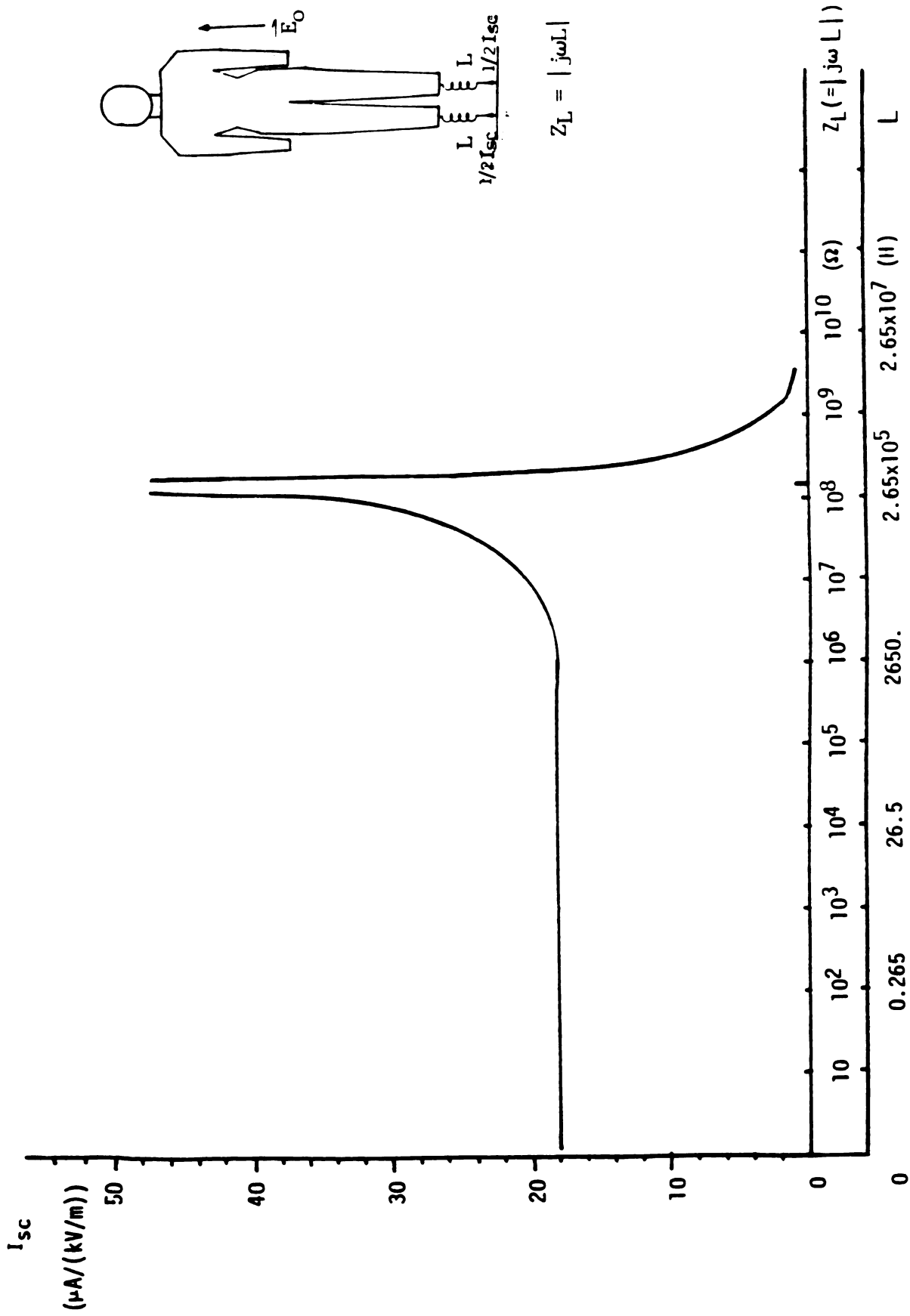
Fig. 4.10. Short-circuit current as a function of grounding inductance.

in Fig. 4.11. Although their model is not quite realistic for a human
body, it is appropriate to compare present numerical results with their
results. In Fig. 4.12 to 4.15, the comparison of present numerical
results with their results for an incident electric field of 60-Hz,
1 kV/m are shown. Fig. 4.12 shows the comparison on vertical body
sectional currents for standing (upright) grounded human models. It
can be observed that the agreement between the two methods is good at
various sections. Fig. 4.13 shows the comparison on vertical body
sectional current densities for the same models. The agreement is
good at various sections except at the ankle. The discrepancy is due
to different ankle geometries of the two models. Fig. 4.14 and 4.15
depicts the comparison on vertical body sectional currents and current
densities for the grounded human model with stretching arms (for *SCIE*)
and the same model used by Chiba et al. It can be observed that present
numerical results are generally higher than the numerical results of
Chiba et al., since the posture of stretching arms increases induced
currents inside the human body.

4.5 Frequency Range Limitation of Surface Charge Integral Equation Method

The numerical examples given so far are all computed for the
case of 60-Hz. In order to examine the frequency range over which the
SCIE method is applicable, the present method has also been employed
to compute the short-circuit currents induced by electric fields
at frequencies over the ELF and HF range (60-Hz – 50 MHz). Table
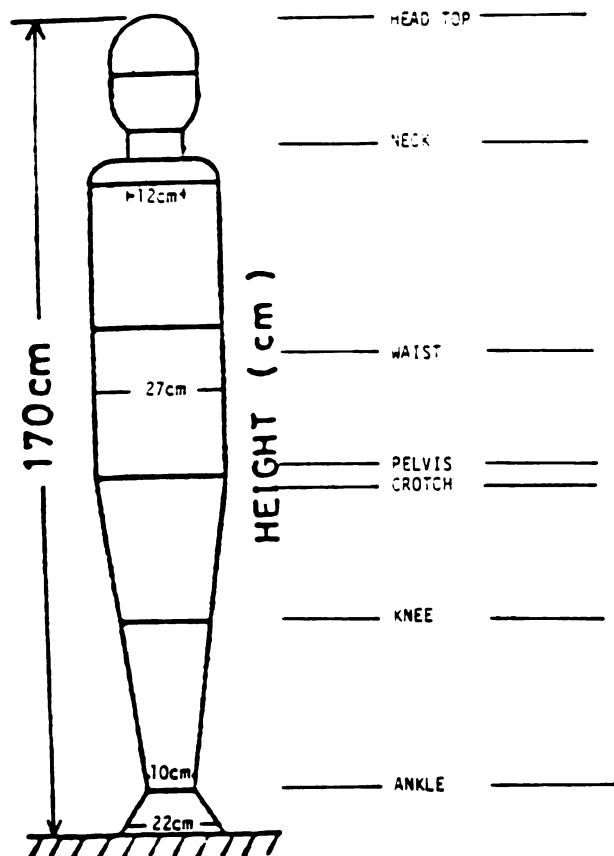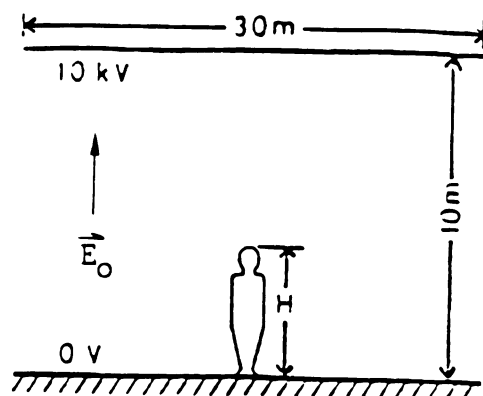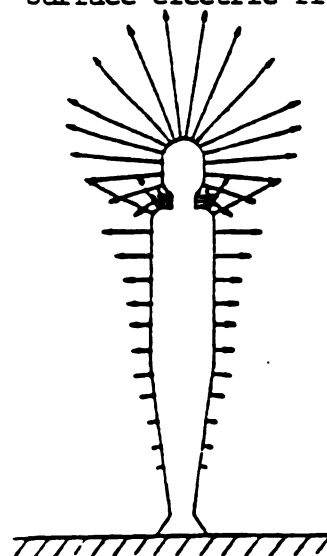
Fig. 4.11. Human model and experimental set-up by Chiba et al. [15].

Chiba [15]
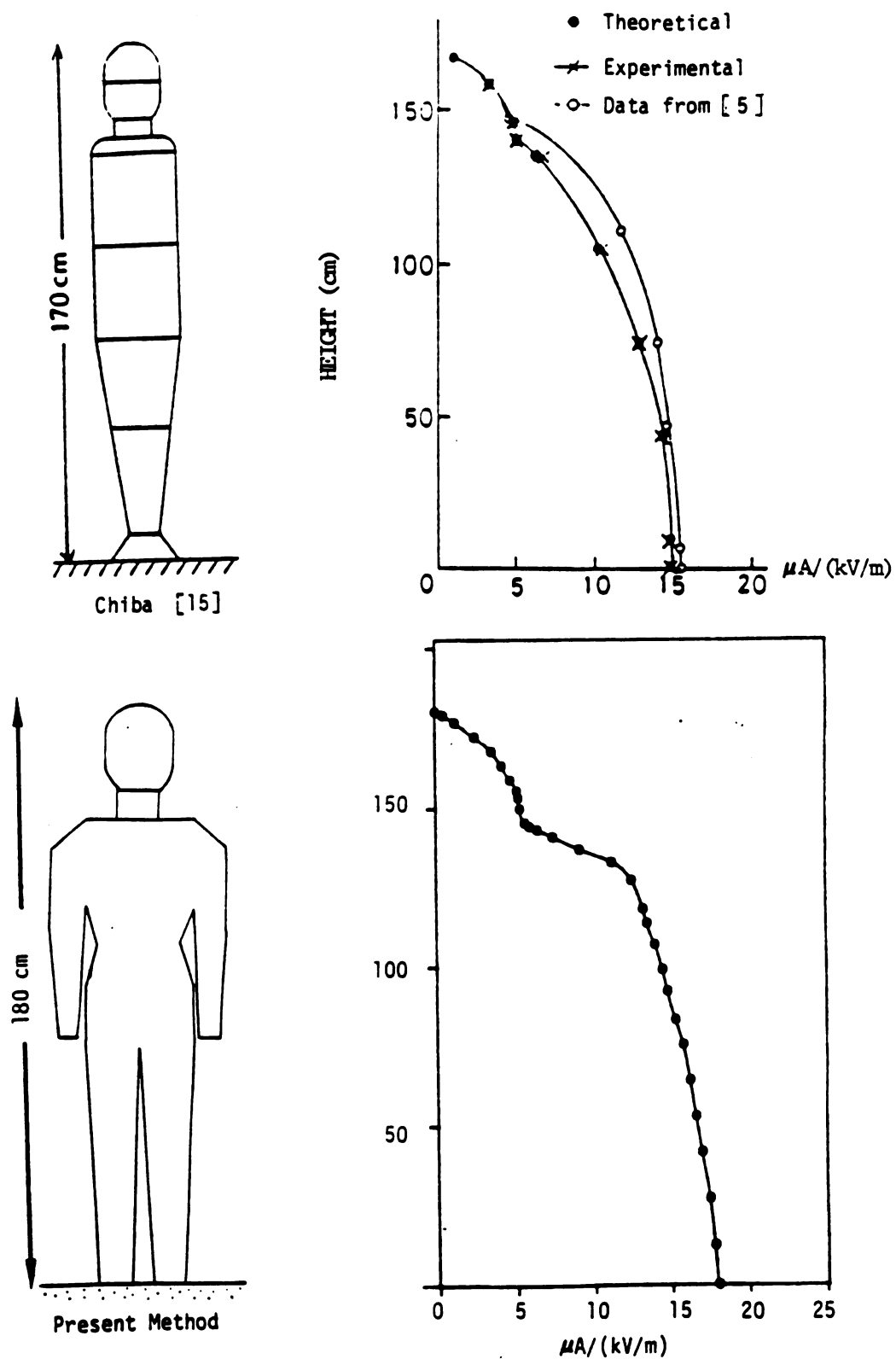
Present Method

Fig. 4.12. Comparison of theoretical results by the present method with results of Chiba et al on vertical sectional currents for a grounded human model exposed to a 60-Hz, 1 kV/m electric field.
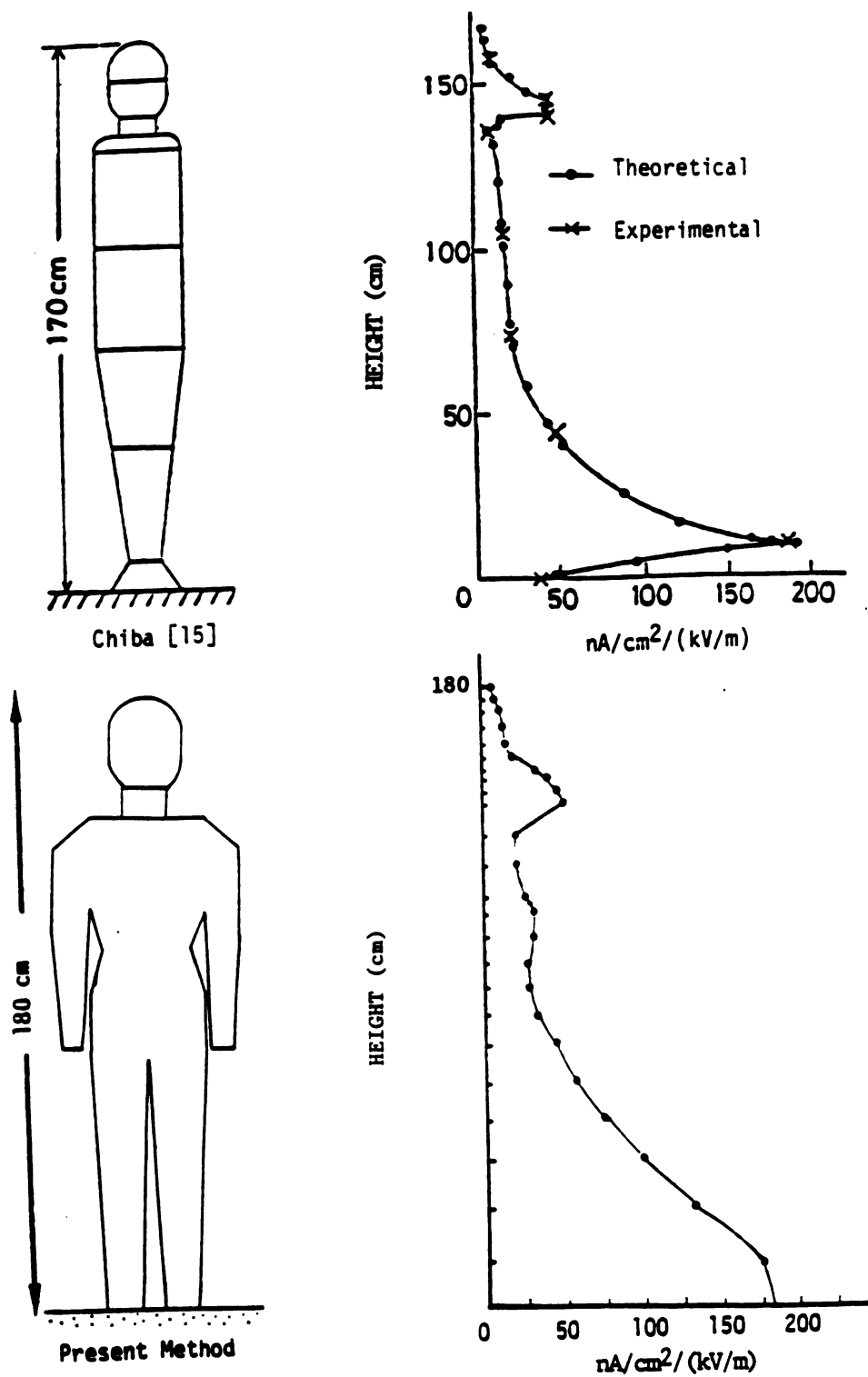
Fig. 4.13. Comparison of theoretical results by the present method
with results of Chiba et al on vertical sectional current
densities for a grounded human model exposed to a 60-Hz,
1 kV/m electric field.
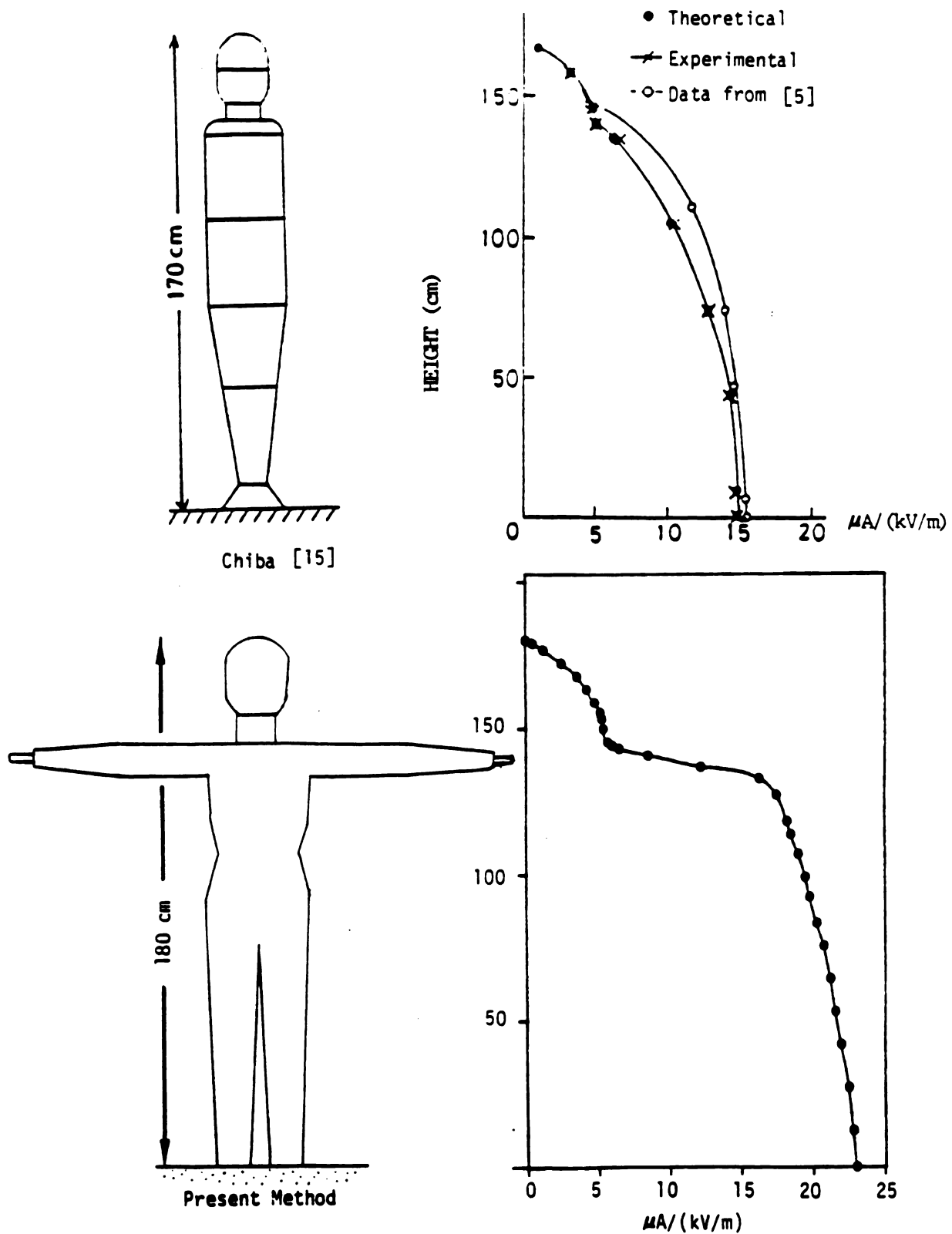
Fig. 4

Fig. 4.14. Comparison of theoretical results by the present method
with results of Chiba et al on vertical sectional currents
for a grounded human model with hands stretching horizontally
exposed to a 60-Hz, 1 kV/m electric field.
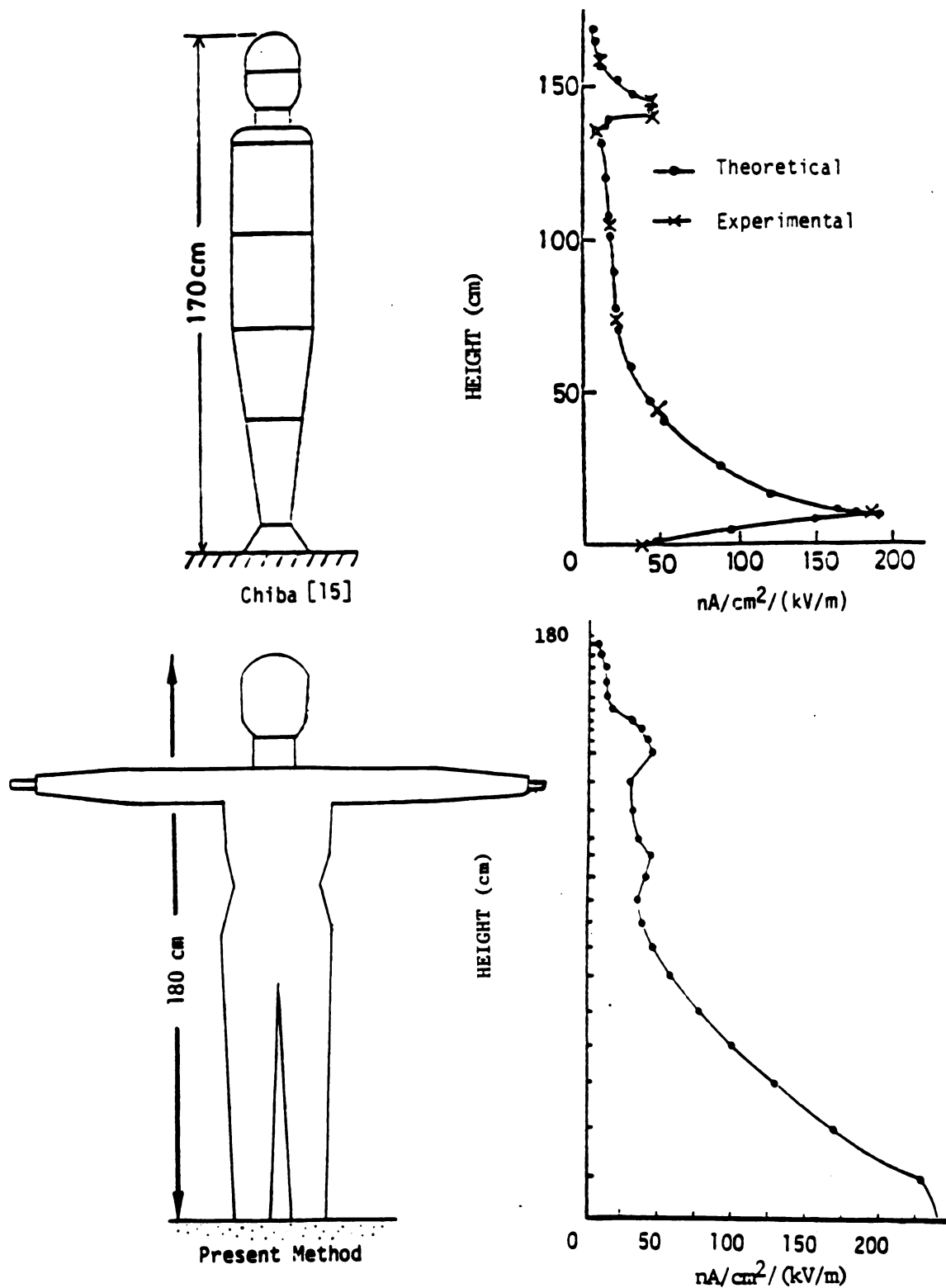
Fig. 4.15. Comparison of theoretical results by the present method with results of Chiba et al on vertical sectional currents densities for a grounded human model with hands streching horizontally exposed to a 60-Hz, 1 kV/m electric field.

4.1 and

the shor

at freqı

numeric

agreeme

40 MHz.

data sł

which

standi

resona

human

polar

Chen

methc

for ﹍

curr

the

incr

tha

fre

boo

4.1 and Fig. 4.16 show the comparison of experimental results on the short-circuit current, measured by various workers [19] – [23] at frequencies over the ELF and HF range, and the corresponding numerical results generated by the present method. A satisfactory agreement is obtained between theory and experiment up to about 40 MHz. It is interesting to note that in Fig. 4.16 the experimental data show a maximum current being measured at the frequency of 40 MHz, which is the resonant frequency for the human body (1.7m ~ 1.8m) standing on the ground. This is consistent with the fact that the resonant frequency of the human body in free space, at which the human body absorbs a maximum RF energy in response to a vertically polarized EM wave, is 80 MHz. This resonant frequency was found by Chen et al. [27] using the *electric field integral equation* (EFIE) method and it has been verified experimentally by many workers [28], for a human model in free space.

It is well known and as depicted in Fig. 4.16 that the induced current in the body starts to decrease once the frequency exceeds the resonant frequency. However, the *SCIE* method predicts a linear increase of the induced current with the frequency. This indicates that the *SCIE* method may be applicable up to the first resonant frequency in the HF range when the method is applied to the human body.
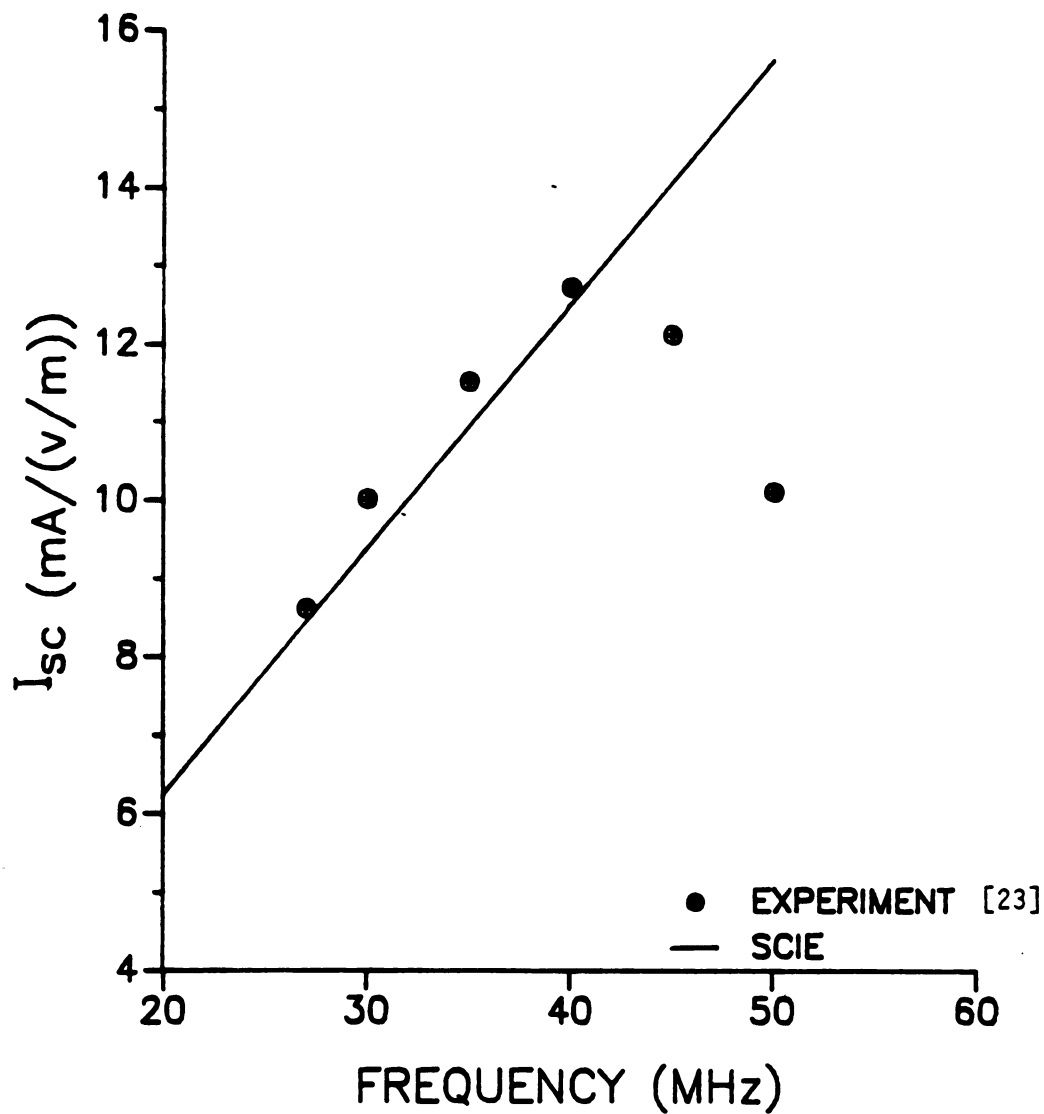
Fig. 4.16. Comparison of theoretical results by the SCIE method with
experimental results of Gandi et al [23] on the short-circuit
current for a grounded human model (~1.75 m in height) at
frequencies from 20 MHz to 50 MHz.

Table 4.1

Comparison of experimental and empirical results on the short-circuit
current with theoretical results by the present method.

f (MHz)	I_{sc} (mA/(V/m))		
	H = 1.75 m	H = 1.75 m	H = 1.80 m
	Eq. (*)	MEASURED	PRESENT METHOD
subject barefoot			
0.630	0.208	0.210	0.189
0.700	0.232	0.280	0.212
1.510	0.499	0.391	0.453
27.405	9.060	9.330	8.230
subject barefoot & arms raised			
0.700		0.384	0.272
1.510		0.555	0.586
27.405		9.850	10.600
comparison data			
0.146 [21]	0.048	0.035	0.044
0.720 [20]	0.238	0.277	0.216
0.920	0.304	0.316	0.276
1.145	0.379	0.366	0.344
1.350	0.447	0.405	0.405
1.470	0.486	0.560	0.441
27.000 [22]	8.930	8.400	8.130

(*) $I_{sc} = 0.108 \times E_o H^2 f_{MHz}$ [19]

CHAPTER 5

TENSOR ELECTRIC FIELD INTEGRAL EQUATION METHOD

FOR INDUCED ELECTRIC FIELDS INSIDE

BIOLOGICAL BODIES

5.1 Introduction

In this chapter, in order to compare the *surface charge integral
equation* (SCIE) method with other existing theoretical methods, the
tensor *electric field integral equation* (EFIE) method is applied to
quantify the interaction between ELF electromagnetic fields and biological
bodies. The induced electric field and current inside an arbitrarily-
shaped biological body can be quantified by this tensor integral equation
method. Instead of using low-frequency approximations as the SCIE method,
the EFIE method is an exact formulation for quantifying the interaction of
electromagnetic fields with biological bodies. Hence, it is appropriate
to compare the accuracy and efficiency of the SCIE method with the EFIE
method. Also, iterative methods will be employed to solve a large matrix
equation transformed from the tensor integral equation. The convergence
rate of various iterative algorithms will be compared.

5.2 Theoretical Development

The tensor integral equation method used in this chapter was
developed by Chen and Liversay [26]. When a biological body is

98

illuminated by an electromagnetic wave, an electromagnetic field is induced inside the body and an electromagnetic wave is scattered by the body in the region exterior to the body. In general, the biological body is an irregularly-shaped heterogeneous system with frequency dependent permittivity and conductivity. The induced electromagnetic field inside the body and the scattered electromagnetic wave will depend on the body's physiological parameters, geometry as well as frequency and polarization of the incident electromagnetic field. The electric field induced inside the body is the key quantity which determines the induced current inside the body.

Consider a finite irregularly-shaped biological body, as shown in Fig. 5.1, with electrical parameters expressed as:

conductivity : $\sigma = \sigma(\omega, \vec{r})$

permitivity : $\epsilon = \epsilon(\omega, \vec{r})$

permeability : $\mu = \mu_o$

where the biological body is assumed to be a non-magnetic medium. When it is illuminated by an incident electromagnetic wave with an electric field $\vec{E}^i(\vec{r})$ and a magnetic field $\vec{H}^i(\vec{r})$, the incident EM fields in the free space satisfy the following Maxwell's equations :

$$\nabla \times \vec{E}^i(\vec{r}) = -j\omega\mu_o \vec{H}^i(\vec{r}) \qquad (5.1a)$$

$$\nabla \times \vec{H}^i(\vec{r}) = j\omega\epsilon_o \vec{E}^i(\vec{r}) \qquad (5.1b)$$

$$\nabla \cdot \vec{E}^i(\vec{r}) = 0 \qquad (5.1c)$$

$$\nabla \cdot \vec{H}^i(\vec{r}) = 0 \qquad (5.1d)$$
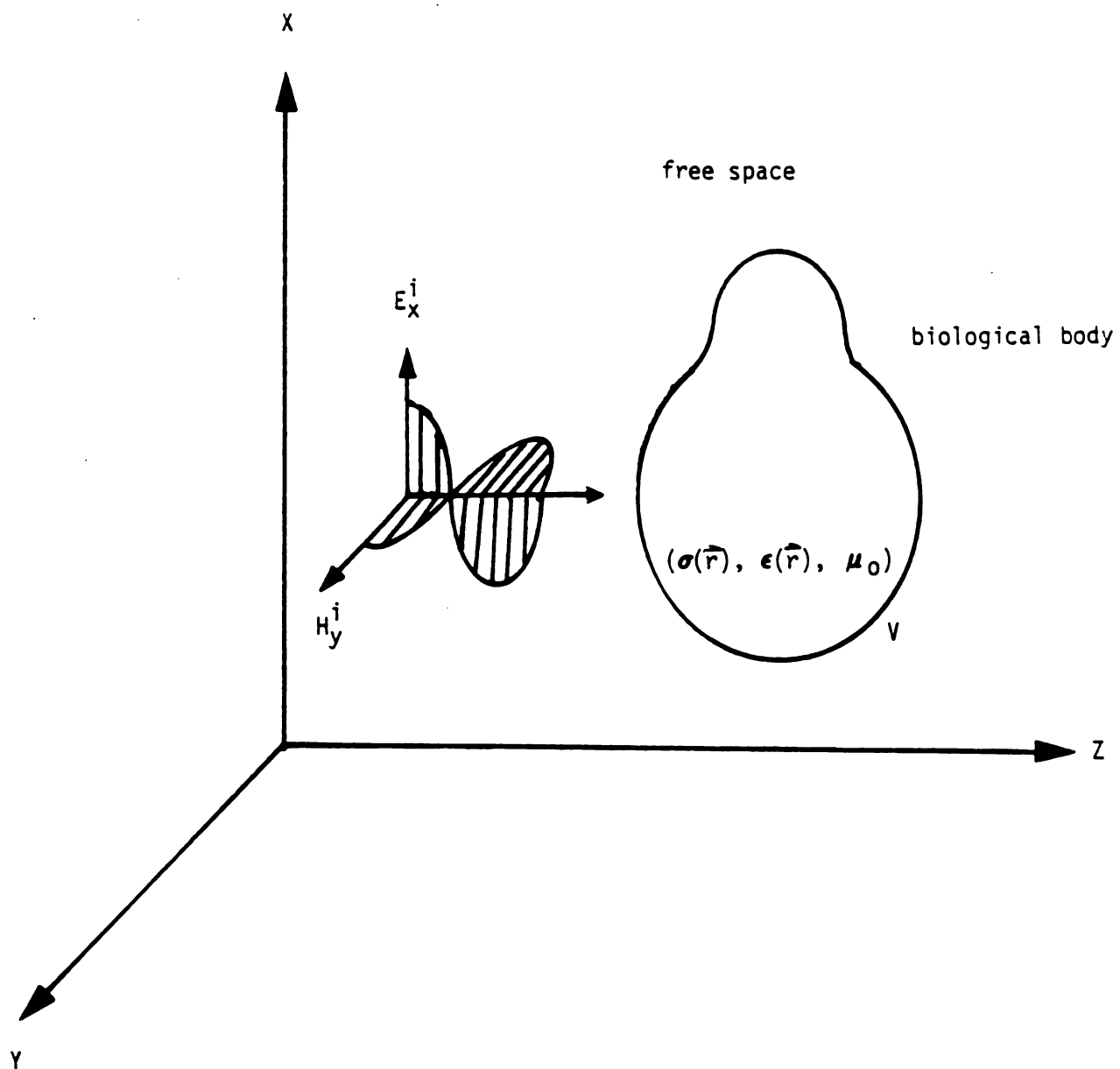
Fig. 5.1. An arbitrarily-shaped biological body in free space, illuminated by an EM plane wave.

where ϵ_o and μ_o are the permitivity and permeability of the free space. The induced charge and current in the body produce scattered fields $\vec{E}^s(\vec{r})$ and $\vec{H}^s(\vec{r})$. Thus the total field is the sum of the incident field and the scattered field :

$$\vec{E}(\vec{r}) = \vec{E}^i(\vec{r}) + \vec{E}^s(\vec{r}) \tag{5.2a}$$

$$\vec{H}(\vec{r}) = \vec{H}^i(\vec{r}) + \vec{H}^s(\vec{r}) \tag{5.2b}$$

where $\vec{E}(\vec{r})$ and $\vec{H}(\vec{r})$ are the total electric field and magnetic field.

The total EM field existing at any point in space including the biological system should also satisfy the Maxwell's equations :

$$\nabla \times \vec{E}(\vec{r}) = -j\omega\mu_o\vec{H}(\vec{r}) \tag{5.3a}$$

$$\nabla \times \vec{H}(\vec{r}) = \sigma(\vec{r})\vec{E}(\vec{r}) + j\omega\epsilon(\vec{r})\vec{E}(\vec{r}) \tag{5.3b}$$

$$\nabla \cdot [(\sigma(\vec{r}) + j\omega\epsilon(\vec{r}))\vec{E}(\vec{r})] = 0 \tag{5.3c}$$

$$\nabla \cdot \vec{H}(\vec{r}) = 0 \tag{5.3d}$$

By using Eqs. (5.1) through (5.3), the following equations can be derived :

$$\nabla \times \vec{E}^s(\vec{r}) = -j\omega\mu_o\vec{H}^s(\vec{r}) \tag{5.4a}$$

$$\nabla \times \vec{H}^s(\vec{r}) = [\sigma(\vec{r}) + j\omega(\epsilon(\vec{r}) - \epsilon_o)]\vec{E}(\vec{r}) + j\omega\epsilon_o\vec{E}^s(\vec{r}) \tag{5.4b}$$

An equivalent volume current density $\vec{J}_{eq}(\vec{r})$ is defined as

$$\vec{J}_{eq}(\vec{r}) - \tau(\vec{r})\vec{E}(\vec{r}) \tag{5.5}$$

where

$$\vec{\tau}(r) - \sigma(\vec{r}) + j\omega(\epsilon(\vec{r}) - \epsilon_o)$$

is the equivalent complex conductivity. Eq. (5.4b) can then be rewritten as

$$\nabla \times \vec{H}^{s}(\vec{r}) - \vec{J}_{eq}(\vec{r}) + j\omega\epsilon_o\vec{E}^{s}(\vec{r}) \tag{5.6}$$

$\vec{J}_{eq}(\vec{r})$ has two components; $\sigma(\vec{r})\vec{E}(\vec{r})$ the conduction current component and $j\omega(\epsilon(\vec{r}) - \epsilon_o)\vec{E}(\vec{r})$ the polarization current component. $\vec{J}_{eq}(\vec{r})$ exists only inside the biological system.

From the equation of continuity for $\vec{J}_{eq}(\vec{r})$, an equivalent volume charge density $\rho_{eq}(\vec{r})$ can be defined as

$$\nabla \cdot \vec{J}_{eq}(\vec{r}) + j\omega\rho_{eq}(\vec{r}) - 0 \tag{5.7}$$

Taking divergence of Eq. (5.6) and using Eq. (5.7), it leads to

$$\nabla \cdot \vec{E}^{s}(\vec{r}) - \rho_{eq}(\vec{r})/\epsilon_o \tag{5.8}$$

Now, Maxwell's equations for $\vec{E}^{s}(\vec{r})$ and $\vec{H}^{s}(\vec{r})$ can be expressed in terms of $\vec{J}_{eq}(\vec{r})$ and ρ_{eq} as

$$\nabla \times \vec{E}^S(\vec{r}) = -j\omega\mu_o\vec{H}^S(\vec{r}) \qquad (5.9a)$$

$$\nabla \times \vec{H}^S(\vec{r}) = \vec{J}_{eq}(\vec{r}) + j\omega\epsilon_o\vec{E}^S(\vec{r}) \qquad (5.9b)$$

$$\nabla \cdot \vec{E}^S(\vec{r}) = \rho_{eq}(\vec{r})/\epsilon_o \qquad (5.9c)$$

$$\nabla \cdot \vec{H}^S(\vec{r}) = 0 \qquad (5.9d)$$

The scattered field anywhere in the space can be written as [26]

$$\vec{E}^S(\vec{r}) = P.V. \int_V \vec{J}_{eq}(\vec{r}') \cdot G(\overleftrightarrow{r}, \vec{r}') dv' - \frac{\vec{J}_{eq}(\vec{r})}{3j\omega\epsilon_o} \qquad (5.10)$$

where

$$\overleftrightarrow{G}(\vec{r}, \vec{r}') = -j\omega\epsilon_o[\overleftrightarrow{I} + \frac{\nabla\nabla}{k_o^2}]\Psi(\vec{r}, \vec{r}')$$

$$\Psi(\vec{r}, \vec{r}') = \frac{e^{-jk_o|\vec{r}-\vec{r}'|}}{4\pi|\vec{r} - \vec{r}'|}$$

$$\overleftrightarrow{I} = \hat{x}\hat{x} + \hat{y}\hat{y} + \hat{z}\hat{z}$$

$$k_o = \omega\sqrt{\mu_o\epsilon_o}$$

P.V. symbol means the principle value of the integral and $\overleftrightarrow{G}(\vec{r}, \vec{r}')$ is the free space dyadic Green's function.

By substituting Eq. (5.10) into (5.2a) and rearranging terms, a tensor *electric field integral equation* (EFIE) can be obtained

$$[1 + \frac{r(\vec{r})}{3j\omega\epsilon_o}]\vec{E}(\vec{r}) - P.V.\int_V r(\vec{r}')\vec{E}(\vec{r}')\cdot\overset{\leftrightarrow}{G}(\vec{r},\vec{r}')dv' = \vec{E}^i(\vec{r}) \qquad (5.11)$$

where $r(\vec{r})$ and $\vec{E}^i(\vec{r})$ are known quantities and $\vec{E}(\vec{r})$ is the unknown total field inside the body.

5.3 Moment Method Solution of Tensor Integral Equation

In the actual calculation, it is very difficult to solve the tensor integral equation by performing the integral which involves unknown $\vec{E}(\vec{r})$ inside the integral. The Moment Method provides some simplification and approximation to solve the integral equation numerically.

In the Moment Method, the total volume of the biological body is partitioned into N subvolumes or cells as shown in Fig. 5.2. $\vec{E}(\vec{r})$ and $r(\vec{r})$ are assumed to be constant within each cell. Therefore, the accuracy of this method depends upon the dimensions of the cell. The integral equation (5.11) can be transformed into 3N simultaneous equations for (E_x, E_y, E_z) unknown quantities at central points of N cells by point matching method. These simultaneous equations can be written into a matrix form as

$$\begin{bmatrix} [G_{xx}] & [G_{xy}] & [G_{xz}] \\ [G_{yx}] & [G_{yy}] & [G_{yz}] \\ [G_{zx}] & [G_{zy}] & [G_{zz}] \end{bmatrix} \begin{bmatrix} [E_x] \\ [E_y] \\ [E_z] \end{bmatrix} = -\begin{bmatrix} [E_x^i] \\ [E_y^i] \\ [E_z^i] \end{bmatrix} \qquad (5.12)$$
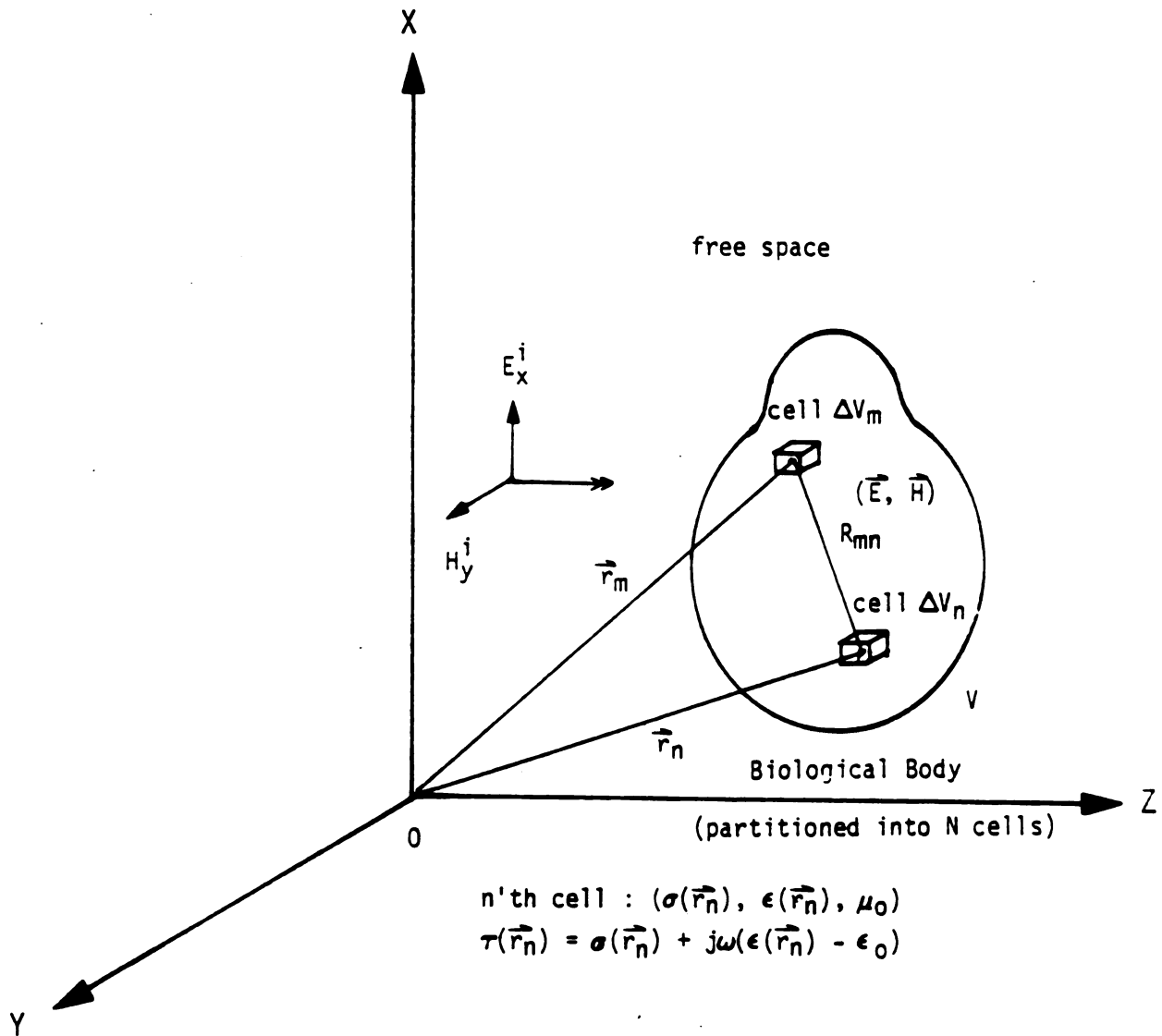
Fig. 5.2. The biological body is partitioned into many small cubic cells for numerical calculation of the induced electric field.

where the matrix [G] represents a (3N × 3N) matrix, while [E] and $[E^i]$ are 3N column matrices expressing E and E^i at central points of N cells.

The explicit expressions for each (N × N) submatrix $[G_{x_p x_q}]$ elements, (p,q = 1,2,3), are given in [26]. Let

$$(x_1 = x, \ x_2 = y, \ x_3 = z)$$

Then the (m,n)th off-diagonal element of the $[G_{x_p x_q}]$ matrix is

$$G_{x_p x_q} = \frac{-j\omega\mu_o k_o \tau(\vec{r}_n)\Delta V_n e^{-\alpha_{mn}}}{4\pi\alpha_{mn}^3} \times \qquad (5.13)$$

$$[(\alpha_{mn}^2 - 1 - j\alpha_{mn})\delta_{pq} + \cos\theta_{x_p}^{mn}\cos\theta_{x_q}^{mn}(3 - \alpha_{mn}^2 + 3j\alpha_{mn})], \quad m \neq n$$

where

$$\alpha_{mn} = k_o R_{mn} \qquad ; \qquad R_{mn} = |\vec{r}_m - \vec{r}_n|$$

$$\cos\theta_{x_p}^{mn} = \frac{x_p^m - x_p^n}{R_{mn}}$$

$$\cos\theta_{x_q}^{mn} = \frac{x_q^m - x_q^n}{R_{mn}}$$

$$\vec{r}_m = (x_1^m, x_2^m, x_3^m) \qquad ; \qquad \vec{r}_n = (x_1^n, x_2^n, x_3^n)$$

ΔV_n = volume of the nth cell

The (m,m)th diagonal element of $[G_{x_p x_q}]$ matrix is

$$G_{x_p x_q}^{mm} = - \delta_{pq} \left\{ \frac{2j\omega\mu_o \tau(\vec{r}_n)}{3k_o} [e^{-jk_o a_m}(1 + jk_o a_m) - 1] + [1 + \frac{\tau(\vec{r}_m)}{3j\omega\epsilon_o}] \right\}$$

where

$$a_n = [\frac{3\Delta V_m}{4\pi}]^{1/3} \qquad (5.14)$$

After all elements of the [G] matrix are determined, the total induced electric field $\vec{E}(\vec{r})$ inside the body can be obtained by inverting the matrix as

$$[E] = [G]^{-1}[-E^i] \qquad (5.15)$$

The induced body current density $\vec{J}(\vec{r})$ can then be determined as

$$\vec{J}(\vec{r}) = \tau(\vec{r})E(\vec{r})$$

$$(5.16)$$

5.4 Iterative Methods for Solving the Matrix Equation

In order to yield accurate numerical results from the tensor *electric field integral equation* method, sometimes the body needs to be partitioned into a large number of small cells. This will produce a large matrix equation transformed from the integral equation.

Conventional methods for solving the matrix equation, such as *Guassian Elimination Method* (GEM) or *LU decomposition*, require the computer memory storage of the whole matrix. When the matrix equation becomes excessively large, it often exceeds the storage capacity of the computer.

Iterative techniques offter the possibility of solving large matrix equations without requiring the storage of any matrix. In a survey of numerical techniques for solving large system of linear equations, Sarkar et al. [36] compare the relative advantages and disadvantages of various iterative methods. Here the *Conjugate Gradient Method* (CGM) and the *Guass-Seidel Method* (GSM) are adopted to solve the matrix equation iteratively.

5.4.1 Conjugate Gradient Method (CGM)

The basic principles of the *Conjugate Gradient Method* are described in an original paper by Hestenes and Stiefel [29]. For the solution of any complex matrix equation, $AX = b$, the iterative process of the CGM starting with an initial guess X_o is defined as :

$$r_1 = AX_o - b$$

$$p_1 = -A^H r_o$$

$$t_n = \|A^H r_n\|^2 \; / \; \|AP_n\|^2 \; , \qquad n = 1,2,3 \; \ldots$$

$$r_{n+1} = r_n + t_n AP_n$$

$$q_{n+1} = \|A^H r_{n+1}\|^2 \; / \; \|A^H r_n\|^2$$

and

$$x_{n+1} = x_n + t_n p_n$$

$$p_{n+1} = -A^H r_n + q_{n+1} p_n$$

where

A^H : the complex conjugate transpose matrix of the matrix A

r_n : the residual vector of iteration

p_n : the direction vector of iteration

It has been proven that [31], if A is a positive-definite matrix, the CGM converges to the exact solution of the matrix equation in at most N-step iterations (N = the order of the matrix A), assuming no round-off errors occurs. This finite-step convergence is an important advantage of the CGM over other iteration methods. However practically, due to round-off error in the computation, the CGM needs more than N steps iteration for the desired solution. But the iteration can be terminated at an earlier step, if the degree of accuracy is within the acceptable range. Also, in order to guarantee the positive-definite nature of the matrix A, instead of solving the matrix equation, $Ax = b$, we will solve the matrix equation,

$$[A^H A]x = A^H b \qquad (5.17)$$

since $[A^H A]$ must be positive-definite and the solutions of both matrix

equations are the same. In order to check the convergence of the iterative process, the following measure of accurracy is defined :

$$\text{ERROR RATE} = \frac{\|Ax_n - b\|}{\|b\|} \tag{5.18}$$

A value of 10^{-4} may be a reasonably good choice for this measure.

5.4.2 Guass-Seidel Method (GSM)

The description of the *Guess-Seidel method* can be found in [31]. For the complex matrix equation, $Ax = b$, the matrix can be written as,

$$A = L + D + U \tag{5.19}$$

where D,L,U are the diagonal, lower, uper triangular matrices of the matrix A. Thus the matrix equation is rewritten as

$$[D + L]x + Ux = b \tag{5.20}$$

Starting with an initial guess x_o, the iterative process of the GSM is defined as

$$[D + L]x_{n+1} = -Ux_n + b \tag{5.21}$$

or

$$x_{n+1} = -[D + L]^{-1} U x_n + [D + L]^{-1} b$$

$$= M_G x_n + [D + L]^{-1} b \tag{5.22}$$

The matrix $M_G = -[D + L]^{-1} U$ is called the Guass-Seidel matrix. It can be shown [31] that the GSM iteration process will converge for an arbitrary initial guess if and only if

$$\rho(M_G) = \max_{1 \leq i \leq N} |\lambda_i(M_G)| < 1 \tag{5.23}$$

where

$\rho(M_G)$: spectrum radius of the matrix M_G

$\lambda_i(M_G)$: ith eigenvalue of the matrix M_G

It has also been shown that [31], if the matrix A ia symmetric and positive-definite, then the spectrum radius $\rho(M_G)$ is smaller than 1. Hence, to guarantee the convergence of the GSM, we will solve the following matrix equation,

$$[A^H A] x = A^H b \tag{5.24}$$

The convergence rate of the GSM can be improved by so-called *Successive Over-Relaxation* (S.O.R) process (or *accelerated Guass-Seidel Method*). The S.O.R method is a modified scheme of the GSM. Instead of using x_{n+1} of Eq. (5.22) in the iteration process, the following equation is used,

$$x_{n+1}^* = \omega x_{n+1} + (1 - \omega) x_n$$

$$= \omega(-[D + L]^{-1}[Ux_n + b]) + (1 - \omega)x_n \qquad (5.25)$$

where the parameter ω is a constant that can be determined so as to yield the fastest rate of the convergence. The *Guass-Seidel Method* is the special case $\omega = 1$ of Eq. (5.25). It has been proven that [31], any fixed constant ω, $1 < \omega < 2$, will accelerate the rate of convergence in the iteration process.

5.4.3 Initial Guess for the Iterative Method

Iterative methods as discussed in previous sections, the CGM and the GSM, will converge for any initial guess as long as the matrix is positive-definite. However, a good initial guess (close to the exact solution) can reduce iterative times to yield a solution in a desired accuracy. A good choice for the initial guess x_0 of the iterative process for solving a matrix equation $Ax = b$ is

$$x_0 = \begin{bmatrix} x_1^o \\ x_2^o \\ . \\ . \\ . \\ x_N^o \end{bmatrix} = \begin{bmatrix} b_1/a_{11} \\ b_2/a_{22} \\ . \\ . \\ . \\ b_N/a_{NN} \end{bmatrix} \qquad (5.26)$$

where $[a_{ii}]$ are diagonal elements of the matrix A and $[b_i]$ are column

elements of b. This is equivalent to solve a matrix equation

$$Dx_o = b \qquad\qquad (5.27)$$

where D is the diagonal matrix of the matrix A. If the matrix A is diagonally dominant, x_o of Eq. (5.26) is a fairly good choice for the iteration. A better choice for x_o is to solve a tridiagonal matrix equation which is

$$Tx_o = b \qquad\qquad (5.28)$$

where T is the tridiagonal matrix of the matrix A,

$$T = \begin{bmatrix} a_{11} & a_{12} & & & & \\ a_{21} & a_{22} & a_{23} & & 0 & \\ & a_{32} & a_{33} & a_{34} & & \\ & & \cdot & \cdot & \cdot & \\ & & & \cdot & \cdot & \cdot \\ & & & & \cdot & \cdot & \cdot \\ & 0 & & & \cdot & \cdot & \cdot \\ & & & & & & \cdot \\ & & & & & & a_{NN} \end{bmatrix}$$

Obviously the solution of this matrix equation is closer to the exact solution of the original matrix equation Ax = b than that of the diagonal matrix equation (5.27). The tridiagonal matrix equation of Eq. (5.28) can be solved by a simple algorithm — *Thomas Method* [34] as follows,

and

a

$$w_1 = a_{11}$$

$$w_r = a_{rr} - a_{r,r-1}q_{r-1} \qquad r = 2,3 \ldots\ldots N$$

$$q_{r-1} = a_{r-1,r}/w_{r-1}$$

and

$$g_1 = b_1/w_1$$

$$g_r = (b_r - a_{r,r-1}g_{r-1})/w_r \qquad r = 2,3 \ldots\ldots N$$

and these transform (5.28) to

$$x_N^o = g_N$$

$$x_r^o = g_r - q_r x_{r+1}^o \qquad r = 1,2 \ldots\ldots N-1 \qquad (5.29)$$

If the w, q, and g are calculated in order of increasing r, it follows that (5.29) can be used to calculate the x^o in order of decreasing r, that is, x_N^o, x_{N-1}^o, $\ldots\ldots x_2^o$, x_1^o.

The algorithm is easily described in matrix notation. The T matrix is decomposed into two triangular matrices

$$T = WQ \qquad (5.30)$$

where

$$
W = \begin{bmatrix}
w_1 & & & & \\
a_{21} & w_2 & & 0 & \\
& a_{32} & w_3 & & \\
& & \cdot & \cdot & \\
& & & \cdot & \cdot \\
0 & & & \cdot & \cdot \\
& & & & w_N
\end{bmatrix}
$$

and

$$
Q = \begin{bmatrix}
1 & w_1 & & & & \\
& 1 & w_2 & & 0 & \\
& & 1 & w_3 & & \\
& & & \cdot & \cdot & \\
& & & & \cdot & \cdot \\
0 & & & & \cdot & w_{N-1} \\
& & & & & 1
\end{bmatrix}
$$

Thus

$$WQx_o = b \tag{5.31}$$

By defining the column vector g

$$g = Qx_o \tag{5.32}$$

Eq. (5.31) can be written as

$$Wg = b \tag{5.33}$$

The algorithm (5.29) can be derived from solutions of matrix equations Eq. (5.32) and (5.33).

5.4.4 Numerical Example

In order to compare the convergence rate of the CGM and the GSM when employed to solve the matrix equation transformed from the EFIE Eq. (5.12) at the ELF range, a numerical example on a biological tissue-layer illuminated by a plane EM wave of 60-Hz (Fig. 5.3) is given. The dielectric constant ϵ_r and the conductivity σ of the tissue-layer are assumed to be 7×10^4 and 0.04 $(\Omega m)^{-1}$ at this frequency. The tissue-layer is illuminated by the incident wave at normal incidence, and the incident electric field is directed in the x-direction, as shown in Fig. 5.3. The tissue-layer is partitioned into 144 cubic cells. This leads to 108 (= 3 × 36) unknowns in the matrix equation (5.12) when a quarter-body symmetry is applied. Convergences of the CGM and the GSM when solving the matrix equation for the induced current in the tissue-layer are shown in Fig. 5.4. Comparisons of the x-component induced current densities computed by using the GEM (*Guassian Elimination Method*), the CGM and the GSM (300 iterations) are shown in Figs. 5.5 − 5.8. It can be observed that the GSM has a faster convergence rate than the CGM for solving the matrix equation of EFIE at the ELF range. More numerical examples will be shown in the following section.

5.5 Numerical Results for the Human Model and Comparison with the SCIE method

In order to compare the scalar *SCIE* method with the tensor *EFIE* method, the electric field integral equation is applied to quantify the induced current inside the phantom model of man used in the experiment by Kaune and Forsythe [10] , when illuminated by a 60-Hz plane EM wave.

INCIDENT WAVE
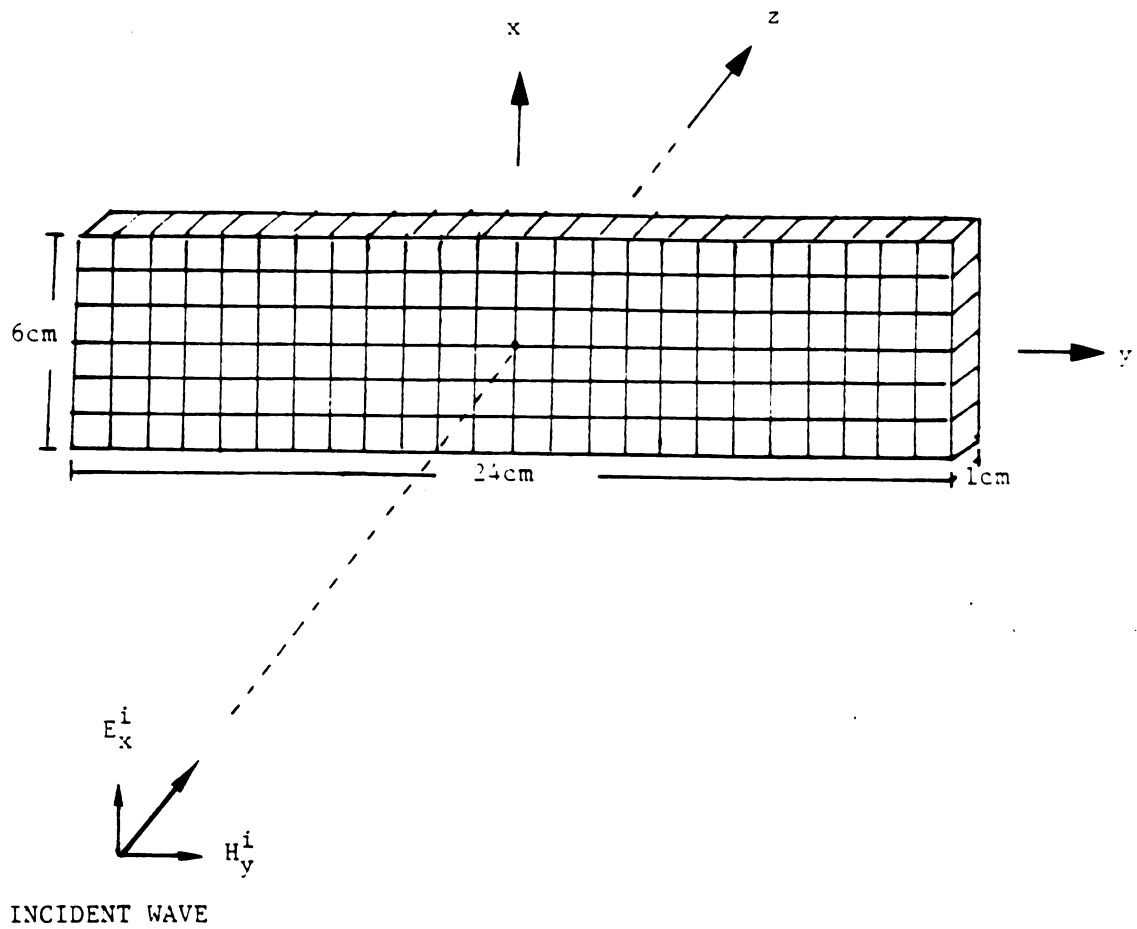
* FREQUENCY = 60 Hz

* TISSUE: σ = 0.04 $\mho$/m

ϵ = 7×10^4 ϵ_o

Fig. 5.3. A biological tissue-layer exposed to a 60-Hz EM plane wave.
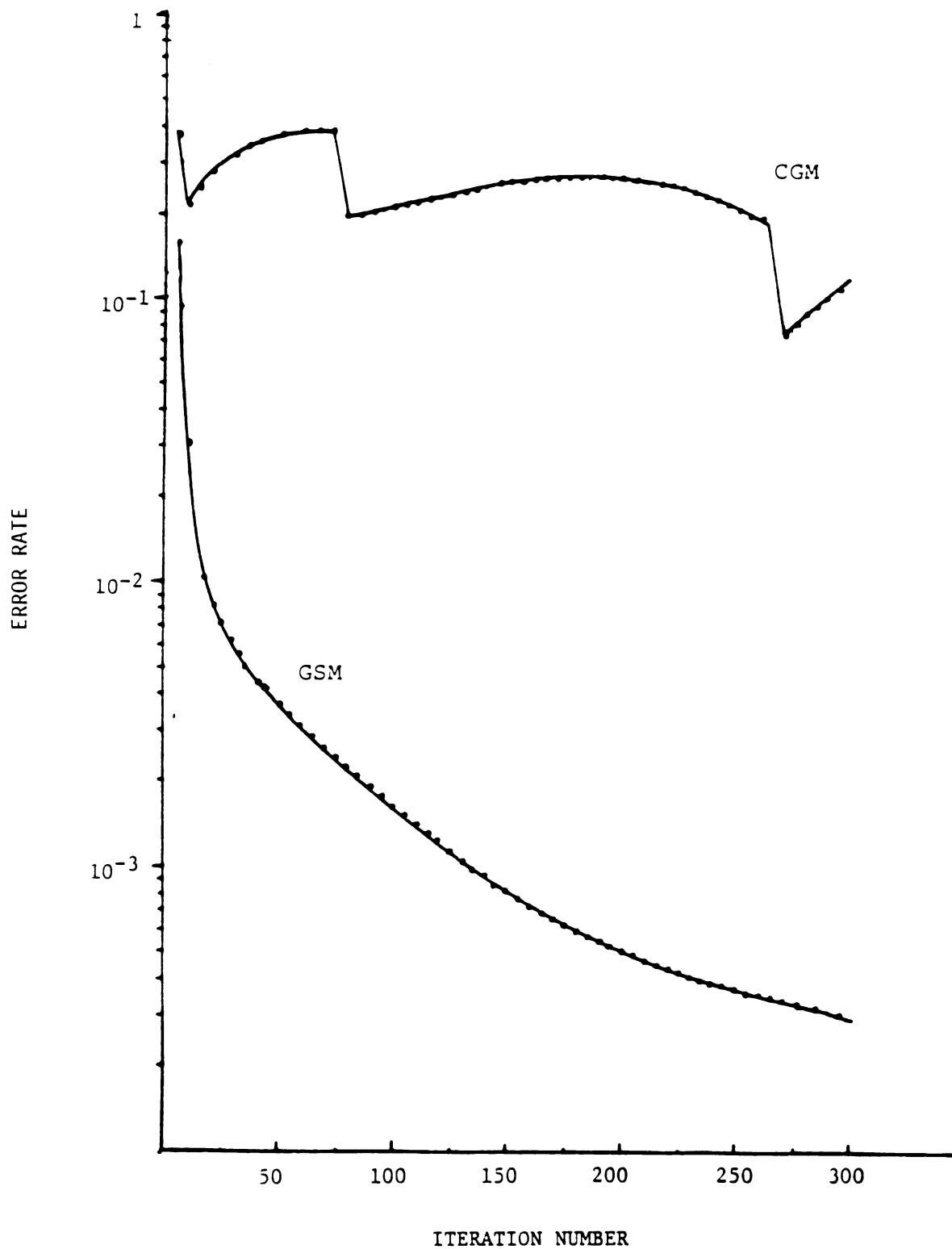
Fig. 5.4. Convergences of the CGM and the GSM when solving the induced current in the tissue-layer of Fig. 5.3 by the EFIE method.
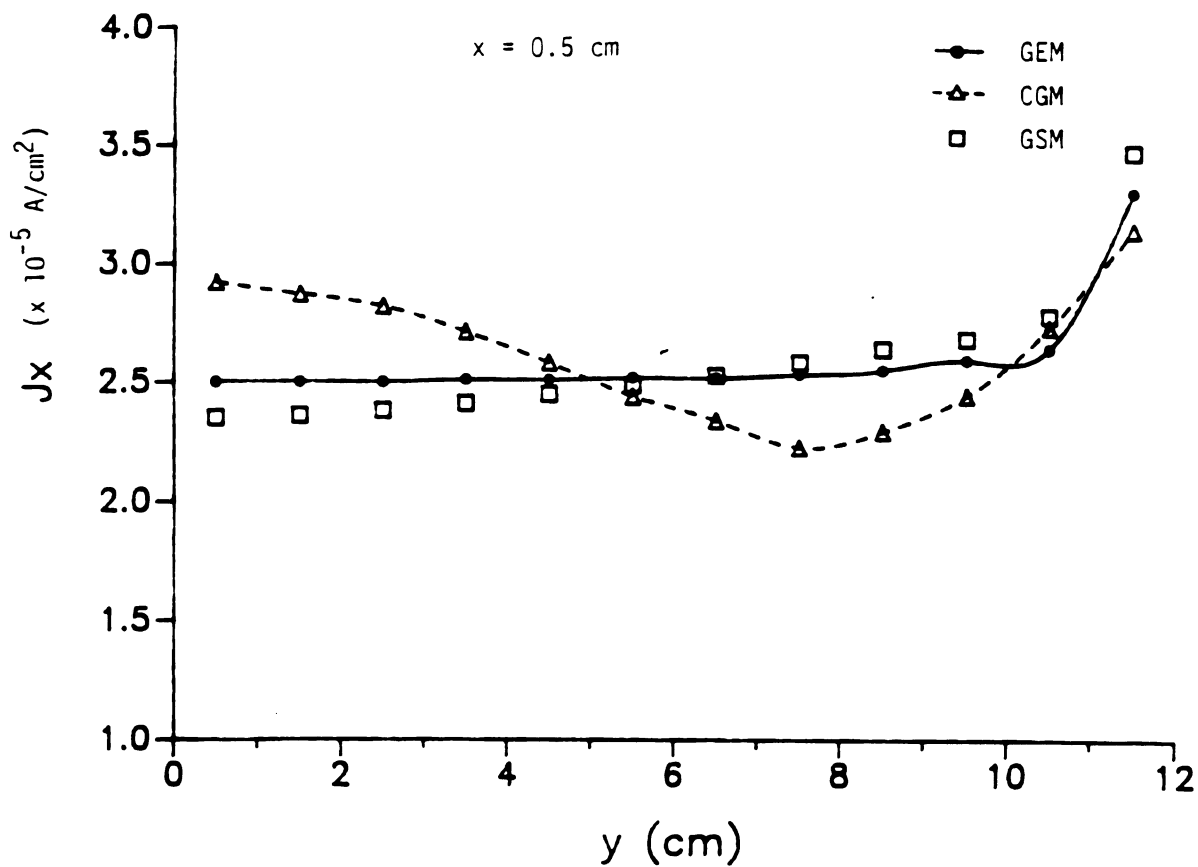
Fig. 5.5. Distribution of the x-component induced current densities
in the tissue-layer of Fig. 5.3. when illuminated by a 60-Hz.
1 kV/m EM plane wave.
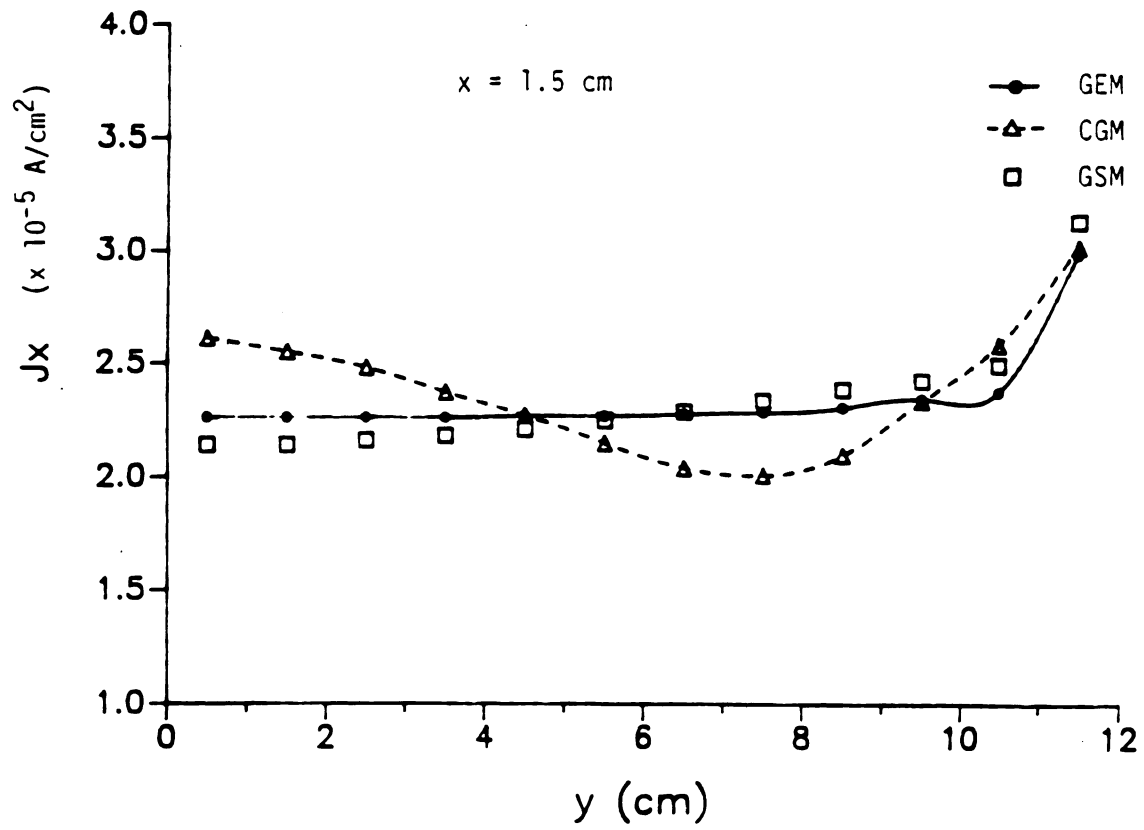
Fig. 5.6. Distribution of the x-component induced current densities in the tissue-layer of Fig. 5.3, when illuminated by a 60-Hz, 1 kV/m EM plane wave.
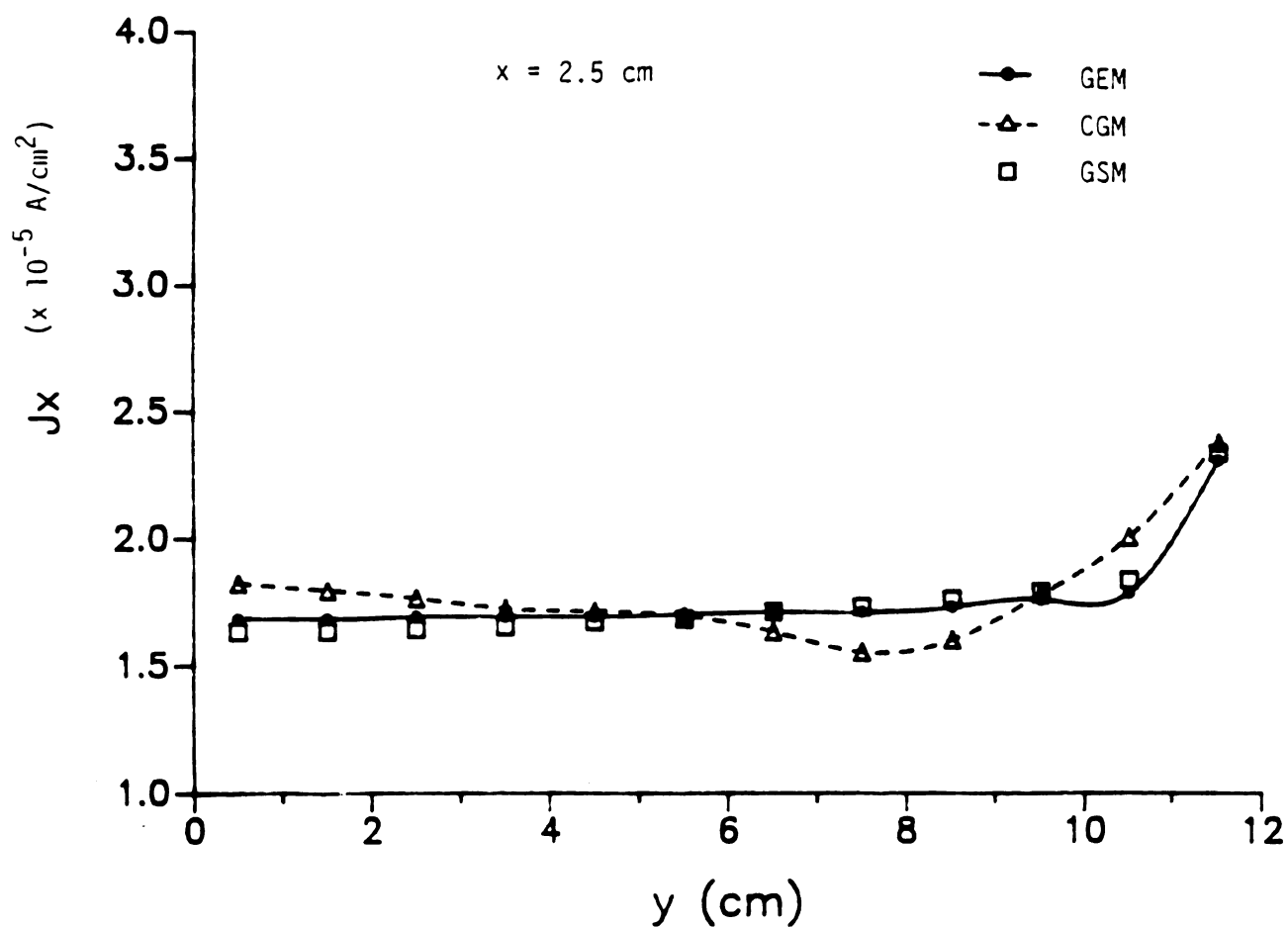
Fig. 5.7. Distribution of the x-component induced current densities
in the tissue-layer of Fig. 5.3. when illuminated by a 60-Hz,
1 kV/m EM plane wave.

122

CGM

(300 iterations)

J_x

$(\times 10^{-5})$

J_y

$(\times 10^{-5})$

J_z

$(\times 10^{-21})$

GSM

(300 iterations)

J_x

$(\times 10^{-5})$

J_y

$(\times 10^{-5})$

J_z

$(\times 10^{-21})$

GEM

J_x

$(\times 10^{-5})$

J_y

$(\times 10^{-5})$

J_z

$(\times 10^{-21})$
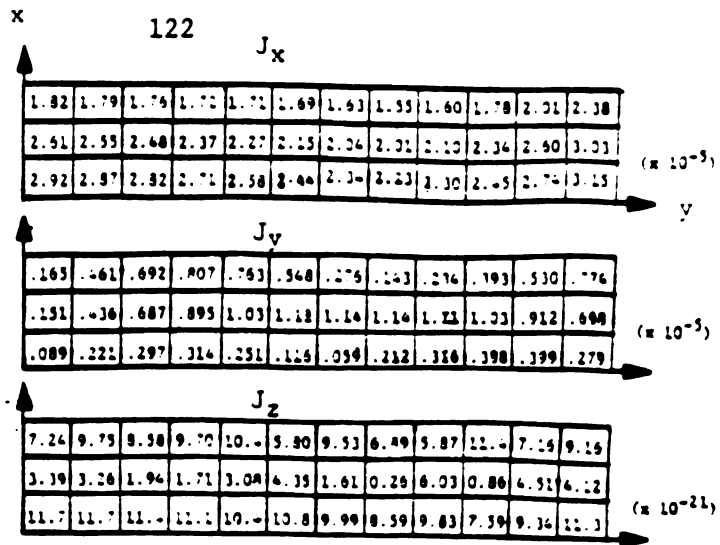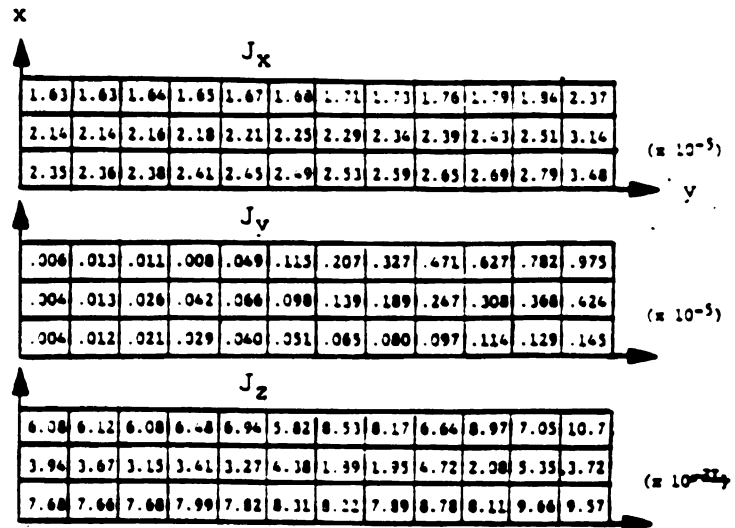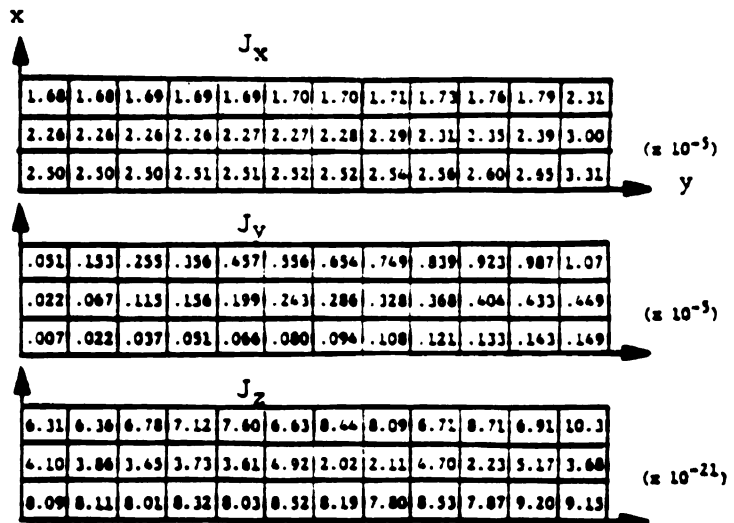
Fig. 5.8. Comparison of the CGM and the GSM with the GEM on induced
current densities for the tissue-layer of Fig. 5.3,
illuminated by a 60-Hz, 1 kV/m EM plane wave. Induced
current densities are given in units of A/cm^2.

These results are then compared with the numerical results by the *SCIE* method for the same model (sec. 4.2). Fig. 5.9 depicts the theoretical model of man which approximates the experimental model. Also, the experimental model and theoretical models for the *SCIE* method as well as the *EFIE* method are shown in Fig. 5.10 for comparison. The model used for the *EFIE* method is subdivided into several hundred cubical cells and a half-body symmetry is applied to reduce the number of unknowns. The electric properties of the body are assumed to be $\epsilon_r = 7 \times 10^4$ and $\sigma = 0.04$ $(\Omega m)^{-1}$ at the frequency of 60-Hz. The model is illuminated by the incident wave at normal incidence, and the incident electric field is directed in the x-direction, as shown in Fig. 5.11.

Fig. 5.12 depicts the comparison of numerical results by the *EFIE* method and corresponding numerical results by the *SCIE* method as well as experimental results of the induced current density inside the body. In the numerical calculation of the *EFIE* method, two cases have been studied : (1) the body is subdivided into 536 cubic cells which leads to a (804 × 804) matrix equation with a half-body symmetry (268 cells) and (2) the body is subdivided into 674 cubic cells which leads to a (1011 × 1011) matrix equation with a half-body symmetry (337 cells). Also in the calculation, the incident electric field is assumed to be 10 kV/m. Due to the symmetry, only one half of the body is shown for both cases. In the Fig. 5.12 it can be observed that, numerical results of the first case (268 cells) by the *EFIE* method disagree with those by the *SCIE* method and experimental results. Specifically, the direction of the induced current in the arm is upward which is opposite to the downward direction predicted by the *SCIE* method and experimental
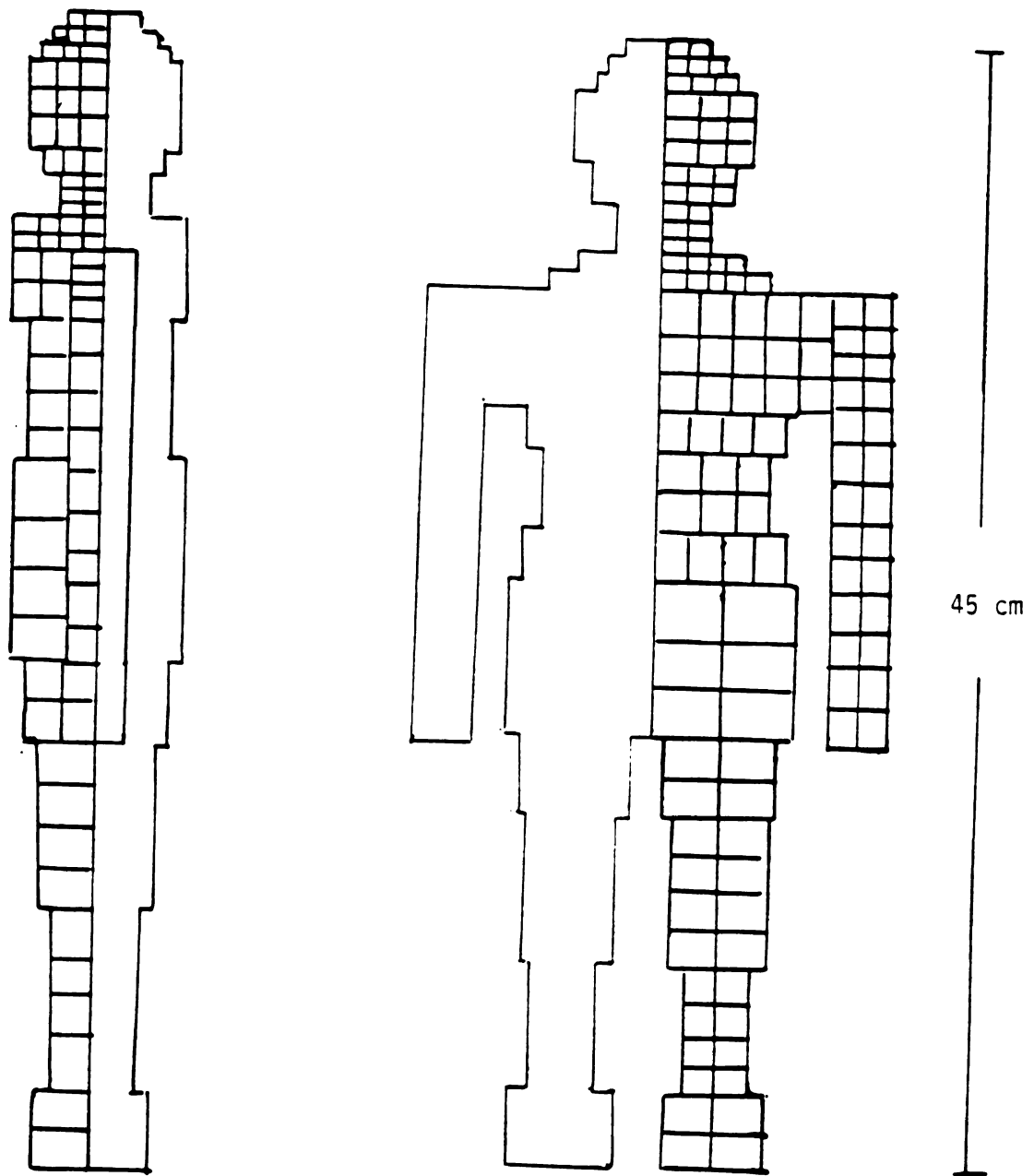
Fig. 5.9. Geometries of the theoretical human model for the numerical calculation of the EFIE method.

EXPERIMENT (Kaune & Forsythe)

SCIE
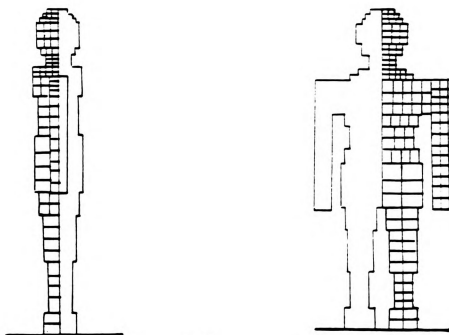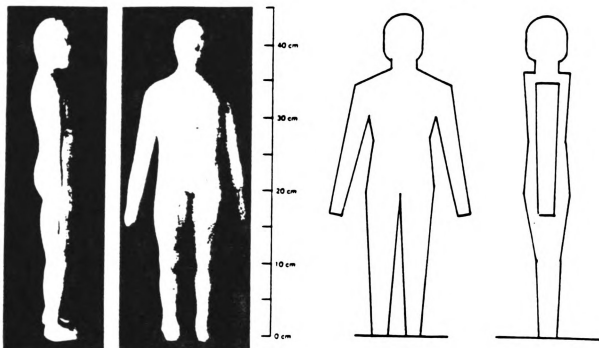
EFIE

Fig. 5.10. Comparison of experimental human model with theoretical
models for the SCIE method and The EFIE method which
approximate the experimental model.

$$\epsilon_r = 7 \times 10^4$$

$$\sigma = 0.04$$

GROUND

IMAGE BODY

E_x^i

H_y^i

INCIDENT WAVE

f = 60-Hz
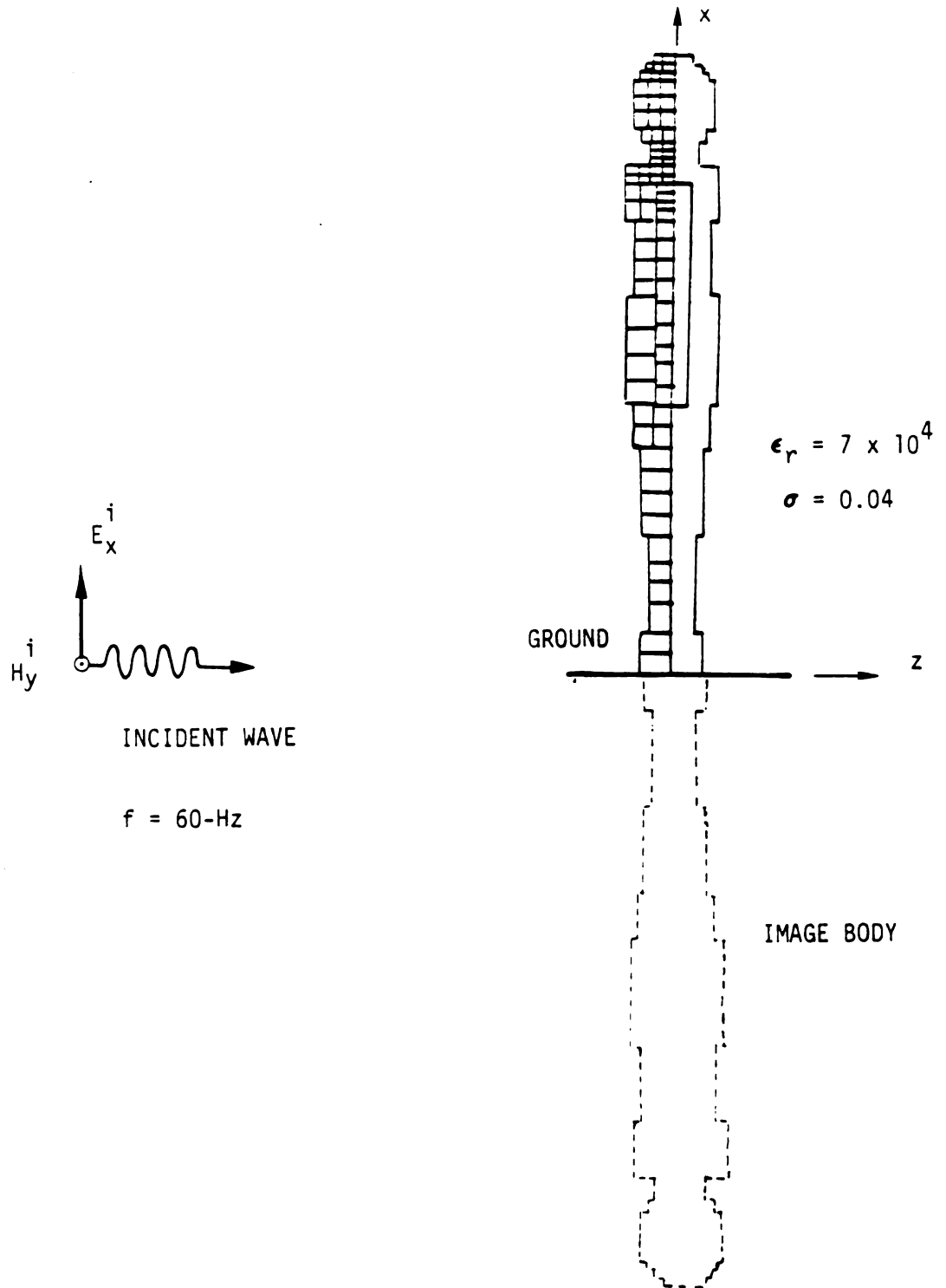
Fig. 5.11. The theoretical human model of Fig. 5.9 standing on the ground is exposed to a 60-Hz EM plane wave.

SCIE

EXPERIMENT

(Kaune & Forsythe)

268 cells

(804 x 804)

matrix equatiom

337 cells

(1011 x 1011)

matrix equation
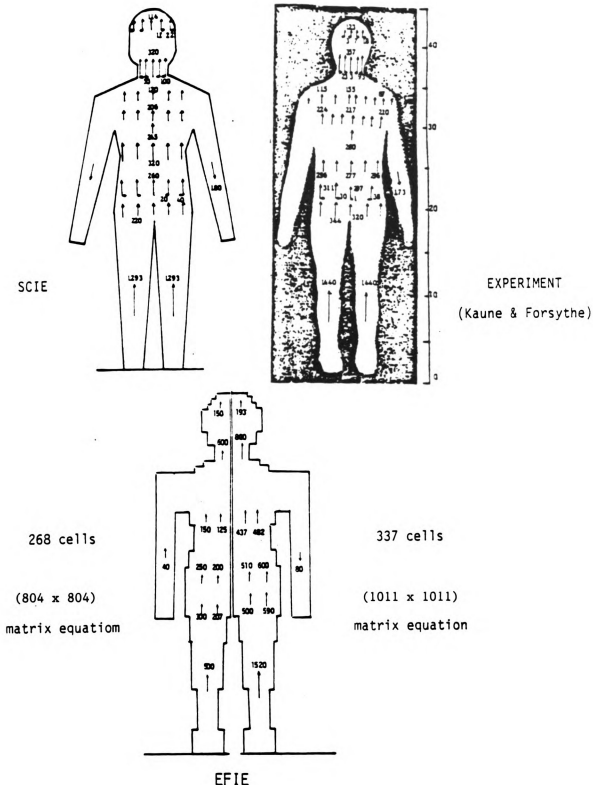
EFIE

Fig. 5.12. Comparison of theoretical results by the EFIE method with that by the SCIE method and experimental results of Kaune and Forsythe on vertical current densities for a grounded human model exposed to a 60-Hz, 10 kV/m EM field. Induced current densities are given in units of nA/cm^2.

measurement. This disagreement is mainly due to insufficient partitioning of the body model in the numerical calculation. The accuracy of numerical results by the *EFIE* method can be improved by subdividing the body into more cells. Fig. 5.12 shows that the second case (337 cells) yields more agreeable numerical results than the first case, when compared with corresponding results by the *SCIE* method and experimental results. As shown in the figure, the induced current density in the leg is 1500 nA/cm^2 which is close to 1293 nA/cm^2 calculated by the *SCIE* method and 1440 nA/cm^2 measured in the experiment. Moreover, the induced current in the arm is directed downward now, which is consistent with the result given by the *SCIE* method and the experiment. The accuracy of the *EFIE* method can be further improved by more partitioning of the body at the expense of excessive computer memory and CPU time. Also, the comparison of the convergence rate for solving the matrix equation by the CGM and the GSM is shown in Fig. 5.13. It is noticed that the GSM again has a faster convergence rate than the CGM at the ELF range.

From the above comparison we note that, for quantifying the interaction of ELF electromagnetic fields with a human body, the *EFIE* method needs to solve a ~ (1000 × 1000) matrix equation while the *SCIE* method only requires ~ (100 × 100) matrix equation, also the *EFIE* method takes much more computational time to calculate matrix elements than the *SCIE* method. Furthermore, the *SCIE* method can be used to calculate the body's surface electric field and the short-circuit current through grounding impedances of the body which cannot be achieved by the *EFIE* method. To conclude, the *SCIE* method has much better numerical accuracy and computational efficiency than the *EFIE* method

in quantifting the interaction between biological bodies (or conducting bodies) and low frequency EM fields.
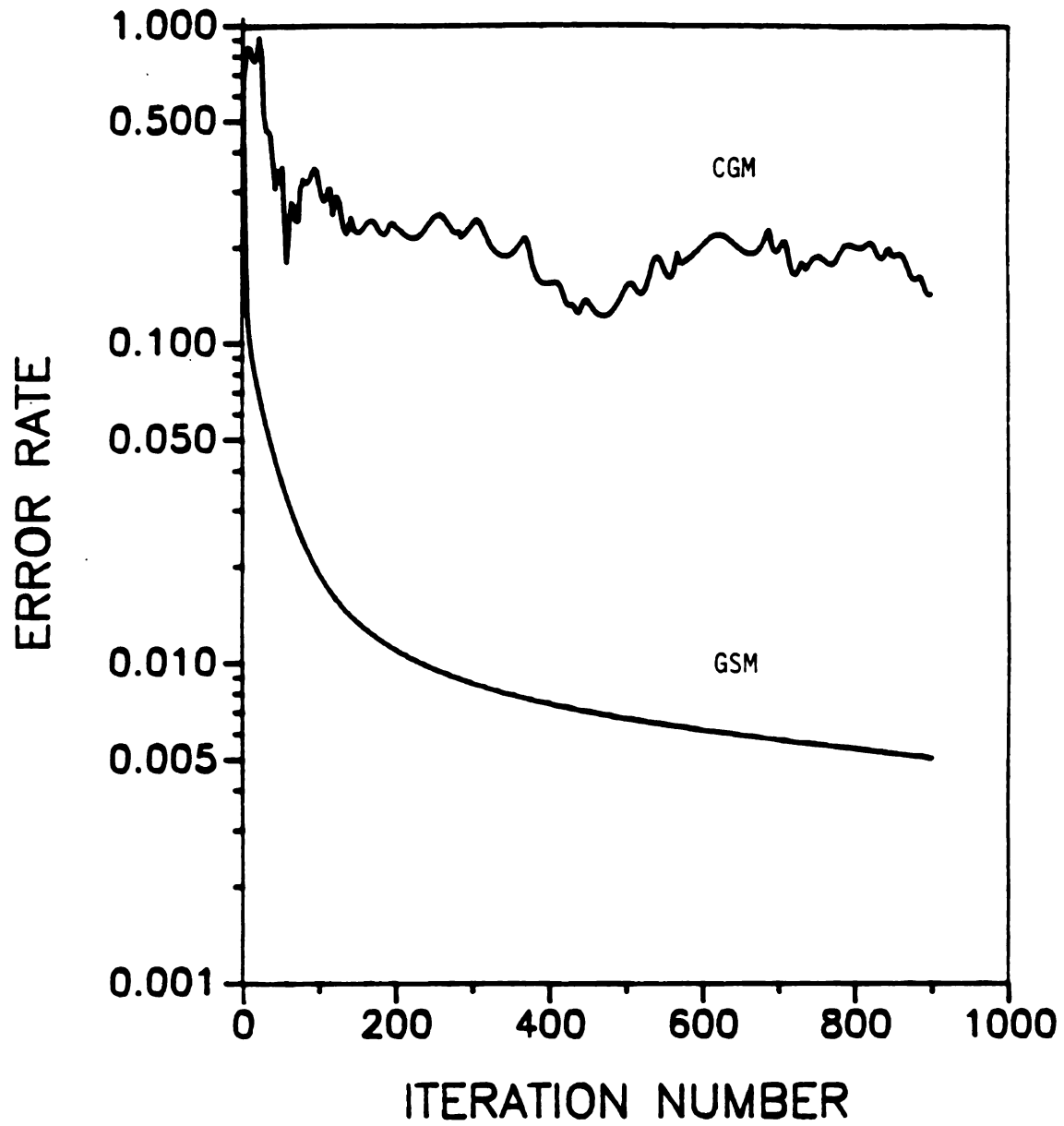
Fig. 5.13. Convergences of the CGM and the GSM when solving for the
induced current in the body model of Fig. 5.11 based on
the EFIE method.

CHAPTER 6

ANALYSIS OF SHOCK CURRENT BETWEEN HUMAN BODY AND
METALLIC OBJECTS UNDER THE EXPOSURE OF
ELF ELECTRIC FIELDS

6.1 Introduction

In previous chapters, the *SCIE* method was applied to quantify the steady-state induced current and field of the biological body under the exposure of the ELF-LF electric field. In this chapter, transient response of the interaction between a human body and a metallic object both exposed to the ELF electric field of a high-voltage transmission line is studied. The *SCIE* method and the equivalent-circuit model will be adopted to analyze the shock current flowing between a human body and a conducting object. Numerical results on the transient shock current predicted by the present method will be compared with the experimental results by Reilly [32].

6.2 Theoretical Development of the Shock Current Analysis

When a man and a nearby metallic object, such as a vehicle, are both illuminated by the ELF electric field emitted from an EHV power line, both the human body and the metallic object will acquire certain induced body potentials. If they are located very close, a large shock current may be generated between the man and the vehicle through direct contact or spark discharges, as shown in Fig. 6.1. This shock current is
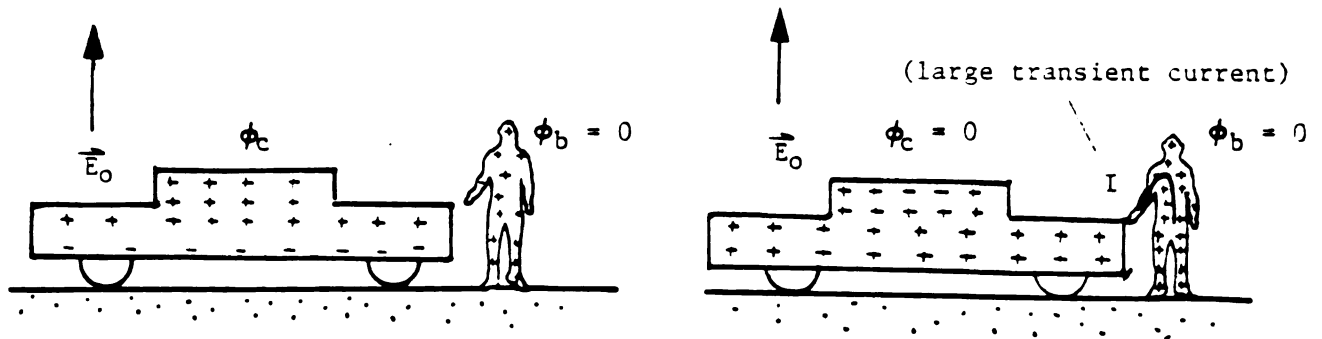
(a) Human body short-circuited to the ground
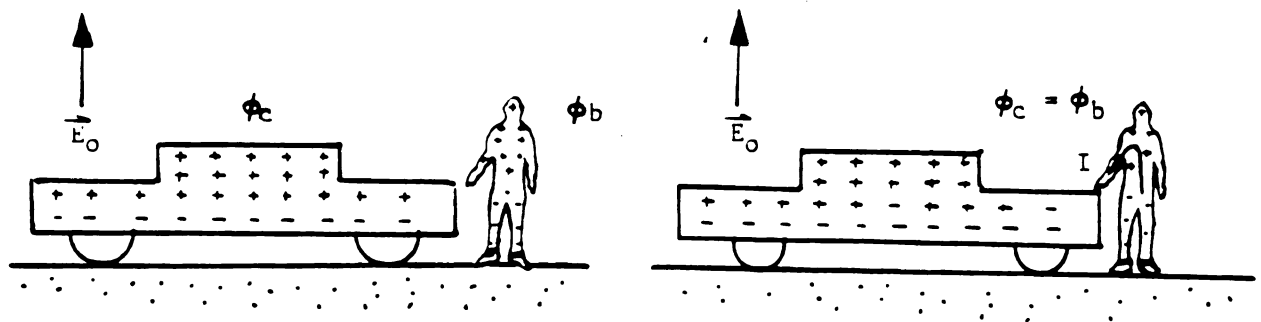
(b) Human body with grounding impedances

Fig. 6.1. Large shock currents flow between a vehicle and a nearby human body through direct contact or spark discharge, when both are exposed to the ELF electric field of an EHV power line.

due to a large potential difference between two objects ($\sim$ kV, if $E_o =$ 1 kV/m), and it may cause serious hazards to the human body. To analyze the shock current, we will develop equivalent-circuit models for the human body and the vehicle based on their floating potentials and short-circuit currents calculated by the SCIE method. The time-dependent behavior of the shock current is then determined from a transient analysis of a system composed of the equivalent circuits.

6.2.1 Equivalent-Circuit Models

Consider a biological body standing on the ground plane with a grounding impedance Z_L and exposed to an ELF electric field, as shown in Fig. 6.2. This system can be modeled by two kinds of equivalent circuits [31] as shown in Fig. 6.2:

(a) Thevenin equivalent circuit

$$\Rightarrow Z_{eq} = \phi_{bo}/I_{sc}$$

(b) Norton equivalent circuit

$$\Rightarrow Y_{eq} = I_{sc}/\phi_{bo} \qquad (Y_{eq} = 1/Z_{eq})$$

where ϕ_{bo} is the floating potential of the body ($Z_L = \infty$), I_{sc} is the short-circuit current of the body ($Z_L = 0$) and Z_{eq} is the equivalent impedance of the body with respect to the system in the equivalent circuit. ϕ_{ob} and I_{sc} can be determined by using the SCIE method as discussed in Sec. 2.2.

When a biological body and a nearby metallic object are both exposed to an ELF electric field, the same equivalent circuit models
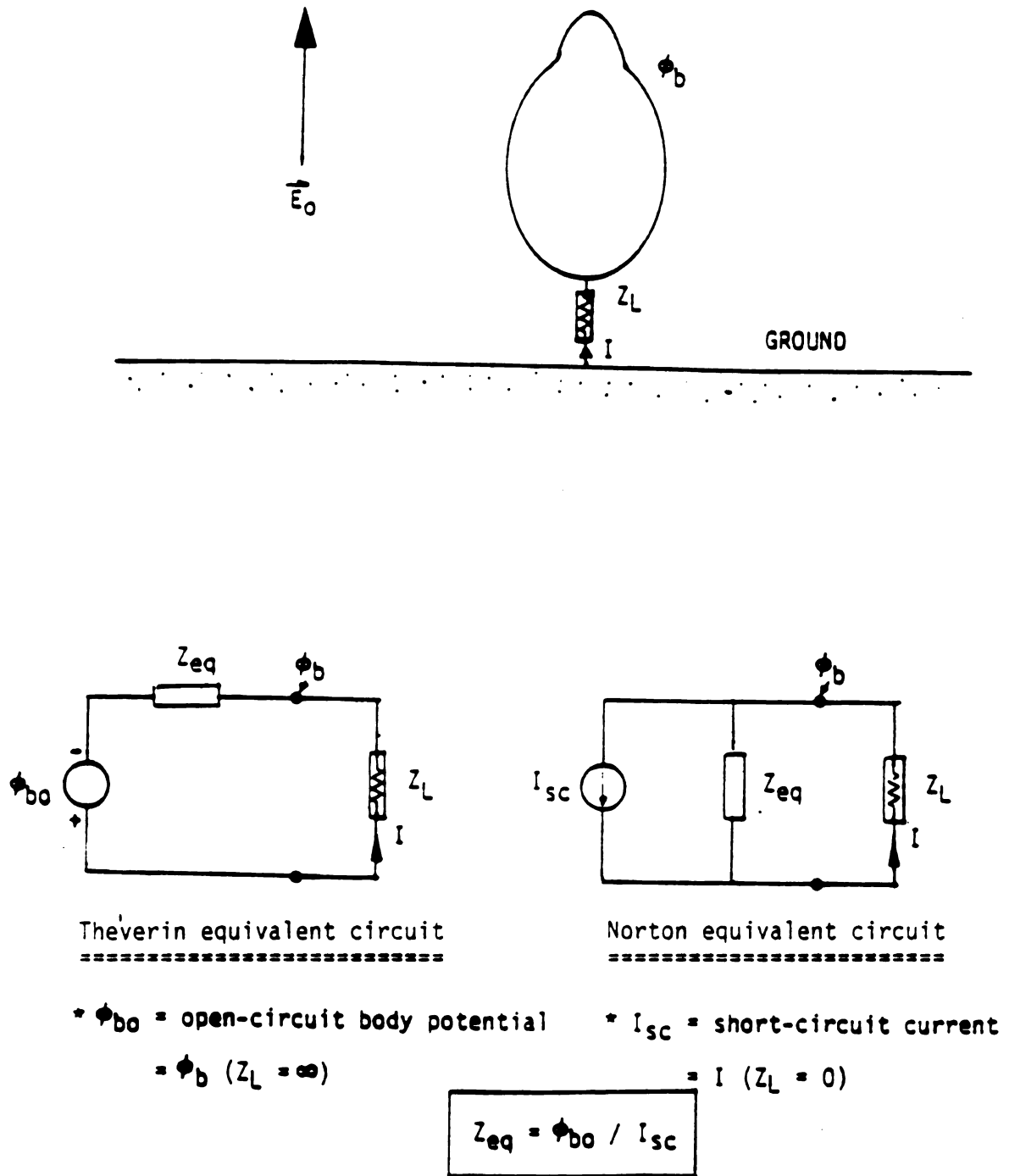
Fig. 6.2. A biological body standing on the ground with a grounding impedance Z_L is exposed to an ELF electric field. The circuits shown in the figure are the Thevenin and Norton equivalent circuit for this system.

can be constructed to represent the whole system. Fig. 6.3 depicts the the Thevenin equivalent circuit of a biological body and a metallic object at proximity. It is important to note that, due to the coupling effect between the biological and metallic objects, the floating potential and the short-circuit current of each object will be different from those when each object is isolated. To determine the coupled floating potential and the coupled short-circuit current of each object, a set of *coupled surface-charge integral equation* are developed as follows:

$$\frac{1}{4\pi\epsilon_o} \int_{S_b+S_b^i+S_c+S_c^i} \frac{\eta(\vec{r}')}{|\vec{r}_b - \vec{r}'|} \, ds' + \phi_{bo}(\vec{r}_b) - \phi_b \qquad (6.1a)$$

$$\frac{1}{4\pi\epsilon_o} \int_{S_b+S_b^i+S_c+S_c^i} \frac{\eta(\vec{r}')}{|\vec{r}_c - \vec{r}'|} \, ds' + \phi_{co}(\vec{r}_c) - \phi_c \qquad (6.1b)$$

$$I_b - \phi_b/Z_{Lb} - j\omega Q_b - j\omega \int_{S_b} \eta(\vec{r}')ds' \qquad (6.1c)$$

$$I_c - \phi_c/Z_{Lc} - j\omega Q_c - j\omega \int_{S_c} \eta(\vec{r}')ds' \qquad (6.1d)$$

where

S_b - surface area of the biological body b

S_b^i - surface area of the image of the biological body b
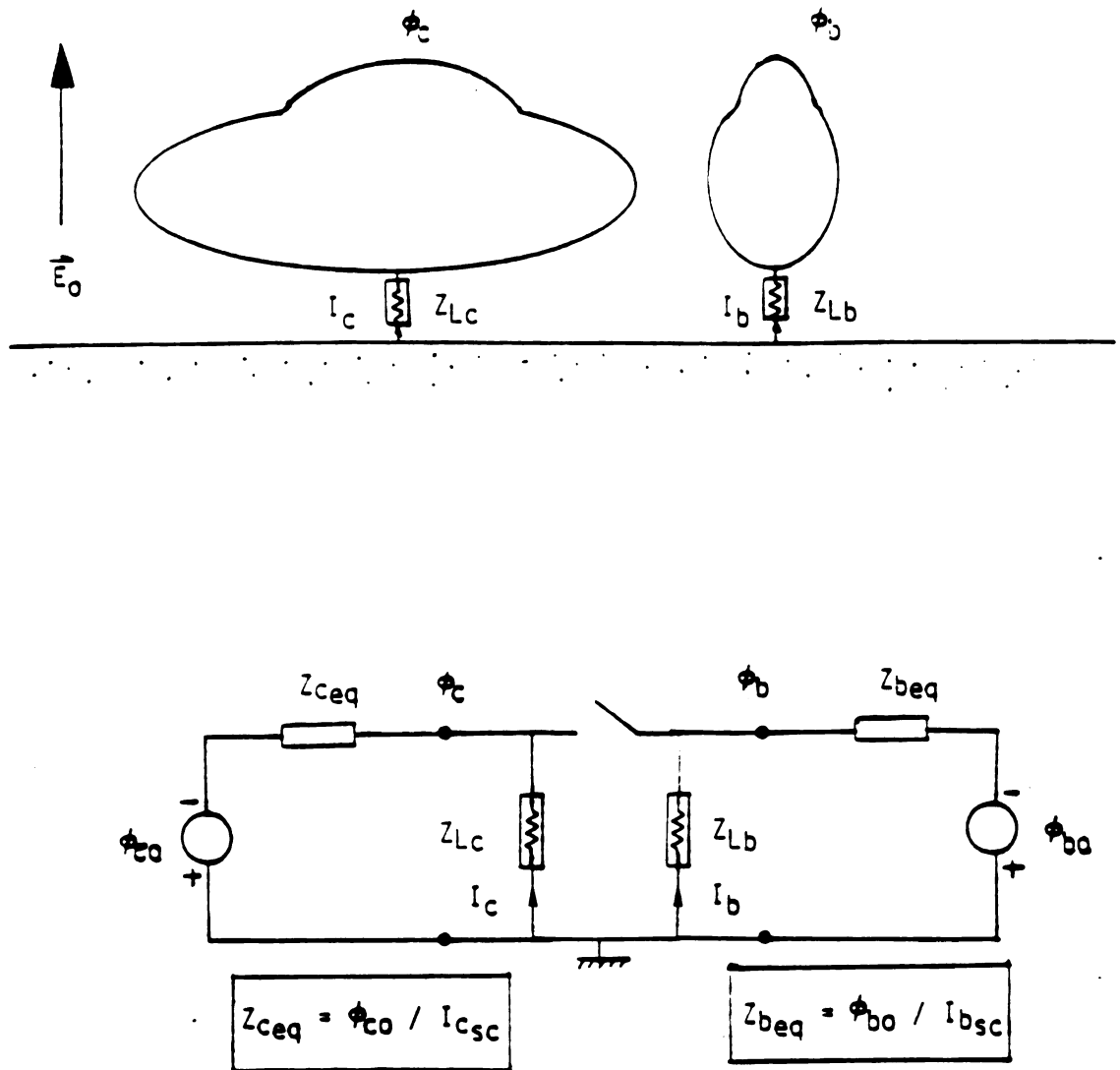
Fig. 6.3. A biological body b and a nearby metallic object c standing on the ground with grounding impedances Z_{Lb} and Z_{Lc}, respectively, are both exposed to an ELF electric field. The circuit shown in the figure is the Thevenin equivalent circuit for the whole system.

S_c — surface area of the metallic object c

S_c^i — surface area of the image of the metallic object c

ϕ_b — body potential of the biological body b

ϕ_c — body potential of the metallic object c

I_b — current flowing through the impedance Z_{Lb}

I_c — current flowing through the impedance Z_{Lc}

$\phi_{bo}(\vec{r}_b)$ — impressed potential on the bilogical body b maintained by the incident electric field

$\hspace{1cm}$ = $-E_o z_b$

$\phi_{co}(\vec{r}_c)$ — impressed potential on the metallic object c maintained by the incident electric field

$\hspace{1cm}$ = $-E_o z_c$

and

$$\vec{r}_b = (x_b, \ y_b, \ z_b)$$

$$\vec{r}_c = (x_c, \ y_c, \ z_c)$$

By using the Moment Method, the body surface S_b and the object surface S_c are partitioned into N and K patches, respectively. Let $P_b(\vec{r}_{bn})$ be the central point of the ΔS_n^b patch on the body b and $P_c(\vec{r}_{cn})$ be that of the ΔS_n^c patch on the object c, the induced surface charge density on each patch is assumed to be a constant and represented by η_n^b (for the patch ΔS_n^b) and

η_n^c (for the patch ΔS_n^c). Eqs. (6.1a) - (6.1d) can then be transformed

into a $(N + K + 2) \times (N + K + 2)$ matrix equation

$$
\begin{bmatrix}
M_{11}^{bb} & M_{12}^{bb} & \cdots & M_{1N}^{bb} & -1 & M_{11}^{bc} & M_{12}^{bc} & \cdots & M_{1K}^{bc} & 0 \\
M_{21}^{bb} & M_{22}^{bb} & \cdots & M_{2N}^{bb} & -1 & M_{21}^{bc} & M_{22}^{bc} & \cdots & M_{2K}^{bc} & 0 \\
\vdots & \vdots & & \vdots & \vdots & \vdots & \vdots & & \vdots & \vdots \\
M_{N1}^{bb} & M_{N2}^{bb} & \cdots & M_{NN}^{bb} & -1 & M_{N1}^{bc} & M_{N2}^{bc} & \cdots & M_{NK}^{bc} & 0 \\
\Delta S_1^b & \Delta S_2^b & \cdots & \Delta S_N^b & -1/(j\omega Z_{Lb}) & 0 & 0 & \cdots & 0 & 0 \\
M_{11}^{cb} & M_{12}^{cb} & \cdots & M_{1N}^{cb} & 0 & M_{11}^{cc} & M_{12}^{cc} & \cdots & M_{1K}^{cc} & -1 \\
M_{21}^{cb} & M_{22}^{cb} & \cdots & M_{2N}^{cb} & 0 & M_{21}^{cc} & M_{22}^{cc} & \cdots & M_{2K}^{cc} & -1 \\
\vdots & \vdots & & \vdots & \vdots & \vdots & \vdots & & \vdots & \vdots \\
M_{K1}^{cb} & M_{K2}^{cb} & \cdots & M_{KN}^{cb} & 0 & M_{K1}^{cc} & M_{K2}^{cc} & \cdots & M_{KK}^{cc} & -1 \\
0 & 0 & \cdots & 0 & 0 & \Delta S_1^c & \Delta S_2^c & \cdots & \Delta S_K^c & -1/(j\omega Z_{Lc})
\end{bmatrix}
\begin{bmatrix}
\eta_1^b \\ \eta_2^b \\ \vdots \\ \eta_N^b \\ \phi_b \\ \eta_1^c \\ \eta_2^c \\ \vdots \\ \eta_K^c \\ \phi_c
\end{bmatrix}
=
\begin{bmatrix}
\phi_{o1}^b \\ \phi_{o2}^b \\ \vdots \\ \phi_{oN}^b \\ 0 \\ \phi_{o1}^c \\ \phi_{o2}^c \\ \vdots \\ \phi_{oK}^c \\ 0
\end{bmatrix}
$$

where $\hspace{8cm}$ (6.2)

$$
M_{mn}^{bb} = \frac{1}{4\pi\epsilon_o} \Delta S_n^b \left\{ \frac{1}{|\vec{r}_{bm} - \vec{r}_{bn}|} - \frac{1}{|\vec{r}_{bm} - \vec{r}_{bn}^i|} \right\}
$$

$$M_{mn}^{bc} = \frac{1}{4\pi\epsilon_o} \Delta S_n^c \left\{ \frac{1}{|\vec{r}_{bm} - \vec{r}_{cn}|} - \frac{1}{|\vec{r}_{bm} - \vec{r}_{cn}^i|} \right\}$$

$$M_{mn}^{cb} = \frac{1}{4\pi\epsilon_o} \Delta S_n^b \left\{ \frac{1}{|\vec{r}_{cm} - \vec{r}_{bn}|} - \frac{1}{|\vec{r}_{cm} - \vec{r}_{bn}^i|} \right\}$$

$$M_{mn}^{cc} = \frac{1}{4\pi\epsilon_o} \Delta S_n^c \left\{ \frac{1}{|\vec{r}_{cm} - \vec{r}_{cn}|} - \frac{1}{|\vec{r}_{cm} - \vec{r}_{cn}^i|} \right\}$$

for $m \neq n$

$$M_{mm}^{bb} = \frac{1}{4\pi\epsilon_o} \Delta S_m^b \left\{ \frac{2\sqrt{\pi}}{(\Delta S_m^b)^{1/2}} - \frac{1}{|\vec{r}_{bm} - \vec{r}_{bn}^i|} \right\}$$

$$M_{mm}^{bc} = \frac{1}{4\pi\epsilon_o} \Delta S_m^c \left\{ \frac{1}{|\vec{r}_{bm} - \vec{r}_{cm}|} - \frac{1}{|\vec{r}_{bm} - \vec{r}_{cm}^i|} \right\}$$

$$M_{mm}^{cb} = \frac{1}{4\pi\epsilon_o} \Delta S_m^b \left\{ \frac{1}{|\vec{r}_{cm} - \vec{r}_{bm}|} - \frac{1}{|\vec{r}_{cm} - \vec{r}_{bm}^i|} \right\}$$

$$M_{mm}^{cc} = \frac{1}{4\pi\epsilon_o} \Delta S_m^c \left\{ \frac{2\sqrt{\pi}}{(\Delta S_m^c)^{1/2}} - \frac{1}{|\vec{r}_{cm} - \vec{r}_{cm}^i|} \right\}$$

for $m = n$

and

$$\phi_n^b = -E_o z_{bn} \quad ; \quad \vec{r}_{bn} = (x_{bn}, \ y_{bn}, \ z_{bn})$$

$$\phi_n^c = -E_o z_{cn} \quad ; \quad \vec{r}_{cn} = (x_{cn}, \ y_{cn}, \ z_{cn})$$

The $(N + K + 2)$ unknowns, $(\eta_1^b \ \dots \ \eta_N^b, \ \phi_b)$ and $(\eta_1^c \ \dots \ \eta_K^c, \ \phi_c)$, can be determined from this matrix equation.

6.2.2 Numerical Examples

To analyze the shock current between a human body and a nearby vehicle both exposed to the electric field of a 60-Hz EHV power line, a Plymouth automobile (L × W × H = 5.43 × 1.98 × 1.32 m) has been chosen for study. Fig. 6.4 shows the numerical results of the floating potential and the short-circuit current of the vehicle as functions of the total partitioned patch numbers of the vehicle's metallic surface. The figure also shows the comparison of numerical results on the floating potential and the short-circuit current of the vehicle with the corresponding experimental results [32]. A satisfactory agreement between theory and experiment was obtained. Next, to observe the coupling effect between a human body and a vehicle at proximity, a man (180 cm in height) and a Plymouth automobile on the same ground and both exposed to a 1 kV/m, 60-Hz electric field as shown in Fig. 6.5, are studied. The capacitance of the vehicle tires is assumed to have a value of 500 pF ($\approx -j5.3$ MΩ at the frequency of 60-Hz), and the grounding impedance of the man is assumed to be infinity (floating). The floating potential ϕ_{bo} of the body and the
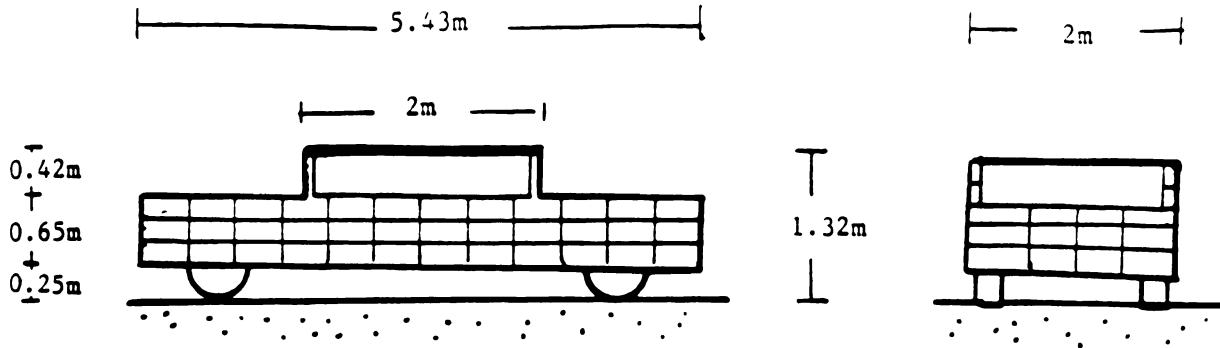
PLYMOUTH (L x W x H) - 5.43 x 1.98 x 1.32 (m)

	MEASUREMENT	PRESENT METHOD (190 patches)
ϕ_{co}	367 V/(kV/m)	428 V/(kV/m)
I_{csc}	.093 mA/kV/m	.108 mA/kV/m
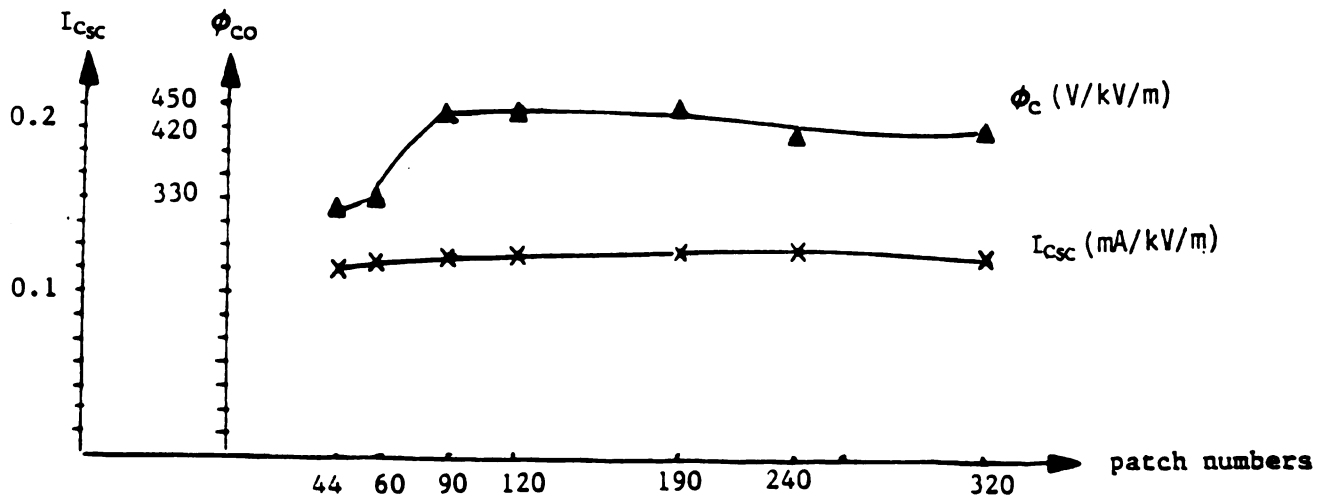
Fig. 6.4. Comparison of numerical results by the present method with experimental measurements by Reilly on the floating potential and the short-circuit current of a Plymouth automobile. Also shown are the convergences of numerical values for ϕ_{co} and I_{csc} with respect to the partitioned patch number on the vehicle's metallic surface.
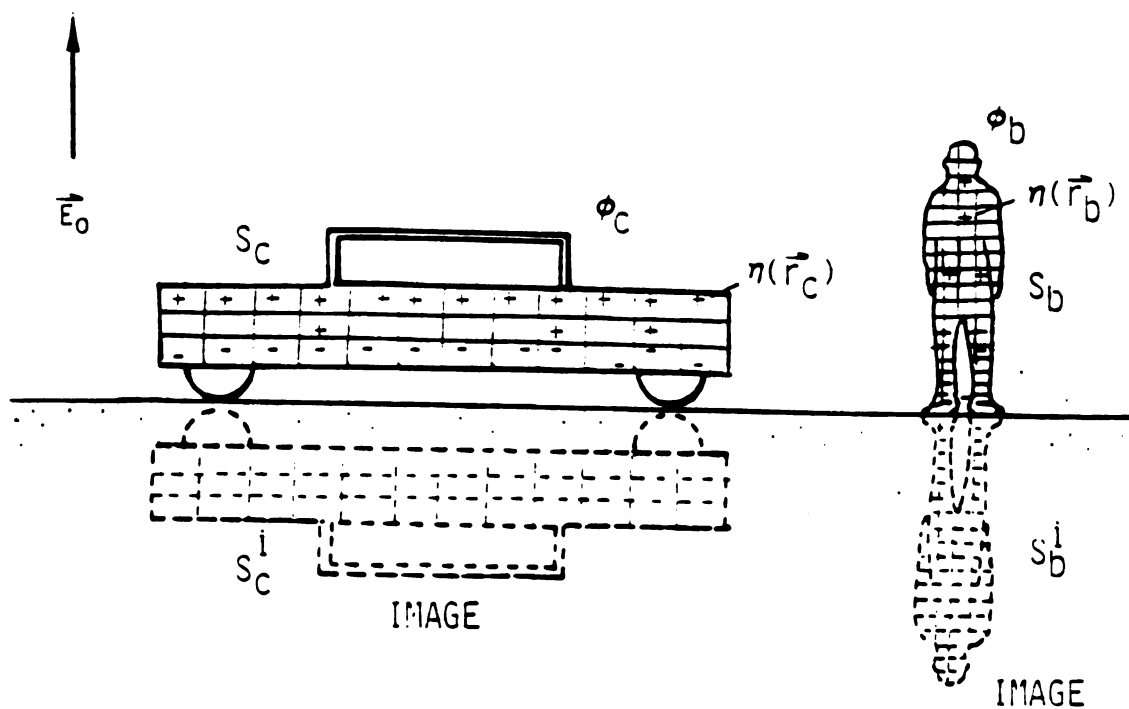
Fig. 6.5. A man and a vehicle (Plymouth) standing on the ground are both exposed to an ELF electric field.

car potential ϕ_c are calculated as functions of the separation D between the body and the vehicle, and the results are shown in Fig. 6.6(a). The short-circuit current I_{bsc} of the body and the current I_c of the vehicle flowing through the tires to the ground, used in the previous example, are calculated as functions of the separation D with results shown in Fig. 6.6(b). It is noted to calculate I_{bsc}, the grounding impedance of the man is set to zero (short-circuited to the ground). It can be observed that, as the distance between the man and the vehicle is deduced the body and vehicle potentials and the currents of both objects flowing to the ground decrease, which indicate an increasing coupling effect. The physical explanation for the decrease of the potentials and currents due to the coupling effect is the following. The scattered electric field from one object tends to cancel the original electric field which illuminates the other object, as depicted in Fig. 6.7. This effect reduces the strength of the net incident field to the body and hence reduces the body and vehicle potentials and the currents of both objects. It is also observed that the coupling has less effect on the vehicle than on the man since the physical dimension of the vehicle is much larger than that of the man.

The coupling effect between a car and a grounded man can be calculated the same way. Fig. 6.8(a) depicts the floating potential ϕ_{co} of the car (the car is floating) and Fig. 6.8(b) shows the short-circuit currents I_{csc} of the car (the car is short circuited to the ground), all as functions of the separation distance D between the vehicle and the grounded man. The coupling effect which slightly reduces the floating potential and the short-circuit current of the vehicle is again observed.
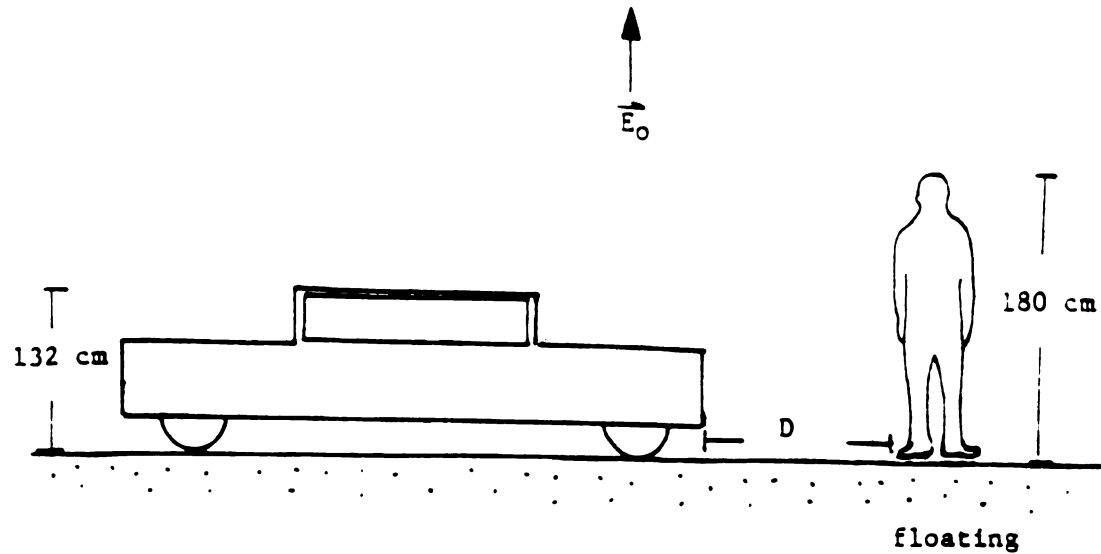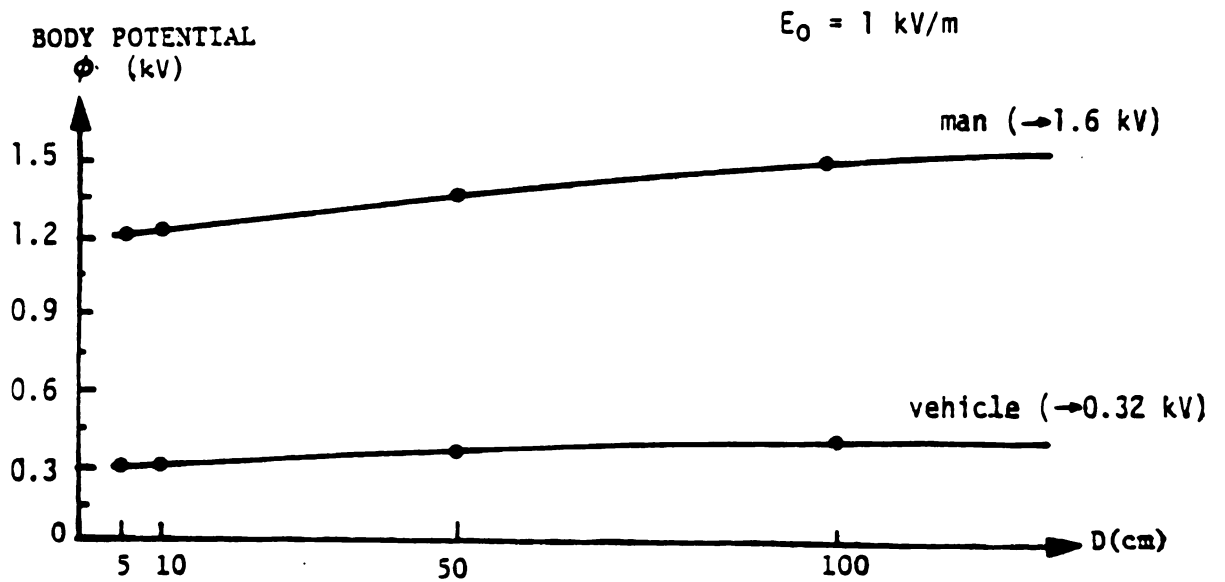
Fig. 6.6.(a)   The floating potential of a man and the vehicle (Plymouth)
              potential (with tires) as functions of their separation distance.
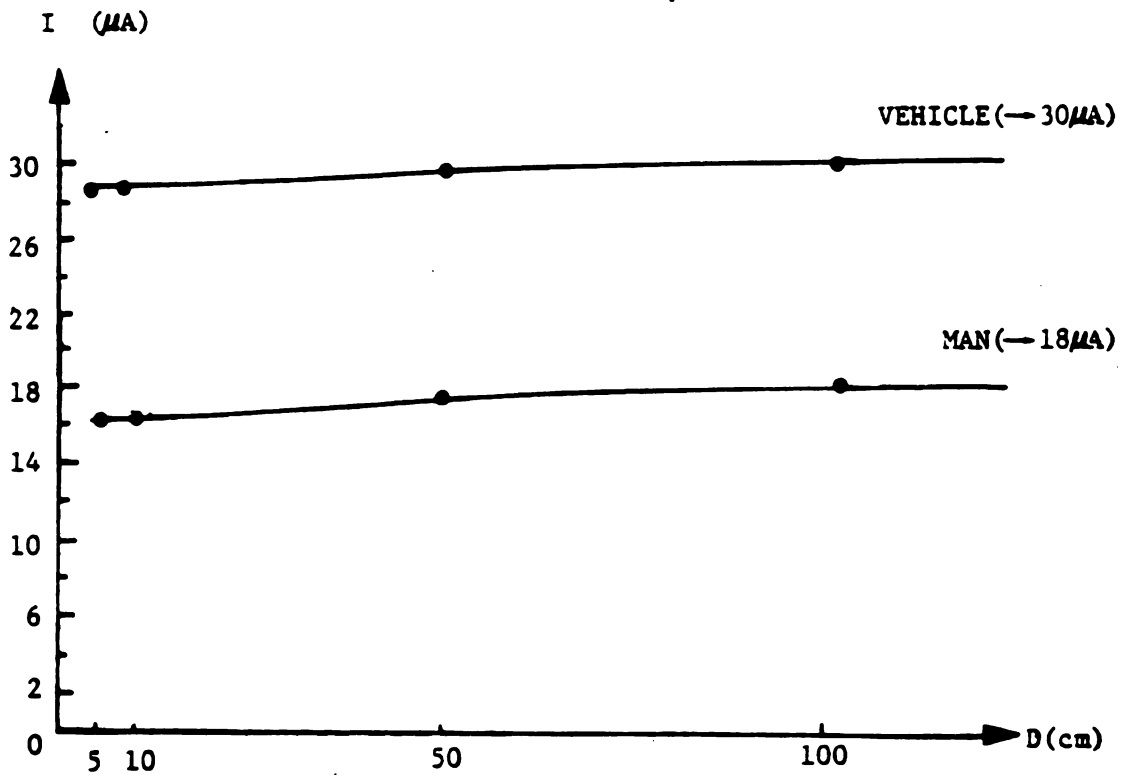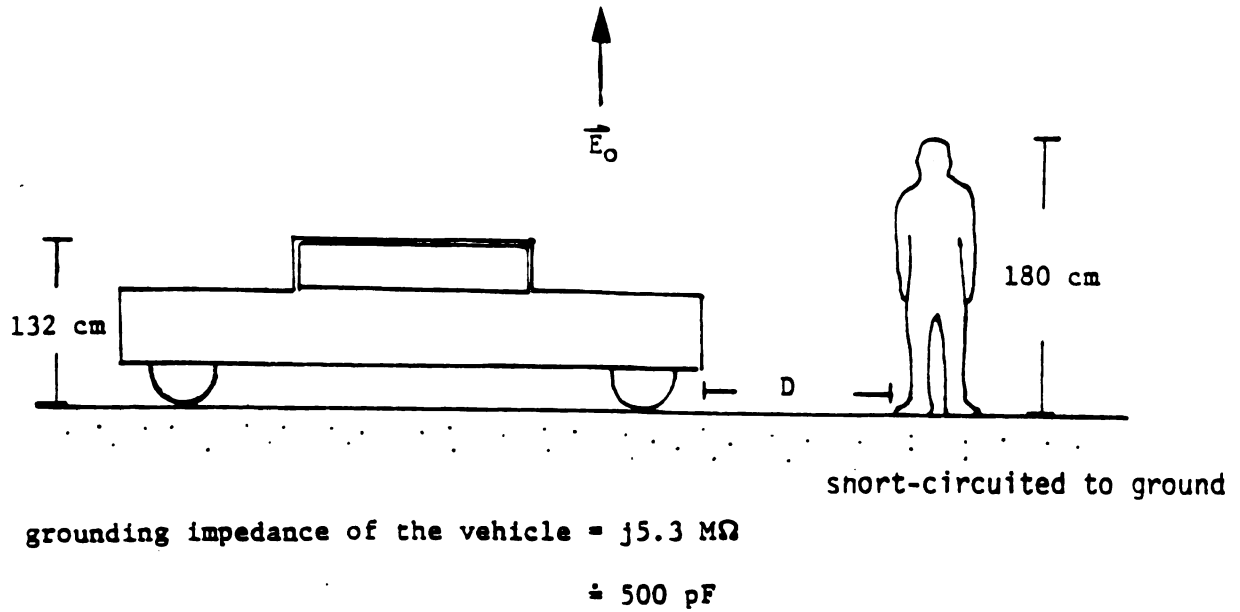
Fig. 6.6.(b)   The short-circuit current of a man and the current flowing
               between a vehicle (Plymouth) and the ground as functions of their
               separation distance.
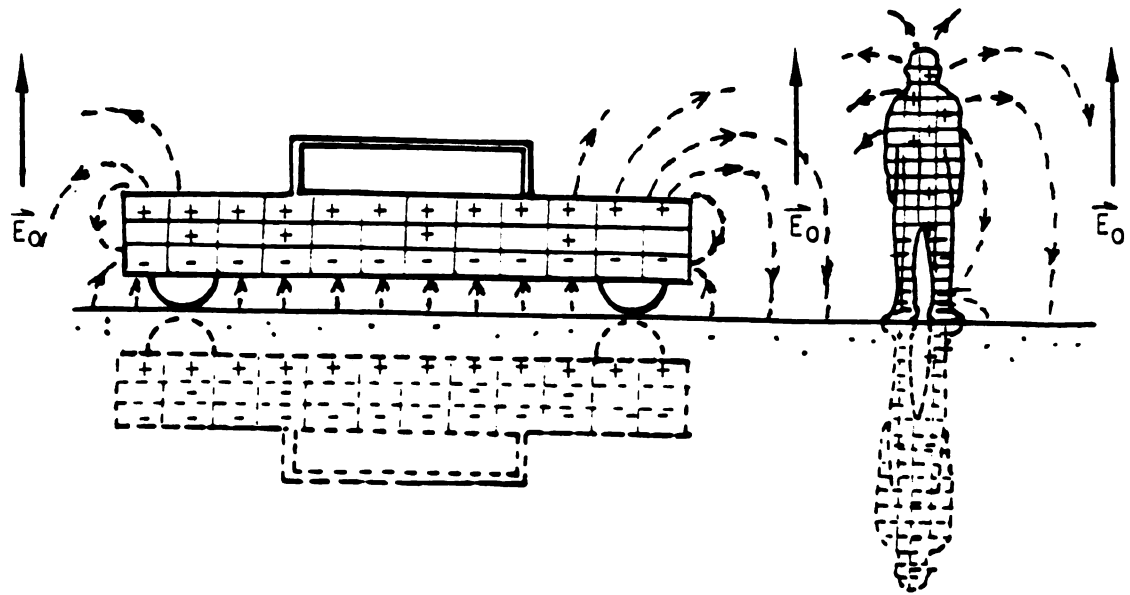
---- SCATTERED ELECTRIC FIELD

Fig. 6.7.   Scattered electric fields maintained by induced surface charges
           on the surface of a man and a vehicle.
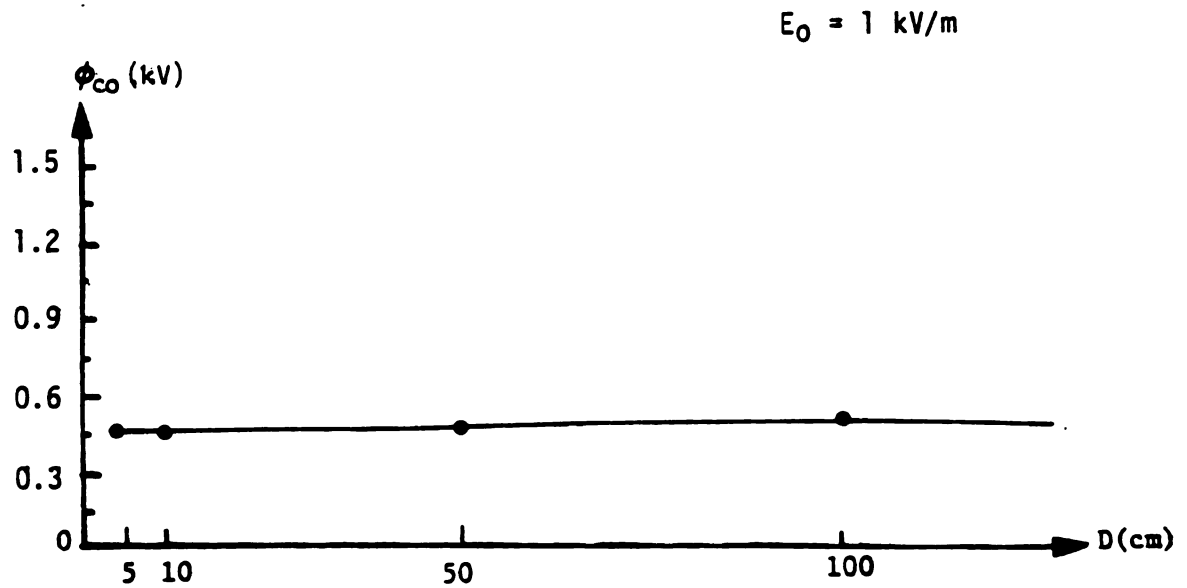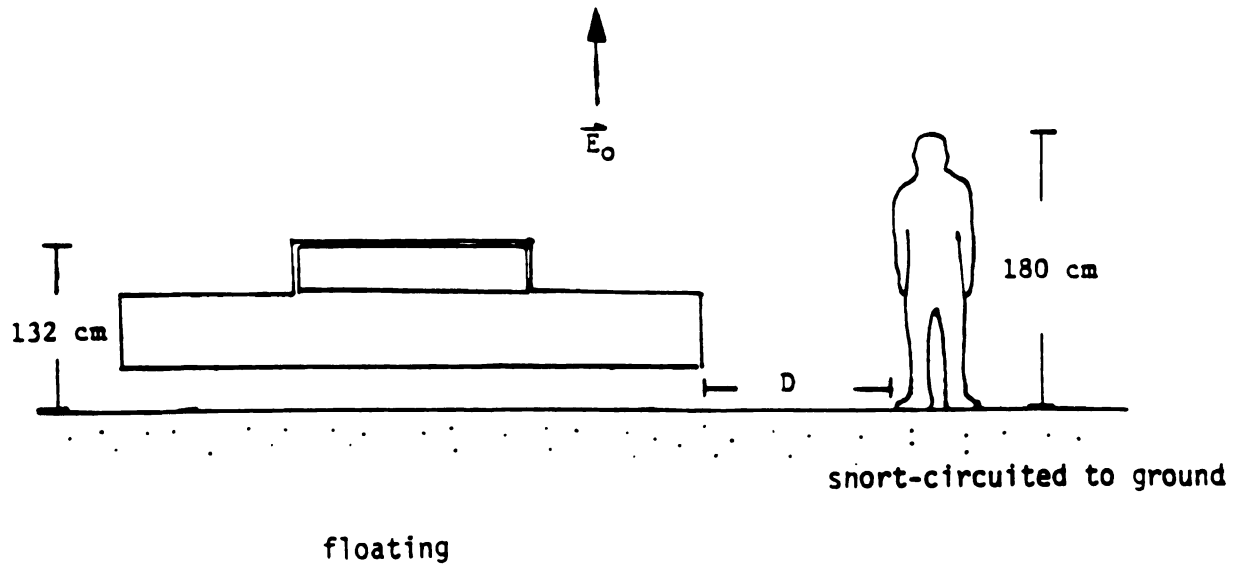
Fig. 6.8(a) The floating potential of a vehicle (Plymouth) as functions of the separation distance between the vehicle and a grounded man.
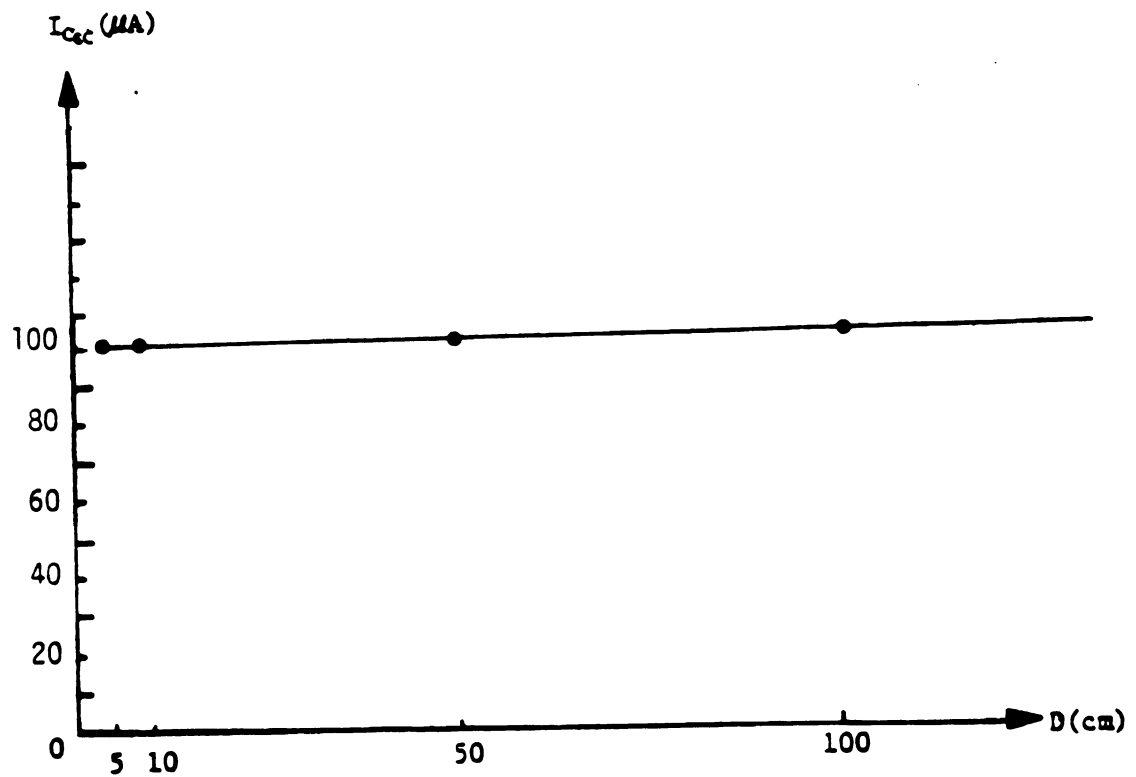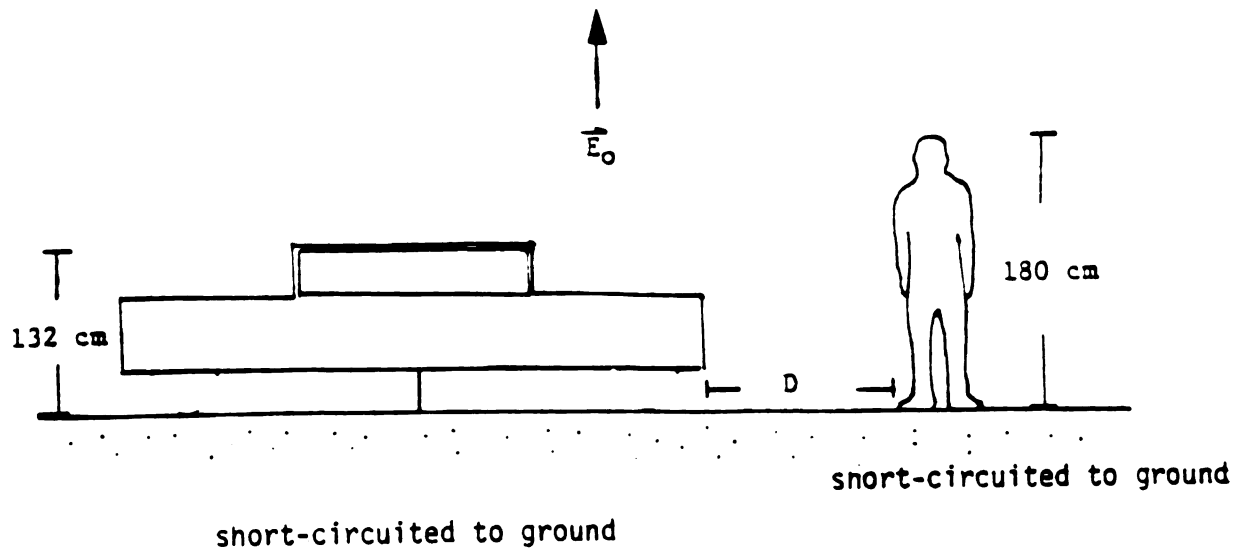
Fig. 6.8(b)   The short-circuit current of a vehicle (Plymouth) as functions
              of the separation distance between the vehicle and a grounded man.

6.2.3 Equivalent Circuits for a Grounded Man and a Vehicle at Proximity

After the open-circuit voltages (floating potentials) and the short-circuit currents of the man and the vehicle (a Plymouth automobile) at proximity have been determined (by coupled SCIE method), an equivalent circuit for the whole system (the grounded man and the vehicle at proximity) can then be constructed as shown in Fig. 6.9. Note that the equivalent capacitance of the man (C_b) and that of the vehicle (C_c) with respect to the system are determined as follows:

$$Z_{b_{eq}} = 1/j\omega C_b = \phi_{bo}/I_{bsc} \bigg|_{\text{(with a vehicle at proximity)}}$$

$$(6.3)$$

$$Z_{c_{eq}} = 1/j\omega C_c = \phi_{co}/I_{csc} \bigg|_{\text{(with a grounded man at proximity)}}$$

where ϕ_{bo} (ϕ_{co}) and I_{bsc} (I_{csc}) are the floating potential and the short-circuit current of the man (the vehicle). In Fig. 6.9, C_t is the capacitance of the vehicle's tires, and a contact resistance (or spark resistance) R_g as well as a human body resistance R_b are added to the equivalent circuit to simulate a realistic environment and an appropriate internal resistance of the human body. The internal body resistance is composed of tissues, organs, and body fluids (i.e., blood, urine, bile) and can be appreciably altered by several variables, such as moisture, the skin intactness, physical constitution of the individual (e.g., fat, muscularity, fatigue), and area of contact [33]. Fig. 6.10, Table 6.1 and Fig. 6.11 show some information about the estimated body impedance and internal resistance of the human body [33]. The time-dependent behavior of the shock current between the man and the vehicle can then be determined from a transient analysis of this equivalent circuit.
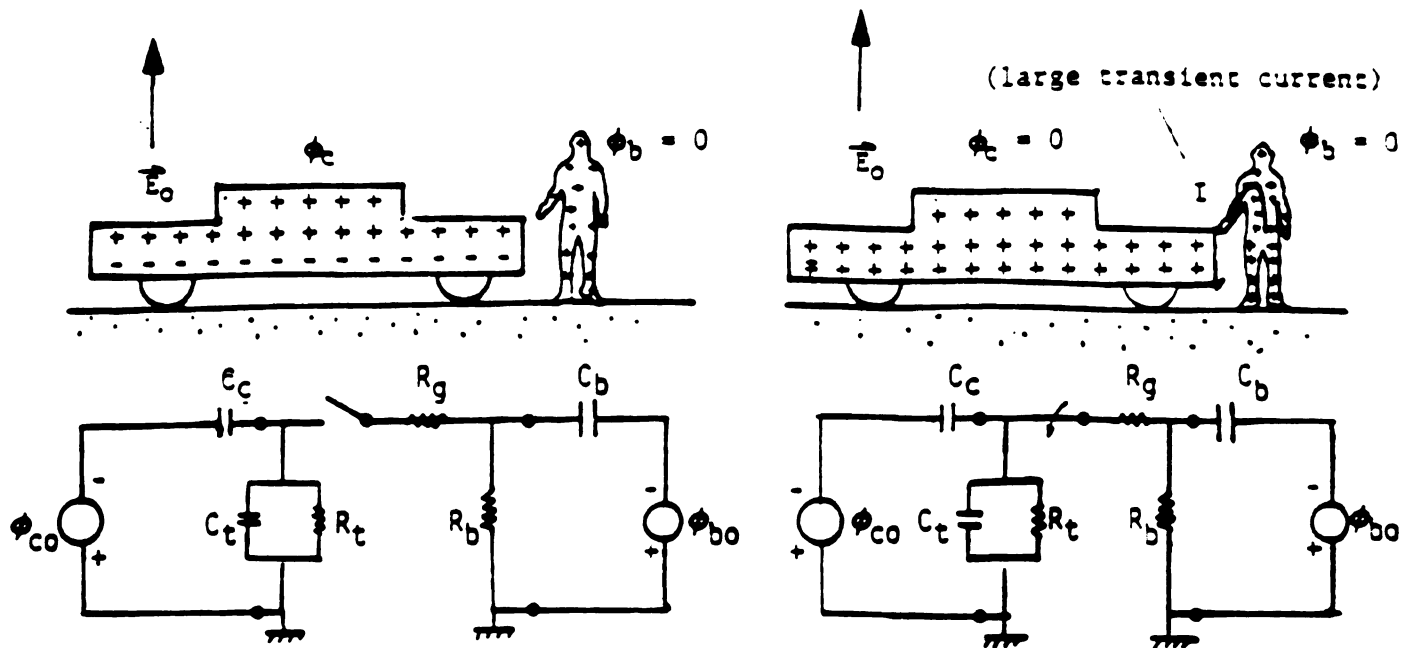
$$E_0 = 1 \text{ kV/m}$$

ϕ_{co} = open-circuit voltage of the car (0.407 kV)

$I_{c_{sc}}$ = short-circuit current of the car (101 μA)

C_c = capacitance of the car with respect to the system (670 pF)

C_t = capacitance of the tires (470 pF)

R_t = resistance of the tires ($\gg Z_{C_t}$)

ϕ_{bo} = open-circuit voltage of the human body (1.2 kV)

$I_{b_{sc}}$ = short-circuit current of the human body (15.5 μA)

R_g = contact resistance or spark resistance between the human body & the car

C_b = capacitance of the human body with respect to the system (35 pF)

R_b = human body resistance

Fig. 6.9. Equivalent circuits of a grounded man (180 cm in height) and a vehicle (Plymouth) at proximity, under the exposure of a 1kV/m, 60-Hz electric field.
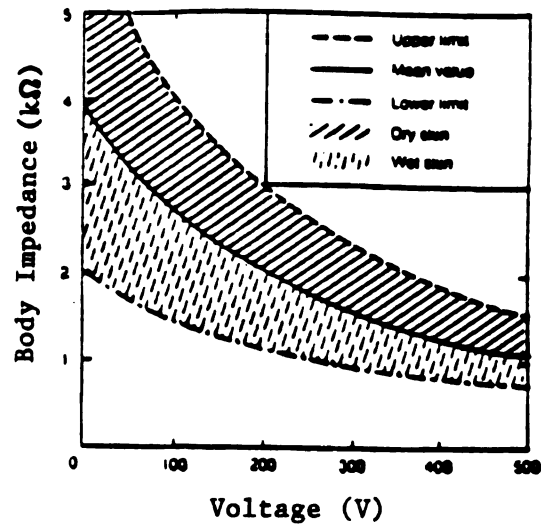
Fig. 6.10. Relation between body impedance and voltage [33].

Subject	Hands-To-Feet		Right Hand-to-Feet	
	Dry	Wet	Dry	Wet
Adult (n°=40)				
Maximum	13,300	1,280		1,950
Minimum	1,500	810		820
Average	4,838	865	N.A.°°	1,231
Child (n°=47)				
Maximum	35,000	4,290	35,450	5,700
Minimum	1,810	860	1,900	1,270
Average	6,046	1,443	7,800	2,815

°n = number of subjects tested
°°N.A. = not available

Table 6.1. Body resistance of adult and child in ohms [33].
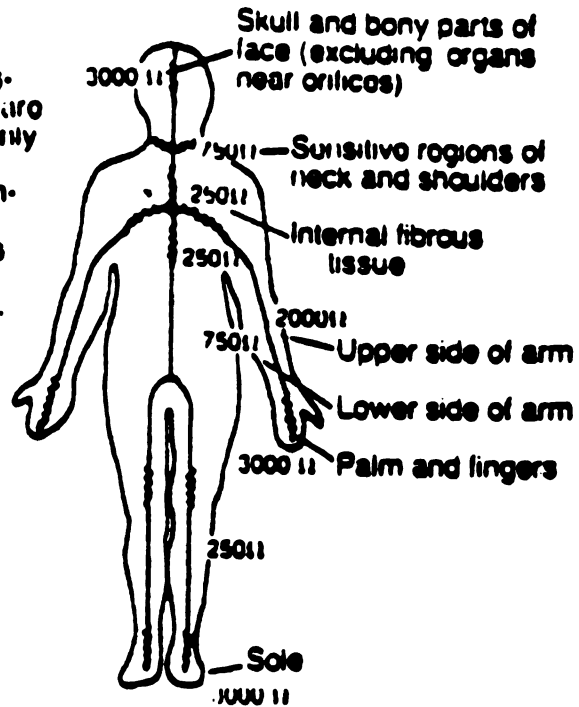
Fig. 6.11. Internal resistance of the human body [33].

6.3 Transient Analysis of the Shock Current

The experiment by Reilly [32] for measuring the spark discharge
current is illustrated in Fig. 6.12. The vehicle was a Plymouth and the
human body was replaced by a load resistor R_d. The experimental set-up
was exposed to the electric field of a 60-Hz, 500 kV transmission line.
The electric field was approximately 4.5 kV/m. In order to compare
theoretical results of the present method with experimental results,
the equivalent circuit for the human body in Fig. 6.9 is replaced by a
resistor R_d as shown in Fig. 6.13. Since the open-circuit voltage is
0.428 kV for the incident field E_o - 1 kV/m, it is 1.926 kV when E_o -
4.5 kV/m. Hence, $\phi_{co}(t)$ in the Fig. 6.13 can be expressed as

$$\phi_{co}(t) - \phi_{cm}e^{j\omega t}, \qquad \omega - 2\pi \times 60 \tag{6.4}$$

where ϕ_{cm} - 1.926 kV. When the switch in the equivalent circuit is open
(t < 0), the voltage across the capacitor C_t is

$$\phi_1(t) - \phi_{cm} \frac{Z_{Ct}}{Z_{Cc} + Z_{Ct}} e^{j\omega t} \tag{6.5}$$

where

$$Z_{Cc} - 1/j\omega C_c \quad ; \quad Z_{Ct} - 1/j\omega C_t$$

After the switch is closed (t > 0), the time response of the current
$I_{sh}(t)$ flowing through the resistor R_d can be obtained from the circuit
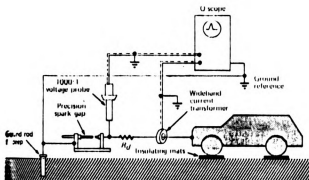
Current and voltage measurement system
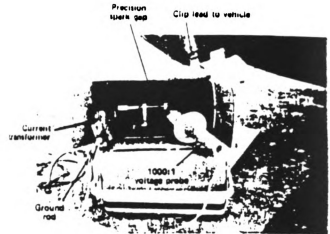
Spark instrumentation
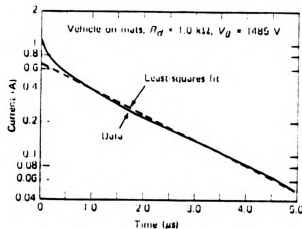
Measured transient current for a Plymouth automobile

Fig. 6.12. Reilly's [32] experimental set-up and measured transient current for a Plymouth automobile which was exposed to a 4.5 kV/m, 60-Hz electric field.

$$\vec{E}_0$$

C_c

ϕ_{co}

C_t

R_d
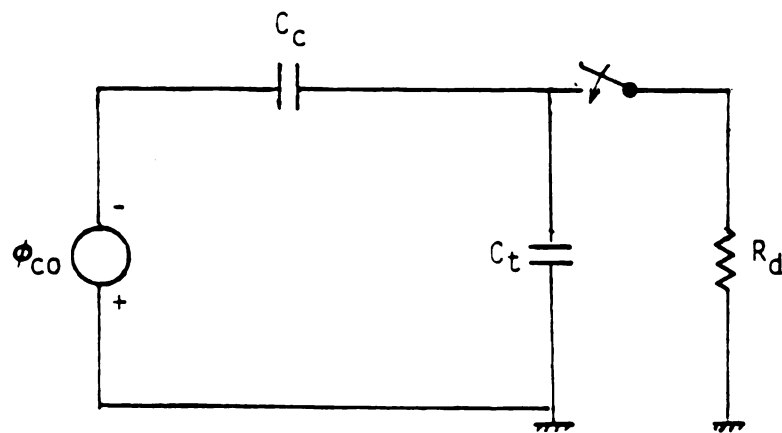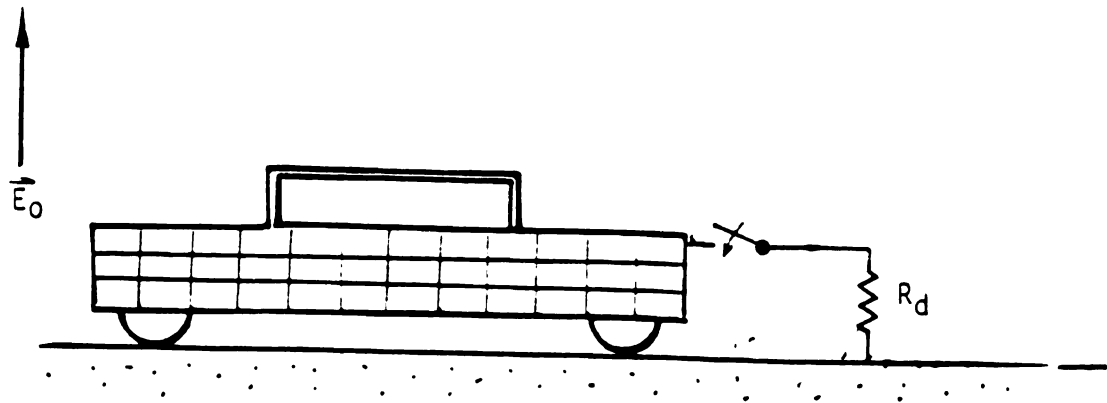
(R_t is neglected since $R_t \gg Z_{C_t}$)

Fig. 6.13. An equivalent circuit for a vehicle and a grounding resistance R_d under the exposure of a 4.5 kV/m, 60-Hz electric field.

analysis as

$$I_{sh}(t) = k_0 \exp[-t/(C_c + C_t)R_d] + Re(I_m e^{j\omega t}) \qquad (6.6)$$

where

$k_0 =$ a constant to be determined

$$I_m = [\phi_{cm} \times (Z_{Ct}// R_d)/(Z_{Cc} + (Z_{Ct}// R_d))]/R_d$$

and

$$Z_{Ct}// R_d = (Z_{Ct} \times R_d)/(Z_{Ct} + R_d)$$

The first term of the R.H.S. in Eq. (6.6) is due to discharges of the capacitor C_c and C_t, while the second term is the steady-state current response due to the voltage source $\phi_{co}(t)$. The constant k_0 can be determined by using the initial condition $\phi_1(0)$ of Eq. (6.5) which is,

$$Re[\phi_1(0)]/R_d = Re[\phi_{cm} \frac{Z_{Ct}}{(Z_{Ct} + Z_{Cc})}]/R_d = I_{sh}(0) = k_0 + Re(I_m) \quad (6.7)$$

hence

$$k_0 = Re[\frac{\phi_{cm} \times Z_{Ct}}{(Z_{Ct} + Z_{Cc})R_d}] - Re(I_m)$$

Fig. 6.14 shows the current $I_{sh}(t)$ flowing through the resistor R_d for the case of $R_d = 1.0$ KΩ and $R_d = 1.6$ KΩ as functions of the time. Experimental
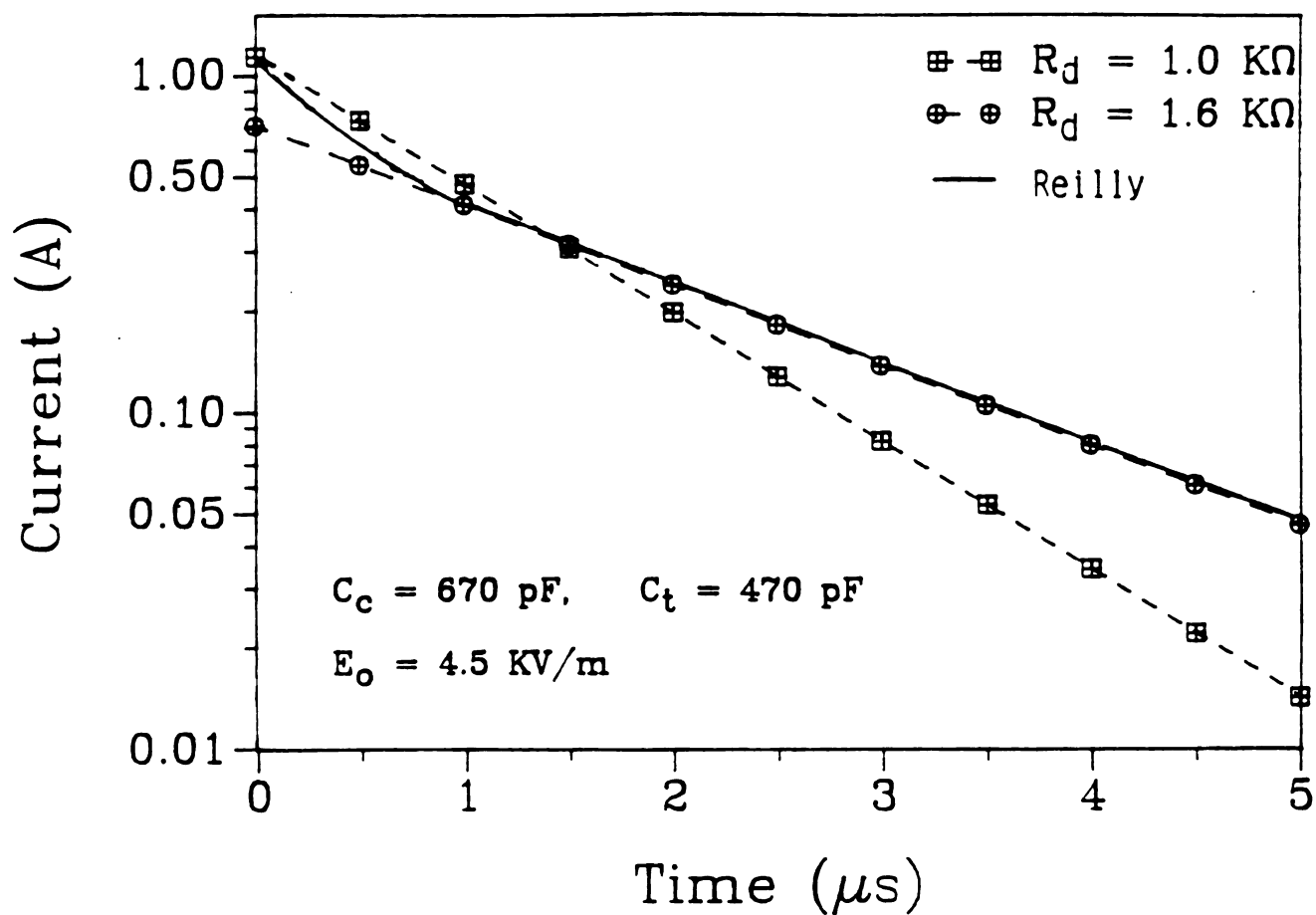
Fig. 6.14. Comparison of numerical results by the present method (dash
lines) with experimental results of Reilly [32] on the transient
shock current between a vehicle (Plymouth) and a grounding
resistance, both exposed to a 4.5 kV/m, 60-Hz electric field.

results by Reilly [32] are also shown in Fig. 6.14 for comparison. It is observed that instead of a straight line in the figure 6.14 (logarithmic scale) as predicted by the present method, Reilly's measured result is a slight curve. If the load is purely resistive, the transient current should be exponentially decreasing and hence it should be a straight line in the logarithmic scale. Reilly's explanation to the curve of his measurement is that there may be some resistance and capacitance in the circuit loop of the experimental set-up. It is noted that when R_d = 1.0 KΩ the present method obtains the same initial value of the current as the experiment, while for R_d = 1.6 KΩ the data line of the present method has the same slope as the curve of the experiment after t > 0.5 μs.

To investigate the realistic situation of the shock current between a vehicle and a grounded human body, the equivalent circuits in Fig. 6.9 should be adopted and analyzed. Since ϕ_{co} = 0.407 kV and ϕ_{bo} = 1.2 kV for E_o = 1 kV, when E_o = 4.5 kV ϕ_{co} and ϕ_{bo} can be expressed as

$$\phi_{co}(t) = \phi_{cm}e^{j\omega t}, \qquad \phi_{cm} = 1.832 \text{ kV}$$

$$\phi_{bo}(t) = \phi_{bm}e^{j\omega t}, \qquad \phi_{bm} = 5.400 \text{ kV}$$

(6.8)

where

$$\omega = 2\pi \times 60$$

Before the spark contact between the vehicle and the human body (the switch in the equivalent circuits of Fig. 6.9 is open for t < 0), the voltages across the capacitor C_t ($\phi_1(t)$), the resistor R_b ($\phi_2(t)$), and the capacitor C_b ($\phi_3(t)$) are

$$\phi_1(t) = \phi_{cm}[Z_{Ct}/(Z_{Ct} + Z_{Cc})]e^{j\omega t}$$

$$\phi_2(t) = \phi_{bm}[R_b/(R_b + Z_{Cb})]e^{j\omega t} \tag{6.9}$$

$$\phi_3(t) = \phi_{bm}[Z_{Cb}/(R_b + Z_{Cb})]e^{j\omega t}$$

where

$$Z_{Cc} = 1/j\omega C_c \quad , \quad Z_{Ct} = 1/j\omega C_t \quad , \quad Z_{Cb} = 1/j\omega C_b$$

When the spark contact happens (the switch in the equivalent circuits is closed for $t > 0$) the total time response of voltages $\phi_1(t)$ and $\phi_2(t)$ across the capacitor C_t and the resistor R_b are (*APPENDICES 2 & 3*)

$$\mathrm{Re}[\phi_1(t)] = k_3\exp(\alpha_1 t) + k_4\exp(\alpha_2 t) + \mathrm{Re}(\phi_{1m}e^{j\omega t})$$

$$\tag{6.10}$$

$$\mathrm{Re}[\phi_2(t)] = k_1\exp(\alpha_1 t) + k_2\exp(\alpha_2 t) + \mathrm{Re}(\phi_{2m}e^{j\omega t})$$

where the first two terms of RHS in these equations are transient responses due to discharges of capacitors, and third terms are steady-state responses due to voltage sources $\phi_{co}(t)$ and $\phi_{bo}(t)$. In *APPENDIX 2*, ϕ_{1m} and ϕ_{2m} are found as

$$\phi_{1m} = \frac{I_{cm}Y_2 + \phi_{bm}(j\omega C_b/R_g)}{Y_1Y_2 - (1/R_g)^2}$$

(6.11)

$$\phi_{2m} = \frac{\phi_{bm}(j\omega C_b)Y_1 + (I_{cm}/R_g)}{Y_1Y_2 - (1/R_g)^2}$$

where

$$Y_1 = j\omega(C_c + C_t) + 1/R_g$$

$$Y_2 = j\omega C_b + 1/R_b + 1/R_g$$

$$I_{cm} = j\omega C_c \phi_{cm}$$

In *APPENDIX 3*, the constants $k_1 - k_4$ and $\alpha_1 - \alpha_2$ in Eq. (6.10) are found to be

$$\alpha_1 = \frac{-1}{2C_bR_g}[R_g/R_b + C_b/(C_c + C_t) + 1] +$$

$$\left\{[\frac{1}{2C_bR_g}(R_g/R_b + C_b/(C_c + C_t) + 1)]^2 - \frac{1}{C_b(C_c + C_t)R_gR_b}\right\}^{1/2}$$

$$\alpha_2 = \frac{-1}{2C_bR_g}[R_g/R_b + C_b/(C_c + C_t) + 1] -$$

$$\left\{[\frac{1}{2C_bR_g}(R_g/R_b + C_b/(C_c + C_t) + 1)]^2 - \frac{1}{C_b(C_c + C_t)R_gR_b}\right\}^{1/2}$$

and (6.12)

$$k_1 = (Re[\phi_1(0)] - Re[\phi_{1m}])/(C_bR_g\alpha_1 - C_bR_g\alpha_2) +$$

$$Re[\phi_{2m}](1 + R_g/R_b + C_bR_g\alpha_2)/(C_bR_g\alpha_1 - C_bR_g\alpha_2)$$

$$k_2 = -k_1 - Re[\phi_{2m}]$$

$$k_3 = (1 + R_g/R_b + C_bR_g\alpha_1)k_1$$

$$k_4 = (1 + R_g/R_b + C_bR_g\alpha_2)k_2$$

where

$$\phi_1(0) = \phi_{cm} \times [C_c/(C_c + C_t)]$$

and ϕ_{1m} as well as ϕ_{2m} can be found in Eq. (6.11). After $\phi_1(t)$ and $\phi_2(t)$ are determined, the shock current $I_{sh}(t)$ can then be calculated by

$$I_{sh}(t) = \frac{Re[\phi_1(t)] - Re[\phi_2(t)]}{R_g} \qquad (6.13)$$

Fig. 6.15 and 6.16 depict numerical examples of the shock current as the function of the time t for $R_g = 1.5$ KΩ and $R_g = 1.0$ KΩ as well as other values of R_b. It can be observed that when $R_b = 2.0$ KΩ, the present method predicts quite similar curves compared with the data curve of

Reilly's measurements as shown in Fig. 6.15. Specifically, the curve for R_g = 1.0 KΩ and R_b = 2.0 KΩ as shown in Fig. 6.16 has the same initial value and a quite similar shape as that of Reilly's measurements. To further verify numerical data by the present method, it is necessary to to set up an experiment which consists of a realistic human model with a nearby vehicle for measuring the shock-current.

For conclusion, from the above numerical examples, it appears that the shock-current phenomenon can be accurately analyzed if the contact resistance and the internal body resistance are known.
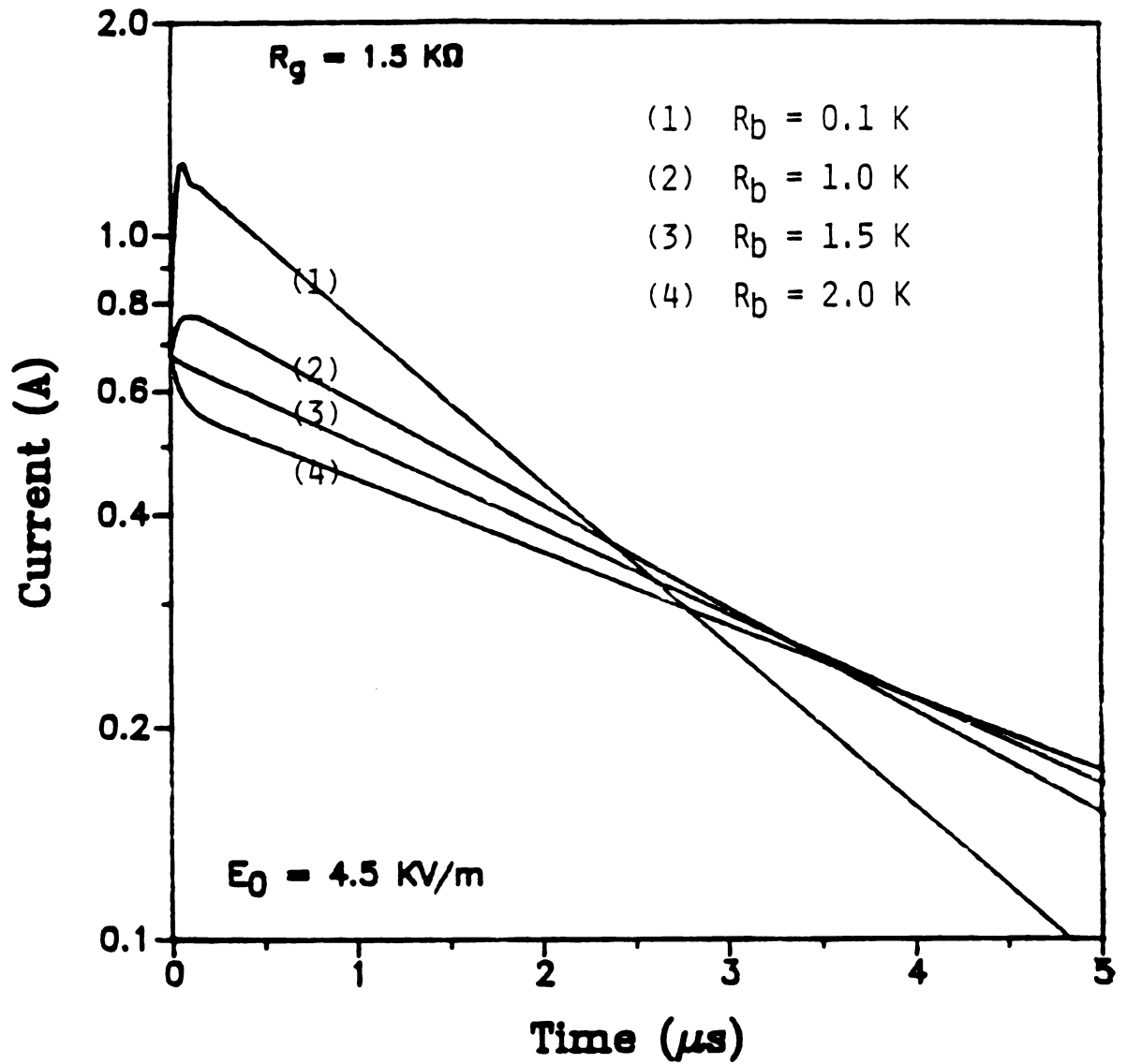
Fig. 6.15. Numerical results by the present method based on the equivalent
circuit of Fig. 6.9 on the transient shock current between a man
(180 cm in height) and a vehicle (Plymouth) at proximity, under
the exposure of a 4.5 kV/m, 60-Hz electric field. The contact
resistance is assumed to be 1.5 kΩ.
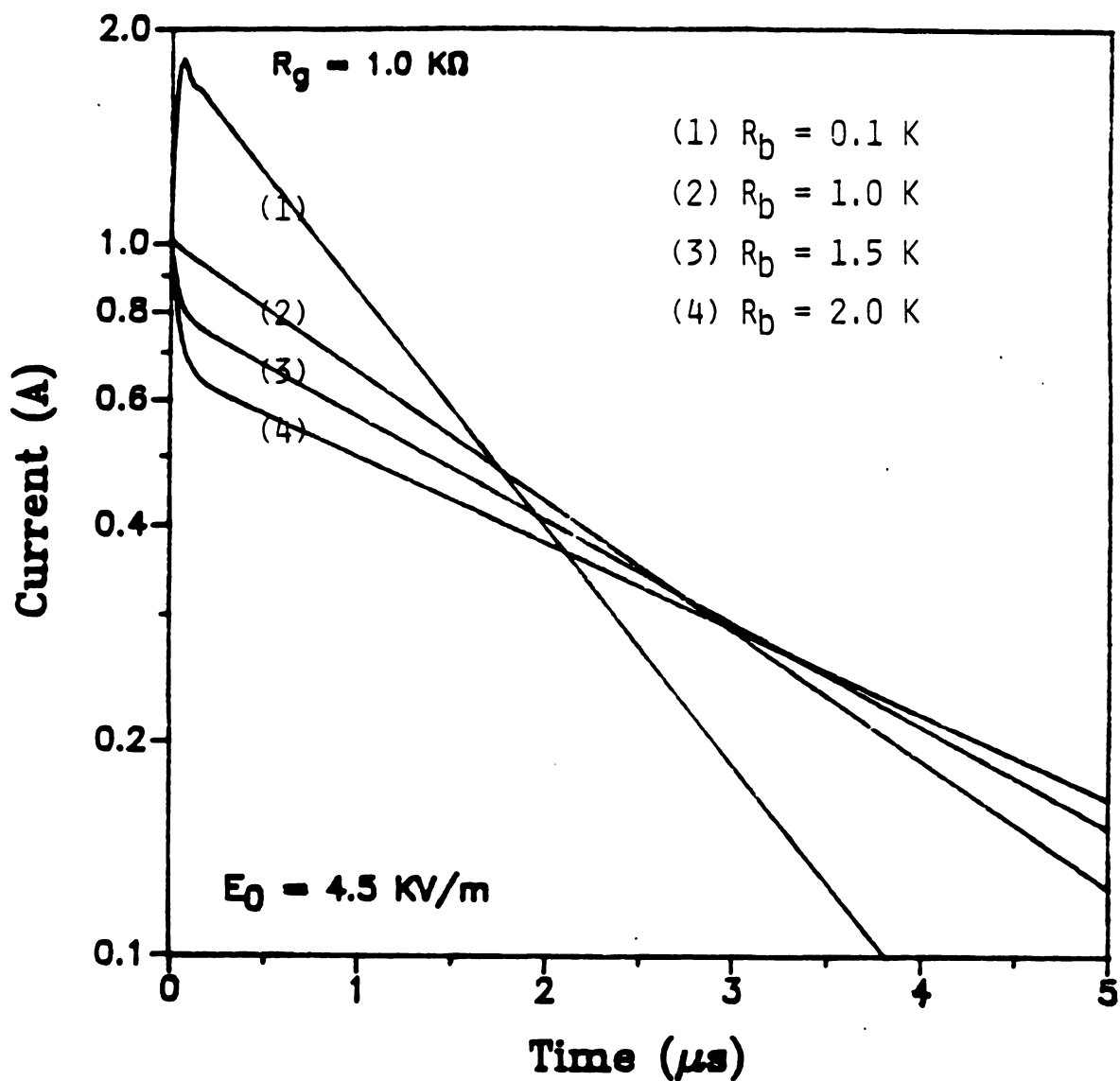
Fig. 6.16. Numerical results by the present method based on the equivalent
circuit of Fig. 6.9 on the transient shock current between a man
(180 cm in height) and a vehicle (Plymouth) at proximity, under
the exposure of a 4.5 kV/m, 60-Hz electric field. The contact
resistance is assumed to be 1.0 kΩ.

CHAPTER 7

CALCULATION OF ELECTRIC CURRENTS INSIDE HETEROGENEOUS BODIES INDUCED BY ELF-LF ELECTRIC FIELDS

7.1 Introduction

In previous chapters, the *surface charge integral equation* (SCIE) method was applied to quantify the interaction of ELF-LF electric fields with homogeneous biological bodies. In this chapter, the SCIE method is combined with an **impedance network method** to treat heterogeneous bodies. A heterogeneous body is modeled as an equivalent impedance network and the induced surface charge is viewed as an equivalent **current source**. With equivalent current sources connected at the outer boundary of the impedance network, the current flowing at any impedance can be determined on the basis of the Kirchhoff's current law. From this current, the induced current density and electric field inside the body can be mapped. To check the validity of this numerical method, a concentric-sphere is chosen as a test case because it has a simple analytical solution at low frequency range. The method can be applied to any heterogeneous biological body when exposed to ELF-LF electric fields.

7.2 Theoretical Development of the Impedance Network Method

Consider a heterogeneous biological body standing on the ground and exposed to an ELF-LF electric field of frequency ω, as shown in Fig. 7.1. The heterogeneous body is partitioned into a number of three dimensional
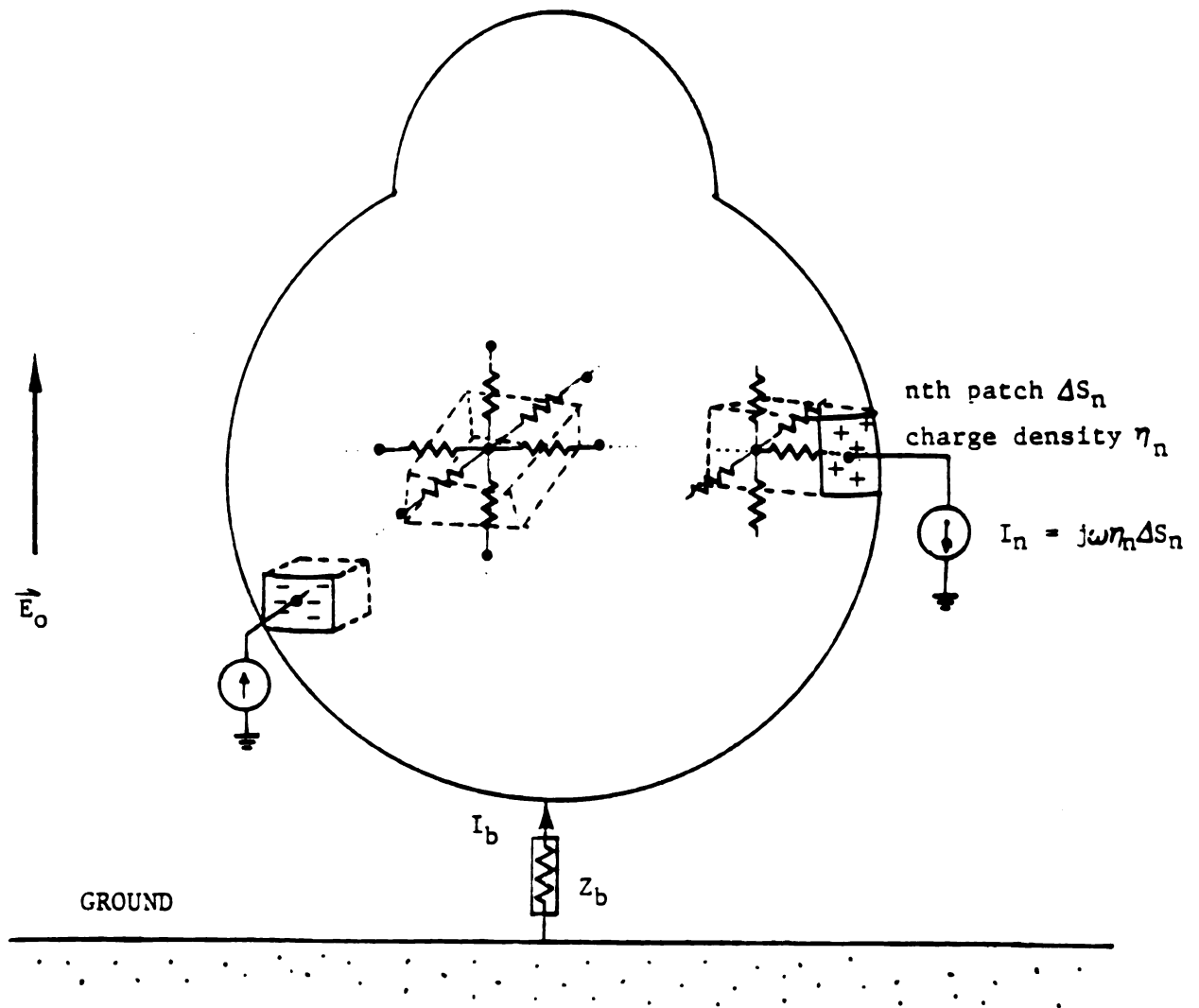
Fig. 7.1. A heterogeneous biological body standing on the ground is exposed to an ELF-LF electric field.

(in u, v, w coordinates) volume cells; each of these cells is homogeneous. To accommodate a current flowing in an arbitrary direction within a volume cell, induced by the impressed electric field, an individual volume cell is represented by three impedances in orthogonal directions determined by the conductivity (σ) and permittivity (ϵ) of that volume cell. These three impedances are connected at a common node located at the center of the cell. The ensemble of volume cells then forms an impedance network, allowing electric currents to flow among these impedances.

On the outer surface of the body, a surface charge distribution is induced by the impressed electric field. This induced surface charge can be determined by the SCIE method as discussed in chapter 2. The induced surface charge can be viewed as the result on a normal component of electric current terminating at the body surface. The continuity equation of electric charge can be used to relate this normal current density to the induced surface charge density. For those volume cells located at the outer layer of the body, there is a net normal current terminating at the body surface. From the viewpoint of an electric circuit, there is an equivalent current source connected at one of the cell surfaces which is in contact with the air, as depicted in Fig. 7.1. The current flowing in inner volume cells can be determined from the potentials of the nodes, located at the centers of the volume cells, and the impedances connected between the nodes, on the basis of the Kirchhoff's current law (KCL).

Consider a volume cell with surface areas (A_u, A'_u, A_v, A'_v, A_w, A'_w) and lengths (L_u, L_v, L_w) between central points of each surface-pair, as shown in Fig. 7.2. The three orthogonal impedances (Z_{cu}, Z_{cv}, Z_{cw}) associated with the cell (Fig. 7.2) are approximated from the expressions
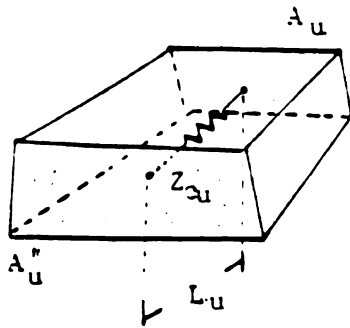
$$\hat{\sigma} = \sigma + j\omega\epsilon$$

$$Z_{Cu} = \frac{L_u}{\hat{\sigma}(A_u + A_u')/2}$$
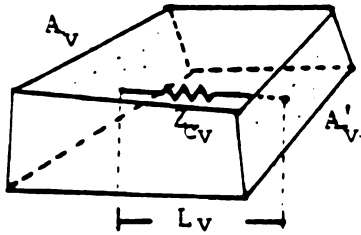
$$Z_{Cv} = \frac{L_v}{\hat{\sigma}(A_v + A_v')/2}$$
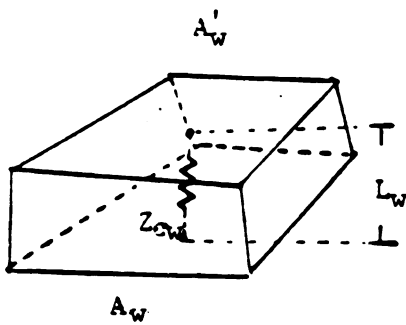
$$Z_{Cw} = \frac{L_w}{\hat{\sigma}(A_w + A_w')/2}$$

Fig. 7.2. A volume cell is represented by 3 orthogonal impedances (Z_{cu}, Z_{cv}, Z_{cw}) for the current to flow along (u, v, w) directions.

$$Z_{cu} - L_u / [\hat{\sigma}(A_u + A'_u)/2]$$

$$Z_{cv} - L_v / [\hat{\sigma}(A_v + A'_v)/2] \qquad (7.1)$$

$$Z_{cw} - L_w / [\hat{\sigma}(A_w + A'_w)/2]$$

where the complex conductivity $\hat{\sigma}$ is defined as

$$\hat{\sigma} - \sigma + j\omega\epsilon$$

Z_{cu}, Z_{cv} and Z_{cw} are connected at a common node located at the center of the volume cell. When those impedances of adjacent cells are connected together, they form an impedance network.

Let V_n be the potential of the central node of the nth cell and $(V_{n+1}, V_{n+2}, V_{n+3}, V_{n+4}, V_{n+5}, V_{n+6})$ be the potentials of the central nodes of its 6 adjacent cells located in (u, v, w) directions, as shown in Fig. 7.3. The impedances between adjacent nodes are expressed as

$$Z_{nu} - (Z_{cun} + Z_{cun+1})/2$$

$$Z'_{nu} - (Z_{cun} + Z_{cun+2})/2$$

$$Z_{nv} - (Z_{cvn} + Z_{cvn+3})/2 \qquad (7.2)$$

$$Z'_{nv} - (Z_{cvn} + Z_{cvn+4})/2$$

$$Z_{nw} - (Z_{cwn} + Z_{cwn+5})/2$$

$$Z'_{nw} - (Z_{cwn} + Z_{cwn+6})/2$$
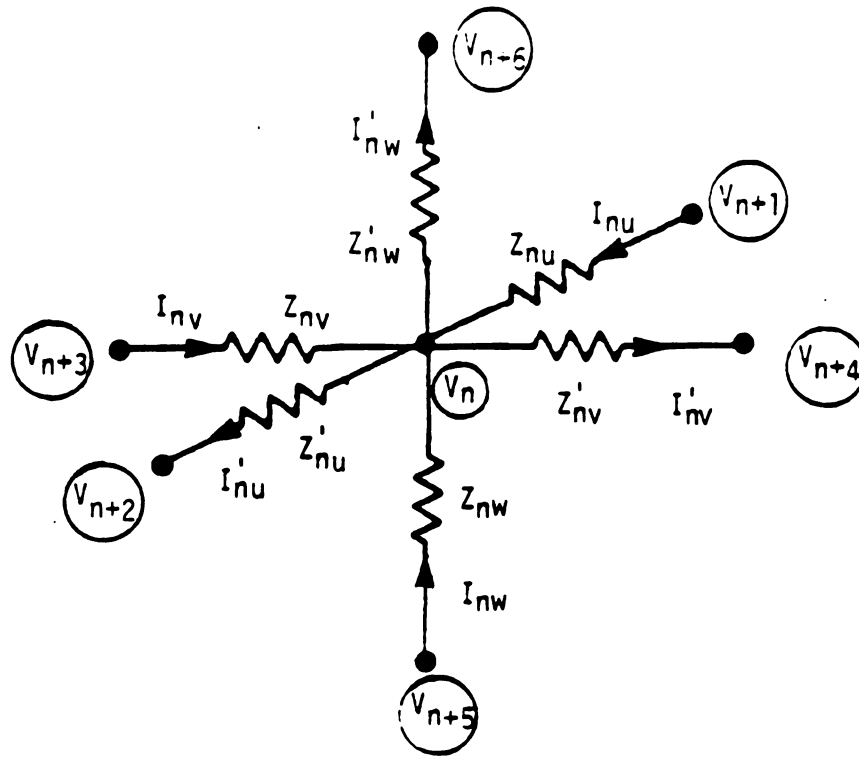
$$\text{KCL} : \quad I_{n_u} + I_{nv} + I_{nw} = I'_{n_u} + I'_{nv} + I'_{nw}$$

$$(V_{n+1} - V_n)/Z_{n_u} + (V_{n+3} - V_n)/Z_{nv} + (V_{n+5} - V_n)/Z_{nw}$$

$$= (V_n - V_{n+2})/Z'_{n_u} + (V_n - V_{n+4})/Z'_{nv} + (V_n - V_{n+6})/Z'_{nw}$$

Fig. 7.3. Impedances connected to the nth node of an inner volume cell and the KCL of the current flow.

The currents between adjacent nodes in (u, v, w) directions are

$$I_{nu} = (V_{n+1} - V_n)/Z_{nu}$$

$$I'_{nu} = (V_n - V_{n+2})/Z'_{nu}$$

$$I_{nv} = (V_{n+3} - V_n)/Z_{nv}$$

$$I'_{nv} = (V_n - V_{n+4})/Z'_{nv}$$

$$I_{nw} = (V_{n+5} - V_n)/Z_{nw}$$

$$I'_{nw} = (V_n - V_{n+6})/Z'_{nw}$$

(7.3)

and the induced current densities in the nth cell in (u, v, w) directions are expressed as

$$J_{nu} = \frac{(I_{nu} + I'_{nu})/2}{(A_{un} + A'_{un})/2}$$

$$J_{nv} = \frac{(I_{nv} + I'_{nv})/2}{(A_{vn} + A'_{vn})/2}$$

(7.4)

$$J_{nw} = \frac{(I_{nw} + I'_{nw})/2}{(A_{wn} + A'_{wn})/2}$$

The induced electric fields in nth cell can then be determined from

$$E_{nu} = J_{nu} / \hat{\sigma}_n$$

$$E_{nv} = J_{nv} / \hat{\sigma}_n \qquad (7.5)$$

$$E_{nw} = J_{nw} / \hat{\sigma}_n$$

In order to determine the potential of each node in the body, the KCL of circuit theory is applied to each node. For the inner volume cells, the net node current is zero :

$$(V_{n+1} - V_n)/Z_{nu} + (V_{n+3} - V_n)/Z_{nv} + (V_{n+5} - V_n)/Z_{nw} -$$

$$(V_n - V_{n+2})/Z'_{nu} - (V_n - V_{n+4})/Z'_{nv} - (V_n - V_{n+6})/Z'_{nw} = 0 \qquad (7.6a)$$

For the outer volume cells, there is a net normal current I_n or an equivalent current source I_n connected at the outer cell surface as depicted in Fig. 7.4 :

$$(V_{n+1} - V_n)/Z_{nu} + (V_{n+3} - V_n)/Z_{nv} + (V_{n+5} - V_n)/Z_{nw} -$$

$$(V_n - V_{n+4})/Z'_{nv} - (V_n - V_{n+6})/Z'_{nw} = I_n \qquad (7.6b)$$

or

$$(V_{n+1} - V_n)/Z_{nu} + (V_{n+3} - V_n)/Z_{nv} + (V_{n+5} - V_n)/Z_{nw} -$$

$$(V_n - V_{n+4})/Z'_{nv} - (V_n - V_{n+6})/Z'_{nw} = I_n - I_b \qquad (7.6c)$$

where I_b is the extra current when a grounding impedance is also connected
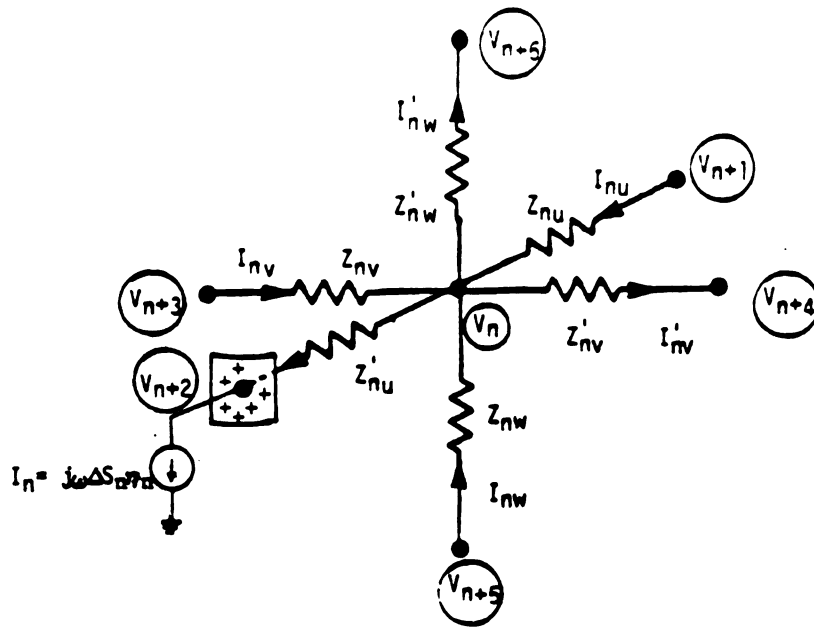
$$I_{nu} + I_{nv} + I_{nw} = I'_{nv} + I'_{nw} + I_n$$
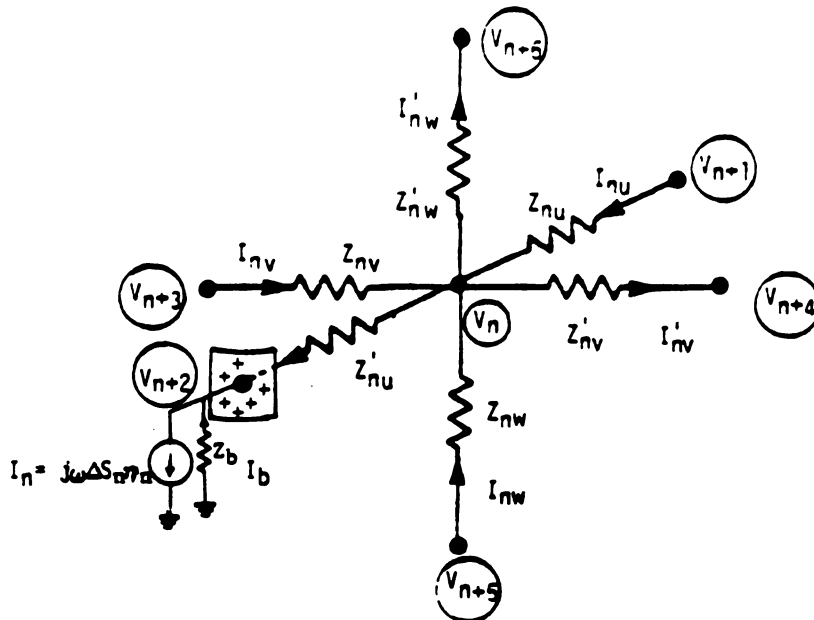
$$I_{nu} + I_{nv} + I_{nw} = I'_{nv} + I'_{nw} + I_n - I_b$$

Fig. 7.4. Impedances connected to the nth node of an outer cell. There is a net current terminating at the outer cell surface.

at this volume cell. The normal current I_n (or the current source) terminating at the outer cell surface with an area of ΔS_n is determined from the electric charge continuity equation as

$$I_n = j\omega\eta_n\Delta S_n \qquad (7.7)$$

where η_n is the induced surface charge density at ΔS_n. Eqs. (7.6) can be rewritten as

$$(1/Z'_{nu} + 1/Z'_{nv} + 1/Z'_{nw} - 1/Z_{nu} - 1/Z_{nv} - 1/Z_{nw})V_n +$$

$$(1/Z_{nu})V_{n+1} - (1/Z'_{nu})V_{n+2} + (1/Z_{nv})V_{n+3} - (1/Z'_{nv})V_{n+4} +$$

$$(1/Z_{nw})V_{n+5} - (1/Z'_{nw})V_{n+6} = 0 \qquad (7.8a)$$

for inner volume cells, or

$$(1/Z'_{nv} + 1/Z'_{nw} - 1/Z_{nu} - 1/Z_{nv} - 1/Z_{nw})V_n +$$

$$(1/Z_{nu})V_{n+1} + (1/Z_{nv})V_{n+3} - (1/Z'_{nv})V_{n+4} +$$

$$(1/Z_{nw})V_{n+5} - (1/Z'_{nw})V_{n+6} = I_n \qquad (7.8b)$$

or

$$(1/Z'_{nv} + 1/Z'_{nw} - 1/Z_{nu} - 1/Z_{nv} - 1/Z_{nw})V_n +$$

$$(1/Z_{nu})V_{n+1} + (1/Z_{nv})V_{n+3} - (1/Z'_{nv})V_{n+4} +$$

$$(1/Z_{nw})V_{n+5} - (1/Z'_{nw})V_{n+6} = I_n - I_b \qquad (7.8c)$$

for outer volume cells. The KCL equations of all the nodes (N nodes) inside the body form a matrix equation for the impedance network as

$$[Y][V] = [I] \tag{7.9}$$

where [Y] is a (N × N) matrix and [V] as well as [I] are (n × 1) column vectors. From Eqs. (7.8), it is observed that each row of the matrix has at most 7 non-zero elements. After the matrix equation (7.9) is solved, the potential of each node and hence the induced current and current density in each cell can be determined.

7.3 Numerical Examples and Comparison with Analytical Solutions

In order to test the validity of the present method which combines the SCIE method and an impedance network method, it is necessary to apply the method to some bodies with simple geometries of which analytical solutions exist and can be used to compare with numerical solutions. A lossy concentric-sphere is a good example to be considered because an "almost" exact solution for the induced current excited by a slowly time-varying electric field can be obtained under the quasi-static approximation [35].

Consider a concentric-sphere located in a homogeneous medium of complex conductivity $\hat{\sigma}$ and immersed in a slowly time-varying electric field, as shown in Fig. 7.5. The inner core of the sphere has a radius a and a complex conductivity $\hat{\sigma}_1$, while the outer shell of thickness (b − a) has a complex conductivity $\hat{\sigma}_2$. Under the quasi-static approximation,
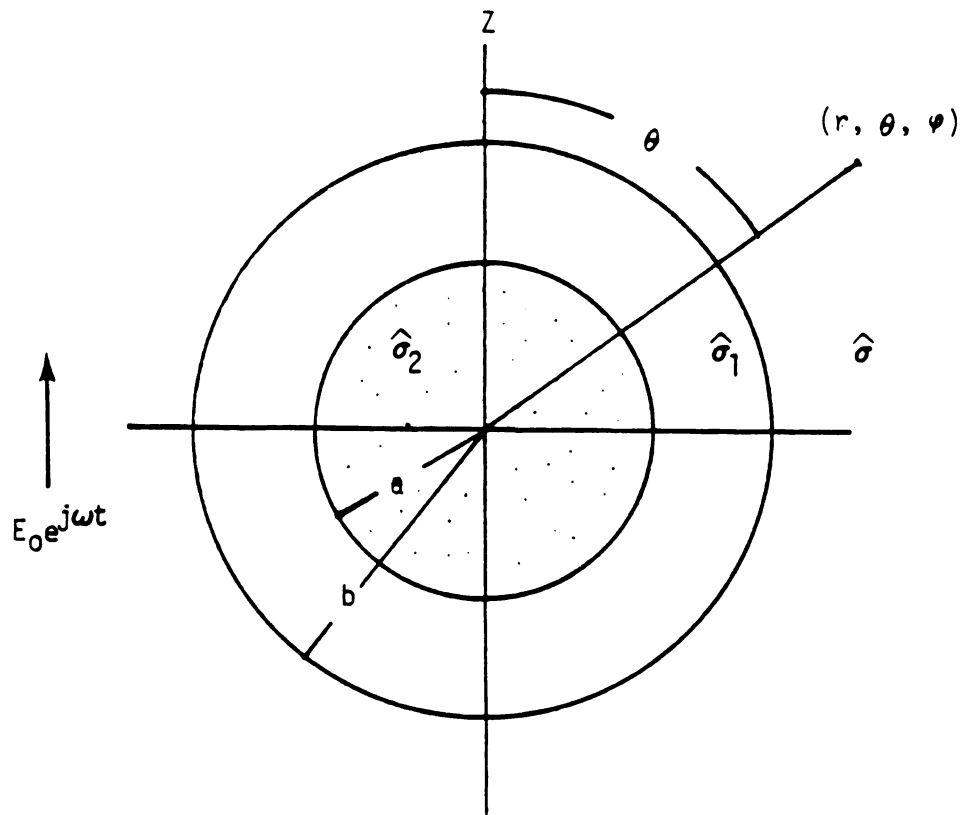
Fig. 7.5. A conducting concentric-sphere located in a homogeneous
conducting medium is immersed in a slowly time-varying
electric field.

the primary potential $V^P(r,\theta)$ associated with the primary incident field $\vec{E}_o$ is

$$V^P(r,\theta) = -E_o r\cos\theta \qquad (7.10)$$

The secondary potentials due to the induced charges in the sphere are

$$V^S(r,\theta) \quad \text{for} \quad b < r$$

$$V_1^S(r,\theta) \quad \text{for} \quad a < r < b \qquad (7.11)$$

$$V_2^S(r,\theta) \quad \text{for} \quad 0 < r < a$$

The total potentials are

$$V(r,\theta) = V^P(r,\theta) + V^S(r,\theta) \qquad \text{for} \quad b < r$$

$$V_1(r,\theta) = V^P(r,\theta) + V_1^S(r,\theta) \qquad \text{for} \quad a < r < b \qquad (7.12)$$

$$V_2(r,\theta) = V^P(r,\theta) + V_2^S(r,\theta) \qquad \text{for} \quad 0 < r < a$$

It can be found that (*Appendix 4*)

$$V(r,\theta) = -E_o r\cos\theta + H_1\cos\theta/r^2 \qquad \text{for} \quad b < r$$

$$V_1(r,\theta) = (-E_o + G_1^1)r\cos\theta + H_1^1\cos\theta/r^2 \qquad \text{for} \quad a < r < b \qquad (7.13)$$

$$V_2(r,\theta) = -E_o r\cos\theta + G_1^2 r\cos\theta \qquad \text{for} \quad 0 < r < a$$

where

$$G_1^1 = \left[\frac{(\hat{\sigma}_1 - \hat{\sigma})(2\hat{\sigma}_1 + \hat{\sigma}_2) - (\hat{\sigma}_1 - \hat{\sigma}_2)(\hat{\sigma}_1 - \hat{\sigma})2a^3/b^3}{(\hat{\sigma}_1 + 2\hat{\sigma})(2\hat{\sigma}_1 + \hat{\sigma}_2) - (\hat{\sigma}_1 - \hat{\sigma}_2)(\hat{\sigma}_1 - \hat{\sigma})2a^3/b^3} \right] E_o$$

$$G_1^2 = \left[\frac{(\hat{\sigma}_1 - \hat{\sigma})(2\hat{\sigma}_1 + \hat{\sigma}_2) - (\hat{\sigma}_1 - \hat{\sigma}_2)(\hat{\sigma}_1 - \hat{\sigma})2a^3/b^3 + 3\hat{\sigma}(\hat{\sigma}_2 - \hat{\sigma}_1)}{(\hat{\sigma}_1 + 2\hat{\sigma})(2\hat{\sigma}_1 + \hat{\sigma}_2) - (\hat{\sigma}_1 - \hat{\sigma}_2)(\hat{\sigma}_1 - \hat{\sigma})2a^3/b^3} \right] E_o$$

$$H_1^1 = \left[\frac{3\hat{\sigma}(\hat{\sigma}_2 - \hat{\sigma}_1)a^3}{(\hat{\sigma}_1 + 2\hat{\sigma})(2\hat{\sigma}_1 + \hat{\sigma}_2) - (\hat{\sigma}_1 - \hat{\sigma}_2)(\hat{\sigma}_1 - \hat{\sigma})2a^3/b^3} \right] E_o$$

$$H_1 = \left[\frac{(\hat{\sigma}_1 - \hat{\sigma})(2\hat{\sigma}_1 + \hat{\sigma}_2) + (\hat{\sigma}_2 - \hat{\sigma}_1)(2\hat{\sigma}_1 + \hat{\sigma})a^3/b^3}{(\hat{\sigma}_1 + 2\hat{\sigma})(2\hat{\sigma}_1 + \hat{\sigma}_2) + (\hat{\sigma}_2 - \hat{\sigma}_1)(\hat{\sigma}_1 - \hat{\sigma})2a^3/b^3} \right] b^3 E_o$$

It is noted that under a quasi-static approximation, the effect of vector potential is much less than that of scalar potential, thus, it is ignored. This is a verified approximation commonly used in low frequency problem. The induced electric fields inside the sphere can then be determined as

$$\vec{E}_1(r,\theta) = -\nabla V_1(r,\theta) = - \hat{r}(\partial V_1/\partial r) - \hat{\theta}(\partial V_1/\partial\theta)/r$$

$$= \hat{r}\cos\theta(E_o - G_1^1 + 2H_1^1/r^3) + \hat{\theta}\sin\theta(-E_o + G_1^1 + H_1^1/r^3)$$

$$\text{for} \quad a < r < b \qquad (7.14a)$$

$$\vec{E}_2(r,\theta) = -\nabla V_2(r,\theta) = - \hat{r}(\partial V_2/\partial r) - \hat{\theta}(\partial V_2/\partial\theta)/r$$

$$= \hat{r}\cos\theta(E_o - G_1^2) + \hat{\theta}\sin\theta(-E_o + G_1^2)$$

$$= \hat{z}(E_o - G_1^2)$$

$$\text{for} \quad 0 < r < a \qquad (7.14b)$$

A special case of a concentric-sphere is a homogeneous sphere of which $\hat{\sigma}_1 = \hat{\sigma}_2$ and the induced field inside the sphere is (*Appendix 4*)

$$\vec{E}_1(r,\theta) = [3(\hat{\sigma}/\hat{\sigma}_1)/(1 + 2\hat{\sigma}/\hat{\sigma}_1)](\hat{r}\cos\theta - \hat{\theta}\sin\theta)E_o$$

$$= \hat{z}[3(\hat{\sigma}/\hat{\sigma}_1)/(1 + 2\hat{\sigma}/\hat{\sigma}_1)]E_o \qquad (7.15)$$

It is observed that the induced electric field inside a homogeneous conducting sphere is uniform and in the z-direction which is the same as that in a dielectric sphere except the permittivity (ϵ) of the latter is replaced by the complex conductivity ($\hat{\sigma}$) of the former. Also, it is interesting to note that the induced field inside the inner core of a concentric-sphere (Eq. 7.14b) is uniformly distributed along the z-direction which is similar to that in a homogeneous sphere. Fig. 7.6 depicts numerical results of analytical solutions of induced electric fields and currents inside a homogeneous fat and a muscle sphere at 60-Hz frequency. Fig. 7.7 shows the induced electric field and current (the distributions of the current and field only shown in a half sphere due to the symmetry) in a concentric fat-muscle sphere at 60-Hz frequency.
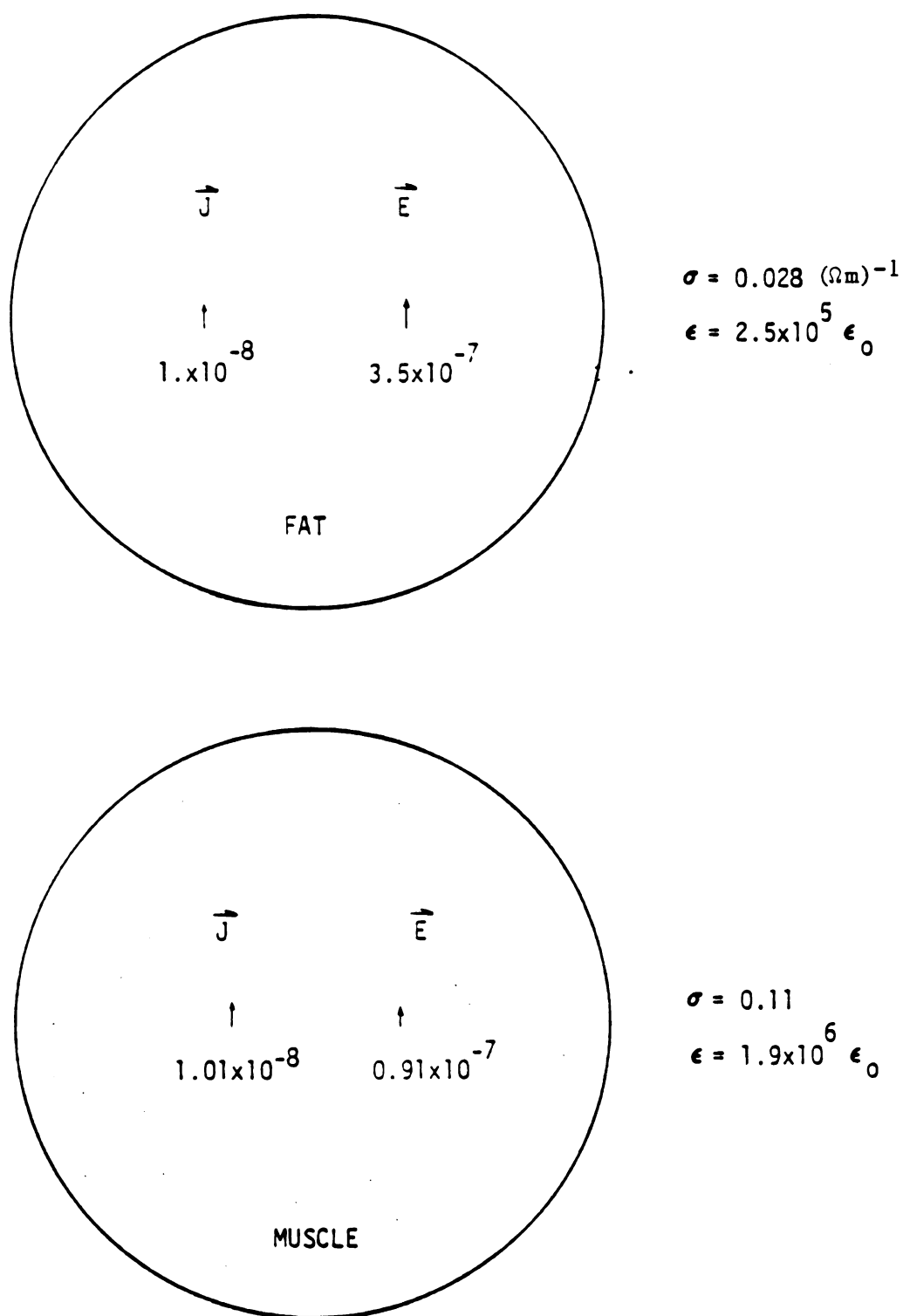
Fig. 7.6. The uniform distributions of the induced current density J (nA/cm^2) and electric field E (10 kV/m) inside a homogeneous fat and a muscle sphere when exposed to a 60-Hz, 1 kV/m electric field.
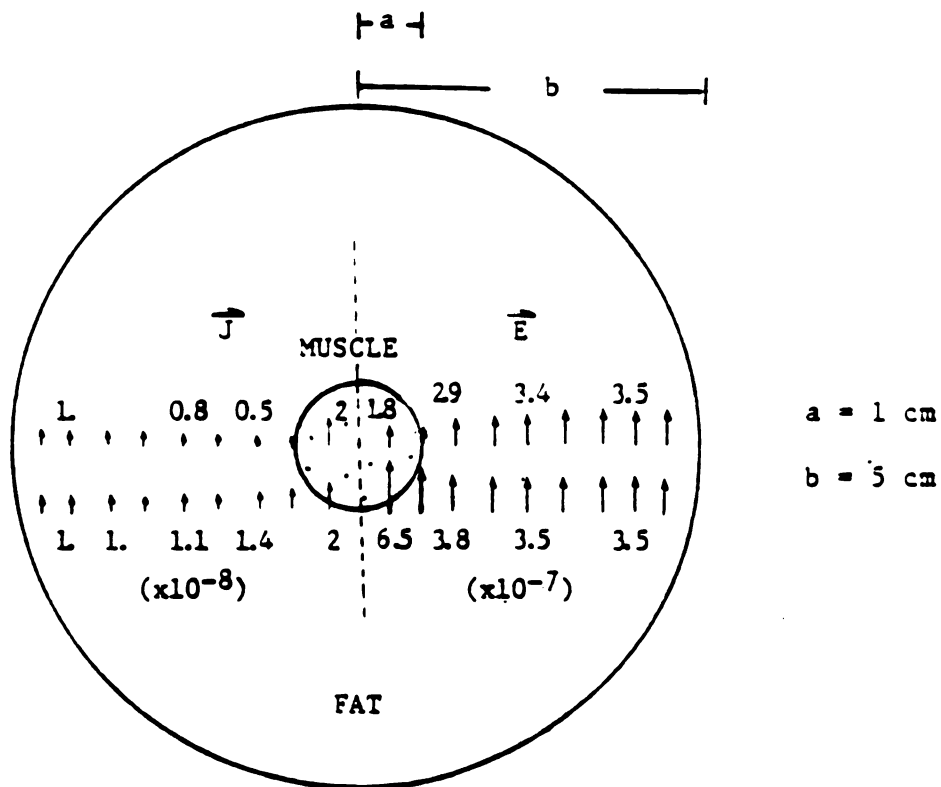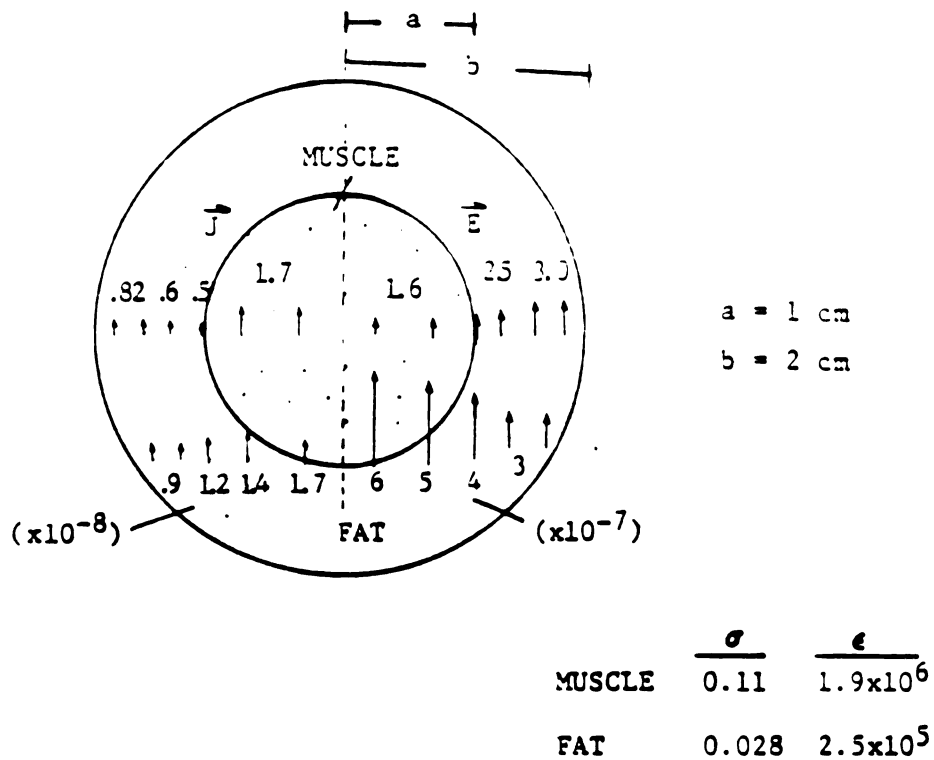
Fig. 7.7. The distributions of the induced current density J (nA/cm^2) and electric field E (10 kV/m) inside a concentric fat-muscle sphere when exposed to a 60-Hz, 1 kV/m electric field.

It is observed from Fig. 7.7 that, tangential electric fields and normal electric currents are continuous at the tissue-boundary of fat and muscle which satisfy the boundary conditions of Maxwell's equations.

To carry out numerical computation of the impedance network method for a concentric-sphere (radius — b), only an eighth of the sphere needs to be considered due to its symmetry (Fig. 7.8). The eighth-sphere is cut into M sections and each section is divided into (N × N) sector-cells, as shown in Fig. 7.9 (N divisions in r-direction and N divisions in θ-direction). The central point of a cell has coordinates (r, θ, φ) and the coordinate-lengths of a cell are characterized in Fig. 7.9. A cell can then be modeled as 3 impedances (Z_c^r, Z_c^θ, Z_c^φ) for the currents flowing along ($\hat{r}$, $\hat{\theta}$, $\hat{\varphi}$) directions as shown in Fig. 7.10. The impedances (Z_c^r, Z_c^θ, Z_c^φ) are defined according to the dimensions of the cell as

$$Z_c^r = \Delta r \ / \ [\hat{\sigma}(A_r + A_r')/2]$$

$$Z_c^\theta = r\Delta\theta \ / \ [\hat{\sigma}(A_\theta + A_\theta')/2] \qquad (7.16)$$

$$Z_c^\varphi = r\sin\theta\Delta\varphi \ / \ [\hat{\sigma}(A_\varphi)]$$

where

$$\Delta r = b/N$$

$$\Delta\theta = \pi/2N$$

$$\Delta\varphi = \pi/2M$$
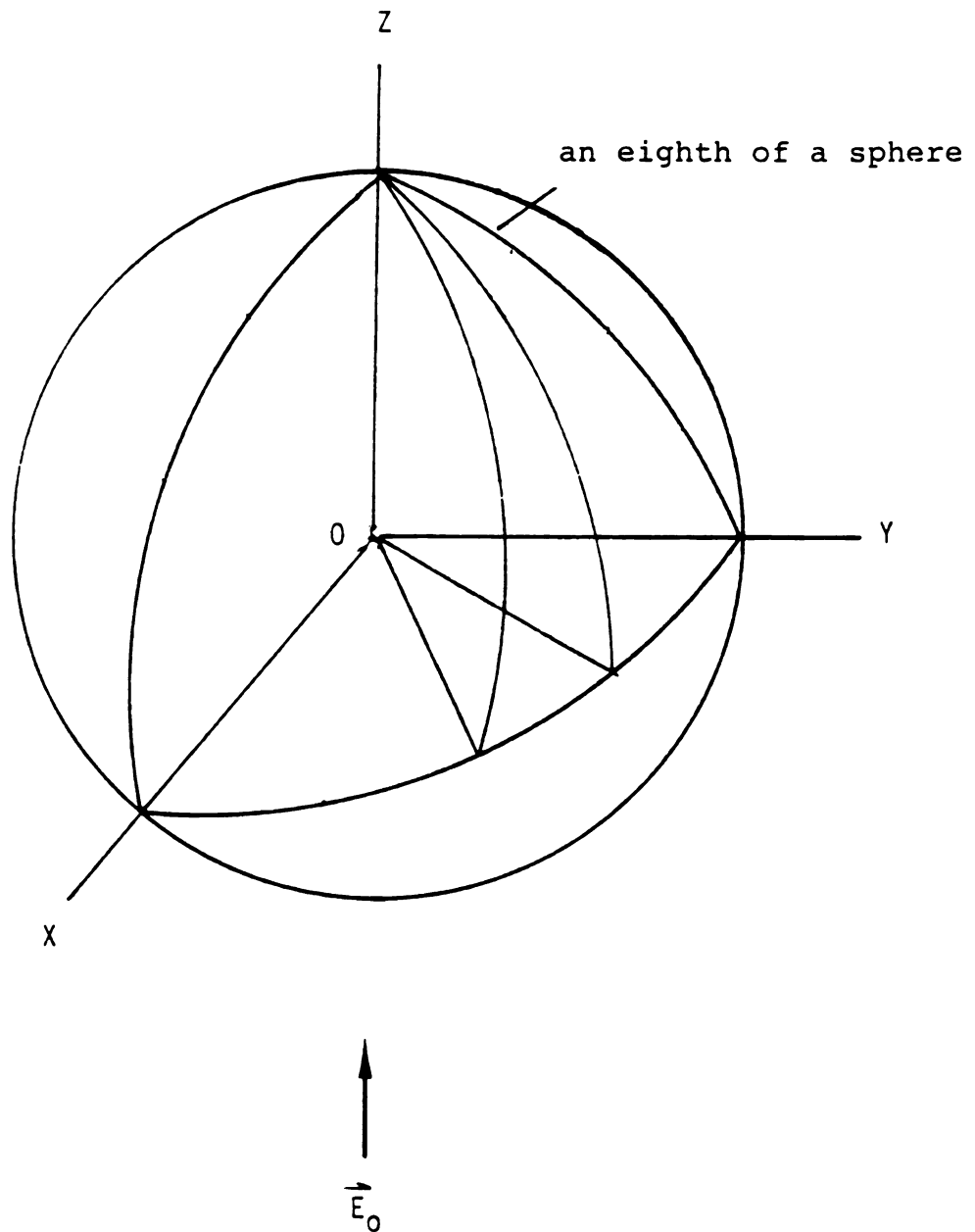
Fig. 7.8. A concentric sphere is immersed in a slowly time-varying
electric field. Only an eighth-sphere needs to be considered
for numerical computation due to the symmetry.

$\Delta\varphi(r+\Delta r/2)\sin(\theta-\Delta\theta/2)$

$(r+\Delta r/2)\Delta\theta$

$\Delta\varphi(r-\Delta r/2)\sin(\theta-\Delta\theta/2)$

$(r-\Delta r/2)\Delta\theta$

$\Delta\varphi(r+\Delta r/2)\sin(\theta+\Delta\theta/2)$

$\Delta\varphi(r-\Delta r/2)\sin(\theta+\Delta\theta/2)$
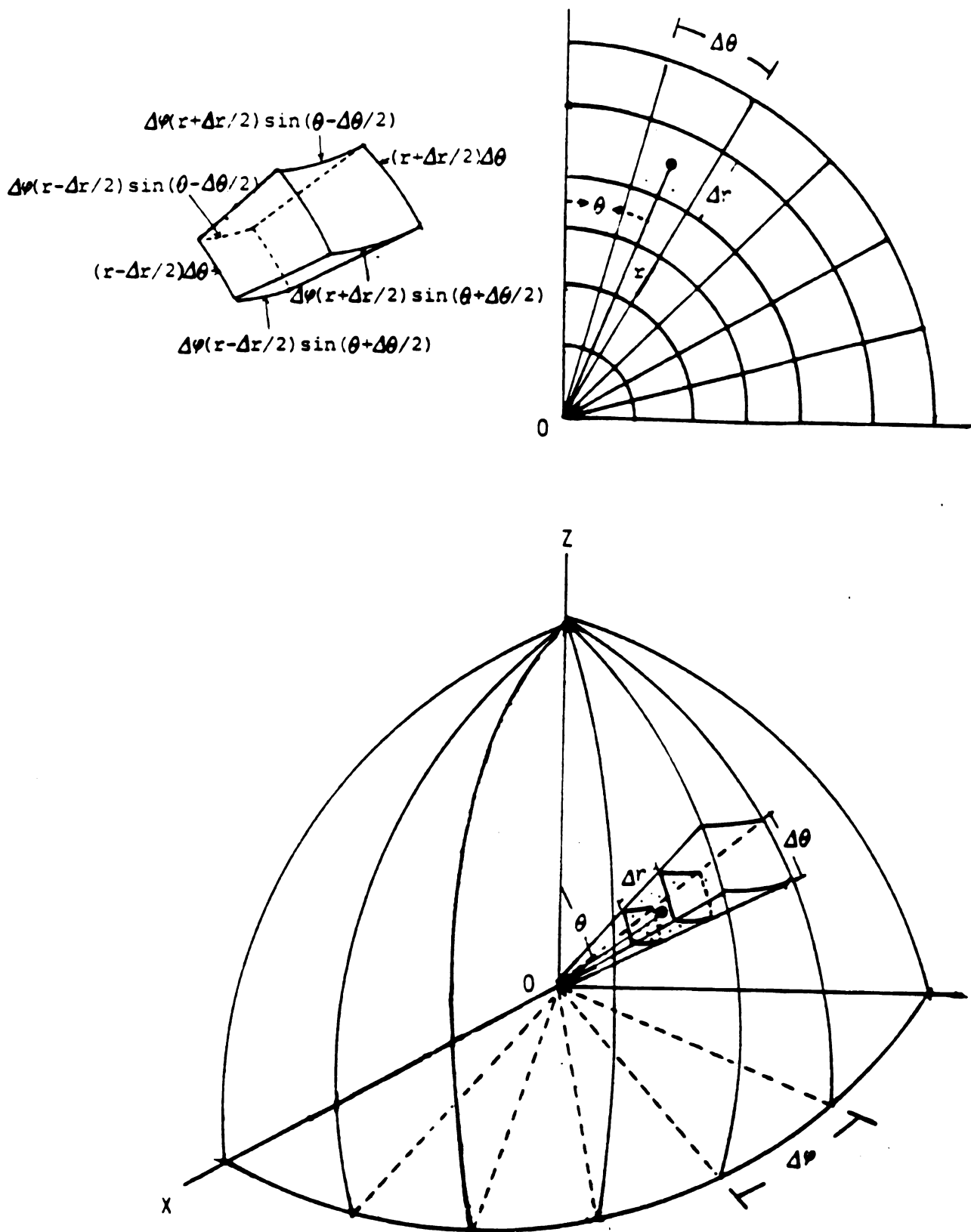
Fig. 7.9. An eighth-sphere is cut into M sections and each section is divided into (N x N) sector-cells.

$$A_r = w_5(w_1 + w_2)/2 \qquad A_\theta = \Delta r(w_1 + w_3)/2 \qquad A_\varphi = \Delta r(w_5 + w_6)/2$$

$$A'_r = w_6(w_3 + w_4)/2 \qquad A'_\theta = \Delta r(w_2 + w_4)/2$$
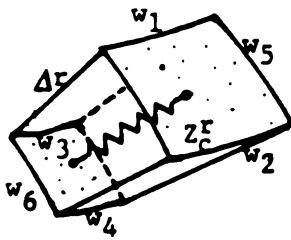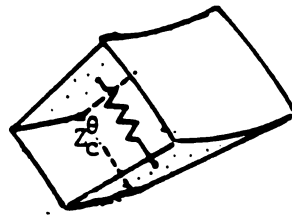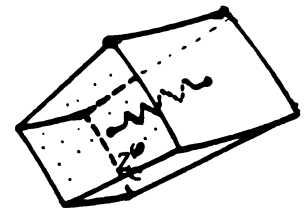
$$Z_c^r = \frac{\Delta r}{\hat{\sigma}(A_r + A'_r)/2} \qquad Z_c^\theta = \frac{r\Delta\theta}{\hat{\sigma}(A_\theta + A'_\theta)/2} \qquad Z_c^\varphi = \frac{r\sin\theta\Delta\varphi}{\hat{\sigma} A_\varphi}$$

Fig. 7.10. A sector-cell is modeled as 3 impedances $(Z_c^r, Z_c^\theta, Z_c^\varphi)$ for the current flowing along (r, θ, φ) directions. $w_1 - w_6$ are listed in Fig. 7.9.

and the surface areas (A_r, A'_r, A_θ, A'_θ, A_φ) of the cell are listed in Fig. 7.10. The impedances of each cell can thus be connected to those of adjacent cells to form a impedance network. Since there is no circumferential (φ-directional) current due to the spherical symmetry, only Z_c^r's and Z_c^θ's in a section need to be considered to form an impedance network as shown in Fig. 7.11. In the impedance network of Fig. 7.11, the potential of the central node of each cell is to be computed first. Let the potential of the central node in (i, j)th cell be $V_{i,j}$ (for (i, j) notation, i designates location in θ direction and j in r direction). The impedance between (i, j)th node and $(i, j-1)$th node, and that between $(i+1, j)$th node are expressed as $Z_{i,j}^r$ and $Z_{i,j}^\theta$, respectively. These impedances are

$$Z_{i,j}^r = (Z_{c(i,j)}^r + Z_{c(i,j-1)}^r)/2$$

$$\text{for } i \neq N, \ j \neq 1 \qquad (7.17a)$$

$$Z_{i,j}^\theta = (Z_{c(i,j)}^\theta + Z_{c(i+1,j)}^\theta)/2$$

and

$$Z_{i,1}^r = (Z_{c(i,1)}^r)/2 \qquad \text{for } j = 1$$

$$(7.17b)$$

$$Z_{N,j}^\theta = (Z_{c(N,j)}^\theta)/2 \qquad \text{for } i = N$$

The KCL equation for the (i, j)th node is
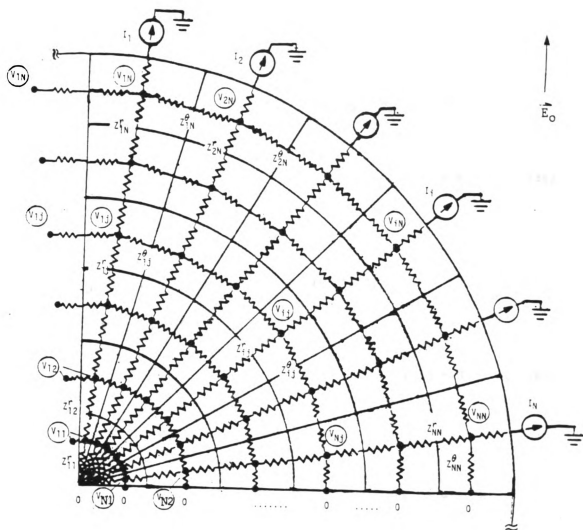
Fig. 7.11. An equivalent impedance network for an eighth-sphere when exposed to an ELF-LF electric field.

$$(V_{i+1,j} - V_{i,j})/(Z_{i,j}^{\theta}) + (V_{i,j-1} - V_{i,j})/(Z_{i,j}^{r}) -$$

$$(V_{i,j} - V_{i-1,j})/(Z_{i-1,j}^{\theta}) - (V_{i,j} - V_{i,J+1})/(Z_{i,j+1}^{r}) = 0$$

$$\text{for } j \neq N \qquad (7.18a)$$

or

$$(V_{i+1,N} - V_{i,N})/(Z_{i,N}^{\theta}) + (V_{i,N-1} - V_{i,N})/(Z_{i,N}^{r}) -$$

$$(V_{i,N} - V_{i-1,N})/(Z_{i-1,N}^{\theta}) = I_i$$

$$\text{for } j = N \qquad (7.18b)$$

where

$$V_{0,j} = V_{1,j} \qquad\qquad \text{for } i = 1, N$$

$$V_{N+1,j} = 0$$

as indicated in the Fig. 7.11 which can be observed from the symmetry of the sphere. The current source I_i can be calculated from the induced surface charge density on the desired surface patch (Eq. (7.7)).

A matrix equation can thus be constructed from Eqs. (7.18) and solved to determine the potential of each node. The r-component and θ-component of current densities in (i, j)th cell can then be computed from

$$J^r_{i,j} = \frac{[(V_{i,j-1} - V_{i,j})/(Z^r_{i,j}) + (V_{i,j} - V_{i,j+1})/(Z^r_{i,j+1})]/2}{[(A_{ri,j} + A'_{ri,j})/2]}$$

$$J^\theta_{i,j} = \frac{[(V_{i,j} - V_{i-1,j})/(Z^\theta_{i-1,j}) + (V_{i+1,j} - V_{i,j})/(Z^\theta_{i,j})]/2}{[(A_{\theta i,j} + A'_{\theta i,j})/2]}$$

$$(7.19)$$

And the z-component of current density in (i, j)th cell is

$$J^z_{i,j} = J^r_{i,j}\cos\theta - J^\theta_{i,j}\sin\theta \qquad (7.20)$$

To compare with the analytical solution, the induced currents in several cases of homogeneous spheres and concentric-spheres exposed to an incident electric field of 60-Hz frequency have been computed. Figs. 12 and 13 show comparisons between analytical and numerical solutions on the induced currents for a homogeneous fat and a homogeneous muscle sphere. A (10 × 10) subdivision was made for a section of an eighth of a sphere which was cut into 10 sections (N = M = 10, see Figs. 7.9 and 7.10). It is observed that, in numerical solutions uniform distributions of the induced current are achieved which agrees with the analytical solutions. Fig. 14 to Fig. 19 depict comparisons between analytical solutions and numerical solutions (M = 10, N = 12) on induced currents for concentric fat-muscle and muscle-fat spheres with various thicknesses. Again, excellent agreements between analytic and numerical solutions are achieved. The validity of the impedance network method is thus confirmed.

The method can be applied to any heterogeneous biological body as long as a proper impedance network is constructed to model the body.

FAT

σ $\overline{0.028}$ $(\Omega m)^{-1}$

ϵ_r 2.5×10^5

analytical solution
(uniform distribution)

i0

9.8 ~ 10.1

numerical solution

Fig. 7.12. Comparison of the analytical and numerical solutions on the induced current density J (nA/cm^2) inside a fat sphere when exposed to a 60-Hz, 1 kV/m electric field.

MUSCLE

σ 0.11 $(\Omega m)^{-1}$

ϵ_r 1.9 x 10^6

analytical solution
(uniform distribution)

numerical solution

Fig. 7.13. Comparison of the analytical and numerical solutions on the induced current density J (nA/cm^2) inside a muscle sphere when exposed to a 60-Hz, 1 kV/m electric field.

Fig. 7.14. Comparison of the analytical and numerical solutions on the induced current density J (nA/cm^2) inside a concentric fat-muscle sphere when exposed to a 60-Hz, 1 kV/m electric field.
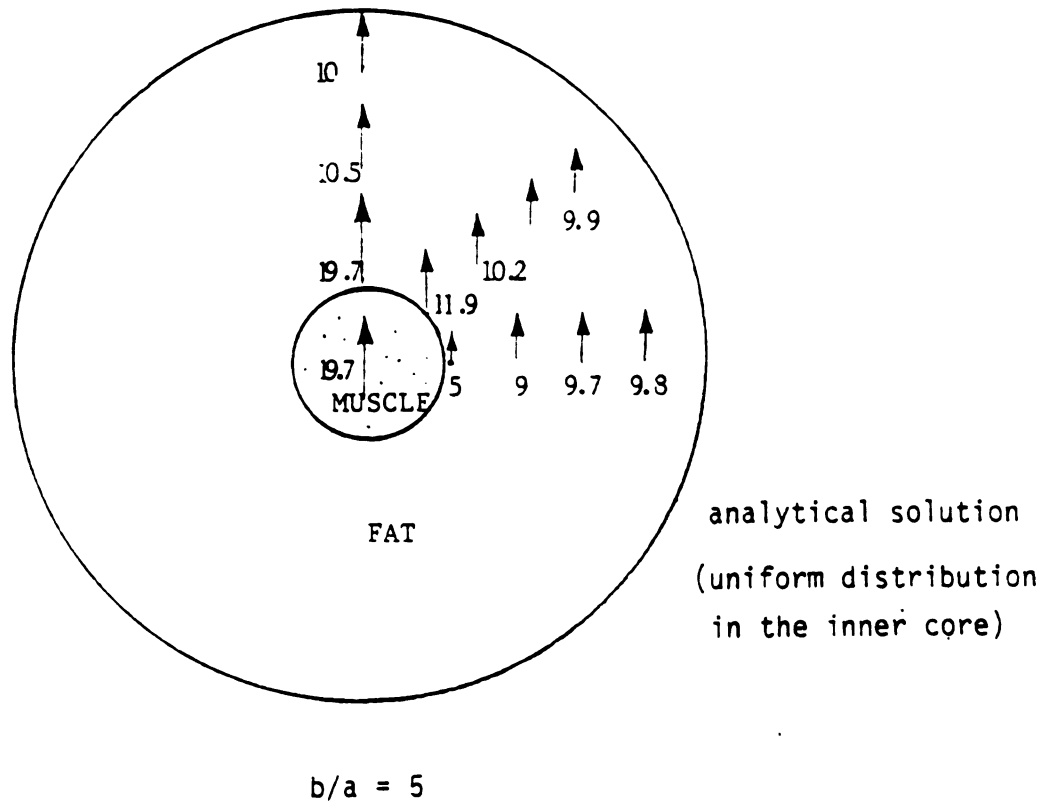
Fig. 7.15. Comparison of the analytical and numerical solutions on the induced current density J (nA/cm^2) inside a concentric fat-muscle sphere when exposed to a 60-Hz, 1 kV/m electric field.

Fig. 7.16. Comparison of the analytical and numerical solutions on the induced current density J (nA/cm^2) inside a concentric fat-muscle sphere when exposed to a 60-Hz, 1 kV/m electric field.

analytical solution

(uniform distribution
in the inner core)

b/a = 2
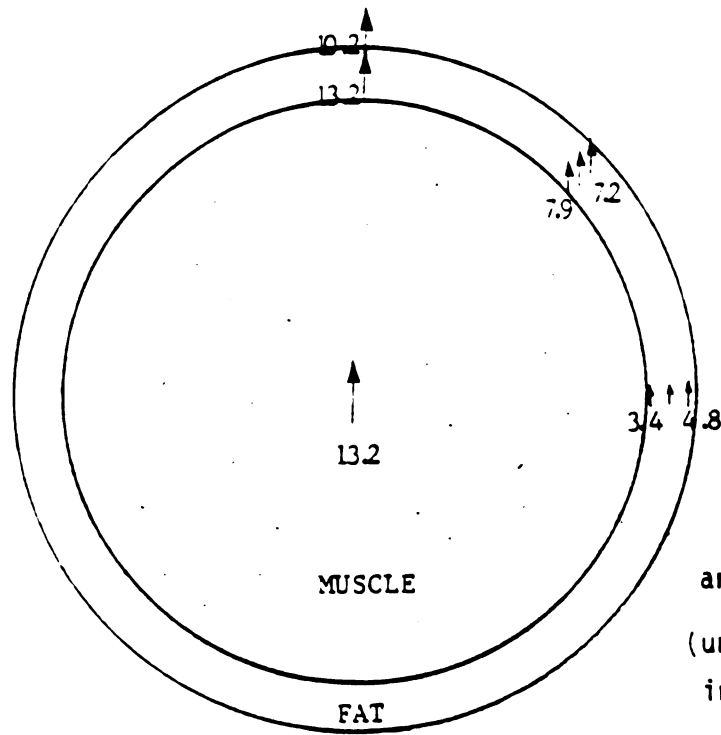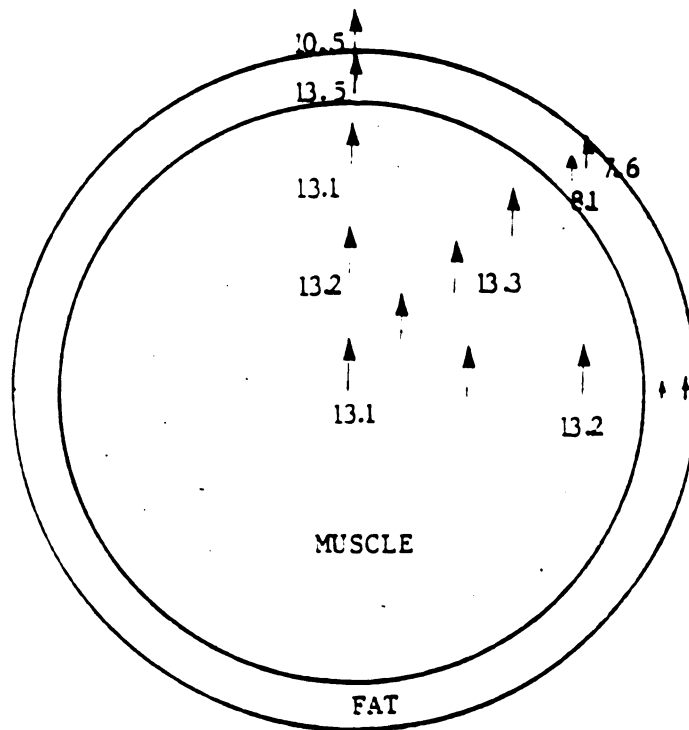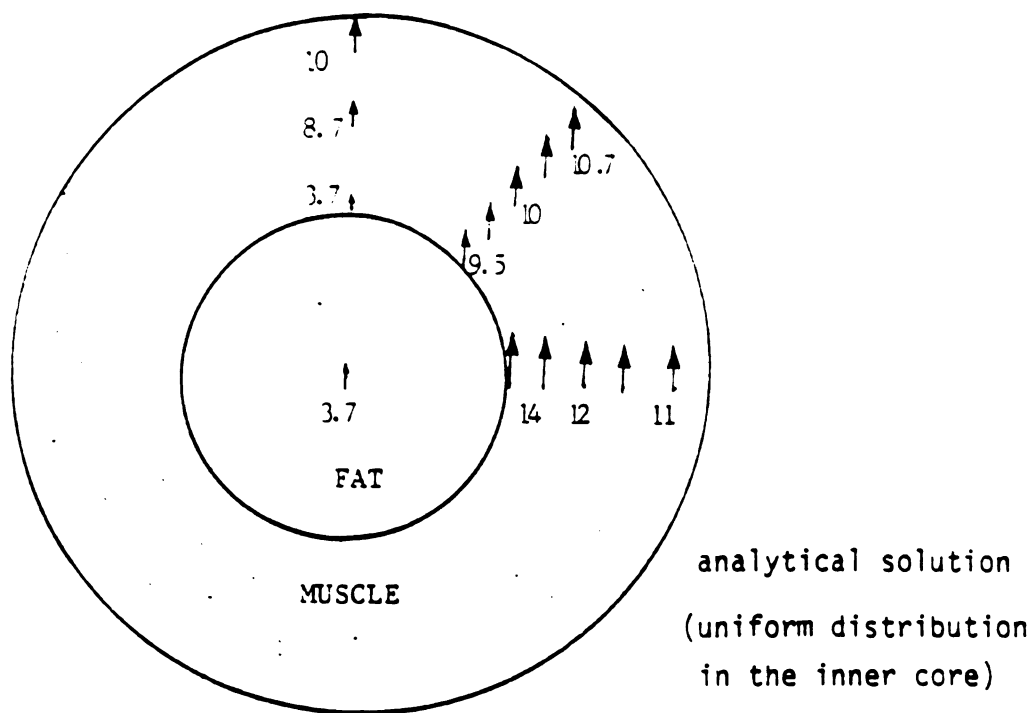
numerical solution
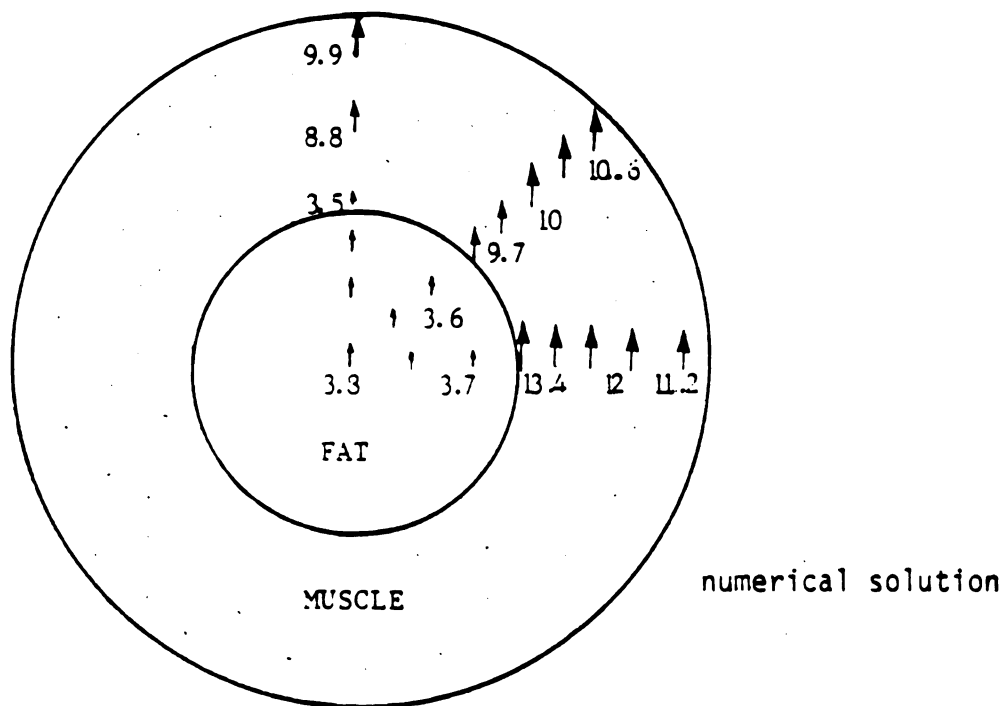
Fig. 7.17 Comparison of the analytical and numerical solutions on the
induced current density J (nA/cm^2) inside a concentric muscle-
fat sphere when exposed to a 60-Hz, 1 kV/m electric field.
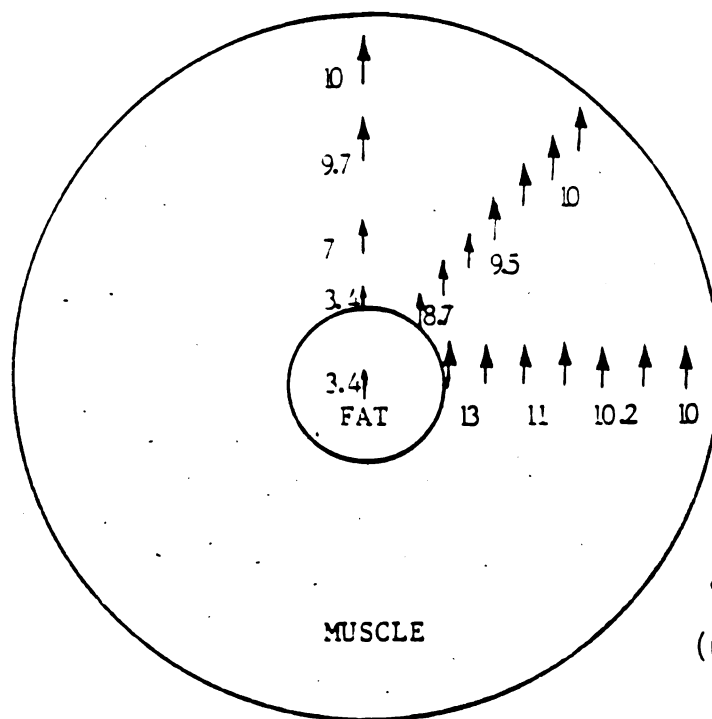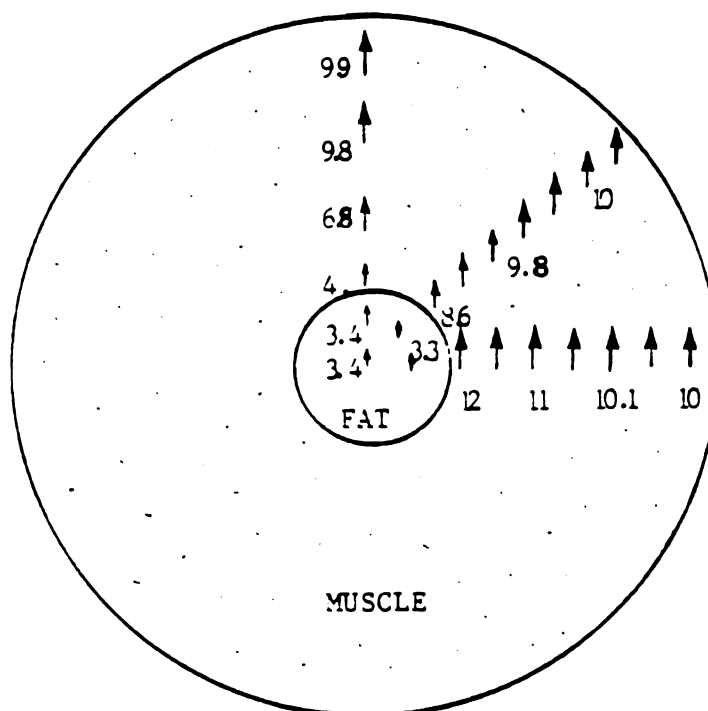
Fig. 7.18. Comparison of the analytical and numerical solutions on the induced current density J (nA/cm^2) inside a concentric muscle-fat sphere when exposed to a 60-Hz, 1 kV/m electric field.

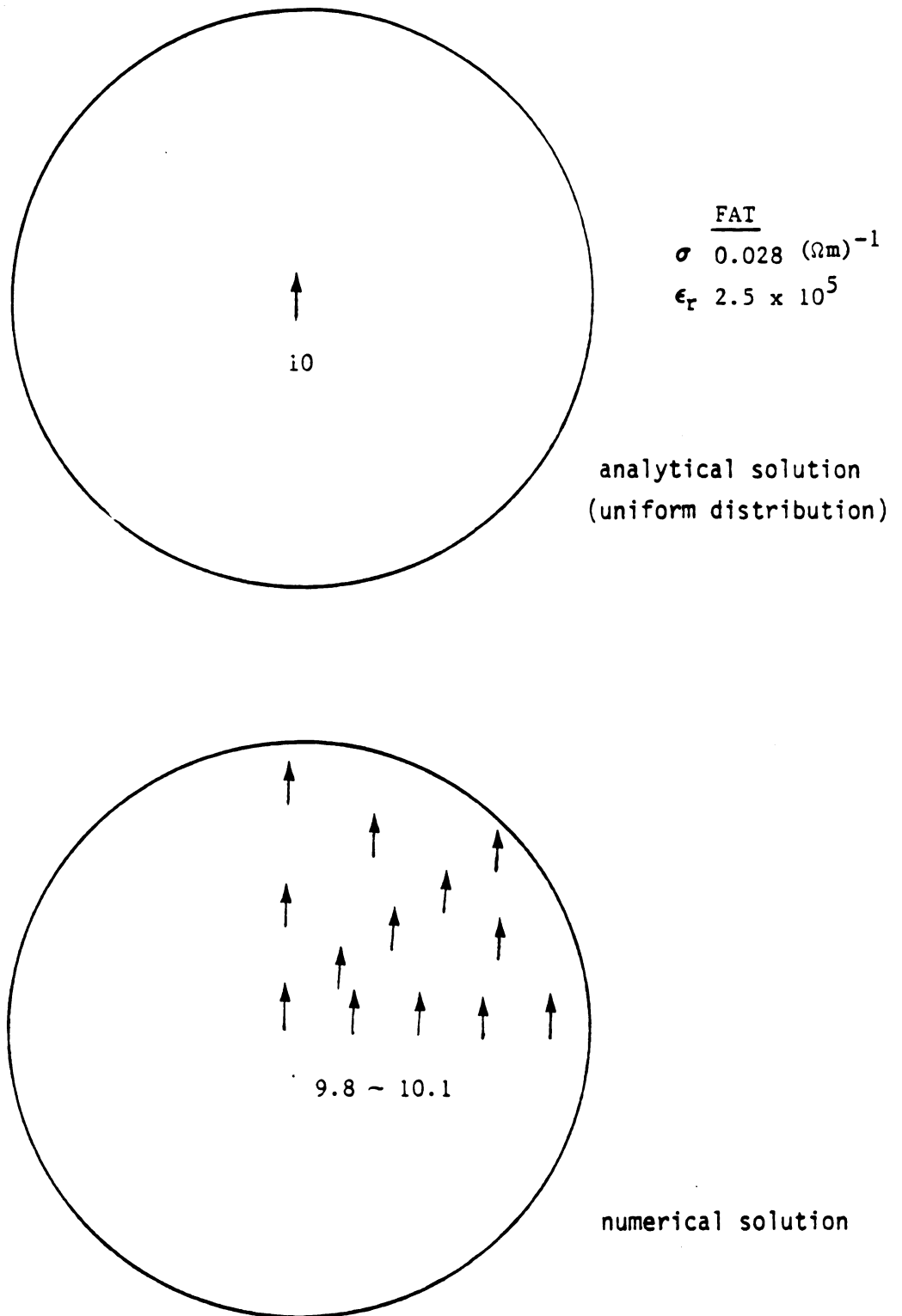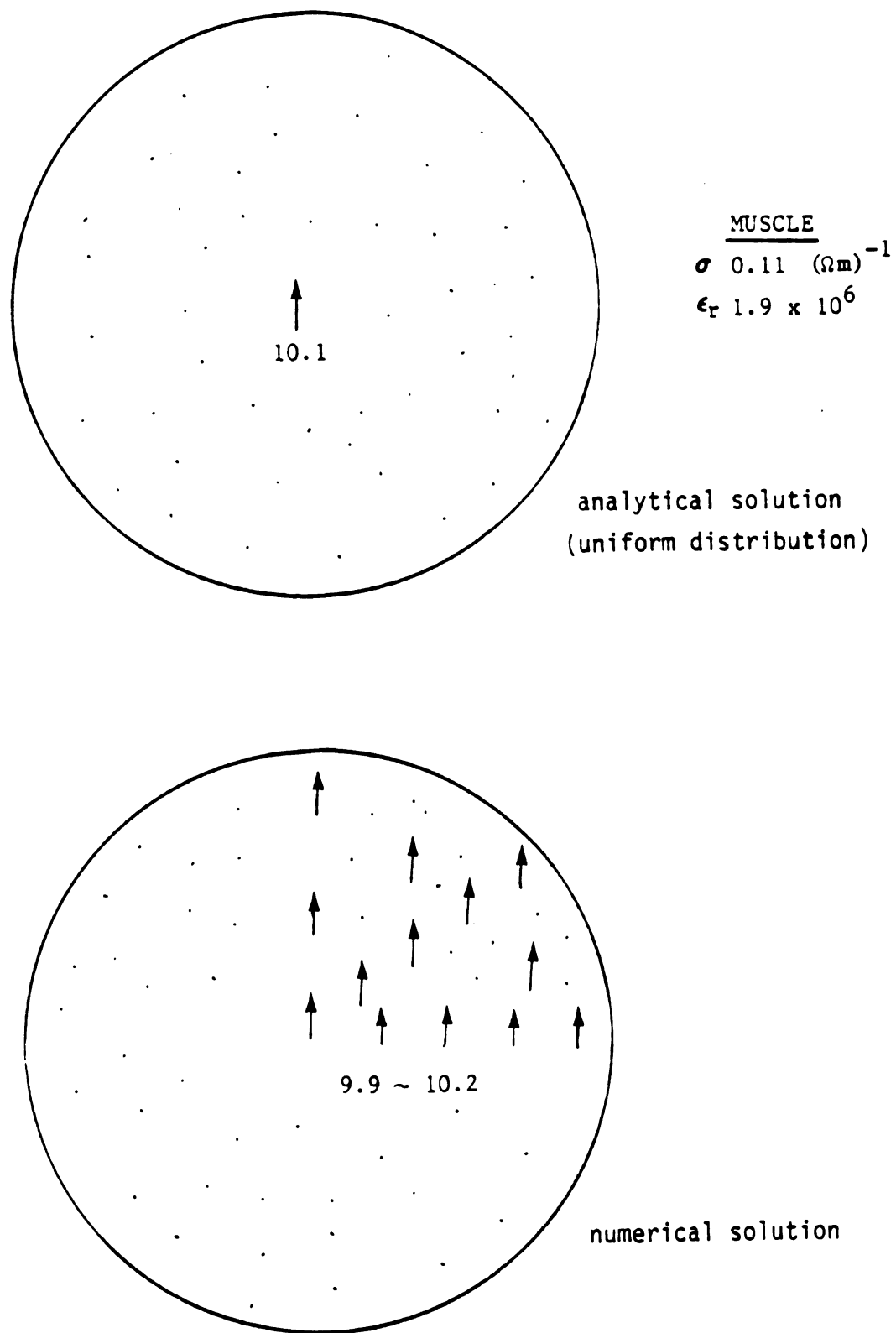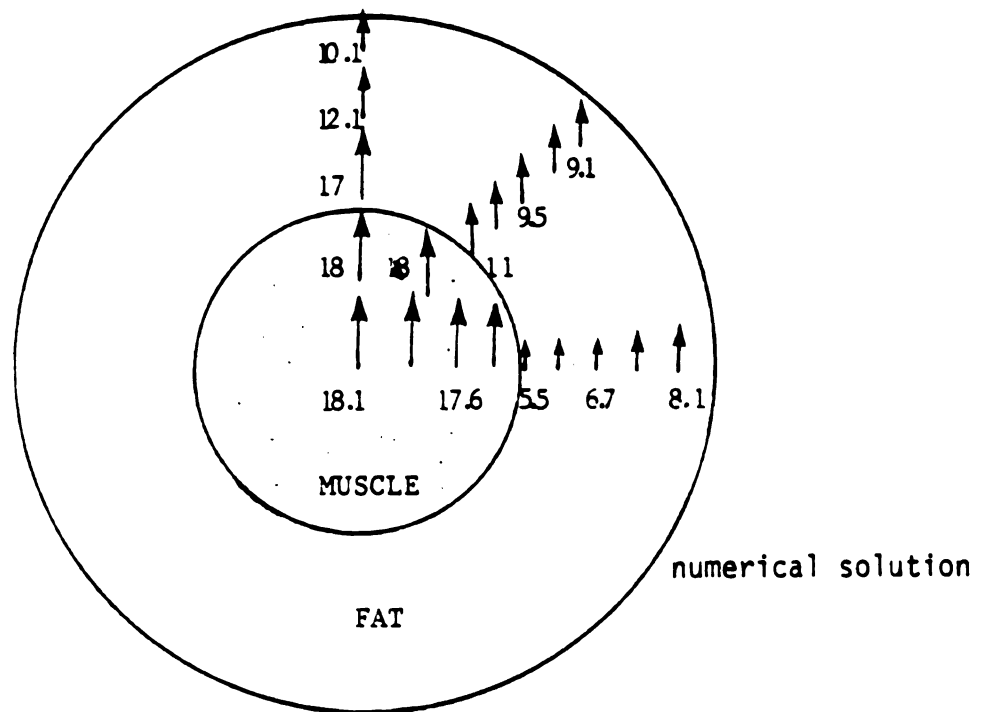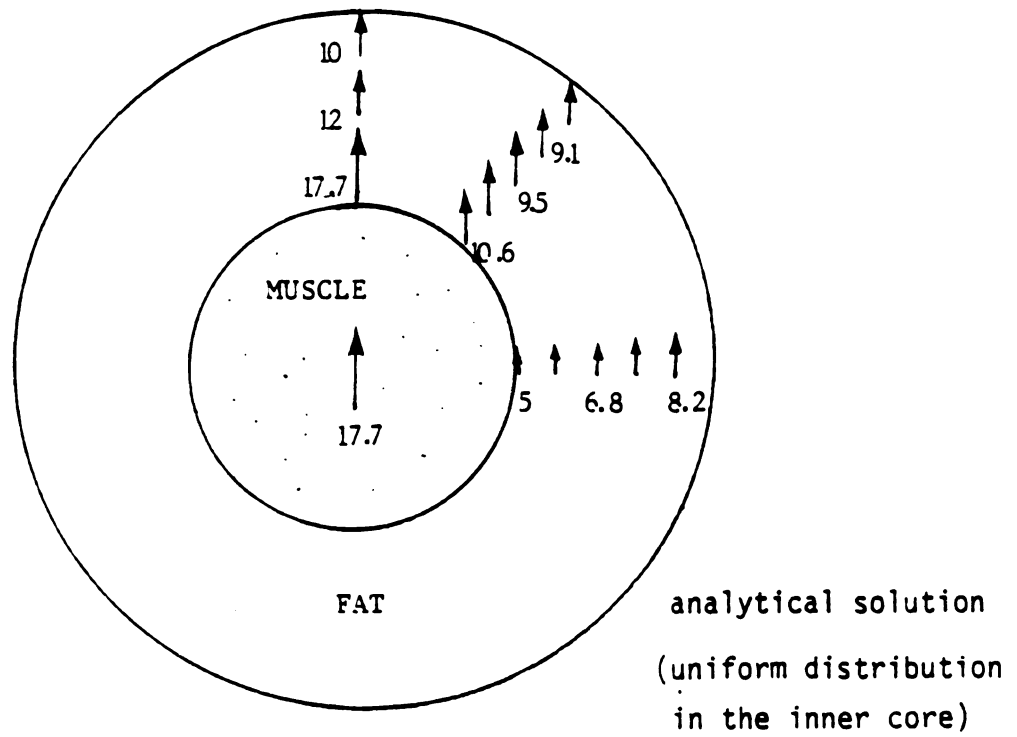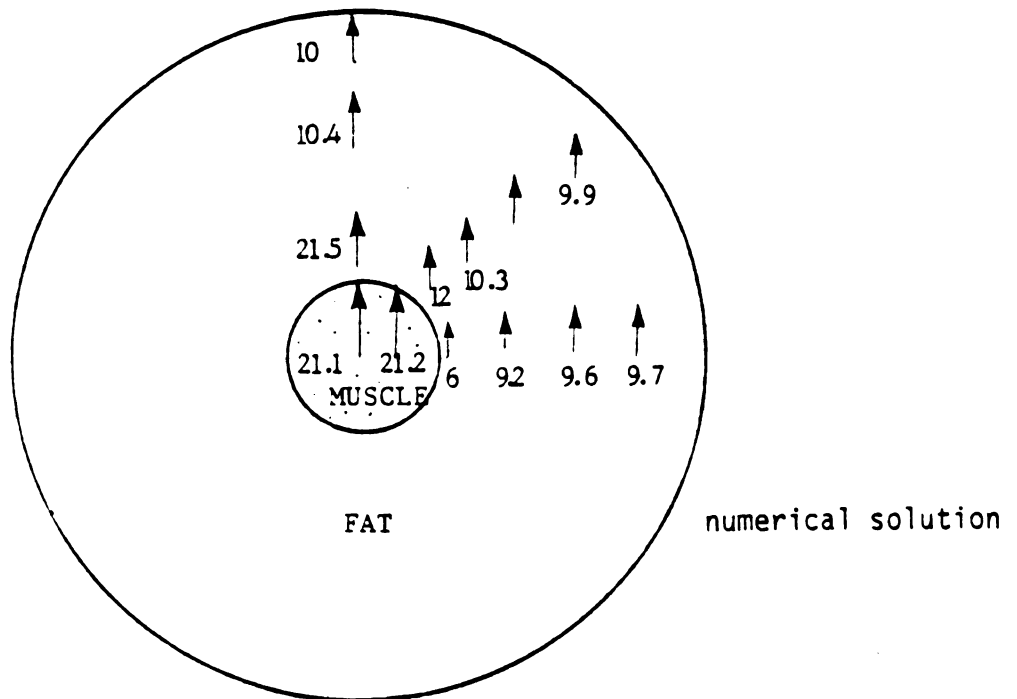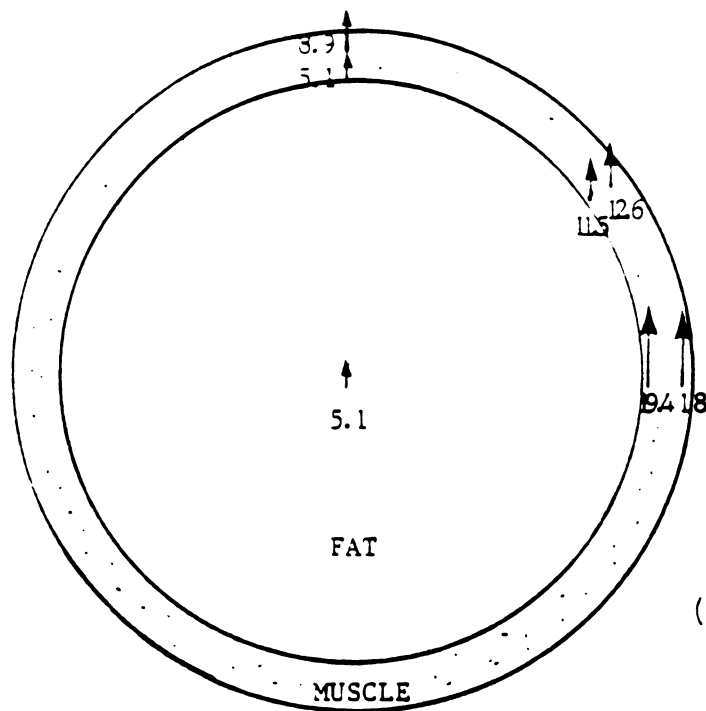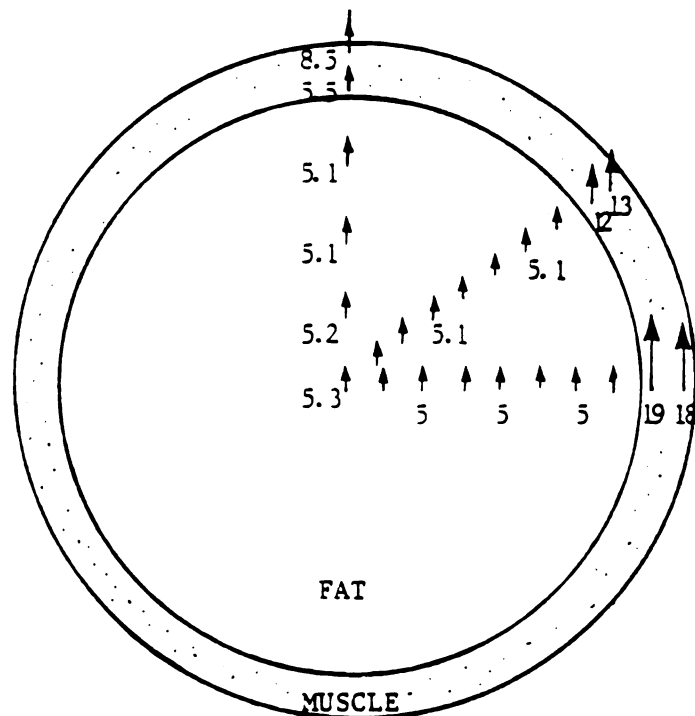Fig. 7.19. Comparison of the analytical and numerical solutions on the induced current density J (nA/cm^2) inside a concentric muscle-fat sphere when exposed to a 60-Hz, 1 kV/m electric field.

CHAPTER 8

CONCLUSIONS

This thesis presents a new numerical technique, the *surface charge integral equation* (SCIE) method, for quantifying the interaction of ELF-LF electric fields with biological bodies and conducting objects. The body-model is realistic and can have arbitrary shape, posture, composition, and is under a realistic environmental condition such as connecting with arbitrary grounding impedances. The induced electric field at the body surface, the induced electric field and current density inside the body, effects of grounding impedances, as well as the transient shock current can be analyzed when bodies are exposed to ELF-LF electric fields. The present method is numerically efficient and accurate, and is found to be applicable up to HF range.

First, based on the quasi-static approximation, a scalar integral equation for the induced body-surface charge density was derived when the body is illuminated by an ELF-LF electric field. By using the *Moment Method*, the body surface is partitioned into a number of patches and the integral equation is transformed into a matrix equation for numerical calculation. From the calculated induced surface charge and using the Ohm's law and the conservation law of electric charge, the induced current density inside the body can be determined. Since this integral equation is for the scalar surface charge, not a vector field quantity, the matrix equation transformed from the integral equation has a much smaller size

than that from the conventional tensor *electric field integral equation*
(**EFIE**). This renders the **SCIE** method especially efficient for numerical
computation.

A variety of numerical examples for spherical and spheroidal models
have been calculated and those numerical results were compared with
analytical solutions and existing experimental results for establishing
the validity and accuracy of the present method. The **SCIE** method was
further employed to quantify the induced surface charge, the induced body
current density and electric field, and the short-circuit current for
animal and human body models with various sizes (heights) and postures
when the models are exposed to 60-Hz electric fields. An excellent
agreement between the numerical results and existing experimental results
was obtained. The effects of grounding impedances have also been
calculated. It was found that, for an inductive grounding impedance,
it is possible to cause a resonance and excite a large current inside
the body when the inductance has a value in the order of 3×10^5 H.
This may cause a serious health hazard for human body. To investigate
the frequency range limitation of the **SCIE** method, the present method was
employed to compute the short-circuit current of a human body (180 cm in
height) induced by incident electric field at frequencies over the ELF
and HF range (60 Hz ~ 50 MHz). These numerical data were compared with
existing measured results, and it was found that a satisfactory agreement
was obtained up to the first body resonant frequency of about 40 MHz.
This seems to extend the frequency range applicability of the **SCIE** method
to the HF range.

To compare the **SCIE** method with the conventional **EFIE** method, the
EFIE method was applied to calculate the induced current excited by a

60-Hz EM fields in a model of man used in the SCIE method. The EFIE method is valid for the whole frequency range without making any low frequency approximation as implicit in the SCIE method. Hence, it is appropriate to compare the accuracy and efficiency of these two methods. The comparison shows that the SCIE method has much better numerical efficiency and accuracy than the EFIE method at the low frequency range. In the course of application of the EFIE method, various iterative methods such as the *Conjugate Gradient Method* (CGM) and the *Guass-Seidel Method* (GSM) have been used to solve the large matrix equation transformed from the EFIE method. The convergent rate for these iterative methods were compared and discussed.

When a human body and a nearby metallic object, such as a vehicle, are both exposed to a strong electric field of a power line, a large shock current may flow between them through direct or spark contact; this will cause serious health hazards to the human body. To analyze this transient shock-current phenomenon, the *coupled surface charge integral equations* were applied to determine floating potentials and short-circuit currents of a human body and a nearby vehicle both under the exposure of a 60-Hz strong electric field. The equivalent circuits of a human body and a vehicle at proximity were then constructed based on these data. From the equivalent-circuit model, the transient shock current phenomenon was analyzed. Numerical results were compared with existing experimental results and discussed.

Lastly, a more challenging and difficult problem of a heterogeneous-body was studied. The problem was successfully solved by combining the SCIE method with an *impedance network method*. The body

is modeled as an equivalent impedance network and the induced surface charges at the body surface are viewed as equivalent current sources which are connected at the outer boundary of the impedance network. The currents flowing in the impedance network can be determined on the basis of Kirchhoff's current law (KCL), and from which the induced current density and electric field inside the body can be mapped. A muscle-fat concentric-sphere was chosen as a test case because there exists an analytical solution at the low frequency range for this geometry. Induced currents inside concentric-spheres with various thicknesses immersed in 60-Hz electric fields were computed and compared with corresponding analytical solutions. An excellent agreement was obtained, and thus the validity of the method was confirmed. This method can be applied to any heterogeneous biological body when it is exposed to ELF-LF electric fields, provided an impedance network is appropriately constructed to model the body.

An interesting future topic for this research is to quantify the interaction of low-frequency magnetic fields with biological bodies. The findings from such a study may be very useful for some medical therapies.

APPENDIX

APPENDIX 1
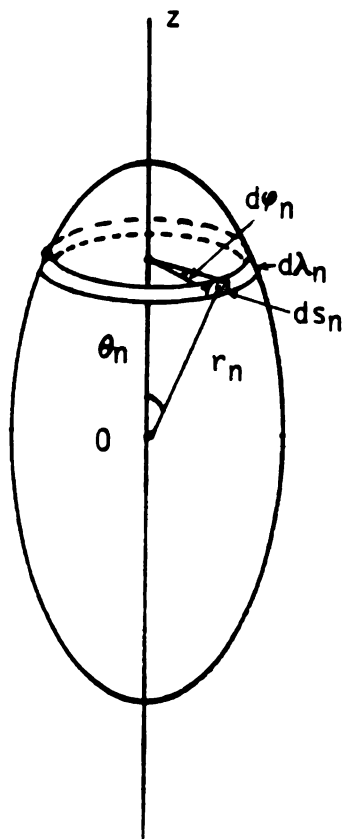
$$\text{surface integration} = \int ds_n$$

$$ds_n = r_n \sin\theta_n d\varphi_n \cdot d\lambda_n$$
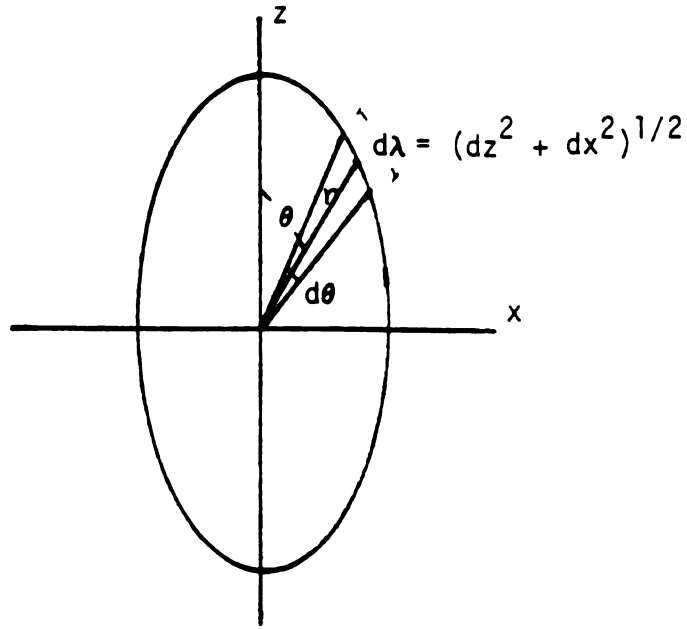
$$z = r\cos\theta \quad , \quad x = r\sin\theta$$

$$dz = -r\sin\theta + \cos\theta dr$$

$$dx = r\cos\theta + \sin\theta dr$$

and

$$r = \frac{ab}{(a^2\sin^2\theta + b^2\cos^2\theta)^{1/2}}$$

$$dr = \frac{-ab\sin\theta\cos\theta(a^2 - b^2)}{(a^2\sin^2\theta + b^2\cos^2\theta)^{3/2}}$$

hence

$$d\lambda = (dz^2 + dx^2)^{1/2}$$

$$= (dr^2 + r^2 d\theta^2)^{1/2}$$

$$= \frac{ab}{\sqrt{a^2\sin^2\theta + b^2\cos^2\theta}}\left[1 + \frac{\sin^2\theta\cos^2\theta(a^2 - b^2)^2}{(a^2\sin^2\theta + b^2\cos^2\theta)^2}\right]^{1/2}$$

APPENDIX 2

STEADY-STATE RESPONSE OF THE EQUIVALENT CIRCUIT

The equivalent circuit in Fig. 7.9 can be replaced by the other equivalent circuit as shown in the Fig. A2.1. The voltages across the capacitor C_t and resistor R_b are ϕ_1^S and ϕ_2^S. The voltage source V_{co} is replaced by a current source I_{co} which is

$$I_{co}(t) = j\omega C_c \phi_{co}(t) \tag{A2.1}$$

Let $\phi_1^S(t)$, $\phi_2^S(t)$, and $I_{co}(t)$ be represented as

$$\phi_1^S(t) = \phi_{1m}e^{j\omega t} \tag{A2.2a}$$

$$\phi_2^S(t) = \phi_{2m}e^{j\omega t} \tag{A2.2b}$$

$$I_{co}(t) = I_{cm}e^{j\omega t} \tag{A2.2c}$$

where

$$I_{cm} = j\omega C_c \phi_{cm}$$

Then, from KCL two equations can be obtained as follows,
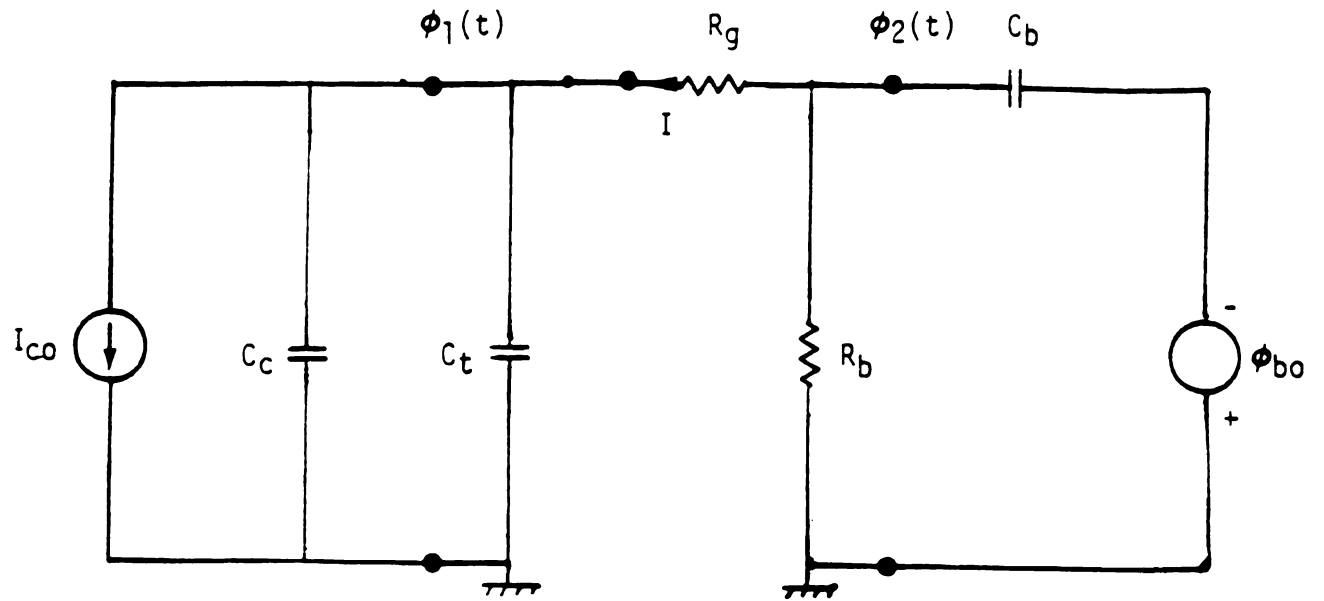
Fig. A2.1. Equivalent circuit for computing the steady-state response
of the equivalent circuit of Fig. 6.9.

$$I_{cm} = \phi_{1m}/(Z_{Cc}//Z_{Ct}) + (\phi_{1m} - \phi_{2m})/R_g \qquad \text{(A2.3a)}$$

$$(\phi_{1m} - \phi_{2m})/R_g = \phi_{2m}/R_d + (\phi_{2m} - \phi_{bm})/Z_{Cb} \qquad \text{(A2.3b)}$$

where

$$Z_{Cc}//Z_{Ct} = (Z_{Cc} \times Z_{Ct})/(Z_{Cc} + Z_{Ct})$$

$$Z_{Cc} = 1/j\omega C_c \; ; \quad Z_{Ct} = 1/j\omega C_t \; ; \quad Z_{Cb} = 1/j\omega C_b$$

Eqs. (A2.3) can be rearranged to be as

$$\phi_{1m} Y_1 - \phi_{2m}/R_g = I_{cm} \qquad \text{(A2.4a)}$$

$$- \phi_{1m}/R_g + \phi_{2m} Y_2 = j\omega C_b \phi_{cm} \qquad \text{(A2.4b)}$$

where

$$Y_1 = j\omega(C_c + C_t) + 1/R_g$$

$$Y_2 = j\omega C_b + 1/R_d + 1/R_g$$

From Eqs. (A2.4) ϕ_{1m} and ϕ_{2m} can then be solved as follows,

$$\phi_{1m} = \frac{I_{cm}Y_2 + \phi_{bm}(j\omega C_b/R_g)}{Y_1Y_2 - (1/R_g)^2} \tag{A2.5a}$$

$$\phi_{2m} = \frac{\phi_{bm}(j\omega C_b)Y_1 + (I_{cm}/R_g)}{Y_1Y_2 - (1/R_g)^2} \tag{A2.5b}$$

APPENDIX 3

TRANSIENT RESPONSE OF THE EQUIVALENT CIRCUIT

When the switch in the equivalent circuit (Fig. A3.1(a)) is open $(t < 0)$, the voltages across C_t, R_b, and C_b are

$$\phi_1(t) = \phi_{cm} \frac{Z_{Ct}}{Z_{Cc} + Z_{Ct}} e^{j\omega t} \qquad (A3.1a)$$

$$\phi_2(t) = \phi_{bm} \frac{R_b}{Z_{Cb} + R_b} e^{j\omega t} \qquad (A3.1b)$$

$$\phi_3(t) = \phi_{bm} \frac{Z_{Cb}}{Z_{Cb} + R_b} e^{j\omega t} \qquad (A3.1c)$$

where

$$Z_{Cc} = 1/j\omega C_c \ , \quad Z_{Ct} = 1/j\omega C_t \ , \quad Z_{Cb} = 1/j\omega C_b$$

After the switch in the circuit is closed $(t > 0)$, for transient analysis the circuit in Fig. A3.1(b) is used. Let the voltages across
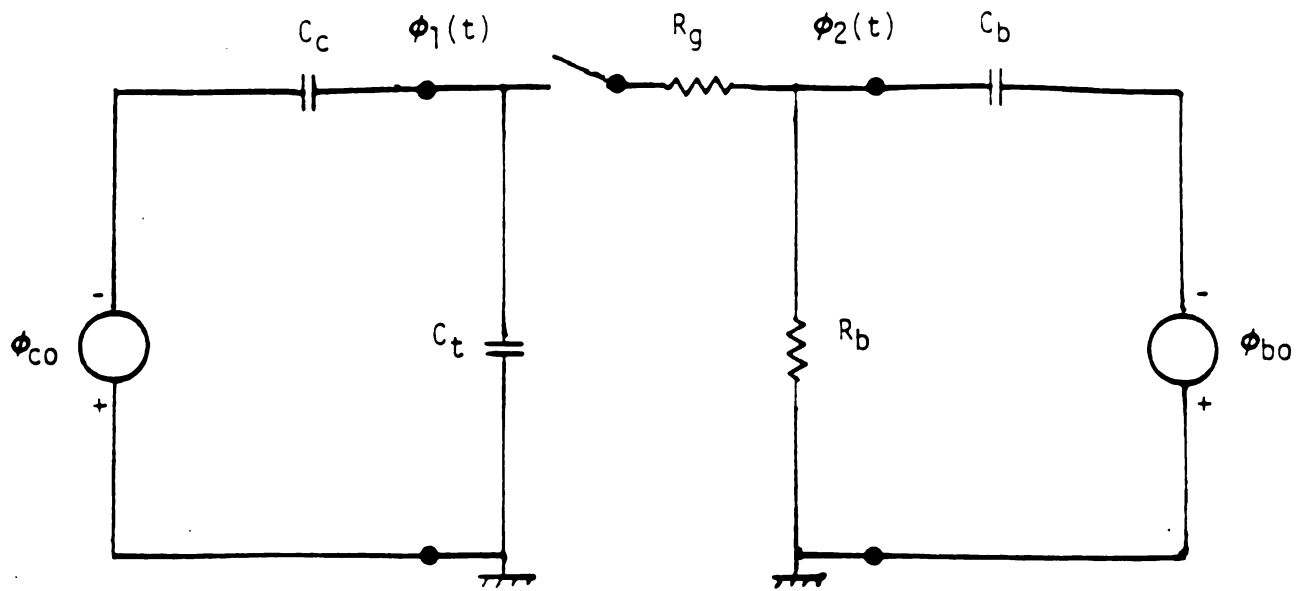
Fig. A3.1(a). Equivalent circuit of Fig. 6.9 before the spark contact (the switch in the circuit is open).
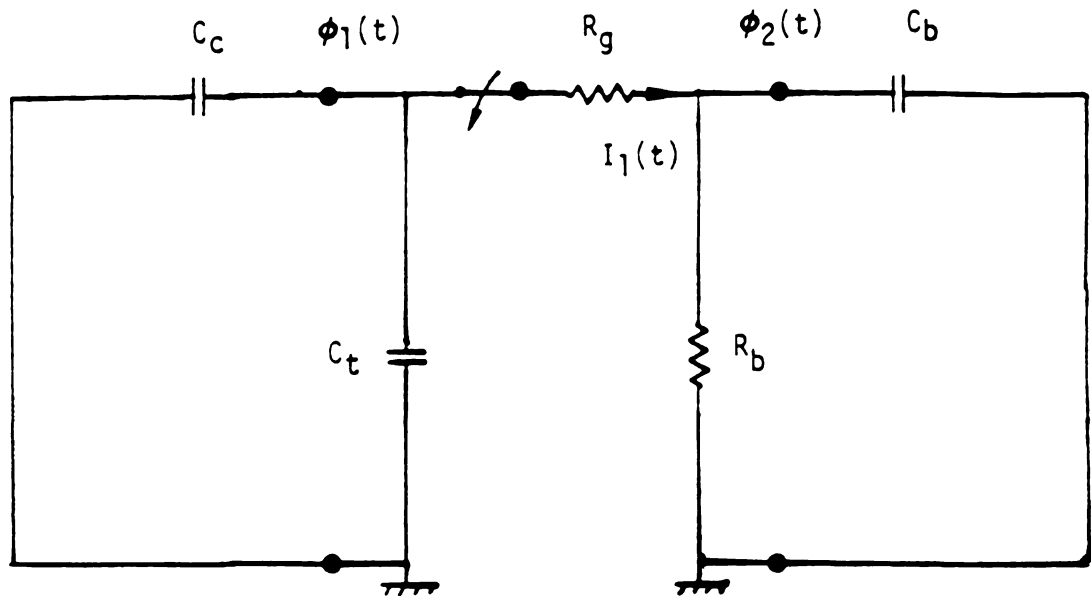
Fig. A3.1(b). Equivalent circuit for computing the transient response of the equivalent circuit of Fig. 6.9 (the switch in the circuit is closed).

the capacitor C_t and R_b be ϕ_1^t and ϕ_2^t. Two equations can be obtained from this circuit by using KCL and KVL,

$$\frac{\phi_2^t(t)}{R_b} + C_b\frac{d\phi_2^t(t)}{dt} = I_1(t) \qquad (A3.2a)$$

$$I_1(t)R_g + \frac{1}{(C_c + C_t)}\int_0^t I_1(t)dt = -\phi_2^t(t) \qquad (A3.2b)$$

Substituting (A3.2a) into (A3.2b) leads to

$$\phi_2^t(t)[1 + \frac{R_g}{R_b}] = -C_bR_g\frac{d\phi_2^t(t)}{dt} - \frac{1}{(C_c + C_t)}\int_0^t [\frac{\phi_2^t(t)}{R_b} + C_b\frac{d\phi_2^t(t)}{dt}]dt \qquad (A3.3)$$

Eq. (A3.3) can be differentiated to become

$$\frac{d^2\phi_2^t(t)}{dt^2} + \frac{1}{C_bR_g}(\frac{R_g}{R_b} + \frac{C_b}{C_t} + 1)\frac{d\phi_2^t(t)}{dt} + \frac{\phi_2^t(t)}{C_b(C_c + C_t)R_gR_b} = 0 \qquad (A3.4)$$

The solution $\phi_2(t)$ of Eq. (A3.4) is

$$\phi_2^t(t) = k_1\exp(\alpha_1 t) + k_2\exp(\alpha_2 t) \qquad (A3.5)$$

where

k_1 & k_2 — constants to be determined

α_1 & α_2 — roots of the characteristic equation of (A3.4)

and

$$\alpha_1 = \frac{-1}{2C_b R_g} [R_g/R_b + C_b/(C_c + C_t) + 1] +$$

$$\left\{ [\frac{1}{2C_b R_g}(R_g/R_b + C_b/(C_c + C_t) + 1)]^2 - \frac{1}{C_b(C_c + C_t)R_g R_b} \right\}^{1/2}$$

$$\alpha_2 = \frac{-1}{2C_b R_g} [R_g/R_b + C_b/(C_c + C_t) + 1] -$$

$$\left\{ [\frac{1}{2C_b R_g}(R_g/R_b + C_b/(C_c + C_t) + 1)]^2 - \frac{1}{C_b(C_c + C_t)R_g R_b} \right\}^{1/2}$$

By using the same procedures as above, $\phi_1^c(t)$ can be obtained as

$$\phi_1^c(t) = k_3 \exp(\alpha_1 t) + k_4 \exp(\alpha_2 t) \tag{A3.6}$$

where

k_3 & k_4 — constants to be determined

To determine $k_1 \sim k_4$, two equations are employed which can be derived from the circuit in Fig. A3.1(b) by using **KCL** and **KVL**,

$$\phi_1^t(t) = I_1(t)R_g + \phi_2^t(t) \qquad \text{(A3.7a)}$$

$$\phi_2^t(t) = [I_1(t) - C_b d\phi_2^t(t)/dt]R_b \qquad \text{(A3.7b)}$$

By substituting (A3.7b) into (A3.7a), it leads to

$$\phi_1^t(t) = [\phi_2^t(t)/R_b + C_b(d\phi_2^t(t)/dt)]R_g + \phi_2^t(t)$$

$$= [1 + R_g/R_b]\phi_2^t(t) + [C_bR_g]d\phi_2^t(t)/dt \qquad \text{(A3.8)}$$

Since $\phi_2^t(t) = k_1\exp(\alpha_1 t) + k_2\exp(\alpha_2 t)$ and $\phi_1^t(t) = k_3\exp(\alpha_1 t) + k_4\exp(\alpha_2 t)$ Eq. (A3.8) can be rearranged to be

$$\phi_1^t(t) = [1 + R_g/R_b + C_bR_g\alpha_1]k_1\exp(\alpha_1 t) + [1 + R_g + C_bR_g\alpha_2]k_2\exp(\alpha_2 t)$$

$$= k_3\exp(\alpha_1 t) + k_4\exp(\alpha_2 t) \qquad \text{(A3.9)}$$

Hence, the relationsbetween $k_1 \sim k_2$ and $k_3 \sim k_4$ are obtained as

$$k_3 = (1 + R_g/R_b + C_b R_g \alpha_1)k_1$$

$$\text{(A3.10)}$$

$$k_4 = (1 + R_g/R_b + C_b R_g \alpha_2)k_2$$

The total time response of voltages $\phi_1(t)$ and $\phi_2(t)$ across the capacitor C_t and the resistor R_b can be expressed as

$$Re[\phi_1(t)] = k_3 \exp(\alpha_1 t) + k_4 \exp(\alpha_2 t) + Re[\phi_1^S(t)]$$

$$\text{(A3.11)}$$

$$Re[\phi_2(t)] = k_1 \exp(\alpha_1 t) + k_2 \exp(\alpha_2 t) + Re[\phi_2^S(t)]$$

where $\phi_1^S(t)$ and $\phi_2^S(t)$ are in Eqs. (A2.2). By using initial conditions $\phi_1(0)$ and $\phi_2(0)$ of Eqs. (A3.1) and Eqs. (A3.11), we have

$$Re[\phi_1(0)] = Re[\phi_{cm}(Z_{Ct}/(Z_{Cc} + Z_{Ct}))] = k_3 + k_4 + Re[\phi_{1m}] \quad \text{(A3.12a)}$$

$$Re[\phi_2(0)] = Re[\phi_{bm}(R_b/(Z_{Cb} + R_b))] = k_1 + k_2 + Re[\phi_{2m}] \quad \text{(A3.12b)}$$

Since R_b ($\sim$ kΩ) $\ll Z_{Cb}$ ($\sim$ MΩ) as observed in Fig. 7.9 – Fig. 7.11, the following relation can be obtained

$$\phi_2(0) \approx 0 \quad \Rightarrow \quad k_2 \approx -k_1 - Re[\phi_{2m}] \quad \text{(A3.13)}$$

Now, using Eqs. (A3.10), (A3.11a) and (A3.12) we have

$$k_3 + k_4 = (1 + R_g/R_b + C_bR_g\alpha_1)k_1 - (1 + R_g/R_b + C_bR_g\alpha_2)(k_1 + Re[\phi_{2m}])$$

$$= (C_bR_g\alpha_1 - C_bR_g\alpha_2)k_1 - (1 + R_g/R_b + C_bR_g\alpha_2)Re[\phi_{2m}]$$

$$= Re[\phi_1(0)] - Re[\phi_{1m}] \tag{A3.14}$$

Hence k_1 is found to be

$$k_1 = (Re[\phi_1(0)] - Re[\phi_{1m}])/(C_bR_g\alpha_1 - C_bR_g\alpha_2) +$$

$$Re[\phi_{2m}](1 + R_g/R_b + C_bR_g\alpha_2)/(C_bR_g\alpha_1 - C_bR_g\alpha_2) \tag{A3.15}$$

The following equations are summary of the transient response of $\phi_1^t(t)$ and $\phi_2^t(t)$:

$$\phi_1^t(t) = k_3\exp(\alpha_1 t) + k_4\exp(\alpha_2 t)$$

$$\phi_2^t(t) = k_1\exp(\alpha_1 t) + k_2\exp(\alpha_2 t)$$

where

$$k_1 = (Re[\phi_1(0)] - Re[\phi_{1m}])/(C_bR_g\alpha_1 - C_bR_g\alpha_2) +$$

$$Re[\phi_{2m}](1 + R_g/R_b + C_bR_g\alpha_2)/(C_bR_g\alpha_1 - C_bR_g\alpha_2)$$

$$k_2 = -k_1 - \text{Re}[\phi_{2m}]$$

$$k_3 = (1 + R_g/R_b + C_b R_g \alpha_1)k_1$$

$$k_4 = (1 + R_g/R_b + C_b R_g \alpha_2)k_2$$

and

$$\phi_1(0) = \phi_{cm}[C_c/(C_c + C_t)]$$

ϕ_{1m} and ϕ_{2m} can be found in Eqs. (A2.5a) and (A2.5b).

APPENDIX 4

QUASI-STATIC CURRENT FLOWING IN AN HETEROGENEOUS CONDUCTOR [35]

Consider a conducting body immersed in a slowly time-varying electric field of

$$\vec{E}_o = \vec{E}_o \cos\omega t = Re[\vec{E}_o e^{j\omega t}] \qquad \omega : small \qquad (A4.1)$$

There will be an induced current $\vec{J}$ inside the body, as evidenced by the movement of induced surface charges (Fig. A4.1). Thus, the conductivity (σ) and the permittivity (ϵ) of the body will affect the induced $\vec{E}$ field and the induced current $\vec{J}$ in the body. The current $\vec{J}$ can be calculated from

$$\vec{J} = (\sigma + j\omega\epsilon)\vec{E} = j\omega(\epsilon - j\sigma/\omega)\vec{E}$$

$$= j\omega\hat{\epsilon}\vec{E} \qquad (A4.2)$$

where $\hat{\epsilon} = (\epsilon - j\sigma/\omega)$ is the complex permittivity.

The medium propagation constant γ is defined as

$$\gamma = \omega[\mu\hat{\epsilon}]^{1/2} = [\omega^2\mu\epsilon - j\omega\mu\sigma]^{1/2} \qquad (A4.3)$$

where μ is the permeability of the body. Let ℓ be the physical dimension of the body, if $|\gamma\ell| \ll 1$, then the *quasi-static approximation* can be
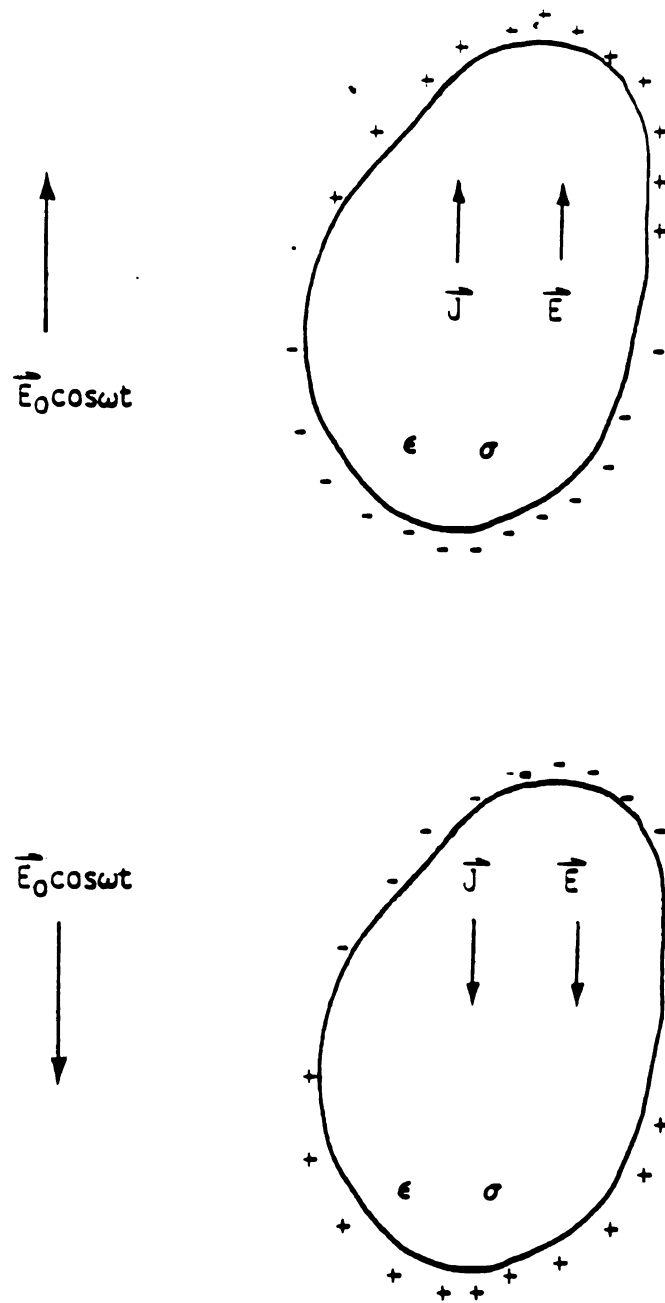
Fig. A4.1. A biological body is immersed ina slowly time-varying
electric field.

applied to this problem as follows. Maxwell's equations for slowly time-varying fields can be written as

$$\nabla \times \vec{E}(\vec{r},t) = -\partial\vec{B}(\vec{r},t)/\partial t \approx 0$$

$$\nabla \times \vec{H}(\vec{r},t) = \sigma\vec{E}(\vec{r},t) + \epsilon[\partial\vec{E}(\vec{r},t)/\partial t]$$

(A4.4)

If $\vec{E}(\vec{r},t) = Re[\vec{E}(\vec{r})e^{j\omega t}]$ and $\vec{H}(\vec{r},t) = Re[H(\vec{r})e^{j\omega t}]$, then Eq. (A4.4) can be rewritten as

$$\nabla \times \vec{E}(\vec{r}) = -j\omega B(\vec{r}) \approx 0$$

$$\nabla \times \vec{H}(\vec{r}) = (\sigma + j\omega\epsilon)\vec{E}(\vec{r}) = \vec{J}(\vec{r})$$

(A4.5)

Thus the following equations can be constructed

$$\nabla \times \vec{E}(\vec{r}) \approx 0$$

$$\nabla \cdot \vec{E}(\vec{r}) = 0 \qquad \text{if } \sigma \text{ and } \epsilon \text{ are constant}$$

$$\nabla \times \vec{H}(\vec{r}) = \vec{J}(\vec{r})$$

$$\nabla \cdot \vec{H}(\vec{r}) = 0$$

(A4.6)

The equations for $\vec{E}$ field are the same as that in electrostatic case, therefore, the $\vec{E}$ field can be treated like an electrostatic field and solved using one of the electrostatic methods. Once $\vec{E}(r)$ is determined, the induced current $\vec{J}$ can be calculated from

$$\vec{J} = (\sigma + j\omega\epsilon)\vec{E}(\vec{r})e^{j\omega t} \tag{A4.7}$$

It is noted that the phase of $\vec{J}(t)$ is different from that of $\vec{E}(t)$.

From the quasi-static approximation of

$$\nabla \times \vec{E} = 0, \tag{A4.8}$$

a scalar potential V can be defined as

$$\vec{E} = -\nabla V \tag{A4.9}$$

Since in Eq. (A4.6), $\nabla \times \vec{H} = \vec{J} = (\sigma + j\omega\epsilon)\vec{E}$, the following relation is achieved

$$\nabla \cdot (\nabla \times \vec{H}) = 0 = \nabla \cdot [(\sigma + j\omega\epsilon)\vec{E}]$$

$$= (\sigma + j\omega\epsilon)\nabla \cdot \vec{E} + \nabla(\sigma + j\omega\epsilon)\cdot\vec{E} \tag{A4.10}$$

If σ and ϵ are constants in the body,

$$\nabla(\sigma + j\omega\epsilon) = 0$$

and hence

$$\nabla \cdot \vec{E} = 0 \tag{A4.11}$$

Thus, Eqs. (A4.9) and (A4.11) lead to

$$-\nabla \cdot (\nabla V) = 0$$

or

$$\nabla^2 V = 0 \tag{A4.12}$$

The Laplace equation is still valid in a source-free, homogeneous body for slowly time-varying fields.

Now consider a concentric-sphere located in a homogeneous medium of complex conductivity $\hat{\sigma}$ and immersed in a slowly time-varying electric field, as shown in Fig. A4.2. The inner core of the sphere has a radius a and a complex conductivity $\hat{\sigma}_1$, while the outer shell of thickness $(b - a)$ has a complex conductivity $\hat{\sigma}_2$. Under the quasi-static approximation, the primary potential $V^p(r,\theta)$ associated with the primary incident field $\vec{E}_o$ is

$$V^p(r,\theta) = -E_o r \cos\theta \tag{A4.13}$$

The secondary potentials due to the induced charges in and on the sphere are

$$V^s(r,\theta) \quad \text{for} \quad b < r$$

$$V_1^s(r,\theta) \quad \text{for} \quad a < r < b \tag{A4.14}$$

$$V_2^s(r,\theta) \quad \text{for} \quad 0 < r < a$$

The total potentials are
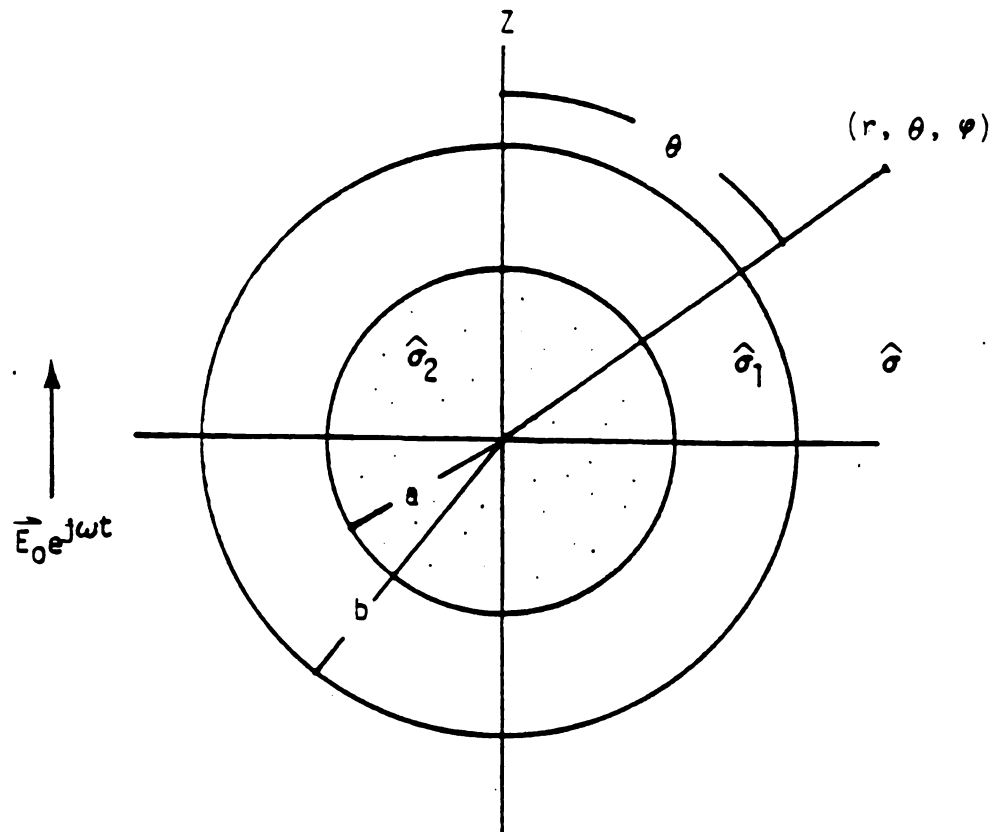
Fig. A4.2. A conducting concentric-sphere located in a homogeneous conducting medium is immersed in a slowly time-varying electric field.

$$V(r,\theta) = V^P(r,\theta) + V^S(r,\theta) \quad \text{for} \quad b < r$$

$$V_1(r,\theta) = V^P(r,\theta) + V_1^S(r,\theta) \quad \text{for} \quad a < r < b \qquad (A4.15)$$

$$V_2(r,\theta) = V^P(r,\theta) + V_2^S(r,\theta) \quad \text{for} \quad 0 < r < a$$

The possible solutions for V^S, V_1^S and V_2^S can be written as [35]

$$V^S(r,\theta) = \sum_{n=0}^{\infty} H_n r^{-(n+1)} P_n(\cos\theta) \qquad \text{for} \quad b < r$$

$$V_1^S(r,\theta) = \sum_{n=0}^{\infty} (G_n^1 r^n + H_n r^{-(n+1)}) P_n(\cos\theta) \qquad \text{for} \quad a < r < b$$

$$V_2^S(r,\theta) = \sum_{n=0}^{\infty} G_n^2 r^n P_n(\cos\theta) \qquad \text{for} \quad 0 < r < a$$

$$(A4.16)$$

Thus, the total potential for these regions are

$$V(r,\theta) = -E_o r\cos\theta + \sum_{n=0}^{\infty} H_n r^{-(n+1)} P_n(\cos\theta) \qquad \text{for} \quad b < r$$

$$V_1(r,\theta) = -E_o r\cos\theta + \sum_{n=0}^{\infty} (G_n^1 r^n + H_n r^{-(n+1)}) P_n(\cos\theta) \quad \text{for} \quad a < r < b$$

$$V_2(r,\theta) = -E_o r\cos\theta + \sum_{n=0}^{\infty} G_n^2 r^n P_n(\cos\theta) \qquad \text{for} \quad 0 < r < a$$

$$(A4.17)$$

where P_n is the Legendre function and $\{H_n\}$, $\{G_n^1\}$, $\{H_n^1\}$, and $\{G_n^2\}$ are constants to be determined by matching boundary conditions at the boundaries of $r = a$ and $r = b$.

The boundary conditions at r = a and r = b are

(1) $V_1(a,\theta) = V_2(a,\theta)$

(2) $J_{r1}(a,\theta) = J_{r2}(a,\theta)$

(3) $V_1(b,\theta) = V(b,\theta)$

(4) $J_{r1}(b,\theta) = J_r(b,\theta)$

where J_{r1} and J_{r2} are r-components of currents.   Following these boundary conditions leads to

(1) $G_n^2 = G_n^1 + H_n^1 a^{-(2n+1)}$

(2) $(\hat{\sigma}_1 - \hat{\sigma}_2)E_o = -(\hat{\sigma}_2 - \hat{\sigma}_1)G_1^1 - (\hat{\sigma}_2 + 2\hat{\sigma}_1)a^{-3}H_1^1$ for n = 1

$(\hat{\sigma}_2 - \hat{\sigma}_1)na^{n-1}G_n^1 + [\hat{\sigma}_2 n + \hat{\sigma}_1(n + 1)]a^{-(n+2)}H_n^1 = 0$ for n = 2,3,..

(3) $H_n = H_n^1 + G_n^1 b^{(2n+1)}$

(4) $(\hat{\sigma}_1 - \hat{\sigma})E_o = (\hat{\sigma}_1 - \hat{\sigma})G_1^1 + (\hat{\sigma} - 2\hat{\sigma}_1)2b^{-3}H_1^1$ for n = 1

$[\hat{\sigma}_1 + \hat{\sigma}(n + 1)]b^{n-1}G_n^1 + (\hat{\sigma} - \hat{\sigma}_1)(n + 1)b^{-(n+2)}H_n^1 = 0$ for n = 2,3,..

By arranging the above relations, the following equations are obtained

$$G_1^1 = \left[\frac{(\hat{\sigma}_1 - \hat{\sigma})(2\hat{\sigma}_1 + \hat{\sigma}_2) - (\hat{\sigma}_1 - \hat{\sigma}_2)(\hat{\sigma}_1 - \hat{\sigma})2a^3/b^3}{(\hat{\sigma}_1 + 2\hat{\sigma})(2\hat{\sigma}_1 + \hat{\sigma}_2) - (\hat{\sigma}_1 - \hat{\sigma}_2)(\hat{\sigma}_1 - \hat{\sigma})2a^3/b^3} \right] E_o$$

$$G_1^2 = \left[\frac{(\hat{\sigma}_1 - \hat{\sigma})(2\hat{\sigma}_1 + \hat{\sigma}_2) - (\hat{\sigma}_1 - \hat{\sigma}_2)(\hat{\sigma}_1 - \hat{\sigma})2a^3/b^3 + 3\hat{\sigma}(\hat{\sigma}_2 - \hat{\sigma}_1)}{(\hat{\sigma}_1 + 2\hat{\sigma})(2\hat{\sigma}_1 + \hat{\sigma}_2) - (\hat{\sigma}_1 - \hat{\sigma}_2)(\hat{\sigma}_1 - \hat{\sigma})2a^3/b^3} \right] E_o$$

$$H_1^1 = \left[\frac{3\hat{\sigma}(\hat{\sigma}_2 - \hat{\sigma}_1)a^3}{(\hat{\sigma}_1 + 2\hat{\sigma})(2\hat{\sigma}_1 + \hat{\sigma}_2) - (\hat{\sigma}_1 - \hat{\sigma}_2)(\hat{\sigma}_1 - \hat{\sigma})2a^3/b^3} \right] E_o$$

$$H_1 = \left[\frac{(\hat{\sigma}_1 - \hat{\sigma})(2\hat{\sigma}_1 + \hat{\sigma}_2) + (\hat{\sigma}_2 - \hat{\sigma}_1)(2\hat{\sigma}_1 + \hat{\sigma})a^3/b^3}{(\hat{\sigma}_1 + 2\hat{\sigma})(2\hat{\sigma}_1 + \hat{\sigma}_2) + (\hat{\sigma}_2 - \hat{\sigma}_1)(\hat{\sigma}_1 - \hat{\sigma})2a^3/b^3} \right] b^3 E_o$$

(A4.18)

and

$$G_n^1 = H_n^1 = 0 \qquad \text{for } n = 2, 3, \ldots\ldots$$

The total potentials can thus be expressed as $(P_1(\cos\theta) = \cos\theta)$

$$V(r,\theta) = -E_o r\cos\theta + H_1\cos\theta/r^2 \qquad \text{for } b < r$$

$$V_1(r,\theta) = (-E_o + G_1^1)r\cos\theta + H_1^1\cos\theta/r^2 \qquad \text{for } a < r < b \qquad \text{(A4.19)}$$

$$V_2(r,\theta) = -E_o r\cos\theta + G_1^2 r\cos\theta \qquad \text{for } 0 < r < a$$

The induced electric fields inside the sphere can then be determined as

$$\vec{E}_1(r,\theta) = -\nabla V_1(r,\theta) = -\hat{r}(\partial V_1/\partial r) - \hat{\theta}(\partial V_1/\partial \theta)/r$$

$$= \hat{r}\cos\theta(E_o - G_1^1 + 2H_1^1/r^3) + \hat{\theta}\sin\theta(-E_o + G_1^1 + H_1^1/r^3)$$

for $a < r < b$

$$\vec{E}_2(r,\theta) = -\nabla V_2(r,\theta) = -\hat{r}(\partial V_2/\partial r) - \hat{\theta}(\partial V_2/\partial \theta)/r$$

$$= \hat{r}\cos\theta(E_o - G_1^2) + \hat{\theta}\sin\theta(-E_o + G_1^2)$$

$$= \hat{z}(E_o - G_1^2)$$

for $0 < r < a$ (A4.20)

A special case of a concentric-sphere is a homogeneous sphere of which $\hat{\sigma}_1 = \hat{\sigma}_2$ and

$$H_1 = [(1 - \hat{\sigma}/\hat{\sigma}_1)/(1 + 2\hat{\sigma}/\hat{\sigma}_1)]b^3 E_o$$

$$H_1^1 = 0$$

$$G_1^1 = [(1 - \hat{\sigma}/\hat{\sigma}_1)/(1 + 2\hat{\sigma}/\hat{\sigma}_1)]E_o$$ (A4.21)

$$G_1^2 = [(1 - \hat{\sigma}/\hat{\sigma}_1)/(1 + 2\hat{\sigma}/\hat{\sigma}_1)]E_o$$

Therefore, the induced field inside the sphere is

$$\vec{E}_1(r,\theta) = [3(\hat{\sigma}/\hat{\sigma}_1)/(1 + 2\hat{\sigma}/\hat{\sigma}_1)](r\cos\hat{\theta} - \theta\sin\hat{\theta})E_o$$

$$= \hat{z}[3(\hat{\sigma}/\hat{\sigma}_1)/(1 + 2\hat{\sigma}/\hat{\sigma}_1)]E_o \qquad (A4.22)$$

It is observed that the induced electric field inside a homogeneous sphere is uniform and in the z-direction which is the same as that in a dielectric sphere except the permittivity (ϵ) of the latter is replacing the complex conductivity ($\hat{\sigma}$) of the former.

BIBLIOGRAPHY

BIBLIOGRAPHY

[1] J.E. Bridges and M. Preache, "*Biological influence of power frequency electric fields-a tutorial review from a physical and experimental viewpoint,*" Proc. IEEE, pp. 1092-1120, 1981.

[2] M.H. Benedick and B. Greenberg, "*The sanguine biological-ecological research program,*" IEEE Trans. Communication (special issue on Extreamely Low Frequency (ELF) Communications), vol. COM-22, pp-570-577, April 1974.

[3] J.D. Grissett, "*Biological effects of electric and magnetic fields associated with ELF communication systems,*" Proc. IEEE, pp. 98-104, 1980.

[4] M.G. Morgan et al., "*Power-line fields and human health,*" IEEE Spectrum, pp. 62-68, February 1985.

[5] D.V. Deno, "*Currents induced in the human body by high voltage transmission line electric field : measurement and calculation of distribution and dose,*" IEEE Trans. Power Appratus and Systems, vol. PAS-96, no. 5, pp. 1517-1527, Sept/Oct. 1977.

[6] A.W. Guy, M.D. Webb and C.C. Sorensen, "*Determination of absorption rate in man exposed to high frequency electromagnetic fields by thermographic measurements on scale models,*" IEEE Trans. Biomedical Engineering, vol. BME-23, pp. 361-371, 1976.

[7] W.T. Kaune and M.F. Gillis, "*General properties of the interaction between animals and ELF electric fields,*" Bioelectromagnetics, vol. 2, pp. 1-11, 1980.

[8] W.T. Kaune and R.D. Phillips, "*Comparison of the coupling of grounded humans, swine and rats to vertical 60-Hz electric fields,*" Bioelectromagnetics, vol. 1, pp. 117-129, 1980.

[9] W.T. Kaune and M.C. Miller, "*Short-circuit currents, surface electric fields, and axial current densities for guinea pigs exposed ELF electric fields,*" Bioelectromagnetics, vol. 5, pp. 361-364, 1984.

[10] W.T. Kaune and W.C. Forsythe, "*Current densities measured in human models exposed to 60-Hz electric fields,*" Bioelectromagnetics, vol. 6, pp. 13-32, 1985.

[11] R.J. Spiegel, "*ELF coupling to spherical models of man and animals,*" IEEE Trans. Biomedical Engineering, vol. BME-23, no. 5, September 1976.

[12] Y. Shiau and A.R. Valentino, "ELF electric field coupling to dielectric spheroidal models of biological objects," IEEE Trans. Biomedical Engineering, vol. BME-28, no. 6, pp.429-437, June 1981.

[13] R.J. Spiegel, "High-voltage electric field coupling to humans using moment method techniques," IEEE Trans. Biomedical Engineering, vol. BME-24, no. 5, pp. 466-472, September 1977.

[14] R.J. Spiegle, "Numerical determination of induced currents in humans and baboons exposed to 60-Hz electric fields," IEEE Trans. Electromagnetic Capatability, vol. EMC-23, no. 4, pp. 382-390, Nov. 1981.

[15] A. Chiba, K. Isaka and K. Kitagawa, "Application of finite element method to analysis of induced current densities inside human model exposed to 60-Hz electric field," IEEE Trans. Power Apparatus and System, vol. PAS-103, no. 7, pp. 1895-1902, July 1984.

[16] W.T. Kaune and F.A. McCreary, "Numerical calculation and measurement of 60-Hz current densities induced in a upright grounded cylinder," Bioelectromagnetics, vol. 6, pp.209-220, 1985.

[17] J. Van Bladel, Electromagnetic Fields. New York, McGraw-Hill, 1964.

[18] G. Arfken, Mathematical Methods for Physics. New York, Acedemic Press, 1973.

[19] O.P. Gandi, I. Chatterjee, D. Wu, and Y.G. Gu, "Likelihood of high rates of energy deposition in the human legs at ANSI recommended 3-30 MHz RF safety levels," Proc. IEEE, vol. 73, pp. 1145-1147, June 1985.

[20] R. Tell, E.D. Mantiply, C.H. Durney, and H. Massoudi, IEEE Tran. Broadcasting, to be published.

[21] A.W. Guy and C.K. Chou, "Hazard Analysis," Final Rep. USAF SAM Contract F 33615-78-D-0617 Task 0065, Feb. 1982.

[22] K.L. Gronhaug and O. Busmundrud, "Antenna effect of the human body to EMP," Rep. FFi/NOTAT-82/3013, Norwegian Defense RES. Establishment, P.O. Box 25-N-2007, Kjeller, Norway.

[23] O.P. Gandi, J.Y. Chen and A. Riazi, "Currents induced in a human being for plane-wave exposure conditions 0-50 MHz and for RF sealers," IEEE. Tran. Biomedical Engineering, vol. BME-33, no. 8. August 1986.

[24] D.A. Hill and J.A. Walsh, "Radio-frequency current through the feet of a grounded human," IEEE. Tran. Electromagn. Compat., vol. EMC-27, pp. 18-23, 1985.

[25] O.P. Gandi, E.L. Hunt, and J.A. D'Andrea, "Deposition of electromagnetic energy in animals and in models of man with and without grounding and reflective effects," Radio Sci., vol. 12, pp.39-47, Nov./Dec. 1977.

[26] D.E. Liversay and K.M. Chen, "Electromagnetic fields induced inside arbitrily shaped biological bodies," IEEE Trans. Microwave Theory and Technique, vol. MTT-22, no. 12, pp. 1273-1280, December 1974.

[27] K.M. Chen and B.S. Guru, "Internal EM fields and absorbed power density in human torsos induced by 1-500 MHz EM waves" IEEE Trans. Microwave Theory and Technique, vol. MTT-25, no. 9, pp. 746-756, September 1977.

[28] C.H. Durney, "Electromagnetic dosimetry for models of humans and animals : A review of theoretical and numerical techniques" IEEE Proc. vol. 68, no. 1, pp. 33-40, January 1980.

[29] M.R. Hestenes and E. Stiefel, "Methods of Conjugate Gradients for solving linear systems," J. Res. Nat. Bur. Standards, vol. 49, pp. 409-436.

[30] J. Stoer and R. Bulirsch, Introduction to Numerical Analysis. New York, Springer-Verlag, 1979.

[31] C.A. Desoer and E.S. Kuh, Basic Circuit Theory, New York, McGraw-Hill, 1969.

[32] J.P. Reilly, "Characteristics of spark discharges from vehicles energized by AC electric fields," IEEE Trans. Power Apparatus and Systems, vol. PAS-101, no. 9, September 1982.

[33] M.S. Hammam and R.S. Baishiki, "A range of body impedance values for low voltage, low source impedances systems of 60 Hz," IEEE Trans. Power Apparatus and Systems, vol. PAS-102, no. 5, May 1983.

[34] L. Lapidus, Digital Compuatation For Chemical Engineer. New York, McGraw-Hill, 1962.

[35] J. R. Wait, Electromagnetic Wave Theory. New York, Harper & Row, 1985.

[36] T. K. Sarkar, K. R. Siarkiewick, and R. F. Stratton, "Survey of numerical methods for solution of large systems of linear equations for electromagnetic field problems," IEEE Trans. Antennas and Propagation, vol. AP-29, pp. 847-856, 1981.